Exploring the dynamics of zero-temperature Bose gases : measurement of the superfluid fraction and observation of Bloch-like oscillations of a magnetic soliton

Guillaume Chauveau

Laboratoire Kastler Brossel — Collège de France

Thèse de doctorat de Sorbonne Université

préparée par

Guillaume Chauveau

sous la direction de

Jérôme Beugnon et Jean Dalibard

Exploring the dynamics of zero-temperature Bose gases:

measurement of the superfluid fraction and observation of Bloch-like oscillations of a magnetic soliton

---

Soutenue le 26 Mars 2024 devant le jury composé de :

Mme. Isabelle Bouchoule	Rapportrice
M. Alessio Recati	Rapporteur
M. Jean-Noël Fuchs	Examinateur
M. Christophe Finot	Examinateur
M. Jérôme Beugnon	Directeur de thèse

Travail réalisé au laboratoire Kastler Brossel, au sein du Collège de France.

Abstract

At sufficiently high phase space densities, the many-body state of a degenerate Bose gas can be described by a single macroscopic wavefunction that undergoes nonlinear dynamics. Ultracold Bose gases are a prominent platform in the field of nonlinear physics, enabling the study of stable stationary wavepackets, known as solitons. In these platforms, atom interactions are often weak and treated within a mean-field approach. However, interactions play a crucial role in the physics of these Bose gases and explain for example the formation mechanism of solitons or the emergence of a remarkable phase of matter: superfluidity. This thesis describes investigations on peculiar dynamics of ultracold Bose gases, which are approximated by zero-temperature physics. After introducing our experimental setup and its theoretical characterization, we discuss the survival of the superfluid property in spatially modulated systems, in connection with Leggett's seminal work in 1970 and the spectacular supersolid phase of matter. We then explore the physics of a specific type of 1D soliton that emerges in a weakly-immiscible two-component mixture, known as the magnetic soliton. Its name originates from its appearance in 1D ferromagnetic spin chains. Magnetic solitons exhibit a captivating periodic motion under a uniform force field, similar to the Bloch oscillations of electrons in solids. Finally, we introduce a new experimental setup for studying Rydberg excitations and the realization of an all-optical Bose-Einstein-Condensate.

Résumé

Pour des densités dans l'espace des phases suffisamment grandes, l'état à N corps d'un gaz de Bose dégénéré peut se décrire par une unique fonction d'onde macroscopique qui obéit à une dynamique non linéaire. Les gaz de bosons ultrafroids sont devenus une plateforme de choix pour la mise en évidence de phénomènes non linéaires, permettant l'étude des solitons, des paquets d'onde stationnaires ayant des propriétés de stabilité remarquables. Les interactions entre atomes dans cette plateforme sont souvent faibles et peuvent être traitées dans une approche de champ moyen. Malgré cela, les interactions jouent un rôle prépondérant dans la physique de ces gaz et permettent d'expliquer notamment le mécanisme de formation des solitons, mais aussi l'émergence d'un état superfluide de la matière à basse température. Cette thèse décrit de récentes études de dynamique de gaz de Bose, menées à température nulle. Après avoir introduit la plateforme expérimentale utilisée ainsi qu'une description théorique de ces gaz de Bose, nous discutons le devenir de la propriété de superfluidité en présence d'une modulation spatiale. Ce travail est en lien direct avec les travaux menés par Leggett en 1970 et avec un état spectaculaire de la matière, connu sous le nom de supersolide. Nous explorons ensuite la physique d'un type spécifique de soliton unidimensionnel, qui apparaît dans des mélanges de spin faiblement immiscibles à deux composantes et qui est connu sous le nom de soliton magnétique. Cette désignation provient d'un autre contexte dans lequel ce soliton apparaît: une chaîne ferromagnétique de spins. Les solitons magnétiques répondent de manière spectaculaire à l'application d'une force uniforme: ils oscillent périodiquement dans le temps, de manière similaire au mouvement d'électrons dans le potentiel périodique créé par des solides, connu sous le nom d'oscillations de Bloch. Pour finir, nous discuterons le début de la construction d'une nouvelle plateforme expérimentale, visant dans le futur à étudier des excitations Rydberg, et la réalisation d'un condensat de Bose-Einstein sans utiliser de pièges magnétiques.

Remerciements

Les quelques lignes qui suivront sont dédiées aux personnes qui m'ont entouré et soutenu durant ce long chemin qu'est une thèse.

Je souhaite commencer par remercier Isabelle, Alessio, Christophe et Jean-Noël d'avoir accepté de faire partie de mon jury. Le choix d'Alessio était une évidence étant donné son expertise sur les deux sujets scientifiques discutés au cours de cette thèse. C'était aussi le cas pour Isabelle, spécialiste des gaz 1D depuis plusieurs années. Je la remercie pour son implication dans son rapport scientifique du manuscrit. Christophe et Jean-Noël, même si leurs activités de recherche actuelles sont un peu plus éloignées de ce que j'ai discuté dans ma thèse, se sont investis dans ce jury et je les remercie pour les discussions intéressantes qu'on a pu avoir.

Les remerciements sont ensuite naturellement dirigés vers mes encadrants durant cette thèse.

Jérôme m'a donné goût à la physique quantique et des atomes froids lors de son enseignement à l'ENS en 2017. Ensuite, après un stage de recherche quelque peu mitigé en Autriche, je pensais directement prendre un poste d'enseignant après l'année d'agrégation. Finalement, j'ai visité les manips du Collège de France, revu Jérôme et cela m'a convaincu de faire une thèse au sein de son équipe, ce que je ne regrette absolument pas. Si je me risque à une blague de physicien quantique, une thèse avec Jérôme c'est être dans une superposition quantique de l'état "accompagnement et discussion quotidiens" et l'état "liberté de prendre des initiatives". Selon mon point de vue, c'est une supervision très intelligente d'autant qu'il sait faire évoluer cet équilibre à notre niveau d'expérience dans l'équipe. Je remercie Jérôme de m'avoir proposé une thèse aussi diversifiée (construction, simulations numériques, prise de données, exploration de nouveaux projets...). En plus de ses qualités pédagogiques, de management et évidemment scientifiques, Jérôme a su m'inculquer des méthodes de travail qui je l'espère me serviront pendant longtemps : gestion du temps de travail (j'ai pu donc éviter d'aller à la formation de 8h qui y était dédiée !), calme et patience (même en des conditions extrêmes comme lorsque j'ai cassé une cellule à vide lors du montage du système à vide Rb4 à cause de ma force de clampeur professionnel), esprit de synthèse, etc. Pour finir, il possède des convictions personnelles que je partage : dépassement de soi, soucis de notre impact écologique, goût des choses simples. Merci Jérôme pour ces quatre années passées sous ta direction.

Dans notre équipe, nous avons l'immense chance d'avoir 3 membres permanents. En plus de Jérôme, Jean et Sylvain participent activement à la vie scientifique de l'équipe. Travailler avec quelqu'un du savoir et de l'expérience de Jean est un privilège et j'ai l'impression d'apprendre énormément à chacune de nos discussions. Je remercie Jean pour son impressionnante humilité, sa porte toujours ouverte, son goût d'aller au bout des choses, ses calculs toujours complets et ses cours du Collège qui, pour le futur enseignant que je souhaite être, sont des exemples extraordinaires de pédagogie. Sylvain est aussi essentiel à l'équipe Rubidium. Ses idées et calculs m'ont beaucoup apporté et inspiré. Je le remercie aussi pour son humilité et son abordabilité. Travailler au LKB et être au contact d'un si grand nombre de chercheurs à la pointe de leur domaine était un privilège qui stimule l'activité scientifique. Je remercie aussi Sandro, Santo et plus récemment Kévin, venus depuis Trente, d'avoir partagé quelques moments en notre compagnie et de nous avoir aidé à appréhender le projet superfluidité en présence d'un réseau.

Le quotidien sur une manip aussi complexe qu'une manip d'atomes froids est presque tout le temps plus facile quand il est partagé avec d'autres étudiants. J'ai eu la chance au cours de ma thèse dans cette équipe d'avoir connu une densité constante de $\gtrsim 3$ étudiants sur mes 4 années. Lorsque je suis arrivé, Édouard était en train de terminer, merci d'avoir formé un exemple de profil que je pouvais suivre ! Le duo très soudé Brice et Chloé a ensuite pris la suite. Je les remercie pour leurs conseils sur la prise en main de la manip. Comme ils le savent, j'aurais aimé qu'ils ouvrent beaucoup plus la porte (au sens propre comme au sens figuré) à la formation d'un trio, au moins sur le plan scientifique, surtout pendant une période difficile pour moi sur le plan personnel. C'est dommage mais il me semble malgré tout que ça n'a pas trop impacté notre travail scientifique. Merci à Brice pour sa présence pendant sa rédaction et pour avoir été une source d'inspiration pour de nombreuses slides de ma soutenance. Merci à Chloé pour avoir défriché une bonne partie du projet Leggett. Je n'oublie pas la présence de Yiquan pendant ma première année de thèse qui m'a fait très souvent me sentir moins seul au bureau et a aussi été d'une précieuse aide sur la construction de Rb4.

Ma thèse a pris une nouvelle tournure quand Franco a rejoint l'équipe en 2021. Son écoute, son soutien et son dynamisme m'ont donné confiance en moi pendant une période personnelle compliquée. Franco est un étudiant extrêmement rigoureux, talentueux et humble avec qui il a tout de suite été facile de travailler. J'ai énormément progressé à ses côtés que ce soit sur le plan expérimental sur Rb4 avec, par exemple, la technique de painting qu'on a mis en place ensemble, ou théorique avec son impressionnante volonté d'aller au bout des choses. Ses qualités de codeur ne sont plus à démontrer et j'ai aussi beaucoup appris grâce à lui dans ce domaine. Son arrivée sur Rb3 a aussi changé beaucoup de choses et a redynamisé le projet Leggett pour arriver à l'amener au bout avec par exemple l'extraction de la deuxième harmonique. Nous avons ensuite attaqué le projet soliton magnétique et l'obtention du premier signal d'oscillations sans fragmentation restera un moment fort que nous avons partagé. Franco a aussi fait preuve d'une remarquable patience pendant les deux mois de galère expérimentale qui ont suivi. En plus de ses qualités scientifiques, Franco a apporté énormément à la vie d'équipe par sa générosité, son franc-parler, ses "unpopular opinion" et ce toujours dans l'écoute, le débat bienveillant et la bonne humeur. Franco, je te remercie pour tes qualités de chercheur et d'ami pendant mes 3 années de thèse, qui auraient été bien différentes si tu n'avais pas décidé de rejoindre l'équipe.

Guillaume, alias GB, a rejoint l'équipe en 2022. Dès son arrivée, il a fait preuve d'une capacité à abattre du travail très impressionnante, toujours avec une humeur constante. Il n'est pas difficile de deviner qu'il a toutes les qualités pour devenir un très grand chercheur et il m'a beaucoup appris sur les quelques mois que nous avons passé ensemble sur Rb4 ou Rb3. À chaque fois, c'était pour prendre des données et j'ai senti quelqu'un qui maîtrisait son sujet et était d'une efficacité bluffante pour son niveau d'expérience sur les manips respectives. C'est toujours plus facile de changer de manip lorsque l'on sait que celle qu'on laisse est entre d'aussi bonnes mains. J'espère pouvoir retravailler avec GB dans les mois à venir. Sur le plan humain, nous avons aussi beaucoup de choses en commun : le goût de la free food, de la Savoie, de la course à pied, des paris vélo et je suis persuadé que nous resterons en contact après mon passage dans l'équipe.

Sarah est la dernière thésarde arrivée dans l'équipe. Elle m'a gentiment accepté dans son bureau pour ma rédaction et je la remercie pour son soutien et sa bonne humeur même lorsque la mienne était plus fluctuante. Sur ces derniers mois, j'ai pu voir sa progression et sa détermination qui sont prometteuses pour son avenir

et celui de l'équipe. Elle a fait preuve d'une grande patience lorsqu'il a fallu déplacer/reconstruire la manip et elle m'a beaucoup impressionné sur son abnégation et son travail souvent solitaire sur les micro-pièges. J'espère aussi pouvoir travailler à ses côtés car c'est en plus quelqu'un que j'apprécie beaucoup sur le plan humain.

Je n'oublie pas les autres personnes qui sont passées dans l'équipe Rubidium pendant ma thèse. Carl nous a rejoints depuis Heidelberg en septembre 2022 et il a été d'une aide (les morning checks sont renommés depuis Morgen Überprüfen) et d'une écoute précieuses sur le projet Leggett. Je le remercie pour sa patience alors que je commençais à m'épuiser sur ce projet. Nous avons ensuite démarré ensemble le projet soliton et c'était très stimulant de travailler avec toi. Merci Carl d'avoir été là pour ma soutenance aussi, ça m'a beaucoup touché. Yifan nous a rejoints début 2024 pour un post doc et même si je n'ai pas encore travaillé avec elle, c'est une personne qui me semble très douée, désireuse d'apprendre, d'aider et qui s'est très bien intégrée dans l'équipe en peu de temps ! Je souhaite aussi avoir un mot pour les stagiaires de l'équipe que j'ai pu côtoyer (Malik, Callum, Sarah, Alexandre, Alice, Thibault, Jonathan, etc.) qui nous ont aidés pendant quelques mois.

Le deuxième étage du Collège n'est pas seulement occupé par des Rubidium. Je remercie les autres équipes que j'ai pu côtoyer. Chez Dy, la présence de JB à mes côtés pendant toute ma thèse m'a énormément apporté. Nous sommes arrivés ensemble au labo en pleine période Covid et même si nous n'avions pas le droit de nous "mélanger" entre manips, le savoir dans la même situation que moi m'a réconforté. Il a été des premiers bataillons des tupeurs + coureurs que j'ai rejoints ensuite et les '{}' que nous avons partagé m'ont souvent détendu !.format(délires) Le stage piscine et le benchmark poké à EGAS, ainsi que les soirées pool ont été d'autres moments marquants. Merci JB d'avoir été un ami présent pendant ces 4 années de thèse. Dans l'équipe Dy, je remercie aussi Quentin, un autre travailleur acharné, pour sa bonne humeur contagieuse et pour m'accompagner dans l'épreuve de la calvitie ; Tanish, Aurélien, Alex pour leurs bonnes humeurs au quotidien ; Nehal, Evgenii pour les déjeuners partagés ensemble. Je pense aussi à Rémy le dernier rescapé de l'équipe Yb qui m'a beaucoup impressionné pendant sa thèse par son acharnement et son flegme caractéristique. Pendant ma thèse, j'ai aussi assisté de très près à la naissance de l'équipe Dy/K ayant partagé un labo avec eux pendant plus d'un an. Je voudrais remercier Raphaël pour nous avoir fait un peu de place dans son labo. Il m'a souvent aidé à débuguer des problèmes sur la manip quand ça n'allait pas et sa capacité de travail et de lecture de photodiode sont inspirantes. Je remercie aussi Maxime et Alex pour les discussions diverses et variées qu'on a pu avoir. Enfin, je n'oublie pas Alexei et son équipe avec qui les échanges sont toujours constructifs. Je souhaite aussi remercier vivement l'administration du LKB et Carmen au Collège pour leur aide et leurs réponses rapides à mes interrogations, ce qui nous rend la vie plus facile au quotidien.

En dehors du labo, j'ai pu compter sur le soutien de nombreux amis et de la famille. Même si je communique pour la plupart peu avec eux étant donné mon peu d'attrait pour le téléphone, ils ont toujours su être présents durant ces 4 années. Je vois la thèse comme un aboutissement de presque 10 années d'études. Celles-ci ont commencé à Champollion en compagnie de la team Thonon: Max, Adri, Antho, .., Ben et Stan. Nos rassemblements annuels à Toulouse, Lille ou Paris restent à chaque fois des moments très forts où mon taux d'alcoolémie est à la hauteur du plaisir de passer du temps avec les bros. J'y ai aussi rencontré Cam's et Ben qui maintenant sont juste à côté du Collège et les déjeuners/jeux/volley en leur compagnie ont toujours été un moment chaleureux. Papy, aussi grenoblois à la base, m'a suivi à Cachan lors de notre passage à l'ENS et même s'il a choisi la facilité en redescendant pour sa thèse

à Lyon, je le remercie pour son soutien à distance. C'est toujours un plaisir de se revoir, désormais souvent pour des aventures plus sportives ! À l'ENS, j'ai rencontré des amis proches qui m'ont aussi beaucoup supporté pendant ma thèse. Je pense à la team Kultte : Thomas, Tom, Lucile, Nicolas, Daudau avec qui au fur et à mesure j'ai partagé bien plus que des séances de course à pied. Je remercie notamment Tom et Lucile pour les nombreux moments partagés ensemble au parc, sur la coulée Verte, chez vous, au ski, en montagne, etc. et votre présence à Bourg-la-Reine pendant les deux premières années de ma thèse ont initialement décidé de mon déménagement dans cette belle ville ! Sans vous, la vie au quotidien y perd de sa saveur, mais même à distance j'ai pu compter sur votre soutien précieux ! Je remercie Thomas pour tous les chemins et routes qu'il m'a fait découvrir au cours de mes années parisiennes, mais aussi pour sa culture générale et ses recettes de cuisine mémorables. Le raid qu'on a partagé ensemble restera un moment fort de cette thèse. Merci à Daudau d'être un aussi bon compagnon d'aventure. J'espère qu'on pourra prendre le temps de se voir pour autre chose qu'un ultra ! J'ai aussi connu Olivier à l'ENS lors de la prépa agrég et j'ai beaucoup appris à ses côtés durant cette année, grâce à sa patience, son sens physique et son sens de la pédagogie. Je le remercie infiniment pour son invitation en Guadeloupe qui est un voyage qui m'a fait un bien fou durant cette thèse à un moment où j'en avais particulièrement besoin. Les moments partagés ensemble, bien que rares, un ballon de volley jamais loin, m'ont beaucoup aidé durant cette thèse et tu es un précieux ami. À Bourg-la-Reine depuis 4 ans, j'ai rejoint le groupe de course du magasin Endurance Shop et découvert des personnes qui ont fait du mercredi soir, la soirée plus détente que je m'octroyais dans la semaine. J'y ai découvert des personnes ouvertes, généreuses et qui sont devenus pour beaucoup d'entre elles des amis sur qui je sais pouvoir compter. Je remercie Romain, Richard, Guillaume, Yoann, Lucie, François, Antoine et tous les autres pour tous ces moments passés ensemble qui se sont vite étendus aux week-end et sorties trail. Le début de notre histoire commune ne fait que commencer !

Enfin, la présence de ma famille à mes côtés durant mes 10 années d'études et particulièrement pendant cette thèse a été mon principal carburant. Je pense d'abord à mes tantes et oncles. Je remercie infiniment Agnès et Emmanuel pour leur accueil au début de ma thèse et pour leurs nombreuses invitations et excellents repas du dimanche à Verrières qui me permettaient bien souvent de décompresser le week-end. Je remercie aussi Christine et Élie pour les beaux moments passés dans votre chère Bretagne que j'aime aussi tant. Je suis aussi très proche de mes cousins et petits-cousins, notamment Manon et Lucas, avec qui j'ai partagé tellement de choses. Le voyage au Canada avec eux, partagé aussi avec Élise, reste un moment mémorable de ma thèse et m'a reboosté à un moment aussi où j'en avais besoin. J'ai aussi eu la chance de pouvoir compter sur Jacques, un parrain très présent pour moi et les visites annuelles à Thionville, avec Clara, Hugo et Magalie, sont toujours de super moments pour moi. Pour finir, cette thèse n'aurait pas été la même sans la présence de la famille montagnarde, Papa, Maman et Élise. Ils ont été d'un soutien constant même dans leurs périodes plus difficiles. Je pense notamment à Élise, qui a énormément souffert l'année dernière et qui a pour autant fait face et continué à me soutenir. Je suis tellement fière d'elle et je veux être plus présent à l'avenir à ses côtés pour plus jouer mon rôle de grand frère. Je remercie aussi Adrien d'être là et de faire maintenant partie intégrante de la famille (même si j'attends que tu te mettes à faire du vrai trail). Je suis souvent redescendu dans les Alpes durant ma thèse pour profiter de ce (ceux) que j'aime le plus et je ne parle pas que des montagnes.

Contents

Introduction 1

I Production and characterization of low-dimensional Bose gases 7

1 Production of ultracold Bose gases in reduced dimensions 8
1.1 Preparation of a 3D ultracold gas . . . 8
1.1.1 ^{87}Rb atom and its structure . . . 9
1.1.2 From a Rb vapour to a 3D BEC . . . 10
1.1.3 Magnetic field and magnetic field gradient controls . . . 11
1.2 Reaching the 2D regime . . . 13
1.3 Tunable shaping of the in-plane potential . . . 14
1.3.1 Tailoring box potentials with DMD1 . . . 15
1.3.2 Precise control of the in-plane potential with DMD2 . . . 16
1.4 Control of the internal state of the cloud . . . 18
1.4.1 Global control - MW transfers . . . 18
1.4.2 Local control - Raman transfers . . . 20
1.5 Conclusion . . . 22

2 Mean-field description of a weakly-interacting 2D Bose gas at $T = 0$ 24
2.1 Description of a weakly-interacting 2D Bose gas at zero temperature . 24
2.1.1 The quantum hamiltonian . . . 24
2.1.2 Ultracold collisions . . . 25
2.1.3 Hartree ansatz and the Gross-Pitaevskii equation . . . 27
2.1.4 The quasi-2D regime . . . 28
2.1.5 Connexion with hydrodynamics . . . 29
2.1.6 Scale invariance of the 2D weakly-interacting Bose gas . . . 30
2.1.7 Conclusion . . . 30
2.2 Precise measurement of atom-dimer interactions . . . 31
2.2.1 Production of dimers via MW photoassociation . . . 31
2.2.2 Atom-dimer interactions . . . 34
2.2.3 Conclusion . . . 35
2.3 A striking property of the 2D weakly-interacting Bose gas at zero temperature: superfluidity . . . 35
2.3.1 Features of superfluidity . . . 35
2.3.2 A link between mean-field description and superfluidity . . . 36
2.3.3 Theoretical description of a superfluid: Two-fluid model and Landau criterion . . . 37
2.3.4 Ground state and elementary excitations of the weakly-interacting 2D Bose gas at $T = 0$ . . . 38
2.3.5 Twisted boundary conditions . . . 40
2.3.6 Conclusion . . . 41
2.4 Is $T = 0$ a reasonable hypothesis? . . . 42

2.4.1 BKT phase transition and the survival of superfluidity 42
2.4.2 Loss of phase ordering and quasi-long range order 42
2.4.3 Conclusion 43
2.5 Summary 43

II Measurement of the zero-temperature superfluid fraction in a spatially modulated Bose gas 45

3 Superfluid fraction in an interacting 2D modulated Bose gas at $T = 0$ 46
3.1 Density modulated systems 46
3.2 Superfluid fraction in a weakly-interacting spatially modulated Bose gas 48
3.2.1 Saturation of Leggett's inequality 48
3.2.2 Sound propagation in a 2D modulated system 50
3.2.3 Limiting cases and analytical estimations 51
3.3 Dynamical determination of the superfluid fraction 54
3.3.1 Numerical simulations 54
3.3.2 Experimental implementation 58
Calibration of the modulation depth 58
Calibration of the magnetic field gradient 61
Experimental measurements of sound velocities 64
3.4 Static determination of the superfluid fraction 66
3.4.1 "Naive" measurements 66
3.4.2 Going further 67
3.5 Comparison of the two methods 69
3.6 Extension of this work to 2D modulated potentials 70
3.6.1 A sufficient condition to saturate Leggett's inequalities? 70
3.6.2 Calculation of the compressibility and the superfluid fraction in 2D weakly-interacting modulated Bose gases 71
3.7 Conclusion 75

III Magnetic solitons and Bloch-like oscillations in a weakly immiscible mixture 77

4 Introduction to the physics of 1D magnetic solitons 78
4.1 1D solitons of the Gross-Pitaevskii equation 78
4.1.1 The 1D regime 79
4.1.2 Soliton background 79
4.1.3 Various classes of solitons of the 1D NLSE 80
Bright solitons 80
Dark solitons 82
Vector solitons 84
The list goes on 85
4.2 Stationary magnetic solitons 86
4.2.1 Magnetization vector in a ferromagnet 86
4.2.2 Stationary magnetic solitons - Easy-plane 89
4.2.3 Stationary magnetic solitons - Easy-axis 91
4.2.4 Connection with BEC mixtures 93
4.2.5 Conserved quantities associated to the magnetic soliton 94
4.3 Conclusion 98

5 Magnetic solitons under a constant force **100**
5.1 Application of a constant force on the magnetic soliton . . . 100
5.1.1 Modification of the coupled nonlinear equations . . . 100
5.1.2 Soliton oscillation . . . 101
5.1.3 Deviation from adiabaticity . . . 106
5.2 Interpretations of the observed oscillations . . . 108
5.2.1 Bloch oscillations and 1D dynamics . . . 108
5.2.2 Analogy with Josephson physics . . . 112
5.2.3 Change of sign for the effective mass . . . 114
5.3 Conclusion . . . 115
5.3.1 Summary . . . 115
5.3.2 Outlook . . . 116

6 Realization of a magnetic soliton and observation of Bloch-like oscillations under a constant force **118**
6.1 Experiments on magnetic solitons in miscible mixtures . . . 118
6.2 Experimental ingredients . . . 121
6.2.1 The 1D regime for spin dynamics . . . 121
6.2.2 An immiscible and long-lived mixture . . . 122
6.2.3 Imprinting a spin-selective spatial profile . . . 124
6.2.4 Imposing a constant differential force . . . 126
6.3 Stationary magnetic soliton . . . 126
6.3.1 Low depleted stationary soliton . . . 126
6.3.2 δg calibration . . . 130
6.3.3 Conclusion . . . 130
6.4 Oscillation of magnetic oscillations under a constant force . . . 132
6.4.1 Short times dynamics . . . 132
6.4.2 Bloch-like oscillations . . . 134
6.4.3 Beyond the adiabatic regime . . . 136
6.4.4 Bath phase evolution . . . 137
6.5 Conclusion . . . 140

IV Production of an all-optical Rb BEC for a new generation of experiments **143**

7 An all-optical Rubidium Bose-Einstein Condensate for Rydberg dressing **144**
7.1 Design and goal of the setup . . . 144
7.1.1 Goal . . . 144
7.1.2 Design and vacuum system . . . 145
7.2 Cooling and imaging: 780 nm lasers . . . 146
7.2.1 Preparation of the beams . . . 146
7.2.2 2D MOT . . . 148
7.2.3 3D MOT . . . 149
7.2.4 Compressed MOT and Molasses . . . 151
7.3 Production of a BEC in a cODT thanks to the painting technique . . . 151
7.3.1 Direct loading in a crossed optical dipole trap . . . 151
7.3.2 All-optical cooling solutions . . . 151
7.3.3 A two-parameter control during the evaporation process . . . 153
7.3.4 Time-averaged potentials . . . 154

Principle . . . 154
Experimental implementation . . . 155
7.3.5 Evaporation . . . 158
7.3.6 Frequencies of the ODT . . . 160
7.4 Outlook . . . 162
7.4.1 The versatily of the painting technique . . . 162
7.4.2 Future of the setup . . . 163
7.5 Conclusion . . . 164

Conclusion **166**

Appendices **169**

A List of publications **170**

B Numerical simulations of the Gross-Pitaevskii equation **172**
B.1 Split-step method . . . 172
B.2 2D GPE numerical resolution . . . 173
B.3 1D coupled GPEs numerical resolution . . . 174

C Analytical expressions of the density modulation under a sinusoidal potential at low modulation depths **177**
C.1 Order 0 in V_0 . . . 177
C.2 Order 1 in V_0 . . . 177
C.3 Order 2 in V_0 . . . 178

D Evaluation of the correcting factors in the *in situ* density measurements **180**
D.1 Notations . . . 180
D.2 Pixelization effect . . . 181
D.3 Determination of the $\beta(q)$ coefficients . . . 182

E Dynamics of solitons of the 1D NLSE under a linear potential **184**
E.1 Bright soliton of the 1D NLSE . . . 184
E.2 Dark soliton of the 1D NLSE . . . 184
E.3 Dark-bright soliton of the 1D NLSE . . . 187

Bibliography **192**

Introduction

Quantum physics governs the behavior of matter at the atomic and subatomic scales. It was developed in the 20^{th} century to explain phenomena that classical physics could not account for, such as Max Planck's black-body radiation problem [1].

The theory elaborated at that time attributed highly counter-intuitive properties to quantum systems by relying on some postulates. These properties include an accessible range of physical quantities (such as energy, momentum, and angular momentum) that are not continuous but discretized, the existence of a certain accuracy limit below which a physical quantity cannot be measured, and the dual behavior of matter and light as both waves and particles. This theory brought controversy to the field, exemplified by the famous Bohr-Einstein debate [2]. The interpretation of quantum mechanics is still highly debated today [3].

One of the most important quantum mechanics postulate concerns the measurement procedure. It is a feature that should be thoroughly reconsidered in the quantum world. In contrast to our daily experiences, it indicates that we can only predict *probabilities* of the outcome of an experiment, rather than certainties. For example, the probability of finding an isolated electron at a given position[1] around a nucleus is obtained by squaring the absolute value of a *complex* number, known as the *wavefunction*, which associates a probability amplitude to each position of the electron. The wavefunction carries the dual property of the quantum object. Each isolated particle is associated with a single wavefunction (particle nature), which evolves according to a wave equation, named the Schrödinger equation[2] (wave nature). In particular, this wave description suggests the possibility of observing striking *matter-wave interferences* when multiple waves overlap [4].

The mathematical description of quantum mechanics postulates that the state describing the quantum object belongs to a Hilbert space, which is a linear space. When it comes to the description of quantum many-body systems, such as a collection of electrons, how can we describe the many-body state? The composite system postulate of quantum mechanics answers this question. In the absence of entanglement, the many-body state is the tensor product state of its individual constituents. Therefore, the size of this tensor-product Hilbert space, in which the many-body wavefunction evolves, grows exponentially with the number of particles. This exponential growth makes it difficult to compute the wavefunction of the many-body problem, both analytically and computationally.

For an ensemble of identical particles, the symmetrization postulate restricts the size of the total Hilbert space. It states that a many-body state of identical particles in 3D is described by a wavefunction that is either completely symmetric (for bosons) or antisymmetric (for fermions) under the exchange of any pair of particles. While Fermi gases of electrons are extensively studied in condensed-matter physics since the early days of quantum physics, Bose gases were less considered. Liquid helium, discovered in 1938 [5, 6], was for a long time the only platform for studying Bose systems and

[1] We do not consider its spin degree of freedom here.

[2] This comes from an other postulate of quantum mechanics.

quantum phenomena such as the observation of a *superfluid* flow, *i.e.* a dissipationless flow [7], or the emergence of vortices were reported [8]. A peculiar characteristic of Bose systems is the *macroscopic* occupation of a single quantum state at sufficiently low temperatures. This phenomenon is known as Bose-Einstein condensation and was initially predicted for a system of non-interacting massive bosons by Bose and Einstein [9]. In liquid helium, strong interactions are present and even though Bose-Einstein Condensation still occurs at low temperature, they complicate the theoretical description of these systems and hinder the role of quantum statistics.

This is only since the development of laser cooling theories and the realization of a Bose-Einstein Condensate with ultracold quantum gases in 1995 [10, 11] that these platforms provide alternative samples for the study of Bose (and later Fermi) systems. The interactions involved are mostly weak, and these dilute, long-lived samples offered the possibility to make quantitative comparison with theoretical models at the beginning of their study [12]. Now, their interest extends far beyond the verification of quantum mechanics predictions. Recent technical developments make them extremely versatile platforms for studying strongly correlated many-body quantum phases of matter, realizing so-called *quantum simulators*. First, the dimension of the system can be changed by strongly confining atoms along one or two directions [13]. Then, beam-shaping techniques allow for the arbitray control of the potential applied on the atomic cloud [14]. Atoms can also be trapped in periodic potentials, known as *optical lattices*, which mimic the trapping of electrons in a crystal [15]. Few-body systems of atoms trapped in optical tweezers have also been shown to be promising platforms for quantum computing [16]. Importantly, in addition to the control of the confinement, interactions between atoms can be tuned thanks to Feshbach resonances [17]. Finally, the internal state of the cloud can be manipulated in a versatile way, allowing for the study of mixtures within the same atomic species, for example.

Our team chose several of these technical developments to focus on the study of 2D uniform Bose gases. The interest in 2D systems mainly lies in the existence of a topological phase transition between a low temperature superfluid phase and a high temperature normal phase, called the Berezinskii-Kosterlitz-Thouless transition [18, 19]. This transition was experimentally demonstrated in 2006 [20] in the platform of ultracold gases. The superfluid properties have been pointed out, such as quantum vortices [21, 22] or the observation of dissipationless flow [23]. Sound propagation has also been studied in 2D Bose gases [24] and the two sound modes of the superfluid system have recently been observed [25]. 2D weakly-interacting Bose gases also exhibit a specific scale invariance which can be seen on the equation of state measurement [26] or on some breather dynamics [27] for example. From an experimental point of view, imaging atomic planes with high resolution microscope objectives allows an efficient characterization of the cloud. Custom-shaped flat-bottom potentials are achieved by shaping light beams with Digital Micromirror Devices (DMD).

Our team studies 2D ultracold dilute Bose gases that undergo weak interactions. Additionally, the weakly-interacting system involves a large number of atoms, making a *mean-field* theoretical approach a suitable approximation. At zero temperature, which is also a good approximation of our system, the Gross-Pitaevskii equation, a Nonlinear Schrödinger Equation (NLSE), is used to describe the system's dynamics [28, 29]. Although this consists to a considerable simplification of the initial quantum description, the physics described by this equation are still extremely rich. This is partly due to the complex nature of the wavefunction entering this equation and the presence of a nonlinear term resulting from the interactions between atoms.

At first sight, it may seem surprising to describe the physics of weakly-interacting quantum systems with a *nonlinear* equation, since quantum mechanics, from the

postulates discussed above, is at its very core a *linear* theory. However, there is no contradiction: the full quantum problem remains linear (the wavefunction still evolves in a linear Hilbert space), and it is the classical mean-field treatment of the interactions that leads to an effective nonlinear equation for the classical wavefunction.

Nonlinear physics refers to situations where a change in "input" does not lead to a proportional change in "output". Although their mathematical treatment is more challenging, their study has become central in physics for several decades now, since most systems are inherently nonlinear in various fields, including biology, climatology, astronomy, mechanics, hydrodynamics, optics, plasma. The presence of *chaos*, as well as the propagation without deformation of stationary waves, known as *solitons*, are two of the key properties of nonlinear systems. The behavior of a chaotic system is highly sensitive to the initial conditions in which the system is prepared. However, the underlying dynamics are not random, but rather exhibit intriguing self-similarities or fractal patterns. Remarkably, chaos may coexist with solitons, which are coherent and stable stuctures [30].

Solitons are fundamental and fascinating objects in nonlinear physics. They are stationary solutions of the associated nonlinear equation. Their discoveries were attributed to J. S. Russell in 1834 [31], when he reported the propagation of a hydrodynamic wave without deformation in a narrow channel. Their observations could not be interpreted by classical linear hydrodynamic equations, and it was not until 1895 that a nonlinear equation derived by Korteweg and de Vries could explain this phenomenon [32]. The term soliton was coined by Zabusky and Kruskal [33] to refer to a stable stationary wave solution of a nonlinear equation. The interest in the study of solitons then grew, especially in photonics where the advances in lasers allow for the generation of high intensity waves that lead to a modification of the refractive index (Kerr effect) in nonlinear media. This is usually the compensation of this effect with a dispersive effect which leads to the formation of a stable solitary wave [34, 35]. The field of photonics has the most diverse range of applications for solitons, particularly in telecommunications.

However, the field of solitons in physics is diverse, and even when restricted to the 1D NLSE, several types of solitons exist, including bright, dark, and Peregrine solitons, to name a few. Solitons have also been produced in the ultracold gas platform. The tunability of the nonlinear term via Feshbach resonances allowed for the creation of bright solitons [36] (stationary solutions of the NLSE with an attractive interaction term) and the ability to imprint a phase pattern on the cloud enabled the formation of dark solitons [37] (stationary solutions of the NLSE with a repulsive interaction term).

The internal state of the cloud can also be controlled in ultracold gas platforms, in addition to the external degrees of freedom. The ultracold gas platforms are thus ideal for creating mixtures of different internal states. Coupled with a spatial control of both density distributions, this approach opens the way to new and exciting phenomena. For instance, vector solitons of the two-component nonlinear Schrödinger equation have been demonstrated to be more stable than their single-component counterpart. The dark-bright soliton [38] is the most well-known example of a vector soliton, arising when the interaction parameters, both for the inter and intra component terms, are identical. It was demonstrated experimentally in the ultracold gas platform in [39, 40]. When the interaction parameters are not equal but are sufficiently close to each other, a different type of vector soliton appears. This soliton is characterized by a constant total density of the mixture. It is called a *magnetic soliton* [41, 42] since in this case, remarkably, the coupled GPEs can be mapped onto the nonlinear Landau-Lifschitz-Equation (LLE), which governs the dynamics of the magnetization vector in

a ferromagnetic spin chain subjected to a magnetic field. Kosevich et al. [43] first introduced the magnetic soliton in this context. The miscible and immiscible mixtures produce two types of magnetic solitons, easy-plane and easy-axis, in the limit of nearly equal interaction parameters. The former was recently demonstrated in the ultracold atoms platform [44, 45] while the latter was only explored numerically [46, 47, 48].

Interest in magnetic solitons arises from their unique response to external forces [49]. Remarkably, within an adiabatic approximation, the magnetic soliton exhibits periodic motion under a linear potential. This is reminiscent of the Bloch oscillations phenomenon [50] at play in crystals with the noticeable difference that there is no lattice breaking the translational invariance. The possibility of observing Bloch-like oscillations in systems without lattices was first predicted in strongly interacting 1D gases for which the dispersion relation is periodic [51, 52, 53] and experimentally demonstrated in [54]. However, achieving adiabatic following of the periodic lowest-energy branch spectrum in this system proved to be challenging, resulting in non-perfectly sinusoidal oscillations. This thesis presents the first experimental deterministic realization of a magnetic soliton within an immiscible mixture, along with its response to a differential linear potential. The cause of the oscillations is attributed to a spin AC Josephson effect [48], which reinforces its broad interest.

Quantum gases also provide a platform for studying phenomena that go beyond classical field descriptions. In particular, Petrov demonstrated in 2015 [55] that self-bound objects can exist in such systems in presence of weak attractive interactions, when quantum fluctuations are considered. These fluctuations provide a repulsive term in the Hamiltonian that can stabilize these objects, which are called *quantum droplets*. They were experimentally demonstrated shortly after their prediction both in Bose-Bose mixtures and dipolar gases platforms [56, 57, 58]. The term "droplet" comes from the liquid-like properties of these self-bound objects, which have similarities with solitons even though the latter are solutions of a *classical field* equation [59].

In dipolar gases, the existence of quantum droplets relies on the anisotropic character of the dipolar interactions. For energetic reasons, this anisotropy can cause a spontaneous spatial arrangement of several droplets inside a confined trap. Remarkably, the global phase coherence of the dipolar droplets array is still maintained. Since 2019 they have been observed in experiments involving highly magnetic Dysprosium and Erbium atoms [60, 61, 62]. The paradoxical coupling between the two previous properties, namely superfluidity and spatial modulation, was explored by Leggett back in 1970, predicting the existence of a so-called *supersolid* phase [63]. According to the current definition, the spatial periodicity in the supersolid phase should arise spontaneously and not be externally imposed. In addition to dipolar gases, the supersolid phase has been observed in other systems, such as gases strongly interacting with optical cavities [64], or spin-orbit coupled BECs [65] and spectacular features of supersolidity were explored. Although the spatial periodicity does not destroy the superfluid phase, the superfluid fraction decreases compared to a non modulated system even at zero temperature. The *superfluid fraction* represents the proportion of the total fluid that is superfluid and not normal. Leggett established bounds within which the superfluid fraction falls [66]. Remarkably, while the superfluid fraction is by definition a *dynamical* quantity, these bounds depend solely on the *static* density profile of the system. Moreover, these predictions are not limited to supersolid systems but apply to other spatially modulated superfluid systems. This opens up possibilities to investigate the coupling between density modulation and superfluidity also in our platform.

In this work, we present an experimental study in a 1D modulated weakly interacting Bose gas aiming at exploring the range of validity of Leggett's result, which

has never been studied experimentally [67], in our platform. We show the first static measurement of the superfluid fraction, as a consequence of the saturation of Leggett's bounds in the considered system, as well as an anisotropic measurement of the sound spectra in the gas. This opens up new possibilities to measure the superfluid fraction in other various platforms.

This thesis is the result of a team effort and its outline is now presented:

- Chapter 1 describes the experimental platform used for the scientific projects of this thesis. The chapter explains how uniform 2D samples of Rubidium 87 are prepared and how the horizontal confinement felt by the atoms and the spin spatial distribution are controlled.

- Chapter 2 discusses the mean-field description of the weakly-interacting Bose gases studied in this thesis. The NLSE governing the dynamics of our system at zero temperature is introduced, and the emergence of superfluid properties in this system is demonstrated.

- Chapter 3 deals with the survival of superfluidity under a spatially modulated potential. Two different and compatible measurements of the superfluid fraction are explored, investigating the range of validity of Leggett's result in our system [63].

- In Chapter 4, we introduce the magnetic soliton, which is a stationary solution of the Landau-Lifschitz equation that governs the dynamics of the magnetization vector in a ferromagnetic chain of spins. We discuss theoretically and numerically the mapping with the miscible and immiscible mixtures of weakly-interacting Bose gases.

- Chapter 5 describes the effect of a weak uniform magnetic gradient on a ferromagnetic chain of spins. We demonstrate the emergence of Bloch-like oscillations for a magnetic soliton moving under an adiabatic approximation, both theoretically and numerically.

- Chapter 6 presents an experimental demonstration of an easy-axis magnetic soliton and the emergence of Bloch-like oscillations in the immiscible mixture system when a differential linear potential is applied. Additionally, we provide measurements of the phase of the majority component matter-wave, confirming the interpretation in terms of Josephson oscillations.

- Chapter 7 discusses the construction of a new experimental setup designed to investigate Rydberg excitations. The chapter demonstrates the production of a Bose-Einstein condensate without a magnetic trap, utilizing time-averaged potentials.

Part I

Production and characterization of low-dimensional Bose gases

Chapter 1

Production of ultracold Bose gases in reduced dimensions

This thesis discusses some properties of confined quantum systems. According to quantum mechanics, physical objects must be described as both a particle of mass m and a wave. The so-called de Broglie wavelength $\lambda_{\text{th}} = \sqrt{2\pi\hbar^2/(mk_BT)}$ gives the typical spatial extension of such a wavepacket at a temperature T. For a macroscopic object, λ_{th} is most often extremely small compared to its size and we can describe its physics ignoring quantum mechanics. However, it is no longer possible to make this approximation when dealing with very lightweight particles, such as atoms. When considering an ensemble of atoms of density n confined spatially in a space of dimension d, one may question what occurs when λ_{th} becomes of the order of n^{-d}, which is the typical interparticle distance, *i.e.* when the individual atomic wavepackets start to overlap. It is the so-called *quantum degeneracy* regime, which has been of interest to many theoretical and experimental physicists for almost a century. The phenomenology of the quantum system in the regime $\lambda_{\text{th}} \gtrsim n^{-d}$ depends on the statistical properties of the atoms being studied (bosons or fermions) and the space dimensionnality d.

To enter the quantum degeneracy regime with a dilute and defect-free sample, it is necessary to ensure that the temperature and pressure of the ensemble are sufficiently low. Although it is favorable to increase the density to enter the degeneracy regime, gases are typically easier to probe than solids and therefore the density of the studied samples is often kept sufficiently low. The associated experimental samples are thus referred to as *ultracold dilute quantum gases*. The collective properties and the exotic phases of matter that may emerge in the degeneracy regime, the high level of control over internal and external degrees of freedom, as well as over the interaction and external potentials experienced by the atoms make ultracold gases an extremely appealing experimental platform, though highly demanding. The experiment that I have been mainly working on during my PhD began 10 years ago with the aim of studying properties of homogeneous Bose gases confined in two dimensions ($d = 2$). Although the construction was finished when I joined in 2020, this chapter provides a brief summary of how we manage to produce a reduced-dimension ultracold sample and highlights the modifications I have been involved in. We refer the reader to the previous Master and PhD theses for further information [68, 69, 70, 71, 72].

1.1 Preparation of a 3D ultracold gas

First, we will explain how we create a 3D Bose-Einstein Condensate of Rubidium atoms. Then, we will discuss the reduction of the dimensionality of the gas.

1.1.1 ^{87}Rb atom and its structure

Our group at LKB, among others, is still exploring new physics with ^{87}Rb atoms, which was the first atom to be brought into the quantum degeneracy regime in 1995 [10], even though it is now possible to bring various atomic species of the periodic table to this regime. One of the reasons for this early success is the easy access to commercial lasers to address the cooling transition at $\lambda_{D2} = 780\,\text{nm}$. Blue-detuned and red-detuned lights at $\lambda = 532\,\text{nm}$ and $2\lambda = 1064\,\text{nm}$ are also commonly used. Another reason is that the sublimation temperature of Rubidium atoms is only $\sim 50\,°\text{C}$ at typical pressures less than $10^{-6}\,\text{mbar}$. Additionally, as an alkali atom, its theoretical description is simplified due to the presence of a single valence electron.

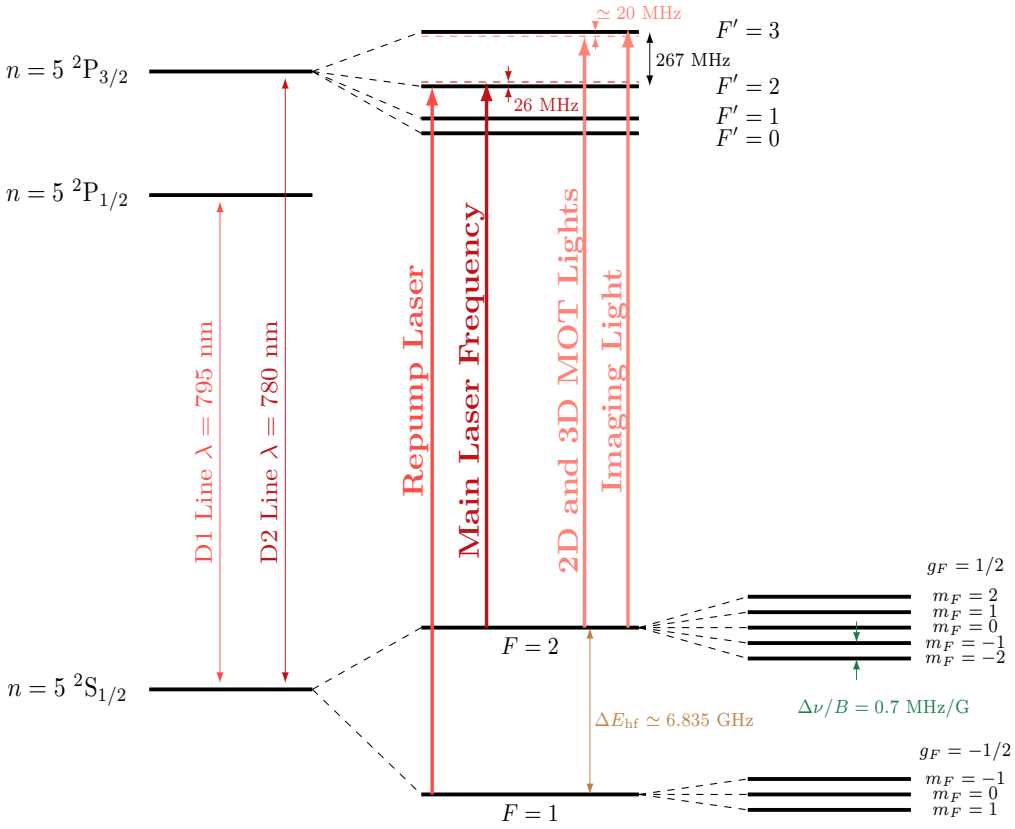

FIGURE 1.1: Electronic structure of ^{87}Rb. Only the relevant levels are shown: the electronic ground state and the first two electronic excited states, split due to the fine structure. The hyperfine structures of $^2S_{1/2}$ and $^2P_{3/2}$ are also represented. The cycling transition used for the cooling and the imaging is the $F = 2$ to $F' = 3$ transition[1]. The 2D and 3D MOT lights are slightly detuned from this transition and are obtained from the Main Laser Frequency light passing through double-pass Acousto-Optic Modulators (AOMs). We can optically pump atoms to $F = 2$ thanks to a Repump Laser. The hyperfine splitting $\Delta E_{\text{hf}} \simeq 6.8\,\text{GHz}$ of the ground state is in the MW domain. In the regime of low magnetic fields (i.e. $\mu_B B \ll \Delta E_{\text{hf}}$), which is relevant in our experiment, the splitting of the hyperfine levels is linear (Zeeman effect). The drawing is not to scale.

Still the physics of Rubidium atoms remains appealing, particularly due to the presence of a hyperfine structure resulting from the coupling of the electron's total

[1] All discussions concerning resonant light will refer to this transition.

angular momentum J and the nuclear spin $I = 3/2$ [73]. This results in various hyperfine states labeled by F, which represents the total angular momentum. Figure 1.1 provides an overview of the relevant states and lines involved.

1.1.2 From a Rb vapour to a 3D BEC

In about 25 seconds, we create a three-dimensional BEC and image it to gather information on the cloud. Doing that, we destroy it using resonant light. We launch repeatidly the sequences of creation and imaging of the cloud with the software Cicero-Word generator [74] which controls the various instruments we use via National Instrument analog and digital cards. The cards are synchronized to a clock, provided by a Field-Programmable Gate Array (FPGA).

However, 50 Hz line frequency noise affects the power supplies used, and the phase of any resulting signal is not identical from one sequence to the next, which is not desirable for a precise control of the magnetic field on the experiment, for example. To compensate for these flucuations, we choose to trigger the synchronization of the National Instruments cards with the FPGA once the AC line reaches an extremum (to be less sensitive to its fluctuations) once per sequence[2]. This is a work done during my PhD and it allows us to keep the same phase for all the relevant signals with respect to each other (FPGA) and with respect to the main line signal (50 Hz synchronization) sequence after sequence.

We now describe the various sequential steps:

- ➢ After heating up a piece of Rb metal in a side glass cell under vacuum (10^{-7} mbar level), we load a 2D Magneto-Optical Trap (2D MOT) combining anti-Helmholtz coils and near-resonant beams with circular polarizations propagating along the y and z directions (see Figure 1.2 for their definitions). The light has sidebands at 6.835 GHz, generated with an EOM, to keep atoms cycling on the $F = 2 \rightarrow F' = 3$ transition.

- ➢ A resonant beam along $-\mathbf{x}$ pushes the resulting cloud inside the main cell of dimensions $105 \times 25 \times 25$ mm, depicted in Figure 1.2, where a 3D MOT is switched on and loaded during 6 s.

- ➢ This is followed by a compressed MOT timestep and a molasses timestep to increase the density and further cool the cloud. The result is a cloud of half a billion atoms at $\simeq 25$ µK.

- ➢ We then turn off the EOM so that the atoms undergo a depumping stage to $F = 1$, a much longer lived state compared to $F = 2$. A pair of anti-Helmholtz coils producing a maximum gradient of ~ 200 G/cm is then progressively switched on. The atoms in the low-field seeking state $|F = 1, m_F = -1\rangle$ are trapped. Since the initial cloud is not polarized, 1/3 of the molasses is trapped. The compression, caused by the high magnetic gradient, leads a high collision rate in the cloud.

- ➢ Radio-frequency evaporation is then performed for 12 s, during which the RF frequency sent to the atoms by a rectangular antenna is ramped down linearly from 35 to 2.5 MHz, lowering the trap depth for the $m_F = -1$ atoms. We get a sample of $\sim 2 \times 10^7$ atoms at 20 µK.

[2] The selected moment in the sequence is typically just prior to the MW transfers, as this is when a precise control of the magnetic field is critical for ensuring experiment repeatability.

➢ The cloud is then transferred to a crossed dipole trap consisting of two tightly focused red-detuned beams from a single 20 W ALS Laser (only 10 W are used in practice)[3]. The atoms are confined in the focused regions and the cloud size is typically reduced to 30 µm in the vertical direction and 90 µm in the horizontal directions. An optical evaporation step lasting 3 s allows to obtain a degenerate cloud of $\sim 5 \times 10^5$ atoms at 100 nK with a typical density of 10^{14} atoms/cm^3, leading to $n\lambda_{\text{th}}^3 \gtrsim 1$: the transition to a 3D BEC is crossed.

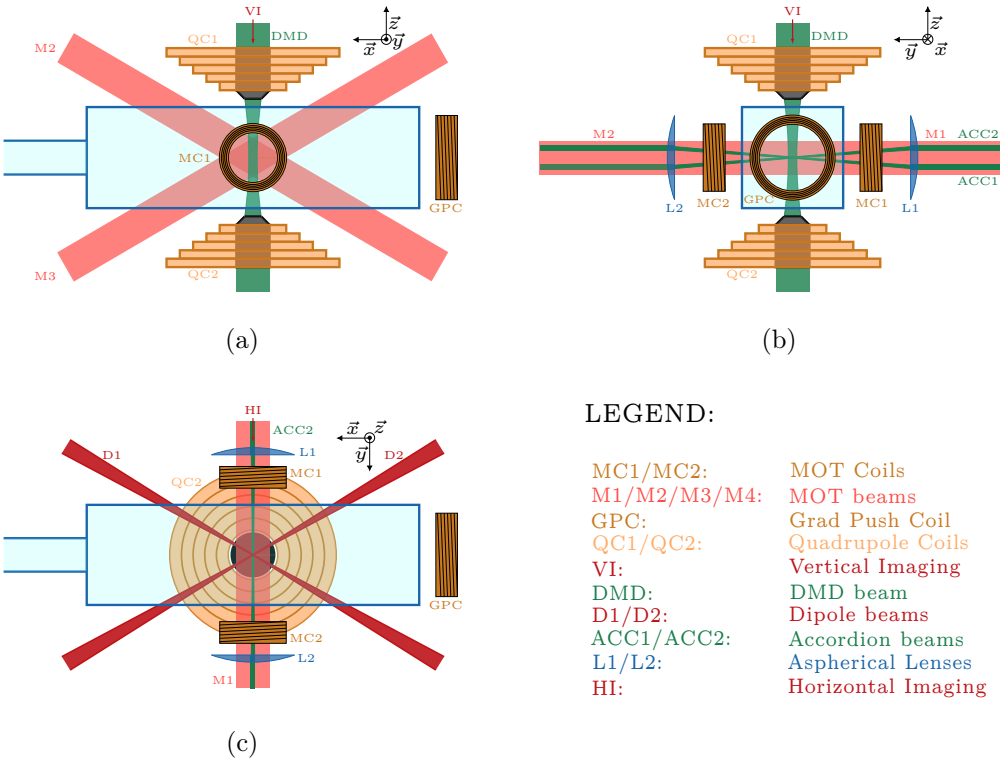

FIGURE 1.2: Experimental setup. (a): Side view. (b): Front view. (c): Top view. The top quadrupole coil and microscope objective are not depicted in the latter view. We did not show the bias coils around the cell (see [69] for details), nor the Raman beams (we will discuss their arrangement later).

1.1.3 Magnetic field and magnetic field gradient controls

The atoms experience a magnetic field with a specific direction, known as the quantization axis. The magnitude (typically a few gauss) and direction of this field are controlled using a set of coils arranged in a Helmholtz configuration around the glass cell[4]. It is necessary to apply this magnetic field to be able to resolve the different Zeeman states and also to avoid spin changing collisions inside the cloud. For the stability and repeatability of the experiment, it is crucial to control both quick and slow fluctuations of this magnetic field to the milliGauss level. Regarding slow variations, we are limited by fluctuations in the magnetic field created by the subway, which passes nearby the laboratory, and is mainly aligned vertically. To compensate for this effect, we measure its vertical component in another room and we

[3] The quadrupole coils are still on but only to compensate the gravity, at 30 G/cm.
[4] These coils also enable a displacement of the cloud (see Chapters 3 and 6).

use a home-made box to extract the fluctuations of this signal and send a resulting feedforward signal to a pair of Helmholtz coils aligned along z, shown in Figure 1.3.

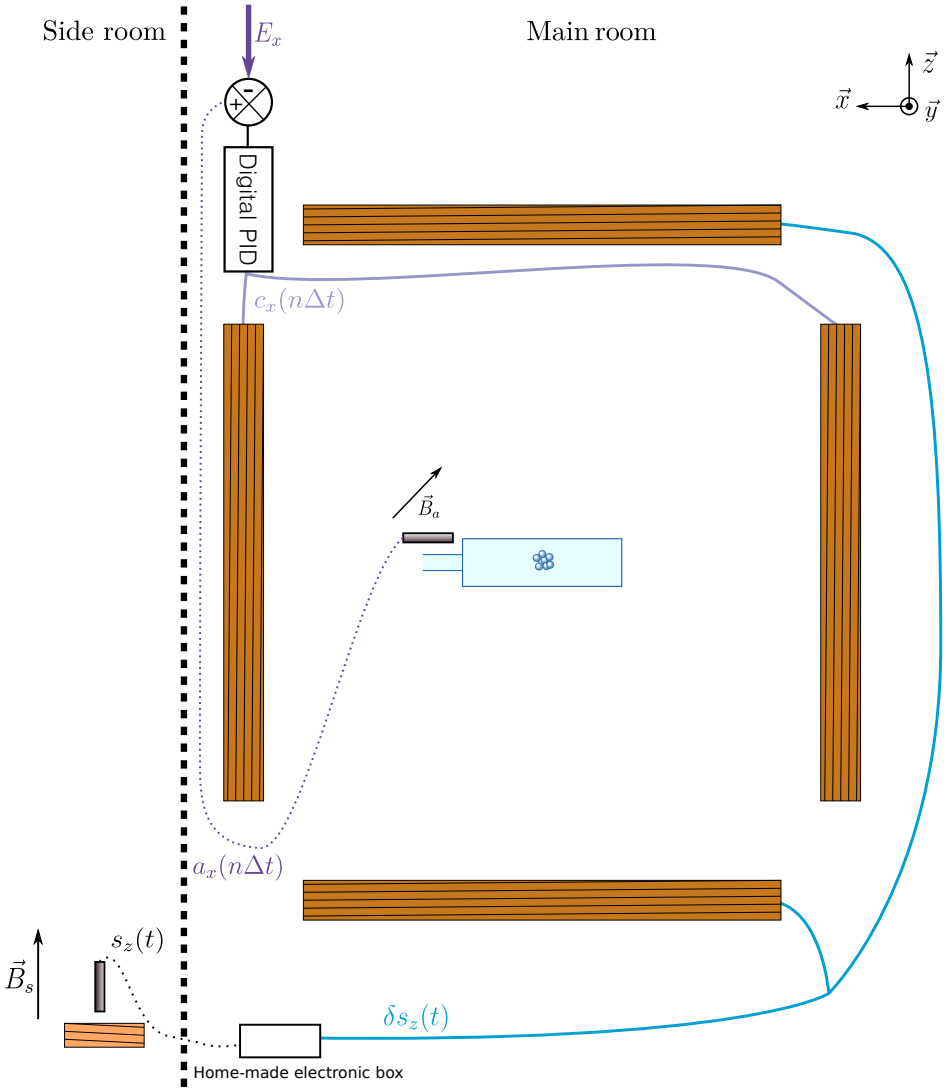

FIGURE 1.3: Magnetic field control. A magnetic field probe (Bartington Mag-03MCTP 500) measures the magnetic field near the atoms $\vec{B}_a$ along the 3 directions (only its component along x a_x is needed here) and another one measures the vertical magnetic field in a side room near an independent coil ($\vec{B}_s$). A large pair of coils along the vertical direction receives the feedforward signal $\delta s_z(t)$, which takes into account the subway induced fluctuations, extracted from the independent signal, measured in the side room ($s_z(t)$)[5]. A microcontroller, reading the magnetic field along x ($a_x(n\Delta t)$) every Δt (sequence duration), together with a large pair of coils along x, can be used to match a command E_x with a digital PID correction. For simplicity, we have not shown the power supplies of the large coils, which receive the signals $\delta s_z(t)$ and $c_x(n\Delta t)$ and send a proportional current to the coils. We choose for the drawing an active compensation along x because this is what will be used in Chapter 6, although it could have been along y or z.

[5]A home-made electronic box transforms the signal $s_z(t)$ into its fluctuations $\delta s_z(t)$. A static gain allows us to tune precisely the compensation so that we do not overcompensate the subway fluctuations. We extract the flucuations with an offset voltage provided by a stabilized power supply.

However, this method cannot correct local fluctuations that arise near the science cell. To address this issue, an active correction loop was implemented during my PhD to adjust the magnitude of the magnetic field along one direction. Once per sequence, typically after the production of the condensate and before the MW transfers, the magnetic field on the atoms is measured and compared to a fixed value for 200 ms. A digital proportional integral correction is performed by a microcontroller, Arduino DUE, to correct for the observed difference. The output is then sent to a pair of coils aligned along the chosen direction (see Figure 1.3).

With these two corrections, we are able to achieve sub-mG RMS fluctuations of the magnetic field near the atoms for an entire day along the corrected directions. A more challenging future improvement would be to actively compensate along all three axes simultaneously (see for example a recent implementation in [75]).

In recent projects (see Chapters 3 and 6), we have improved our control of the magnetic field gradient felt by the atoms. Accurate control of the gradient was found to be crucial, particularly in the horizontal plane. The MOT coils are already in place to create a gradient along the y direction[6]. However, the power supply used has a range of $0 - 20$ A and the analog step precision of the cards is 5 mV, which means that we cannot control the current below 10 mA of accuracy. To improve this point, we put another Delta Electronika power supply of range $0 - 5$ A in parallel of this power supply, which allows to reach 2.5 mA of accuracy.

No coils were mounted along the x direction, while the residual magnetic gradient along this direction is typically ~ 10 G/m. We added only one coil, as it was impossible to have a second one due to the vacuum system. It is shown in Figure 1.2 (called "Grad Push Coil"), its radius is 15 mm and it is placed at a distance of ~ 60 mm to the atoms and consists of 10 turns. The current flowing through is $\simeq 2$ A. This allows the residual gradient to be compensated to an accuracy of ~ 0.2 G/m along the x direction.

1.2 Reaching the 2D regime

After creating a 3D BEC, we freeze the vertical degree of freedom by confining the gas to a plane of height $l_z \simeq 0.18$ µm in order to reach the 2D thermodynamic regime. To achieve this, a plane of atoms is confined inside a node of a blue-detuned optical lattice, obtained by interfering two beams of $\lambda = 532$ nm light. The interfringe of this lattice can be adjusted dynamically using an *accordion lattice* setup. It was first introduced in [76] and its implementation in our experiment is discussed in more details in [70, 71]. Indeed, without any precaution, shining a lattice of a few µm spacing on a 3D BEC with a typical Thomas-Fermi radius of 6 µm would lead to several loaded fringes and a split cloud. To avoid this, we start with a large interfringe configuration (~ 13 µm) into which the 3D BEC can be loaded[7] and we then reduce the interfringe of the lattice to ~ 3 µm by varying the angle at which the 2 beams interfere in ~ 500 ms (Figure 1.4).

For a sufficiently deep lattice, the sinusoidal potential felt by the atoms (directly proportional to the intensity profile) can be approximated by a harmonic potential of angular frequency ω_z, inversely proportional to the interfringe i, and the key experimental quantity to assess the "2D-ness" of the cloud. The vertical degree of freedom

[6] We will only discuss the "strong" axis along which the gradient is twice as large as the other axes, for anti-Helmholtz coils.

[7] Actually, at this step, we increase the power of one of the dipole arms to compress the BEC and load it entirely into one fringe of the lattice.

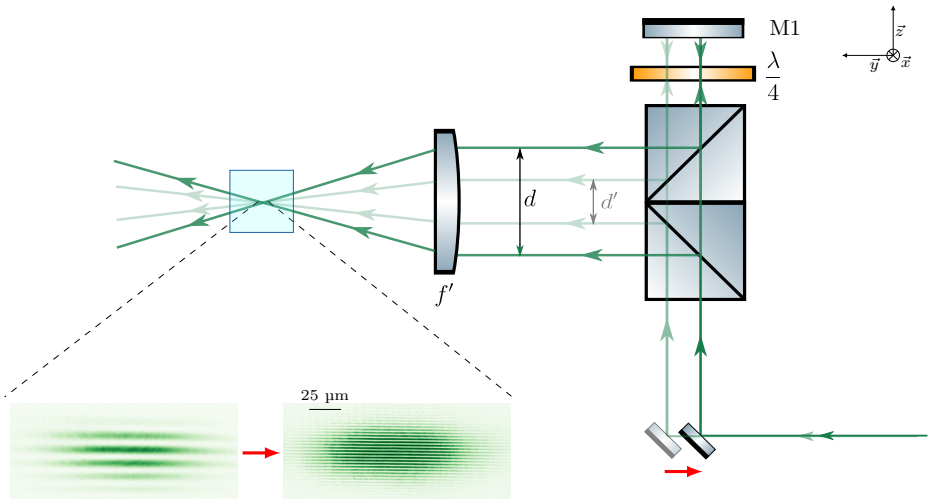

FIGURE 1.4: Accordion lattice optical setup. To reach the 2D regime without loading multiple fringes, we use an accordion lattice setup. Two beamsplitters are vertically glued together, splitting the initial beam into two beams. They then interfere at the position of the BEC (inside the cell depicted as a blue rectangle) after passing through an aspherical lens (Asphericon ALL50-100-S-U, focal length $f' = 100\,\text{mm}$). The interfringe $i = \lambda d/f'$ depends on the distance d between the two beams and can be varied by translating a mirror, placed on a translation stage, the movement being represented by the red arrow. An imaging system, not shown on the drawing, allows the interference pattern to be imaged on a control camera. Examples of light images before and after the compression of the lattice are presented in the figure. The top mirror M1 is mounted on a piezo-electric stack and can control the absolute position of the fringes. A feedback loop is implemented to stabilize the interference pattern once per sequence acting on this mirror [71].

is indeed frozen as soon as the first excited state of the vertical harmonic oscillator cannot be reached with the relevant thermal and interaction energy scales of the cloud, *i.e.* as soon as $\hbar\omega_z \gg k_B T, E_{\text{int}}/N$. When this condition is fulfilled, we speak of *quasi-2D regime*, the term *quasi* comes from the fact that the collisions between the atoms still keep their 3D character (see Chapter 2). At the end of the lattice compression, this is the case for our cloud, where we reach up to $\omega_z \simeq 2\pi \times 4$ kHz, measured thanks to parametric resonance (see for example [77]).

1.3 Tunable shaping of the in-plane potential

The previous section described the vertical confinement of the cloud. Regarding the horizontal confinement, we have full control over it thanks to two Digital Micromirror Devices (V-7000 by Vialux), that are imaged directly on the atoms. They consist of 1024×784 mirrors (pixels) of size $13.7\,\mu\text{m}$, each of which can either reflect the light onto the atoms or reflect it in another direction without affecting the atoms. These two DMDs, used to tailor the potential felt by the atoms, are shined with blue-detuned light at 532 nm and the atoms are trapped in the regions where the light is not reflected to the atoms[8]. DMDs are electric field modulators [78] and thanks to

[8] Another DMD, shined with red-detuned Raman beams allows us to spatially control the spin state of the cloud (see section 1.4.2).

them we can create box-like potentials, instead of more usual harmonic potentials, a peculiarity of our setup.

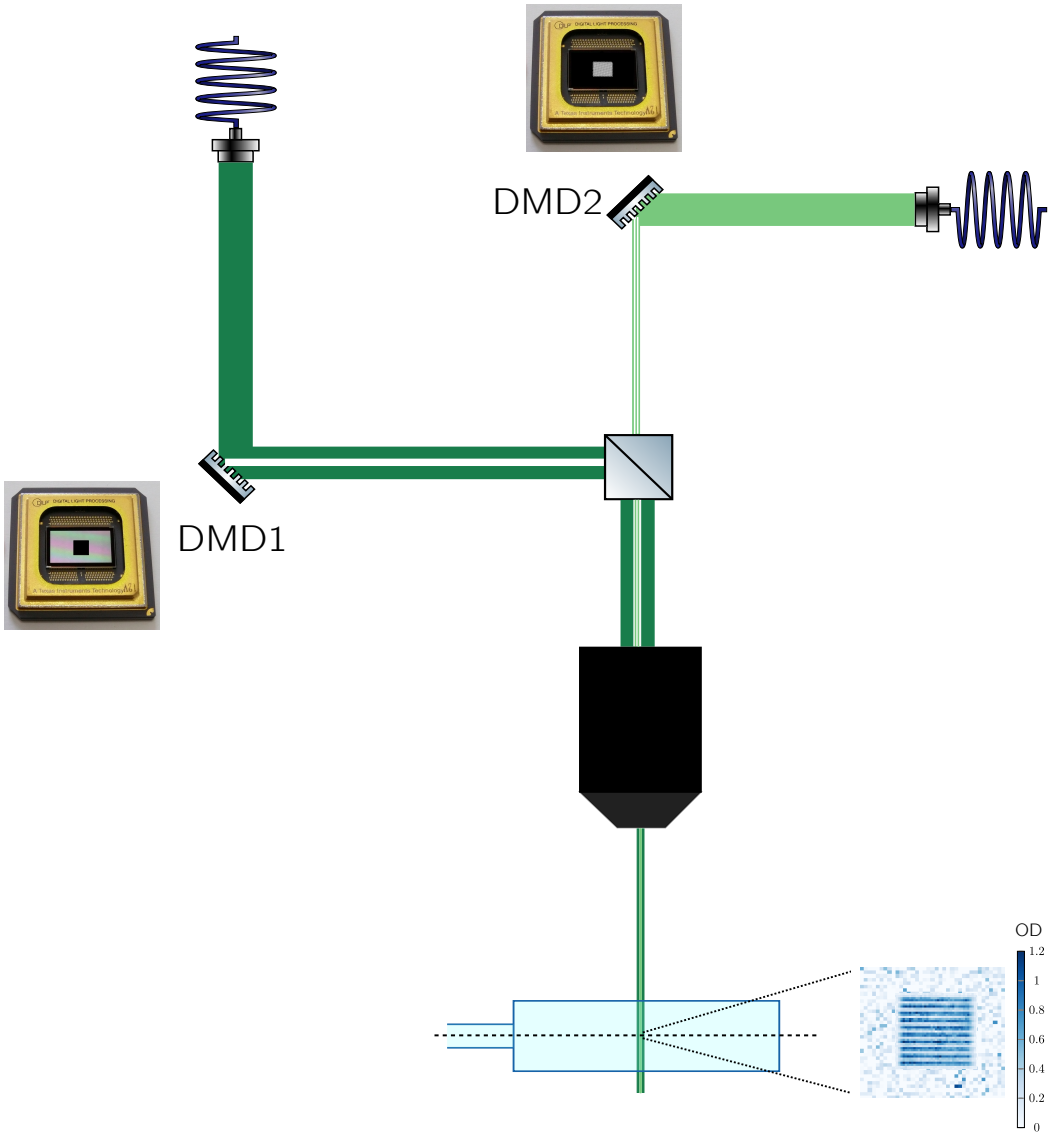

FIGURE 1.5: DMD1 and DMD2 setup. Green beams coming from two fibers are directed to both DMDs. In this example, we choose a black square box pattern for DMD1 and a sinusoidal modulation for DMD2 (zoom in to see the discretization of the mirrors). The beams are shaped according to the patterns after diffraction by the DMDs. A black mirror indicates no light is reflected to the atoms, while a white mirror indicates light is reflected to the atoms. The beams are then combined and directed towards the atoms via a microscope objective. The atomic plane, represented by the dashed line, is then imaged vertically onto a camera (Princeton Instruments, Pixis 1024 BR Excelon) using another microscope objective. An example of an absorption image obtained with these patterns is shown. The imaging setup is not depicted in the drawing. The verticality is not respected.

1.3.1 Tailoring box potentials with DMD1

A first DMD, called DMD1, is used to create the boundaries of the box potential. While loading the plane of atoms inside a node of the accordion lattice, we shine

$\sim 1\,\mathrm{W}$ of green light on DMD1, creating the desired horizontal confinement, for which we usually choose a square shape (see Figure 1.5). We then reduce the height of this box potential to further evaporate the cloud by decreasing the power of the beam. We end up with a 2D homogeneous gas (because placed in a flat potential) of $N \sim 1 \times 10^5$ atoms still in the state $|F = 1, m_F = -1\rangle$ at a temperature $T \sim 20\,\mathrm{nK}$[9]. We discuss in section 1.4.1 how we can vary the final 2D density. The DMD1 plane is imaged on the atoms with a demagnification of 70 through a microscope objective from Nachet with a numerical aperture NA = 0.45, which leads to an effective pixel size of $0.2\,\mu\mathrm{m}$ for a DMD mirror on the atoms. The beam waist in the atomic plane is $\sim 40\,\mu\mathrm{m}$, leading to a typical maximum box size of $\sim 100\,\mu\mathrm{m}$.

Another interesting feature of a DMD is the ability to display a movie of different images on it, with a frequency rate up to 10 kHz. Thanks to this characteristic, more complicated boxes can be loaded efficiently (see Figure 1.6). We will take advantage of this feature in the science project described in Chapter 6.

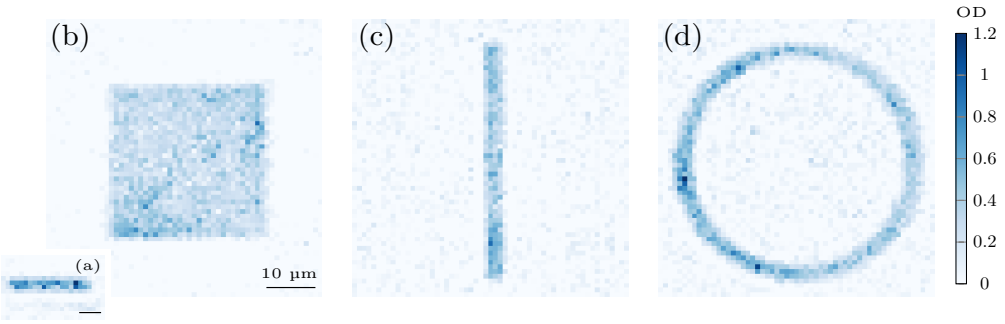

FIGURE 1.6: Example of absorption images of our 2D cloud. Each picture is an average of 10 images. The scale is the same for the images (b), (c) and (d). (a): Decompressed single plane cloud seen from the side with horizontal imaging. (b), (c) and (d): Box-shaped clouds seen from the top with vertical imaging with respectively a square shape of $40\,\mu\mathrm{m}$, a rectangle shape of $3 \times 60\,\mu\mathrm{m}$, and a ring shape with inner and outer radii 27 and $30\,\mu\mathrm{m}$. (c) and (d) are obtained after displaying a movie on DMD1 of 50 frames of 500 ms duration, starting from a rectangle shape of $40 \times 60\,\mu\mathrm{m}$ and a circle of radius $30\,\mu\mathrm{m}$, respectively.

1.3.2 Precise control of the in-plane potential with DMD2

In addition to DMD1, which creates the boundaries of the box potential, we can apply an auxiliary repulsive light potential shaped by another DMD, called DMD2. It is also imaged on the atomic plane via the same microscope objective with a demagnification of 70 (see Figure 1.5). The waist of the beam on the atoms is $\simeq 80\,\mu\mathrm{m}$ and was increased during my thesis to get a flatter beam on the atoms. We take advantage of DMD2 to add potentials to the cloud, which can be used for homogeneity corrections or to imprint density modulations.

Even if the pixels of the DMD are *booleans* (white or black mirrors), we can still shape *continuous* intensity profiles with it. To map the desired continuous intensity profile into a boolean pattern that can be displayed by the DMD, we use the dithering technique. Specifically, we use a certain type of dithering algorithm, the error-diffusion algorithm [80, 78], which propagates the error caused by a binary choice on one

[9] The temperature of the cloud is calibrated using the equation of state of the 2D Bose gas, with a method inspired by [79].

pixel to the neighboring pixels with a given weight. This enables the computation of the appropriate discretized pattern on the DMD to achieve the desired continuous modulation of the electric field of the green light, with a good approximation.

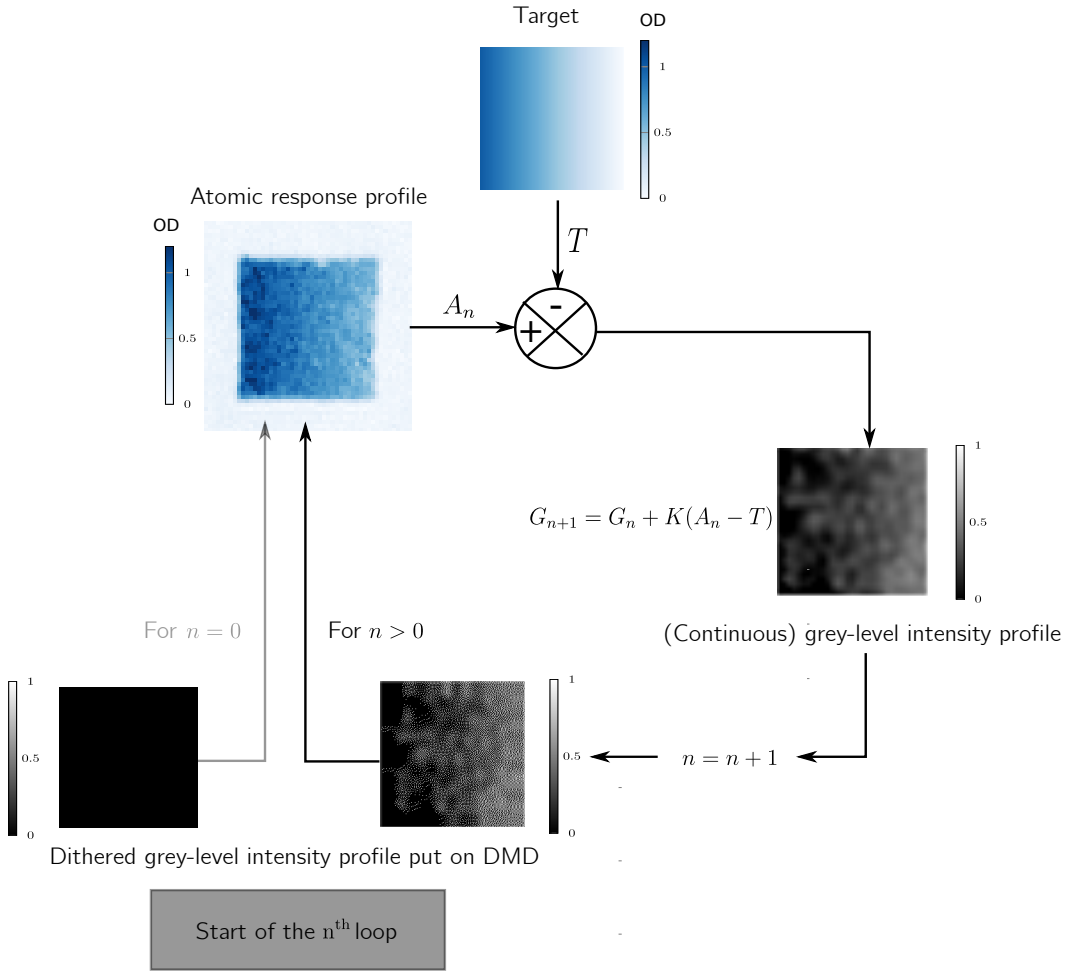

FIGURE 1.7: Feedback loop for optimizing the atomic density profile with the DMD2, example with a linear gradient target profile. In the n$^{\text{th}}$ loop, we compare the atomic density profile A_n with the target T. We perform a proportional correction of factor K[10] and compute a corrected intensity profile G_{n+1}, which modifies the previous pattern G_n put on DMD2 depending on the calculated error. We remove light at the pixel points x where there are not enough atoms $(A_n(x) - T(x) < 0)$ and add light where there are too many atoms. The profile is then dithered and placed on the DMD and the $n + 1$ loop follows. The loop is started with a black pattern on DMD2 and stopped when the error is below a certain level of desired accuracy.

In describing the atomic response to this modulation, we must take into account the finite resolution of our imaging system, which is diffraction limited. In fact, the point spread function of our imaging system is $\simeq 1\,\mu\text{m}$, so we are not able to resolve each mirror of both DMDs of effective size in the atomic plane $0.2\,\mu\text{m}$. Instead, the response of the atoms on a large pixel of $1\,\mu\text{m}$ is a spatial average of the response of $5 \times 5 = 25$ pixels. On the one hand, this smoothes out the sharp edges of the

[10] Actually, the K factor is corrected by a Gaussian weight. Indeed, the correction should be more important at the edges of the image than in the center to compensate for the Gaussian shape of the beam.

box potential felt by the atoms[11] and limits the spatial frequencies of the targeted modulation (see Chapter 3) but, on the other hand, this enables us to overcome the limitation of the binary nature of the DMD (either black or white). Indeed, on our optical system, we then have access to 25[12] levels of "grey" (average of black and white pixels) for a given large pixel on the atomic plane.

It may seem possible to compute the necessary dithered pattern for any given target atomic profile and directly image it onto the atoms. However, this process is complicated by limitations such as optical aberrations, beam imperfections, and residual defects in the error-diffusion algorithm. A feedback loop is implemented to compare the atomic density profile obtained with a given DMD dithered pattern to the targeted density profile and modify the DMD pattern accordingly. The loop is run until the optimal DMD pattern is reached, with any difference from the target then mainly limited by the finite numerical aperture of the system. Figure 1.7 summarizes the principle of the loop. A detailed analysis of this implementation of grey levels can be found in [81, 72].

1.4 Control of the internal state of the cloud

The 2D homogeneous gas is initially prepared in the state $|F = 1, m_F = -1\rangle$. In our setup, we implement two ways to change the hyperfine state, first to precisely image the cloud (we remember that the imaging light is only resonant with $F = 2$ states), also to vary the 2D density and finally to prepare mixtures of Zeeman states. We rely on coherent fields to perform these transfers between $F = 1$ and $F = 2$. If ν_0 is the resonance frequency of the hyperfine transition (which is in the MW domain), ν is the actual frequency of the coherent field, $\delta = \nu - \nu_0$ is the detuning, and Ω is the Rabi frequency of the field (which depends on the electric dipole transition, the field intensity, and its polarization), then the probability of finding the atoms in $F = 2$, starting from $F = 1$, after a field excitation of duration t, is given by:

$$\mathcal{P}_2(t) = \frac{\Omega^2}{\delta^2 + \Omega^2} \sin^2\left(\sqrt{\delta^2 + \Omega^2}\,\frac{t}{2}\right) \tag{1.1}$$

At resonance, $\delta = 0$ and one can transfer all the atoms from $F = 1$ to $F = 2$ for a duration, called the "π pulse", $t_\pi = \frac{\pi}{\Omega}$. We will discuss in 1.4.2 how the two-photon Raman transfer can be mapped to this one-photon formalism. In Figure 1.8, we show examples of such sinusoidal oscillations of spin populations, also called *Rabi oscillations* [82], both with a MW field and with the Raman beams.

1.4.1 Global control - MW transfers

First, let us briefly discuss how we manage to control the internal state of the whole cloud. Remembering that the hyperfine splitting is in the MW domain ($\simeq 6.8\,\mathrm{GHz}$), we use two MW antennas[13] in order to flip the spin state of the cloud. This cannot be a spatially selective transfer, since the wavelength of this MW field (a few cm) is

[11] Even though the stationary density profile in a box potential is obviously not discontinuous, the characteristic decay length on the box borders, given by the healing length (see Chapter 2), is much smaller than the effective pixel size of the camera ($1.15\,\mu\mathrm{m}$).

[12] Actually, this number is a lower bound and the accessible levels are not discretized.

[13] Changing the frequency of the MW generators, done via GPIB control, takes several hundred of ms. However, the lifetime of the $F = 2$ state, limited by 2-body losses, is less than 100 ms, so if several MW transfers are needed (for example, from $|F = 1, m_F = -1\rangle$ to $|F = 1, m_F = +1\rangle$, through $|F = 2, m_F = 0\rangle$), we have to use the 2 MW antennas.

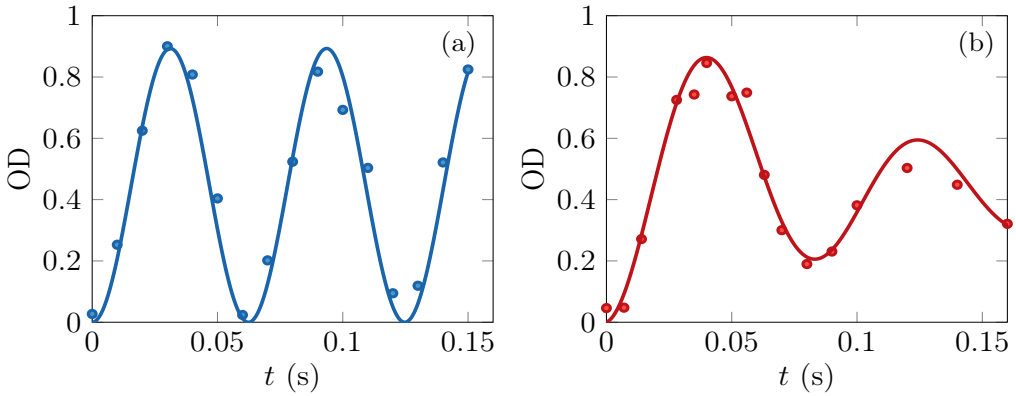

FIGURE 1.8: Examples of Rabi oscillations between $|F = 1, m_F = -1\rangle$ and $|F = 2, m_F = 0\rangle$. (a): With MW field illumination. (b): With Raman beams illumination. The pattern on DMD3 is completely white and we choose a circle with radius 5 µm to calculate the OD in the analysis. The damping of the oscillations is attributed to the intensity inhomogeneities in this region.

much larger than the size of the cloud ($< 100\,\mu m$). Two MW chains are implemented, connected to a horn antenna whose propagation axis is along x, and to a one-loop antenna close to the atoms, respectively. The MW field from each chain comes from a Rohde & Schwartz SMB100AV synthesizer and is amplified by a 10 W amplifier (Kuhne KU PA 700) and a 50 W amplifier (RF Lambda RFLUPA05G08GA), respectively. The resulting Rabi frequencies are on the order of $\Omega \simeq 2\pi \times 10\,\text{kHz}$ for most of the transitions and the remaining magnetic field fluctuations on the order of 1 mG do not affect the MW transitions much. We emphasize that these synthesizers have an extremely good precision and it allows to perform state of the art measurements based on frequency measurements. More details can be found in [83].

We use this tool to accurately image the 2D cloud. We use absorption imaging with a light pulse resonant with the $F = 2$ state to obtain the kind of images shown in Figure 1.6 for example. One might think that applying a pulse of the Repumping Laser is sufficient to transfer atoms from $F = 1$ to $F = 2$, which can then be imaged with the resonant light. However, this is a not a quantitative method and we would not be able to precisely determine the density of the cloud or distinguish between the different Zeeman states of $F = 1$. Instead, we apply a MW pulse of duration t_{MW} from the desired occupied Zeeman state of $F = 1$ to $F = 2$ (transition of π-pulse t_π). Its duration is chosen so that the fraction transferred to $F = 2$ is small enough. More specifically, the Optical Depth (OD) of the cloud, defined as the attenuation of the resonant light passing through the sample $I_{\text{out}} = \mathrm{e}^{-\text{OD}}\, I_{\text{in}}$[14], is kept below 1.2, avoiding collective excitations of the gas [84, 85]. Using the following formula, we can then safely calculate the 2D density of the cloud in the initial state $F = 1$:

$$n_{\text{2D}} = \mathcal{F}\,\frac{\text{OD}}{\sigma\,\sin^2\left(\frac{\pi}{2}\frac{t_{\text{MW}}}{t_\pi}\right)} \tag{1.2}$$

where $\sigma = \frac{7}{15}\frac{3\lambda_{\text{D2}}^2}{2\pi}$ is the resonance scattering cross section of the Rb atoms and $\mathcal{F}$ is a correction factor that takes into account the atomic transition involved, the

[14] It is assumed that the number of scattered photons is proportional to the light intensity and that the Beer-Lambert law is valid. This is true in the limit of low light intensities.

polarization of the imaging light and various effects of the atomic environment (*e.g.* magnetic field) during absorption imaging. Its calibration is often done in our setup by two independent and compatible measurements of the 2D density, relying on Tan's contact measurement [86] or a breather dynamic [27].

One can also use the MW tool to vary the 2D density of the cloud. After creating the 2D gas, one can transfer part of the cloud to $F = 2$ with a MW pulse of duration $t < t_\pi$ and remove these selected atoms by applying a short pulse (40 µs) of resonant light. This pulse does not affect the remaining atoms in $F = 1$, and the density of the cloud is then reduced.

In summary, this extremely precise and versatile MW tool allows us to vary the density of the cloud, transfer atoms into different, possibly mixed Zeeman states, perform state of the art measurements (see [86, 87] and Chapter 2) and implement partial transfer imaging.

1.4.2 Local control - Raman transfers

The MW tool is extremely useful, but it does not easily allow for spatially selective transfers between hyperfine states due to the associated wavelength being a few centimeters. To achieve this, one possibility is to use a field with a lower wavelength. However, it is important to consider how to match the resonant condition between the hyperfine states, which lies in the MW domain. The trick is to use two-photon transitions sufficiently detuned from any excited states, which are called in this context Raman transitions. The frequency difference between the two beams must be equal to the hyperfine splitting in order to perform the transfer successfully. This is a well-known experimental tool which can be used in different situations. It is extensively discussed in the case of our setup in [71]. This section highlights the main experimental requirements for Raman beams and their combination with a DMD to perform local spin transfers.

When selecting the wavelengths for the two copropagating beams that perform the two-photon transition, it is crucial to take into account the scalar light shift that the cloud experiences due to the Raman beams. Indeed, finite light shifts cause dephasing and decoherence within the cloud (Figure 1.8). They depend on light intensity and are caused by non perfect Gaussian beam shapes and the finite waists of the Raman beams on the atoms ($\simeq 40$ µm). For certain wavelengths, known as tune-out wavelengths, the atoms experience zero scalar light shift. For the $F = 1$ and $F = 2$ states of Rubidium, $\lambda_R = 790.0\,\text{nm}$ is a tune-out wavelength. This choice also avoids overheating the cloud while shining the Raman beams[15]. For $\lambda_R = 790.0\,\text{nm}$, the effective Rabi frequency of this two-photon transfer Ω_R is large enough compared to the frequencies associated to the spatial dynamics of the atoms ($\sim 2\pi \times 1\,\text{kHz}$) and of order $2\pi \times 50\,\text{kHz}$.

For this choice of wavelength, we can describe the dynamics as if there were only the two hyperfine levels involved and apply the formalism of a two-level system (1.1) subjected to a one-photon transition of detuning δ_R and Rabi frequency Ω_R, proportional to the square root product of each beam intensity. Taking advantage of the ability to modulate the amplitude of light thanks to a DMD, Raman beams can imprint a specific spatial spin profile (*i.e.* control the density profile of the $F = 2$ spin state within a remaining bath of $F = 1$ atoms). More precisely, let us imagine that we want to imprint a density profile $f(x, y)$ of $F = 2$ atoms in the center of the cloud. The atoms, transferred to $F = 2$ by this two-photon coherent process, are located at

[15] The rate Γ_{sc} at which the atoms scatter photons from the Raman beams is on the order of $5\,\text{s}^{-1}$ for this wavelength, which means that for a typical pulse of 20 µs, one atom out of 10^4 will scatter a photon, a negligible number compared to the total atom number $\sim 10^5$.

intensity maxima. Applying (1.1) at resonance with a Raman pulse of duration t_R, we can write:

$$f(x,y) = \mathcal{P}_2(x,y,t_R) = \sin^2\left(\Omega_R(x,y)\,\frac{t_R}{2}\right) \tag{1.3}$$

Remembering that Ω_R is proportional to the total light intensity and that the DMD is an electric field modulator, we obtain the following pattern to be placed on the DMD (after dithering) in order to perform the spatial spin transfer of shape $f(x,y)$:

$$\mathcal{D}(x,y) \propto \sqrt{\Omega_R(x,y)} \propto \sqrt{\frac{2}{t_R}\,\arcsin\left(\sqrt{f(x,y)}\right)} \tag{1.4}$$

This DMD, called DMD3, is imaged on the atoms with a demagnification of ~ 30, resulting in (at least) ~ 9 grey levels. In Chapter 6, we will discuss how we take advantage of the Raman beams in combination with DMD3 to realize a magnetic soliton deterministically. In Figure 1.9, we show the preparation of the two Raman beams with the appropriate frequencies and polarizations, along with a scheme of the Raman setup near the atomic cell.

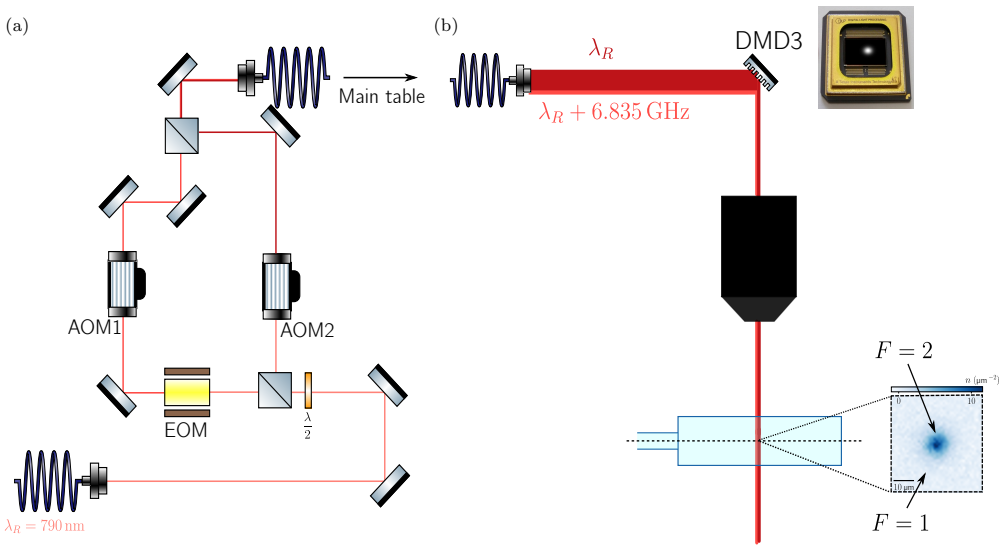

FIGURE 1.9: Raman beams setup. (a): Optical setup for preparing the Raman beams. An EOM at $f_E = 6.8\,\mathrm{GHz}$ produces 2 sidebands on one beam path. The AOM1 has a fixed frequency $f_1 = 115\,\mathrm{MHz}$ and the center frequency of AOM2 can be tuned to match the transition between the desired Zeeman states (it is about $f_E - 6.835 + f_1 \simeq 80\,\mathrm{MHz}$). The setup was built in order to obtain an atomic resonance for only one pair of frequencies (one sideband and the carrier of the other beam [71, 88]). Each beam is intensity locked for reasons of reproducibility [72] (to keep Ω_R constant). They have orthogonal polarizations. (b): Scheme of the setup on the main table where the Raman beams are sent to the atoms. A DMD shapes the beam profiles of the two Raman beams. We have taken the example of Gaussian spatial modulation: $f(x,y) \propto \mathrm{e}^{-(x^2+y^2)/\sigma^2}$. The path is combined with the DMD1, DMD2 and vertical imaging paths (not shown on the drawing) and the beams reach the atomic cell after passing through the microscope objective. An example of an absorption image is shown. Atoms in $F = 1$ are transparent to the imaging light, but are present throughout the dashed square region.

Finally, we note that we are discussing the relevant case of copropagating Raman beams but the optical path can be modified in order to imprint a momentum transfer to the $F = 2$ state (see [71]).

1.5 Conclusion

In this first chapter, we described the production of ultracold gases of reduced dimensions. We emphasized two main aspects of our experiment: the use of an accordion lattice for the vertical confinement and different DMDs for the horizontal confinement with box-like potentials. In Chapter 3, we will use our ability to imprint controlled density modulations to investigate how the superfluidity of the gas is affected by the presence of a spatial modulation. Then, we can control not only the external degrees of freedom of the gas but also its internal states. We discussed the ability to globally control the spin state with MW fields or locally with Raman beams. The MW tool, in combination with high-precision synthesizers, enables the production of Rubidium dimers and the resolution of frequency shifts as low as a few tens of Hz. This will be further discussed in Chapter 2. Chapter 6 will provide an example of a recent study on accessing the physics of immiscible mixtures using the Raman beams tool.

Chapter 2

Mean-field description of a weakly-interacting 2D Bose gas at $T = 0$

In Chapter 1, we discussed the experimental production of an ultracold Bose gas in reduced dimensions, specifically in two dimensions. Here, we will provide a theoretical description of it, using some simplifications that we will explain. We will focus on how to handle the weak interactions that the atoms undergo. We will introduce a key quantity quantifying the strength of these interactions, the scattering length a, and write the equation governing the mean-field dynamics of our experimental system at $T = 0$, the Gross-Pitaevskii equation. After completing the aforementioned task, we will discuss our recent work on producing dimers of Rubidium 87 and studying their interactions with the rest of the cloud. Finally, we will introduce a fascinating property of, among other systems, the weakly-interacting Bose gas at zero temperature, which is superfluidity. Its survival in spatially modulated systems will be the focus of Chapter 3.

2.1 Description of a weakly-interacting 2D Bose gas at zero temperature

In this section, we simplify the general Hamiltonian of the system to write the Gross-Pitaevskii equation, also known as the nonlinear Schrödinger equation.

2.1.1 The quantum hamiltonian

The objective is to describe a dilute quantum system of N bosons with mass m, which are trapped in the potential $V(\mathbf{r})$ and interact via a binary potential $U(\mathbf{r}-\mathbf{r}')$[1]. This approach is described in details in [89] for example. The Hamiltonian governing the physics of the system can be naturally written in first quantization:

$$\hat{H} = \sum_{i=1}^{N} \left[\frac{\hat{\mathbf{p}}_i^2}{2m} + V(\hat{\mathbf{r}}_i) \right] + \frac{1}{2} \sum_{i \neq j} U(\hat{\mathbf{r}}_i - \hat{\mathbf{r}}_j) \tag{2.1}$$

where the first term is the kinetic energy of the system ($\hat{\mathbf{p}}_i$ is the momentum operator acting on the particle i) summed with the trapping energy of the system ($\hat{\mathbf{r}}_i$ is the position operator acting on the particle i) and the last term is the interaction energy of the system.

[1] U depends solely on $\mathbf{r}-\mathbf{r}'$ and not on $\mathbf{r}$ and $\mathbf{r}'$ independently due to the translational invariance property of the interactions in the system.

With respect to the field operator $\hat{\Psi}(\mathbf{r})$ (respectively $\hat{\Psi}^\dagger(\mathbf{r})$), which describes the annihilation (resp. creation) of a particle at position $\mathbf{r}$, the Hamiltonian (2.1) is expressed in the second quantization formalism as:

$$\hat{H} = \int \mathrm{d}^3 r \left[\frac{\hbar^2}{2m} \boldsymbol{\nabla}\hat{\Psi}^\dagger(\mathbf{r}) \cdot \boldsymbol{\nabla}\hat{\Psi}(\mathbf{r}) + V(\mathbf{r})\, \hat{\Psi}^\dagger(\mathbf{r})\, \hat{\Psi}(\mathbf{r}) \right] + \frac{1}{2} \iint \mathrm{d}^3 r\, \mathrm{d}^3 r'\, \hat{\Psi}^\dagger(\mathbf{r})\, \hat{\Psi}^\dagger(\mathbf{r}')\, U(\mathbf{r}-\mathbf{r}')\, \hat{\Psi}(\mathbf{r}')\, \hat{\Psi}(\mathbf{r}) \quad (2.2)$$

Finding the many-body ground state of this Hamiltonian is highly complicated due to the exponential growth of the Hilbert space with the number of particles N. However, it is not necessary to do so to describe our system, as explained in section 2.1.3. First, let us address the interaction energy term in (2.2).

2.1.2 Ultracold collisions

To continue the discussion, we must examine the two-body term $U(\mathbf{r}-\mathbf{r}')$, which describes the interactions in the system. The interactions between atoms play a crucial role in describing various physical phenomena, particularly in the scientific projects discussed in this thesis, such as the formation of dimers, the existence of superfluidity, the formation of a soliton. Describing the interactions between two atoms without any assumptions is an extremely ambitious program. However, considering ultracold atoms simplifies the problem, as we will see in the following.

Accurately representing the interactions between atoms relies on scattering theory and requires the introduction of the scattering amplitude (see [90] and [91] for a review). In this text, we will provide the main physical concepts that lead to the scattering length quantity without going into mathematical details.

The scattering problem can be simplified by considering the rotational invariance of the interaction potential. Indeed, for alkali atoms, such as Rubidium, the interaction potential $U(\mathbf{r})$ is dominated by a repulsive term at short distances and an attractive van der Waals potential at longer distances, both of which are isotropic. As a consequence, we can search for a common eigenstate basis of the Hamiltonian of the relative motion of two atoms $\frac{\hat{\mathbf{p}}^2}{2m_{\mathrm{rel}}} + U(\mathbf{r})$ ($m_{\mathrm{rel}} = m/2$ for two identical atoms of mass m), $\hat{L}^2$ the square of the kinetic moment and $\hat{L}_z$ its projection along a given axis z. We write $\psi(r, \theta, \phi)$ this eigenstate in spherical coordinates. Since this is an eigenstate of $\hat{L}^2$ and $\hat{L}_z$, we can express it as a product of a radial wavefunction $\xi(r)$ and a spherical harmonic $Y_{l,m_z}(\theta, \phi)$ with:

$$\hat{L}^2\, \psi = \hbar^2 l(l+1)\, \psi, \quad \hat{L}_z\, \psi = \hbar m_z\, \psi, \qquad l \in \mathbb{N}^*, \quad m_z \in \{-l, -l+1, ..., l\} \quad (2.3)$$

The Schrödinger equation for the radial part $u(r) = r\xi(r)$, using the expression of $\hat{\mathbf{p}}^2$ in spherical coordinates[2], writes:

$$-\frac{\hbar^2}{2m_{\mathrm{rel}}} \frac{\mathrm{d}^2}{\mathrm{d}r^2}\, u(r) + \left[U(r) + \frac{\hbar^2 l(l+1)}{2m_{\mathrm{rel}} r^2} \right] u(r) = E\, u(r), \quad r \geq 0, \qquad u(0) = 0 \quad (2.4)$$

[2] $\hat{\mathbf{p}}^2 \psi = -\frac{\hbar^2}{r} \frac{\partial^2 (r\psi)}{\partial r^2} + \frac{1}{r^2} \hat{L}^2 \psi$

where E is the energy of the system. Everything happens as if the effective potential felt by the particle of mass m_{rel} is:

$$U_{\text{eff}}(r) = U(r) + \frac{\hbar^2 l(l+1)}{2m_{\text{rel}} r^2} \tag{2.5}$$

In the description of the collision between two atoms, each scattering channel, *i.e.* each value of l, can thus be treated independently, and this *partial wave expansion* greatly simplifies the problem, which is now one-dimensional. In Figure 2.1, we show the qualitative form of this potential for different values of l. In an ultracold quantum gas, the energy associated with the relative motion of two atoms E is generally much smaller than the centrifugal barrier term $\frac{\hbar^2 l(l+1)}{2m_{\text{rel}} r^2}$[3]. For the channels corresponding to $l \neq 0$, atoms remain far apart, resulting in smaller scattering processes compared to the $l = 0$ channel, also known as the *s-wave* channel. Therefore, when this scattering channel is not prohibited, which is the case for bosons, we can disregard the $l \neq 0$ channels at low temperatures.

In the context of low-energy collisions and s-wave scattering, only one relevant quantity is necessary to describe the scattering process[4]. This quantity is defined through a low-energy limit of the scattering amplitude and is known as the *scattering length* a. It is a property of the (complicated) interatomic potential $U(r)$. However, simpler potentials can also yield the same scattering length. Using a different potential with the same value of a should not hinder access to most of the physics, as this quantity is sufficient to describe the interactions in the system.

For all these reasons, the interaction potential $U(\mathbf{r}-\mathbf{r}')$ in the context of ultracold gases can usually be replaced by a contact potential[5], which is a natural choice when the range of the potential is small compared to the wavepacket size:

$$U_{\text{contact}}(\mathbf{r} - \mathbf{r}') = g\,\delta(\mathbf{r} - \mathbf{r}') \tag{2.7}$$

For a three-dimensional gas, in order to recover the same scattering length as the true interatomic potential $U(\mathbf{r} - \mathbf{r}')$, g must have a specific value: $g = \frac{4\pi\hbar^2}{m}a$. In the strictly 2D situation, the scattering problem is more complicated (see [93]), and the scattering amplitude depends on the relative wave vector of the collision. However, in the experimentally relevant case of a sample with a thickness $l_z = \sqrt{\frac{\hbar}{m\omega_z}}$ (see Chapter 1) much larger than the scattering length a (*quasi-2D regime*) and at low collisional wave vectors k ($ka \ll 1$), the collisions keep their 3D character and it leads to an energy independent expression for the scattering amplitude [94, 95, 96]. It is important to note that this development assumes sufficiently small scattering lengths and cannot describe interactions near Feshbach resonances.

[3] For a van der Waals potential, we can typically calculate a centrifugal barrier of $\sim k_B \times 10\,\mu\text{K}$ which is much larger than the typical thermal energies of $\sim k_B \times 0.1\,\mu\text{K}$. In other words, the thermal wavelength λ_{th}, the typical size of the wavepacket of the atoms, is much larger than the potential range.

[4] Actually, this is true for scattering lengths that are sufficiently small compared to the range of the potential. When this is not the case, such as near a Feshbach resonance, higher terms in the development of the scattering amplitude must be taken into account [92].

[5] Actually, due to the singularity of the Dirac distribution at $r = 0$, the contact potential is mathematically ill-defined. Therefore, it is common to use another zero-range interaction potential, known as the pseudo-potential:

$$U_{\text{pp}}[\psi(\mathbf{r})] = g\,\delta(\mathbf{r})\frac{\partial}{\partial r}[r\psi(\mathbf{r})]\Big|_{\mathbf{r}=\mathbf{0}} \tag{2.6}$$

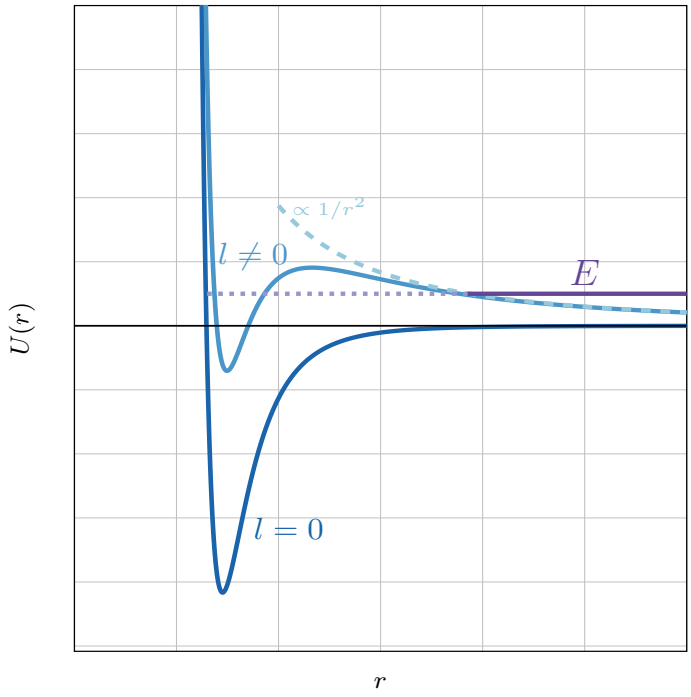

FIGURE 2.1: Interatomic potential of type Lennard-Jones added with centrifugal potentials (2.5). The dark blue curve is the case $l = 0$ and the light blue curve is an example of the case $l \neq 0$. Its asymptote, which behaves in $r \to +\infty$ as $1/r^2$, is drawn with a dashed blue line. For ultracold atoms, the energy involved in a collision E is much smaller than the centrifugal barrier. The atoms do not explore the regions where $U(r) > E$. As a consequence, for $l \neq 0$ channels, the atoms are kept far away from each other and the associated scattering processes are negligible (violet horizontal curve). However, for the $l = 0$ scattering channel (s-wave channel), the atoms can approach each other and the associated scattering process dominates (dashed violet line).

In this subsection, we have shown why considering collisions at low energy allows to simplify the description of the interactions between two atoms. In this context, we introduced the only relevant quantity a, the scattering length, which quantifies the strength of the interactions. The existence of Fano-Feshbach resonances for many atomic species (see [97] for a review and [98] for the case of ^{87}Rb) is an extremely powerful tool to tune the interactions in the system (turn attractive to repulsive interactions or enter the unitary regime $a \to \infty$). We emphasized that describing the interactions with a unique parameter that can be tuned with a single knob on the experiment (magnetic field) makes the ultracold gas platform unique and attractive. Now that a simple model has been introduced to describe the interactions, we can return to the expression of the Hamiltonian (2.2) to simplify it.

2.1.3 Hartree ansatz and the Gross-Pitaevskii equation

At $T = 0$, bosons accumulate in a single quantum state, described by a single-particle wavefunction $\phi(\mathbf{r})$, and form a Bose-Einstein condensate[6]. As a reasonable approximation, we can then search for the ground state $|\Phi\rangle$ as a product state:

[6] It occurs in 3D and 2D at $T = 0$ (see [99]) but not at finite temperature for 2D and 1D gases.

$$\langle \mathbf{r_1}, \ldots, \mathbf{r_N} | \Phi \rangle \propto \phi(\mathbf{r_1}) \ldots \phi(\mathbf{r_N}) \tag{2.8}$$

This is the Hartree ansatz and it considerably simplifies the research of the ground state by replacing the N body problem with a one body problem. This is valid when the number of atoms in the condensate N is sufficiently large, and this method is referred to as a *mean-field description*. This procedure is similar to the transition from quantum electrodynamics to the classical description of electromagnetism when the number of photons is large enough. Inserting the Hartree ansatz (2.8) into $\hat{H}$ (2.2) and assuming a contact potential $U_{\text{contact}}(\mathbf{r}-\mathbf{r}')$ of the form (2.7), we obtain the energy functional associated with $\phi(\mathbf{r})$, which we choose to normalize to the atom number[7]:

$$E[\phi] = \langle \Phi | \hat{H} | \Phi \rangle = \int \mathrm{d}^3 r \left[\frac{\hbar^2}{2m} |\nabla \phi|^2 + V(\mathbf{r}) |\phi(\mathbf{r})|^2 + \frac{g}{2} |\phi(\mathbf{r})|^4 \right] \tag{2.9}$$

We insist that this is allowed for N large enough and for sufficiently weak interactions. Otherwise, ignoring the operational nature of the field leads to incorrect results. In this context, to obtain the equation satisfied by ϕ, we have to minimize the energy of the system with respect to ϕ under the normalization constraint $\int \mathrm{d}^3 r \, |\phi(\mathbf{r})|^2 = N$. To do this, we introduce a Lagrange multiplier [100], μ, and minimize $E[\phi] - \mu \int \mathrm{d}^3 r \, |\phi(\mathbf{r})|^2$. Since μ is the partial derivative of the modified energy with respect to the atom number, it represents the chemical potential of the system and tells us how much the energy is modified when the atom number is changed. Then we reach the stationary nonlinear Schrödinger equation:

$$-\frac{\hbar^2}{2m} \nabla^2 \phi(\mathbf{r}) + V(\mathbf{r}) \, \phi(\mathbf{r}) + g \, |\phi(\mathbf{r})|^2 \, \phi(\mathbf{r}) = \mu \, \phi(\mathbf{r}) \tag{2.10}$$

For the time-dependent problem, the variational method can be generalized and we obtain:

$$-\frac{\hbar^2}{2m} \nabla^2 \, \phi(\mathbf{r}, t) + V(\mathbf{r}) \, \phi(\mathbf{r}, t) + g \, |\phi(\mathbf{r}, t)|^2 \, \phi(\mathbf{r}, t) = \mathrm{i}\hbar \, \frac{\partial \phi}{\partial t}(\mathbf{r}, t) \tag{2.11}$$

This equation was found by Gross [28] and Pitaevskii [29] and is named after them. For the 3D weakly-interacting Bose gas or liquid helium, ϕ is called the *order parameter* of the system, since its square modulus represents the condensed fraction undergoing a phase transition from the BEC (non zero value) to the thermal phase (zero value).

2.1.4 The quasi-2D regime

In quasi-2D systems, such as our experimental platform, the Gross-Pitaevskii equation is slightly modified. The Dirac potential that describes the 3D interactions can be kept because collisions maintain their 3D character in the quasi-2D regime, as explained above. Additionally, at sufficiently low scattering lengths, the scattering length is independent of energy. Therefore we can start with the energy functional (2.9) and integrate out the frozen degree of freedom of the gas, which is denoted as z. To accomplish this, the 3D wavefunction is expressed as the product of a 2D wavefunction and a 1D wavefunction along the z axis. Since the confinement along z is approximated as a harmonic confinement of angular frequency ω_z, the wavefunction along z is written as a Gaussian of width $l_z = \sqrt{\hbar/(m\omega_z)}$, assuming the atoms are in the ground state of the harmonic oscillator along z. Therefore we can write:

[7] Assuming that N is large, we take $N - 1 \simeq N$.

$$\phi(\mathbf{r}) = \varphi(x, y)\,\chi(z) \quad \text{with} \quad \chi(z) = \frac{1}{(\pi\, l_z^2)^{1/4}} \exp\left(-\frac{z^2}{2l_z^2}\right) \tag{2.12}$$

By inserting (2.12) into the energy functional (2.9) and minimizing it with respect to φ under the normalization constraint, the 2D Gross-Pitaevskii equation is obtained:

$$-\frac{\hbar^2}{2m}\nabla^2\varphi + \tilde{V}\,\varphi + \frac{\hbar^2}{m}\,\tilde{g}\,|\varphi|^2\,\varphi = \mathrm{i}\hbar\,\frac{\partial\varphi}{\partial t} \tag{2.13}$$

with $\tilde{g} = \sqrt{8\pi}\,\frac{a}{l_z}$ a non-dimensional parameter characterizing the interactions in two dimensions[8]. $\tilde{V}$ describes the 2D confinement and depends on the coordinates x and y, as does φ. We could have written a time-independent equation for the 2D problem similar to (2.10). The same procedure can be used to enter the 1D regime as we will see in Chapter 4.

Finally, we insist on the fact that this discussion is valid for weakly-interacting Bose gases. To be more quantitative, this limits the value of $\tilde{g}$ to typically $\tilde{g} \ll 2\pi$ [94]. For our 2D experiment we compute with $a \simeq 100\,a_B$ ($a_B \simeq 0.05\,\mathrm{nm}$ is the Bohr radius) and $l_z \simeq 180\,\mathrm{nm}$, a value of $\tilde{g} \simeq 0.15$[9]. The use of the weakly-interacting regime is thus legitimate in our case, and the mean-field description provides a good approximation to the dynamics of the system at sufficiently low temperatures.

2.1.5 Connexion with hydrodynamics

In the previous subsection, we derived the Gross-Pitaevskii equation describing the evolution of the field φ. To do this, we neglected the granularity of the atoms and transformed the operators into wavefunctions. The original quantum problem is transformed into a classical field formulation. Do we completely erase the quantum nature of the problem? To answer this question, we reformulate the Gross-Pitaevskii equation in the density-phase representation with $\varphi = \sqrt{n}\,\mathrm{e}^{\mathrm{i}\theta}$ and introduce an irrotational velocity field $\mathbf{v} = \frac{\hbar}{m}\boldsymbol{\nabla}\theta$ where θ is well defined [89]. The equation (2.13) can then be written as:

$$\begin{cases} \frac{\partial n}{\partial t} = -\boldsymbol{\nabla}\cdot(n\mathbf{v}) \\ \frac{\partial \mathbf{v}}{\partial t} = \boldsymbol{\nabla}\left[-\frac{1}{2}\mathbf{v}^2 - \tilde{V}(x,y) - \frac{\hbar^2}{m^2}\tilde{g}\,n + \frac{\hbar^2}{2m^2}\frac{\Delta\sqrt{n}}{\sqrt{n}}\right] \end{cases} \tag{2.14}$$

The first equation is a continuity equation that guarantees the conservation of the atom number and the second equation is a modified Euler equation. Both equations are also present in hydrodynamics. More precisely, if we neglect the last term of the second equation, the so-called quantum pressure term, which is often small, particularly for uniform systems, we recover the Euler equation, governing the dynamics of non-viscous fluids. Indeed, many phenomena at play in the ultracold atom platform such as demixion, turbulence, vortices or superfluidity are also key words in the hydrodynamic studies.

Since the velocity is proportional to the phase gradient, the circulation of the velocity along any closed contour $\mathcal{C}$ is quantized:

$$\oint_{\mathcal{C}} \mathbf{v}\cdot\mathrm{d}\mathbf{l} = p\,\frac{2\pi\hbar}{m}, \quad p \in \mathbb{Z} \tag{2.15}$$

[8] The value given here is obtained for a harmonic confinement along z and its general definition is $\tilde{g} = 4\pi a \int \mathrm{d}z\,|\chi(z)|^4$. By construction, we find the value given in [95] in the limit of $a \ll l_z$.

[9] The fact that $a > 0$ and thus $\tilde{g} > 0$, *i.e.* the presence of repulsive interactions, ensures the stability of the cloud.

This circulation does not change by a continuous deformation of $\mathcal{C}$, except when the contour intersects a point where the phase is ill-defined *i.e.* a zero of φ. These points, where the density vanishes, are the quantum vortices mentioned above. When a vortex is encountered, the circulation changes by steps of $\pm\frac{2\pi\hbar}{m}$. This quantization of the circulation of the velocity field is one of the quantum aspects that persists in the Gross-Pitaevskii theory [101].

In summary, we demonstrated that the Gross-Pitaevskii equation can be mapped, under some approximations, to *classical* hydrodynamic equations. However, we emphasized the presence of a quantum pressure term and the *complex* nature of the field φ, which in particular causes the circulation of the velocity field to be *quantized*.

2.1.6 Scale invariance of the 2D weakly-interacting Bose gas

We will now examine one of the main properties of the weakly-interacting 2D Bose gas at zero temperature, its scale invariance. A system is said to be *scale invariant* if the energy is modified in the following manner when the time and space coordinates are dilated with a parameter λ:

$$\left.\begin{array}{l} t \to \lambda^2\, t \\ l \to \lambda\, l \end{array}\right\} \Longrightarrow E \to \frac{1}{\lambda^2}\, E \tag{2.16}$$

We can explicitly check that the kinetic energy $\propto \int \mathrm{d}^d r\, |\nabla\varphi|^2$ is always transformed as $E_{\mathrm{kin}} \to \frac{1}{\lambda^2} E_{\mathrm{kin}}$ regardless of the dimension of the system d. For the interaction energy of the weakly-interacting 2D Bose gas $\propto \tilde{g} \int \mathrm{d}^2 r\, |\varphi|^4$, it also transforms into $E_{\mathrm{int}} \to \frac{1}{\lambda^2} E_{\mathrm{int}}$ because $\tilde{g}$ is dimensionless [101]. The weakly-interacting homogeneous 2D Bose gas is thus scale invariant, as is the 3D unitary Fermi gas for example [102].

We now give some properties of scale invariant systems. The equation of state of such a system depends only on the ratio $\mu/k_B T$ and not on μ and $k_B T$ independently. This has been verified experimentally for the weakly-interacting 2D Bose gas in [26, 103]. This scale invariance also has some consequences for the dynamical properties of the system. Placed in a harmonic potential of frequency $\omega/2\pi$, although the system is no longer scale invariant, there exists a breathing mode that oscillates at 2ω regardless of the value of the interactions. It was predicted for example by [104] and verified in [105]. Recently, our team has shown that for certain wavepackets, not only the size of the gas oscillates at 2ω, but also the wavepacket *itself* [27]. This is the case for the equilateral triangle shown in Figure 2.2. A theoretical justification was provided in [106] thanks to a mapping to hydrodynamical equations.

Finally, we emphasize that as soon as $\tilde{g}$ is no longer negligible compared to 2π, the mean-field description fails to describe the interactions, a new length scale enters the problem, and the scale invariance breaks down along with the properties described above. We speak of *quantum anomaly* [107] and an example of a deviation from the mean-field description can be found in [108].

2.1.7 Conclusion

In this section, we presented the derivation of the Gross-Pitaevskii equation, which describes the dynamics of a 2D weakly-interacting Bose gas at zero temperature. We explained the emergence of the scattering length and the different hypotheses that allow for a mean-field description of the gas and its interactions. Finally, we briefly discussed the remarkable properties of the 2D Bose gas resulting from the scale invariance in the system. In the following section, we report how we are able to

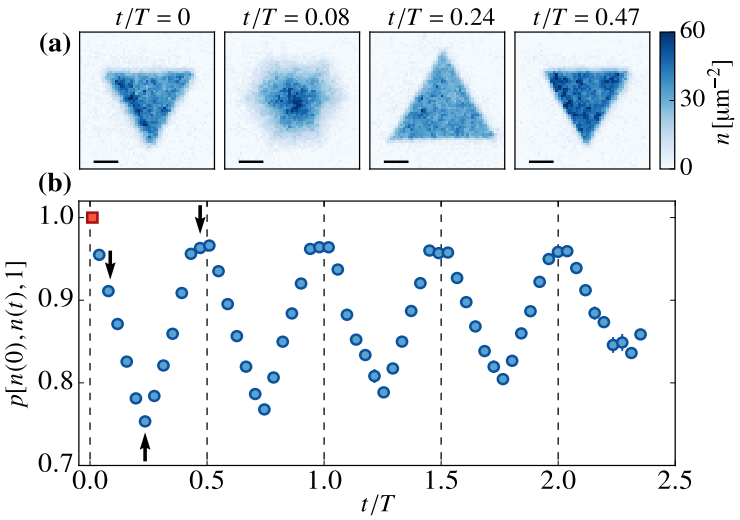

FIGURE 2.2: Breather of the 2D weakly-interacting Bose gas. Figure taken from [27]. (a): A uniform gas is prepared inside an equilateral triangle and placed in a harmonic trap of frequency $1/T$. The wavepacket is inverted after a quarter of the harmonic trap period T and close to the initial one at $T/2$. The black lines represent 10 µm. (b): Evolution of the scalar product between the wavefunction at time t and the initial one. The red dot is the initial point and the 3 arrows represent the times t at which absorption images of the cloud are recorded in (a). The wavefunction oscillates with a period of $T/2$.

produce dimers of ^{87}Rb on our setup and measure their interactions with the rest of the atomic cloud, relying on a mean-field description.

2.2 Precise measurement of atom-dimer interactions

This section presents our recent work on atom-dimer interactions. It has been already extensively detailed in Chloé Maury's thesis [83] and we will give here only the main results. The description of the interaction between two atoms is extended to explain how bound states can emerge. The creation of weakly-bound states is then discussed, followed by a comparison of the spectroscopic measurements with a simple model. Finally, the precise measurements of the frequency transfer used to create a dimer are employed to extract an atom-dimer scattering length.

2.2.1 Production of dimers via MW photoassociation

As previously discussed in section 2.1.2, the interactions between two atoms are attractive at long distances and are of the van der Waals type. At short distances, the potential becomes repulsive, and between the two regimes, a minimum of the potential is reached, as shown in Figure 2.1. This allows for the existence of several bound states of two atoms with energy $E < 0$, known as *dimers*. For strongly bound states, the dimer is often referred to as a *molecule*. Here, the study is limited to weakly bound dimers.

Actually, in addition to the van der Waals interaction and the short-distance repulsive interaction, two other interactions must also be considered. First, hyperfine interactions $\propto \hat{\mathbf{s}} \cdot \hat{\mathbf{i}}$ for each atom, split the electronic ground level into two hyperfine

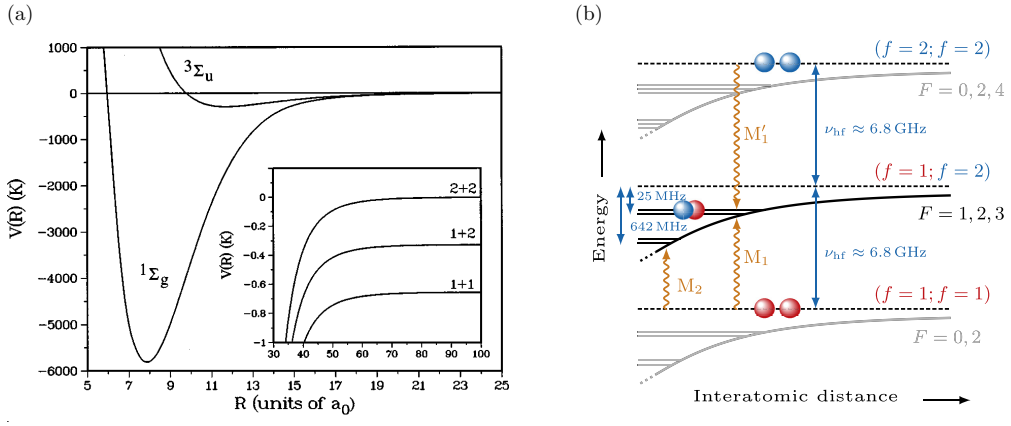

FIGURE 2.3: Molecular potentials. (a): Interatomic potentials between two atoms of ^{87}Rb. Figure taken from [91]. The two interaction potentials for the singlet $^1\Sigma_g$ and the triplet potentials $^3\Sigma_u$ are represented as a function of the interatomic distance. For $R > 20\,a_B$ the two potentials are similar and the hyperfine interaction dominates. It leads to the three collision channels shown in the inset of the figure. The bonding orbital (singlet potential) can host several bound states. (b): Zoom on the large interatomic distance part (basically the interatomic distance range of the inset of (a)). Figure extracted from [87]. The three subspaces, separated by the hyperfine splitting, are shown. The dashed lines are the dissociation limits below which bound states can exist. The thick lines are the molecular potentials. For each subspace we present the two least bound states that split themselves into a group of two or more states due to the singlet-triplet coupling. In the following we focus on the subspace $\{f = 1, f = 2\}$ and its least-bound states, shown in black. The dimers are created by microwave photoassociation from the subspace $\{f = 1, f = 1\}$ (wavy line M_1). The drawing is not to scale.

levels of total angular momentum $f = 1$ and $f = 2$ (s is the electron spin[10] and i is the nuclear spin). Thus, when dealing with dimers, we have to consider three subspaces: $\{f = 1, f = 1\}$, $\{f = 1, f = 2\}$, and $\{f = 2, f = 2\}$. This interaction causes the interatomic potential curve to split into three branches at large interatomic distances (inset of Figure 2.3). At short distances, the interaction is dominated by an effective one, resulting from the fact that the total spin of the pair S can take two different values: $S = 0\,(1/2 - 1/2)$ or $S = 1\,(1/2 + 1/2)$, leading to two slightly different scattering lengths. In chemical terms describing a covalent bond, the $S = 0$ potential, called the singlet potential, corresponds to a bonding orbital of lower energy than the $S = 1$ potential, called the triplet potential, which corresponds to an antibonding orbital. A representation of these potentials is plotted in Figure 2.3. The horizontal axis is the distance between the atoms in units of the Bohr radius a_B. In our dilute ultracold Bose gas, the typical distance between atoms is equal to $d_a \sim n^{-1/3} \simeq 100\,\text{nm} \simeq 200\,a_B$. Naturally, when a bonded dimer is formed, this distance is reduced. However, the two atoms still remain at a distance $\gtrsim 10\,\text{nm} \simeq 20\,a_B$ from each other when considering weakly bound dimers. In this regime, as we can see in the figure, the difference between singlet and triplet potentials is small compared to the hyperfine splitting effect (shown in the inset of Figure 2.3). Therefore, we treat this effective interaction $\hat{H}_{\text{st}} = U\,\hat{\mathbf{s}}_1 \cdot \hat{\mathbf{s}}_2$ as a perturbation of the hyperfine interaction

[10] Contrary to Chapter 1, we do not use $\hat{\mathbf{j}}$ the total electronic angular momentum, because we are only considering the electronic ground state for which $l = 0$ and thus $\hat{\mathbf{j}} = \hat{\mathbf{s}}$. Additionally, unlike Chapter 1, individual momenta are denoted using lowercase letters, while uppercase letters are reserved for the dimer momenta.

($U \ll \Delta E_{\mathrm{hf}} \simeq h \times 6.8\,\mathrm{GHz}$). This will cause each subspace to split into different states.

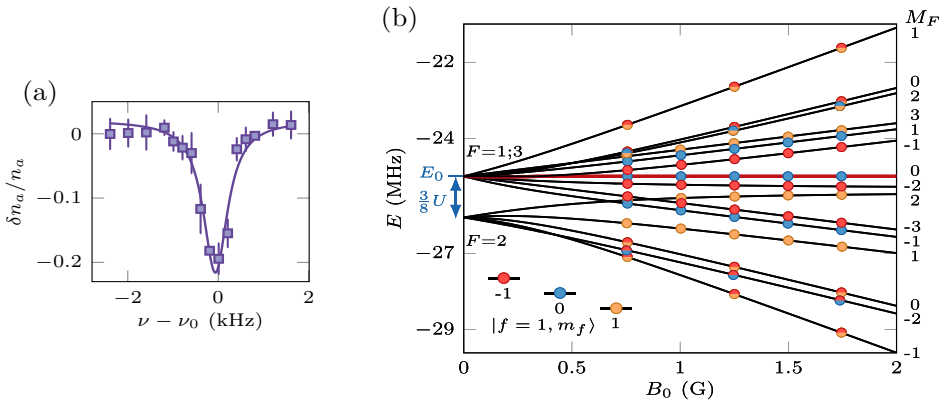

FIGURE 2.4: Observation of dimers. (a): Loss signal at low densities. We detect the formation of dimers by atomic losses δn_a after the application of the MW field at frequency ν. The resonance frequency of the transfer ν_0 is the frequency at which the observed losses are maximal. (b): Energy diagram of the subspace $\{f = 1, f = 2\}$. The circles represent the experimental points, their colors indicate the initial spin composition of the cloud used to reach these lines. Black solid lines are the result of the diagonalization of the full Hamiltonian with free parameters E_0, which is a global offset, and U the parameter describing the singlet/triplet term. The discrepancy between the model and the experimental points is always less than $h \times 3\,\mathrm{kHz}$. The red line highlights a first-order magnetically insensitive state. Figure taken from [87].

In the following, we consider only the first vibrational state (*i.e.* the least bound state) of the subspace of one atom in $f = 1$ and one atom in $f = 2$. More details about the other subspaces and the second vibrational state can be found in [87] and [83]. At zero magnetic field, the Hamiltonian $\hat{H}_{\mathrm{st}}$ results in a splitting of this subspace into two branches. When a non-zero magnetic field is applied, the energy levels do not vary linearly with the magnetic field due to the Zeeman Hamiltonian, which mixes the different F states (Figure 2.4(b))[11].

We now turn to the experimental realization of these dimers. In the subspaces $\{f = 1, f = 1\}$ and $\{f = 2, f = 2\}$ the least bound dimers were obtained in the group of D. J. Heinzen thanks to two-photon photoassociation [109]. Regarding the first vibrational state of the subspace $\{f = 1, f = 2\}$, its bound energy, $\sim -h \times 25\,\mathrm{MHz}$, was already measured in Melbourne [110], where the dimers were produced by radio-frequency association. Here, we use a microwave field, described in Chapter 1, to create the dimers. It has a frequency $\sim 6.8\,\mathrm{GHz}$ and an amplitude $\sim 30\,\mathrm{mG}$. We shine this field on a homogeneous cloud of atoms in the state $|f = 1, m_f\rangle$. We detect dimer formation by atomic losses in the cloud. For each target state, we vary the excitation field frequency, as can be seen in Figure 2.4(a), and we define the resonance frequency as the frequency at which the losses are maximal. By varying the magnetic field and the initial Zeeman state m_f of the $f = 1$ bath, we identify the 15 lines of the $\{f = 1, f = 2\}$ subspace[12]. The finite linewidth of the loss signals ($\sim 1\,\mathrm{kHz}$) can be explained by the finite lifetime of the created dimers. To avoid

[11] For the $\{f = 1, f = 2\}$ subspace, there are $(2 \times 1 + 1) \times (2 \times 2 + 1) = 15$ states.

[12] For some of the lines, we prepare the initial cloud in a mixture of Zeeman states and we use microtraps to prevent the mixture from demixing (see [83] for more details).

additional broadening of the line, it is advantageous to work with homogeneous gases. Figure 2.4(b) shows our measurements of the energy diagram of the dimer alongside the curves obtained thanks to the diagonalization of the phenomenological Hamiltonian taking into account the hyperfine interaction, the singlet/triplet interaction $\hat{H}_{\mathrm{st}}$ and the Zeeman Hamiltonian. The model has only two free parameters: the bonding energy $\sim -h \times 25\,\mathrm{MHz}$ and the phenomenological term that describes the difference between singlet and triplet potentials U.

It should be emphasized that the observation of dimer formation is not guaranteed even if the frequency is known. The field should indeed have the adequate amplitude and polarization to induce photoassociation. The dimer lines targeted in this study mostly exhibit weak coupling with the MW field. Therefore, a 50 W amplifier and up to 10 s of excitation were required to create the dimers.

2.2.2 Atom-dimer interactions

After creating the dimer, a natural question arises regarding its interaction with the rest of the cloud of atoms in $f = 1$, called the bath.

Experimentally, we vary the initial density of the atomic cloud and aim for a dimer state that is insensitive to magnetic field up to first order (red line in Figure 2.4(b)). We find that this line is shifted to smaller resonance frequencies as the density is increased (see Figure 2.5). The shift can go up to $\simeq$ 800 Hz, and can be measured accurately using the high-precision MW chains described in Chapter 1.

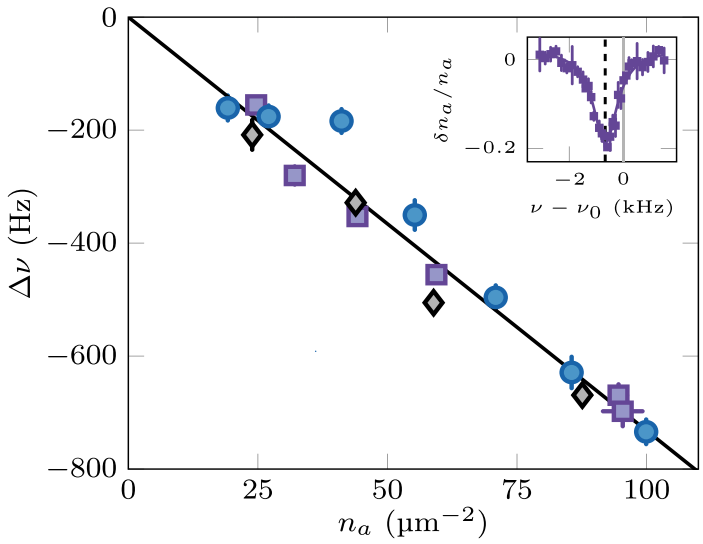

FIGURE 2.5: Measurement of the atom-dimer interaction for the magnetic field insensitive least bound state of the subspace $\{f = 1, f = 2\}$ and a bath of atoms in $f = 1$. Increasing the density of the bath leads to a slightly lower resonance frequency (the inset should be compared with Figure 2.4(a)). The different colors and shapes of the points correspond to different maximum depletions of the bath: circles (respectively squares, diamonds) are obtained for a depletion of 8% (resp. 20%, 14%). They fall on the same curve confirming that we are working in the low excitation regime. Figure taken from [87].

We interpret the observed linear shift $\Delta\nu$ in a mean-field approach, which we introduced in section 2.1. Indeed, the interactions between the dimers and the atoms are described using only the s-wave scattering channel, assuming that the relative velocity of the dimer and the rest of the atomic cloud is sufficiently small. A scattering

length for this process a_{ad} is introduced. A short calculation, which can be found in [87], relates the shift of the line $\Delta\nu$ to this scattering length, the interaction parameter between two atoms in $f = 1$: $g_{11} = 4\pi\hbar^2 a_{11}/m$, and the density of the bath n_a:

$$h\Delta\nu = \left(\frac{\sqrt{3}\, a_{ad}}{2a_{11}} - 2\right) g_{11} n_a \tag{2.17}$$

Since a_{11} is independently well calibrated on our setup (see [86]), the slope of the linear shift of the line gives a direct access to a_{ad}. For the interaction between the first-order magnetically insensitive state of the least-bound state of the subspace $\{f = 1, f = 2\}$ and a bath of atoms in $f = 1$, we then get: $a_{ad} = 184(2)a_B$.

2.2.3 Conclusion

In this section, we provided a brief description of our recent study of atom-dimer interactions in a ^{87}Rb cloud. The measurements were made possible by a mean-field description of the gas. We emphasized the precision of our measurements, which were made possible by our well-developed MW chains and the uniformity of the cloud, which prevented inhomogeneous broadening of the lines. More details can be found in [87, 83].

2.3 A striking property of the 2D weakly-interacting Bose gas at zero temperature: superfluidity

This section briefly describes the property of superfluidity in our system and its relation to the discussion on the Gross-Pitaevskii equation at $T = 0$ (section 2.1). The question of superfluidity at finite temperature is postponed to the next section.

2.3.1 Features of superfluidity

One of the most well-known characteristics of a superfluid is the existence of a dissipation-less flow for sufficiently slow flows. Superfluidity is then often described as the absence of viscosity. This phenomenon was first observed in liquid ^{4}He at low temperatures by Kapitza [5] and independently by Allen [6].

Other important features of superfluids can be considered in a thought experiment of a fluid in a rotating container [111]. Let us first imagine that we start with a fluid at rest in a non-moving container and slowly begin to rotate it. A classical fluid will immediately follow the movement of the container, while for a superfluid, there is a critical rotating velocity below which the superfluid remains at rest. This phenomenon was first observed in 1967 in the case of Helium 4 [7]. This property is commonly referred to as *phase stiffness*. The superfluid does not follow the rotation of the container, resulting in a reduced moment of inertia compared to the classical value. Another key characteristic of a superfluid is its metastability. Let us consider a scenario where we begin with a superfluid that rotates along with its container, and then abruptly stop the container. A classical fluid will stop quickly due to its viscosity, while in superfluids *permanent currents* can persist for a certain amount of time, which can be exceptionally long[13]. Therefore, the superfluid is considered metastable because the rotating state with the container at rest is not the ground state of the system, but it still exists for a certain time. This criterion of metastability

[13] In supraconductors, which are also systems exhibiting superfluidity, this time could be several tens of years [112].

is crucial in defining superfluidity. Indeed, the ideal gas does not satisfy this criterion, although it has the property of phase stiffness, which was discussed previously [111]. The controversial discussion of superfluidity in the ideal gas limit will be postponed until Chapter 3.

Bose-Einstein condensates are systems that exhibit superfluidity, as we will see in the next subsection. The ultracold atom platform is well-suited for the study of superfluidity, notably because interactions between atoms can be controlled. Figure 2.6 displays some results obtained on superfluid ultracold gases, demonstrating the absence of dissipation at low rotating velocities of a defect within the fluid and the metastability of the system when attempting to rotate the fluid.

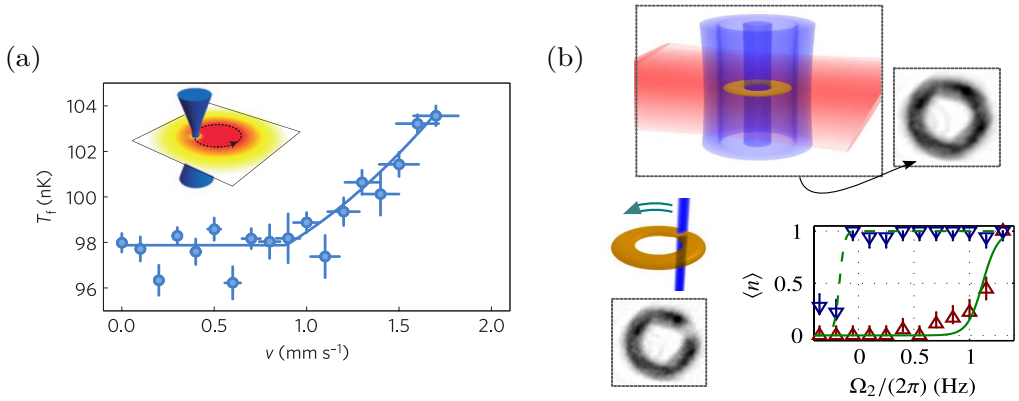

FIGURE 2.6: Examples of superfluidity features in the ultracold atom platform. (a): Experiment conducted at the LKB in Paris. A planar Bose gas (in red) is stirred with a focused laser beam rotating at a constant velocity v (in blue). For low v the cloud is not heated: the flow is dissipation-less, while for $v \gtrsim 1\,\mathrm{mm/s}$ the fluid is heated. The authors also performed the experiment in a thermal gas and showed that there is no dissipation-less zone. Figure taken from [23]. (b): Experience performed in NIST. A repulsive weak link (in blue) is stirred at a velocity Ω_2 for 2 s inside an annular dipole trap (in orange) of initial winding number $\langle n \rangle = 0$ (red triangle) or $\langle n \rangle = 1$ (blue inverted triangle). Depending on the initial state, the curve $\langle n \rangle(\Omega_2)$ is not the same. This reveals the metastability of the superfluid gas. Figure extracted from [113].

2.3.2 A link between mean-field description and superfluidity

In this section, we provide a justification for the superfluidity of the weakly-interacting 2D Bose gas at zero temperature, which is described by a Gross-Pitaevskii equation. As illustrated by its remarkable features, superfluidity is a transport property. Indeed, the connection with the mean-field description is made through the velocity of the fluid, $\mathbf{v}$. More precisely, let us consider two reference frames $\mathcal{R}$ and $\mathcal{R}'$, the second one moving with velocity $-\mathbf{v}_\mathcal{R}$ with respect to the other one. In the mean-field description, we are allowed to characterize the fluid by a unique complex field φ. In $\mathcal{R}$, where the fluid is supposed to be at rest, it can be written as: $\varphi(\mathbf{r}) = \sqrt{n_0}\,\mathrm{e}^{-\mathrm{i}\,\mu t/\hbar}$. In $\mathcal{R}'$, it can be shown, using unitary transformations between Galilean reference frames, that the wavefunction φ' is modified as [111]:

$$\varphi'(\mathbf{r},t) = \mathrm{e}^{\mathrm{i}\,m\,(\mathbf{r}\cdot\mathbf{v}_\mathcal{R} - v_\mathcal{R}^2\,t/2)/\hbar}\,\varphi(\mathbf{r}-\mathbf{v}_\mathcal{R}t,\,t) = \sqrt{n_0}\,\mathrm{e}^{\mathrm{i}\,m\,(\mathbf{r}\cdot\mathbf{v}_\mathcal{R})/\hbar}\,\mathrm{e}^{-\mathrm{i}\,(m\,v_\mathcal{R}^2\,t/2\hbar + \mu t/\hbar)} \quad (2.18)$$

We write it in the density-phase representation as $\varphi'(\mathbf{r}, t) = \sqrt{n}\, e^{i\theta'}$. The superfluid velocity in $\mathcal{R}'$ is defined as the gradient of the phase of the wavefunction in $\mathcal{R}'$, θ', multiplied by $\frac{\hbar}{m}$ (we already introduced a velocity field in the same way in section 2.1.5, but did not connect it to the superfluid velocity at that time). Here we get from (2.18):

$$\mathbf{v_s} \equiv \frac{\hbar}{m}\boldsymbol{\nabla}\theta' = \mathbf{v}_{\mathcal{R}} \tag{2.19}$$

We thus obtain that the superfluid velocity in $\mathcal{R}'$ is equal to the opposite of the velocity at which $\mathcal{R}'$ moves with respect to $\mathcal{R}$, as we expected for a superfluid at rest in $\mathcal{R}$. This calculation, also done for example in [89, 111], justifies the name of the velocity field for the quantity $\mathbf{v_s}$. It also establishes the irrotational nature of the superfluid. More details on the connection between superfluidity and Bose-Einstein condensation can be found in [114].

In this subsection, the relationship between the condensation phenomenon, described by an order parameter, and superfluidity through the superfluid velocity was explored. However, it should not be concluded that a pure condensed gas is fully superfluid or that a pure superfluid is completely condensed. In the following, the concept of superfluid fraction will be introduced and counterexamples of strict coincidence between condensation and superfluidity will be provided.

2.3.3 Theoretical description of a superfluid: Two-fluid model and Landau criterion

Shortly after the discovery of superfluidity in liquid Helium films, Tisza in 1938 [115] and then Landau in 1941 [116] proposed a model to describe the physics of superfluids. It is called the *two-fluid model* and consists in separating the whole fluid into two interpenetrable parts:

- A normal part of density n_n and velocity $\mathbf{v}_\mathrm{n}$. In the thought experiment of a container rotating at angular speed $\boldsymbol{\Omega}$, $\mathbf{v}_\mathrm{n} = \boldsymbol{\Omega} \times \mathbf{r}$, and when the container is stopped, $\mathbf{v}_\mathrm{n} = \mathbf{0}$.
- A superfluid part with zero entropy, described by its density n_s and velocity $\mathbf{v}_\mathrm{s}$ as defined above.

The fluid as a whole has a density $n = n_\mathrm{n} + n_s$. The superfluid fraction is naturally defined as:

$$f_s = \frac{n_s}{n} \tag{2.20}$$

This superfluid fraction does not coincide with the condensed fraction, defined as the ratio of the number of condensed atoms to the total atom number. For example, at zero temperature, liquid Helium is fully superfluid (*i.e.* $f_s = 1$), but the condensed fraction is less than 0.1 due to strong interactions.

From the two-fluid model, hydrodynamic equations for the evolution of the density and the velocity of the superfluid can be derived. These equations are formally equivalent to the hydrodynamic formulation of the Gross-Pitaevskii equation, which was discussed in section 2.1.5. The evolution of the two fluid densities with temperature can also be obtained [89]. The two-fluid model also predicts an important feature of superfluidity: the existence of two sound modes propagating in the superfluid. These two sound modes were first observed in liquid Helium in 1946 [117], and more recently in a 2D weakly-interacting Bose gas [25] and in strongly interacting Fermi gases (another superfluid system) [118].

In his 1941 article, Landau also provided a condition for the existence of a Galilean invariant superfluid (he was discussing liquid Helium at this time)[14]. He considers an object moving at velocity $\mathbf{v}$ in a fluid at rest. The elementary excitations[15] of the fluid are characterized by their dispersion relation $\epsilon(\mathbf{p})$, where ϵ is an energy and $\mathbf{p}$ a momentum. Landau introduced a velocity v_c defined from the energy spectrum of the excitations:

$$v_c = \min_{\mathbf{p}} \frac{\epsilon(\mathbf{p})}{||\mathbf{p}||} \tag{2.21}$$

and he showed that a fluid is superfluid if there exists such a velocity and if it is strictly positive. Then, it can be demonstrated that for velocities of the object $||\mathbf{v}|| < v_c$ the creation of elementary excitations in the fluid, causing dissipation, is not energetically favorable (see for example [89]). In this case, the superfluid remains at rest in the laboratory frame and the motion of the object does not cause heating. In the opposite case, for velocities $||\mathbf{v}|| > v_c$, excitations spread out in the fluid and the flow becomes unstable. This phenomenon is a characteristic of superfluidity, as described in section 2.3.1. This criterion is called the Landau criterion for superfluidity that emphasizes the importance of the spectrum of the fluid's elementary excitations. To conclude, it should be noted that the Landau criterion discussed above assumes excitations above the stationary state that have a well-defined canonical momentum $\mathbf{p}$, *i.e.* plane waves created by point-like defects. However, other types of excitations of the cloud, such as vortex pairs, could be created in the cloud for large enough moving objects [120, 111]. The formulation of Landau criterion as (2.21) should then be modified.

2.3.4 Ground state and elementary excitations of the weakly-interacting 2D Bose gas at $T = 0$

The preceding subsection emphasized the importance of elementary excitations in describing superfluidity. We now return to the weakly-interacting 2D Bose gas and present some properties regarding its ground state and elementary excitations above this ground state, still at zero temperature. This will enable us to introduce key physical quantities of the gas.

The 2D Gross-Pitaevskii (GP) equation (2.13) is generally difficult to solve analytically without relying on some approximations, even in the stationary case. Therefore, numerical tools are often required. Appendix B discusses the GP simulations used in this thesis.

A first approximation, called the *Thomas-Fermi approximation*, which is relevant far from the edges of the gas where the density varies only slightly, is to neglect the kinetic term compared to the interaction term in the GP equation[16]. Then, the

[14] For non-Galilean invariant systems, such as spin-orbit coupled BECs, the critical velocity of superfluidity is dependent on the reference frame [119], and the Landau criterion given here cannot be direcly applied.

[15] Landau introduced them as: "Every weakly excited state must be considered as a combination of simple 'elementary excitations'".

[16] And this is true even when working in the weakly-interacting regime. Indeed, the ratio of the interaction energy to the kinetic energy is roughly given by $N\tilde{g}$, showing that it is not $\tilde{g}$ alone that matters, but the product with the atom number. Since $\tilde{g} \simeq 0.15$ and $N \sim 10^5$ in our experiment, we are deep in the Thomas-Fermi regime. This order of magnitude argument does not hold if the wavefunction varies a lot, for example near the boundaries of the cloud or in spatially modulated situations (Chapter 3).

resolution of (2.13) is greatly simplified and in the so-called Thomas-Fermi regime, we get:

$$\mu = \frac{\hbar^2}{m}\,\tilde{g}\,n(\mathbf{r}) + \tilde{V}(\mathbf{r}) \tag{2.22}$$

where μ is the chemical potential of the gas, $n(\mathbf{r}) = |\varphi(\mathbf{r})|^2$ is the 2D density, and $\tilde{V}(\mathbf{r})$ is the 2D potential.

For a uniform gas, we thus obtain a constant density deep in the bulk: $n(\mathbf{r}) = n_0 \equiv \frac{m}{\hbar^2\tilde{g}}\,\mu$, as expected.

For a non uniform gas, the density variations follow the potential variations, as seen in (2.22). This is a specific case of the *Local Density Approximation* (LDA). This approach states that for a potential profile that varies smoothly enough, the state of the trapped gas of chemical potential μ_{trapped} in $\tilde{V}(\mathbf{r})$ is the same as the state of the homogeneous gas of chemical potential $\mu_{\text{trapped}} - \tilde{V}(\mathbf{r})$. In particular, for the local density, it leads to:

$$n(\mathbf{r}) = n_{\text{homo}}(\mu_{\text{trapped}} - \tilde{V}(\mathbf{r})) \tag{2.23}$$

For the uniform gas, we have $n_{\text{homo}}(\mu_{\text{homo}}) = \frac{m}{\hbar^2\tilde{g}}\,\mu_{\text{homo}}$ and the LDA regime (2.23) gives the same equation as the one obtained with the Thomas-Fermi approximation (2.22).

The Local Density approximation is a more general method than the Thomas-Fermi approximation because it can be applied beyond the mean-field regime and at finite temperature [89]. This method allows for the analytical treatment of systems subjected to a slowly varying potential by referring to the uniform gas up to a change of chemical potential. In Chapter 3, we will utilize it to address sinusoidally spatially modulated systems.

Returning to the uniform case, the evolution of the wavefunction near the boundaries of the system can be actually solved exactly. The gas density decreases from n_0 in the bulk to zero at the borders in both directions of space on a characteristic length scale known as the *healing length*. In 2D, the healing length is expressed as follows[17]:

$$\xi = \frac{1}{\sqrt{\tilde{g}\,n_0}} \tag{2.24}$$

This is the characteristic length scale associated with the interactions. Wherever the density goes to zero, for example near a vortex, the profile adapts on a length scale given by ξ, hence the name healing length. Its value in our 2D experiment is a fraction of µm, typically $\xi \simeq 0.3\,\mu\text{m}$[18] for $n_0 \simeq 80\,\text{atoms}/\mu\text{m}^2$. We plot the evolution of the wavefunction near a zero of density in Figure 2.7(a).

Above this ground state of momentum $\mathbf{p} = 0$, we can consider elementary excitations of momentum p and energy $\epsilon(p)$, which form a weakly excited state[19]. Their dispersion relation can be determined by adding a small perturbation to the ground state in the Gross-Pitaevskii equation and constitute the so-called Bogoliubov spectrum [121]:

$$\epsilon(p) = \frac{1}{2m}\left[p^2\left(p^2 + 4\,\tilde{g}n_0\hbar^2\right)\right]^{\frac{1}{2}} \tag{2.25}$$

[17] Other definitions that differ by a factor $\sqrt{2}$ can also be found.

[18] This is typically three times less than the resolution of our imaging system, hence the impossibility of seeing vortices *in situ* in our setup.

[19] Once again, more complex excitations produced by non point-like defects could also be considered.

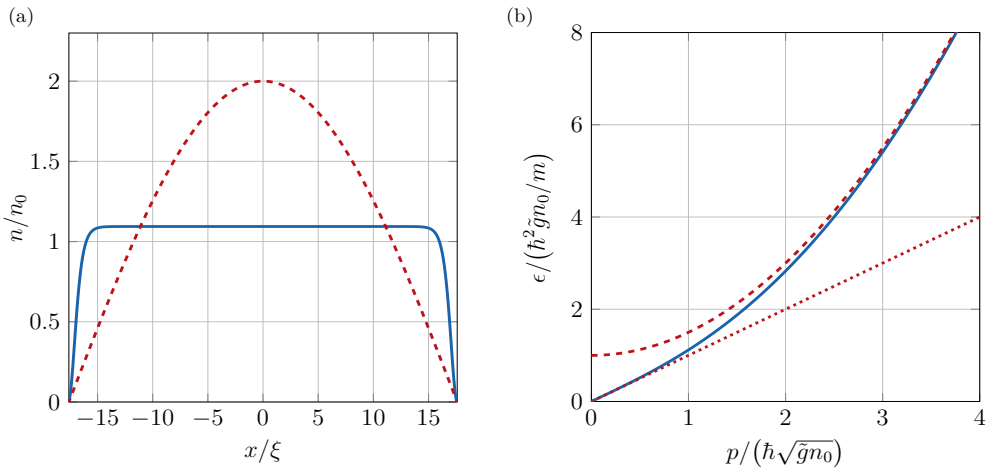

FIGURE 2.7: Uniform weakly-interacting Bose gas properties. (a): Ground state of the uniform weakly-interacting Bose gas (solid blue line) with strict boundary conditions. The red dashed line is the non-interacting limit. The density goes from 0 at the border of the system to n_0, the uniform value in the bulk, on a typical length scale given by the healing length ξ. (b): Bogoliubov spectrum $\epsilon(p)$ represented with the solid blue line. The dashed line is the large momentum asymptote (free particle type spectrum) and the dotted line is the linear low momentum limit (phonon excitations).

We can naturally identify two regimes in this dispersion relation shown in Figure 2.7(b):

- $p \gg 2\hbar\sqrt{\tilde{g}n_0}$ where the dispersion relation is quadratic *i.e.* that of free particles added to an offset: $\epsilon(p) = \frac{p^2}{2m} + \frac{\hbar^2}{m}\tilde{g}n_0$
- $p \ll 2\hbar\sqrt{\tilde{g}n_0}$ where the dispersion relation is linear: $\epsilon(p) = c_B\, p = \hbar\frac{\sqrt{\tilde{g}n_0}}{m}\, p$, hence the name of phonons for the elementary particles propagating in the system. We introduce the so-called Bogoliubov speed of sound $c_B = \hbar\frac{\sqrt{\tilde{g}n_0}}{m} = \frac{\hbar}{m\xi}$, which gives the typical speed at which phonons propagate in the system. Its order of magnitude is $c_B \simeq 2\,\mathrm{mm/s}$ in our experiment. Sound propagation has been observed in 2D Bose gases, for example in [24], by looking at the response to a weak perturbation of the gas. We will also probe sound propagation in a modulated Bose gas to evaluate its superfluid fraction in Chapter 3.

Does the weakly-interacting Bose gas satisfy Landau criterion? The answer is positive, since $\min_{\mathbf{p}} \frac{\epsilon(\mathbf{p})}{p} = c_B > 0$: the gas satisfies the Landau criterion of superfluidity and c_B is the critical velocity of a moving point-like object below which flow can occur without dissipation. We can also immediately see that the ideal gas does not satisfy the Landau criterion, since $\min_{\mathbf{p}} \frac{\epsilon(\mathbf{p})}{p} = 0$. Indeed, this criterion is related to the metastability of the superfluid, and we have already said that the ideal gas is not metastable under the rotation of a container in section 2.3.1.

2.3.5 Twisted boundary conditions

While the Landau criterion, also known as the metastability criterion, provides a necessary condition for superfluidity, it is not a sufficient criterion. To fully describe

this phenomenon, one must also consider the *phase stiffness* of the superfluid, as we saw in section 2.3.1. How can this be quantitatively accounted for?

To describe phase stiffness, it is convenient to consider a fluid, that is decomposed into normal and superfluid parts, rotating at an angular frequency Ω within an annulus container of radius r_0, and parametrize the problem with cylindrical coordinates (r_0, ϕ, z). To treat this problem, we can choose to work with the usual periodic boundary condition for the wavefunction. In this case, a vector potential $\mathbf{A}(\mathbf{r}) = m\,\mathbf{\Omega} \times \mathbf{r}$ is added to the Hamiltonian (2.1) to account for the rotation of the container. A more convenient choice is to keep the bare Hamiltonian (2.1) and incorporate the vector potential into the boundary condition, which then writes [63, 111]:

$$\varphi(r_0, \phi + 2\pi, z) = \mathrm{e}^{-\mathrm{i}\Theta}\varphi(r_0, \phi, z) \tag{2.26}$$

where $\Theta = \frac{2\pi r_0 A}{\hbar}$ and $A = m\,\Omega\,r_0$ is the norm of the vector potential. These boundary conditions, which are associated with the bare Hamiltonian, are referred to as *twisted boundary conditions* due to the inclusion of a phase factor in the boundary condition.

For low rotational velocities, the superfluid component of the fluid remains at rest in the laboratory frame. In the rotating frame, there is an energy cost per surface S that must be paid for not following the movement of the container. This cost can be expressed as [111]:

$$\frac{\Delta E(\Omega)}{S} = \frac{A^2}{2m}\,n_s = \frac{\hbar^2\Theta^2}{8m\pi^2{r_0}^2}\,n_s \tag{2.27}$$

Therefore, by considering a twisted angle Θ on the boundary condition satisfied by the wavefunction and evaluating the excess energy caused by the phase stiffness of the superfluid, one can access the superfluid density of the gas.

Although we have assumed here an annular geometry, the discussion can be naturally extended to linear geometries with dimensions $L_x \times L_y$. When there is a perturbation of velocity v_x along the x axis, the twisted boundary conditions are written as follows:

$$\begin{cases} \varphi(x + L_x, y) = \mathrm{e}^{-\mathrm{i}\Theta_x}\varphi(x, y) \\ \varphi(x, y + L_y) = \varphi(x, y) \end{cases} \text{, with } \Theta_x = \frac{m v_x L_x}{\hbar} \tag{2.28}$$

The energy cost in the moving frame is then: $\Delta E(v_x) = \frac{\hbar^2\Theta_x^2 N}{2mL_x^2}\,f_{s,x}$, where N is the atom number and $f_{s,x}$ is the superfluid fraction along x[20].

The excess in energy given by (2.27) can be seen as a rigorous definition of the superfluid fraction and we will use it in Chapter 3 to calculate the superfluid fraction in a spatially modulated system.

2.3.6 Conclusion

Superfluidity is a hallmark of quantum many-body systems, arising from the interactions in the system. Cold atoms are an ideal platform for studying superfluidity for both Bose and Fermi systems. In this section, we introduced the theoretical tools necessary for discussing superfluidity. We also defined quantities associated with the interactions that are essential for describing weakly-interacting Bose gases, such as the healing length.

[20] In Chapter 3, we will explain in more details the notion of "superfluid fraction along an axis" by describing the superfluid fraction as a rank-two tensor which can have different values along the eigenaxes of the system x and y.

2.4 Is $T = 0$ a reasonable hypothesis?

Throughout this chapter, we deliberately did not discuss the effect of the finite temperature of the system. In the following, we explain why a non-vanishing temperature in a real experimental system does not hinder the application of the Gross-Pitaevskii formalism with good approximation and does not destroy superfluidity.

2.4.1 BKT phase transition and the survival of superfluidity

One first consequence of finite temperature is the non-fully superfluid behavior of the gas. Prokof'ev & Svistunov [122] calculated the decay of the superfluid fraction with temperature for a 2D weakly-interacting Bose gas. The more general theory describing the limitation of phase ordering in a 2D weakly-interacting Bose gas was developed by Thouless, Kosterlitz and Berezinskii [19, 18]. It has been predicted that the proliferation of individual vortices can destroy phase ordering at high temperatures. However, for temperatures below a critical temperature T_c, the vortices exist only in bond pairs of vortex/antivortex, which do not significantly perturb the phase ordering but do reduce the superfluid fraction. The transition between the two regimes is known as the Berezinskii-Kosterlitz-Thouless (BKT) phase transition. This transition is characterized as a topological phase transition, which was first observed in 1980 with 2D liquid helium films [123] and more recently with cold atoms [20]. The critical point where the superfluid fraction jumps from a non zero value for $T < T_c$ to 0 for $T > T_c$ is predicted to occur for a universal value of the superfluid phase space density: $n_s\lambda_{\mathrm{th}}^2 = 4$. Regarding the total phase space density, Prokof'ev & Svistunov [122] numerically predicted that the phase transition arises at:

$$n\lambda_{\mathrm{th}}^2 \simeq \ln\left(\frac{380}{\tilde{g}}\right) \tag{2.29}$$

We can thus evaluate the critical temperature in our experiment for a density $n \simeq 80\,\mathrm{atoms}/\mu\mathrm{m}^2$ and we get $T_c \simeq 300\,\mathrm{nK}$[21]. Since in the work discussed in this thesis we work at temperature $T \lesssim 20\,\mathrm{nK}$, the normal fraction is practically zero (below 1%) and the system is in good approximation fully superfluid (at least when working with homogeneous gases).

2.4.2 Loss of phase ordering and quasi-long range order

Does the mean-field approach we have used throughout this chapter hold for finite temperature? Indeed, a key hypothesis for applying the mean-field formalism is to assume that all particles occupy the same quantum state and form a condensate. However, the Mermin-Wagner-Hohenberg (MWH) [124, 125] theorem states that a phase transition involving a spontaneous breaking of a continuous symmetry cannot exist for a system of dimension $d < 3$ with short-range interactions. Since the transition to a Bose-Einstein condensate for the weakly-interacting 2D Bose gas meets the aforementioned requirements, it is incorrect to speak of 2D Bose-Einstein condensation at $T > 0$. To be more quantitative, one must introduce the first-order correlation function g_1, which expresses the loss of coherence over a distance r in the gas:

$$g_1(r) = \frac{1}{n}\langle\varphi^*(0)\varphi(r)\rangle \tag{2.30}$$

[21] For this temperature, the superfluid fraction in our system is $f_s \simeq \frac{1}{2}$ [122].

where $\langle\cdot\rangle$ represents a spatial average. Berezinskii, Kosterlitz and Thouless demonstrated that in 2D g_1 decays with the distance r as a power law below the phase transition [18, 19]:

$$g_1(r) \sim \left(\frac{\lambda_{\mathrm{th}}}{r}\right)^{\frac{1}{n_s \lambda_{\mathrm{th}}^2}} \tag{2.31}$$

This is consistent with the MWH theorem: the limit of g_1 at large distances is 0 as soon as $T > 0$[22]. However, the algebraic decay of g_1 with r is much slower than an exponential decay, such as the one present above the BKT transition. Evaluating the loss of coherence over $L = 40\,\mu\mathrm{m}$, the typical size of our box, and using the result $n_s \simeq n \simeq 80\,\mathrm{atoms}/\mu\mathrm{m}^2$ justified in section 2.4.1 for $T \lesssim 20\,\mathrm{nK}$, we get: $g_1(L)/g_1(0) \gtrsim 0.93$. Therefore, the two sides of the box remain highly correlated, maintaining a high spatial phase ordering. In a good approximation, the entire gas can still be described by a single wavefunction. The slow decay of the first-order correlation function is a characteristic of the 2D weakly-interacting Bose gas and is related to the existence of a *quasi-long range order*. The measurement of g_1 in a 2D Bose gas was recently conducted using matter-wave interferometry [127].

A reasonable spatial phase coherence is maintained throughout the cloud without violating the MWH theorem, justifying a mean-field description even at strictly non zero temperatures.

2.4.3 Conclusion

The 2D weakly-interacting Bose gas at finite temperature constitutes an example of a strictly non-condensed system with a finite superfluid fraction. We argued that, despite not being a true Bose-Einstein condensate, the 2D ultracold gas exhibits a quasi-long range order and can be effectively treated using a mean-field approach with good approximation due to the practical use of finite size samples. We also briefly discussed the effect of finite temperature on the superfluid fraction. Its decay has been measured indirectly in [118] in the Fermi gas case and in [25] in the 2D Bose gas case. The following chapter will present a direct measurement of the superfluid fraction and its decrease, not due to the modification of the system's temperature, but rather due to the presence of a spatial modulation. In the rest of the manuscript, the temperature used in the experiments is $T \lesssim 20\,\mathrm{nK}$, and the system is well approximated by a zero-temperature gas as described above. Therefore, we will refer to our system as "$T = 0$ gas".

2.5 Summary

This chapter described the theoretical tools used to analyze a weakly-interacting 2D Bose gas at zero temperature. The fundamental Gross-Pitaevskii equation governs the physics of the system under study, resulting from a mean-field treatment and the presence of weak interactions. Additionally, we discussed a mean-field study on the production of Rubidium dimers and the measurement of their interactions with the atomic bath. Finally, we introduced the superfluid property of the weakly-interacting 2D Bose gas and debated the relevance of the zero temperature approximation in our experimental system.

[22] A definition of Bose-Einstein condensation, which we owe to Penrose and Onsager [126], is the existence of a finite limit for $g_1(r)$ as r goes to infinity. Bose-Einstein condensation is then seen as the appearance of an *off-diagonal long range order*.

Part II

Measurement of the zero-temperature superfluid fraction in a spatially modulated Bose gas

Chapter 3

Superfluid fraction in an interacting 2D modulated Bose gas at $T = 0$

The previous chapter presented a theoretical description of the weakly-interacting uniform ultracold Bose gas and its superfluid property. We introduced the superfluid fraction of the system as a physical quantity of interest. It provides the fraction of the total fluid that is superfluid and determines superfluid transport phenomena. This chapter presents a theoretical and experimental description of how spatial modulation, rather than uniformity, affects the superfluid fraction. It is important to note that we work at $T = 0$ in the following as justified in section 2.4. This study was begun in the team at the end of Chloé Maury's thesis and both theoretical and a first analysis of experimental results can be found in her thesis [83]. The last version of the experimental analysis taking into account the second harmonic in the density profiles (see 3.4) was performed within the team afterwards and is detailed in this chapter.

3.1 Density modulated systems

A cold atom experiment is a simulation platform where one can adjust several key experimental parameters, such as interaction strength, density, temperature, and external potential, on a "simple" system. It consists of a dilute gas with a density typically less than 10^{14} atoms/cm^3, easily accessible, which can mimic, in certain conditions, a denser (typically 10^{23} atoms/cm^3 *i.e.* 10 orders of magnitude denser than ultracold gases) and difficult to control bulk sample. This is the idea of quantum simulation first introduced by Feynman in 1981 [128]. For instance, treating the condensed matter problem of conduction in a bulk solid is challenging. However, ultracold atoms trapped in optical lattices offer a fully controllable system that simulates the movement of electrons in solids. This topic is the focus of several cold atom groups worldwide, and they have already demonstrated phenomena such as the formation of antiferromagnetic states [129], the transition to a Mott insulator [130] or the phenomenon of Bloch oscillations [131] (see [132] for a review).

Chapter 2 introduced a theoretical description of a weakly-interacting Bose gas trapped in a flat potential. The Local Density Approximation (LDA) was mentioned to generalize the physics when the potential is not flat but varies smoothly. Let us imagine now that the atoms are localized around some lattice sites, similar to electrons in a solid. The atomic density exhibits significant modulations around these sites, and the LDA description of such a system is no longer valid. In a system that breaks strongly translational invariance, such as an artificial crystal, it is therefore difficult to see at first glance that the features described in the previous chapter, Bose-Einstein

condensation and superfluidity, survive. Penrose and Onsager in 1956 [126] argued that Bose-Einstein condensation may not occur in a solid, such as solid ^{4}He, where the long-range order condition they introduced for both interacting liquids and gases is no longer expected to be present. In 1970, Chester [133] instead justified that systems exhibiting long-range order can exist in the presence of crystalline order if there are a finite number of vacancies in the solid. He also argued that the transport superfluid properties would vanish in a crystalline ordered system[1]. Leggett [63] nuanced this statement by showing that a finite superfluid fraction can still exist in a modulated system. Therefore, he argued that a solid can be a superfluid. However, spatial modulation reduces the superfluid fraction. Leggett quantified this decrease with the following upper bound for the superfluid fraction:

$$f_s \leq \frac{1}{\langle n \rangle \left\langle \frac{1}{n} \right\rangle} \tag{3.1}$$

where n represents the spatial density of the system and the brackets stand for a spatial average.

A supersolid is a state of matter that exhibits both crystalline order and superfluidity. The spatial ordering, which breaks the translational invariance, should arise spontaneously. In 2004, supersolidity was first claimed in solid Helium following an experiment that observed a reduction of moment of inertia caused by phase stiffness [134]. However, it was later shown that the observed phenomena could be explained by changes in the elastic properties of the solid [135]. Kim et al. repeated the experiment with a new apparatus and found no evidence of supersolidity in solid Helium [136]. Regarding the ultracold atom platform, recent results have emerged. In 2017, groups from Zurich [64] and the MIT [65] demonstrated the emergence of the supersolid phase through an increase in interactions in a BEC placed inside two optical cavities or by a spin-orbit coupling, respectively. Although spatial ordering appears spontaneously in these experiments, an external lattice potential is used to pin the atoms. In 2019, supersolid phases were observed on the platform of dipolar gases. These phases emerge from the competition between contact and dipole-dipole interactions, and they were demonstrated without any external lattice potential [137, 61, 62] (see also [138] for a recent review).

The existence of these supersolid phases illustrates the possiblity of having both a crystalline and a superfluid order, a counter-intuitive and remarkable combination. The results of Leggett's original paper apply to other kinds of modulated systems[2], even when the breaking of translational invariance is not spontaneous but externally imposed. The purpose of this chapter is to confirm the predictions of Leggett's formula and to explore its range of validity in the latter situation, which can be easily implemented on our experimental platform. We begin by taking advantage of our weakly-interacting Bose gas system to show that we can write an equality for (3.1) instead of an inequality. This result links a transport quantity, which can also be accessed through sound transport measurements, to the static density variations of the spatially modulated system. It enables us to measure the superfluid fraction in two different ways.

[1] He thus emphasized, as we did in the previous chapter, that Bose-Einstein condensation and superfluidity are not equivalent phenomena.

[2] In section 3.6, we will explore the scope of application of Leggett's formula in more details.

3.2 Superfluid fraction in a weakly-interacting spatially modulated Bose gas

This section discusses the survival of superfluidity in a density modulated weakly-interacting Bose gas placed in a separable potential.

3.2.1 Saturation of Leggett's inequality

We first rewrite Leggett's original argument [63] about the superfluid fraction in the case of a 2D weakly-interacting Bose gas. We assume here that the system remains well described by the Gross-Pitaevskii theory even though density modulations occur. We recall that all the physics discussed below assumes $T = 0$.

To evaluate the superfluid fraction of the modulated gas, we will use the definition given in Chapter 2, which relies on twisted boundary conditions. We consider a 2D system of size $L \times L$ of N bosons. It is placed in a separable potential V which is homogeneous along y and inhomogeneous along x.

In 2D, the superfluid fraction is in general a rank-two tensor. We choose x and y as the proper axes of this tensor *i.e.* the off-diagonal terms have been set to zero. We want to evaluate the superfluid fraction along the modulated axis x, so the twisted angle θ_x is included in the twisted boundary condition along x. Regarding the y axis, the boundary condition is not affected because the superfluid fraction tensor is diagonal in the (x,y) basis.

Therefore, we write the twisted boundary conditions for an angle θ_x on the wavefunction φ_{θ_x} as:

$$\begin{cases} \varphi_{\theta_x}(x + L, y) = \exp(\mathrm{i}\,\theta_x)\,\varphi_{\theta_x}(x, y) \\ \varphi_{\theta_x}(x, y + L) = \varphi_{\theta_x}(x, y) \end{cases} \tag{3.2}$$

For convenience, the state φ_{θ_x} is expressed using the density-phase representation, introduced in section 2.1.5:

$$\varphi_{\theta_x}(x, y) = \sqrt{n_{\theta_x}(x, y)}\,\exp\left[\mathrm{i}\,S_{\theta_x}(x, y)\right] \tag{3.3}$$

The velocity field $\mathbf{v}_{\theta_x} = \frac{\hbar}{m}\boldsymbol{\nabla} S_{\theta_x}$ is directed here along the unitary vector $\mathbf{e}_x$, because the boundary conditions are twisted along x. We note its norm v_{θ_x}. The energy of the system reads:

$$\begin{aligned} E[\varphi_{\theta_x}] &= \int_0^L \int_0^L \mathrm{d}x\,\mathrm{d}y \left[\frac{\hbar^2}{2m} |\nabla \varphi_{\theta_x}|^2 + V(x, y)\,|\varphi_{\theta_x}(x, y)|^2 + \frac{\hbar^2}{2m}\,\tilde{g}\,|\varphi_{\theta_x}(x, y)|^4 \right] \\ &= \int_0^L \int_0^L \mathrm{d}x\,\mathrm{d}y \left[\frac{\hbar^2}{2m} \left|\nabla\left(\sqrt{n_{\theta_x}}\right)\right|^2 + \frac{m}{2} n_{\theta_x} v_{\theta_x}^2 + V(x, y)\,n_{\theta_x} + \frac{\hbar^2}{2m}\,\tilde{g}\,n_{\theta_x}^2 \right] \end{aligned} \tag{3.4}$$

We used the expression of the gradient of the wavefunction written as:
$\nabla \varphi_{\theta_x} = \left[\nabla\left(\sqrt{n_{\theta_x}}\right) + \mathrm{i}\,\sqrt{n_{\theta_x}}\,\nabla S_{\theta_x}\right] \exp(i S_{\theta_x})$.

The ground state of the system with twisted boundary conditions can be found by minimizing the energy functional (3.4) under different constraints. The first one is the conservation of the atom number and we introduce the Lagrange parameter μ_0, the chemical potential of the system, to take it into account. The consideration of twisted boundary conditions requires the introduction of another Lagrange multiplier, which we call β. The associated constraint is imposed by the fact that the phase of the wavefunction at the boundaries of the system must be single-valued. It is the

following: $\int_0^L \frac{\partial S_{\theta_x}}{\partial x}\,\mathrm{d}x = \theta_x$. Expressed in terms of the velocity field, the previous constraint also writes:

$$\int_0^L \mathbf{v}_{\theta_x} \cdot \mathbf{e}_x \,\mathrm{d}x = \frac{\hbar}{m}\theta_x \tag{3.5}$$

Thus, the modified energy functional (3.4) of the twisted system, to be minimized with respect to φ_{θ_x}, is the following (up to a constant):

$$E_{\text{modified}}[\varphi_{\theta_x}] = \int_0^L \int_0^L \mathrm{d}x\,\mathrm{d}y \left[\frac{\hbar^2}{2m}\left|\nabla\left(\sqrt{n_{\theta_x}}\right)\right|^2 + \frac{m}{2} n_{\theta_x} v_{\theta_x}^2 + V\, n_{\theta_x} + \frac{\hbar^2}{2m}\,\tilde{g}\, n_{\theta_x}^2\right] - \mu_0 \int_0^L \int_0^L \mathrm{d}x\,\mathrm{d}y\, n_{\theta_x}(x,y) - \beta L \int_0^L v_{\theta_x}\,\mathrm{d}x \tag{3.6}$$

Minimizing this energy with respect to both $\sqrt{n_{\theta_x}} = \chi_{\theta_x}$ and v_{θ_x} gives access to the ground state of the twisted system. For the amplitude of the order parameter χ_{θ_x} we get a modified Gross-Pitaevskii equation:

$$-\frac{\hbar^2}{2m}\frac{\partial^2 \chi_{\theta_x}}{\partial x^2} + V(x,y)\,\chi_\theta + \tilde{g}\frac{\hbar^2}{m}\,\chi_{\theta_x}^3 + \frac{m}{2} v_{\theta_x}^2\,\chi_{\theta_x} = \mu_0\,\chi_{\theta_x} \tag{3.7}$$

The minimization with respect to v_{θ_x} leads to: $v_{\theta_x} = \frac{\beta}{m n_{\theta_x}}$. Using the value of its circulation (3.5), we obtain:

$$v_{\theta_x} = \frac{\hbar\,\theta_x}{m n_{\theta_x}} \frac{1}{\int \frac{1}{n_{\theta_x}}\,\mathrm{d}x} \tag{3.8}$$

To go further, we recall that the superfluid fraction is defined by an expansion of the energy excess due to the twisted boundary conditions (2.27) with respect to the untwisted case ($\varphi_0(y) = \chi_0 = \sqrt{n_0}$) in powers of the twisted angle:

$$\Delta E \equiv E[n_{\theta_x}, v_{\theta_x}] - E[n_0, 0] = \frac{\hbar^2 \theta_x^2 N}{2mL^2}\, f_{s,x} + \mathcal{O}(\theta_x^4) \tag{3.9}$$

So we consider the case of a small twisted angle and write the amplitude of the wavefunction as $\chi_{\theta_x}(x) = \chi_0(x) + \delta\chi_{\theta_x}(x)$. χ_0 is the solution of (3.7) without the term $\frac{m}{2} v_{\theta_x}^2\,\chi_{\theta_x}$, which corresponds to the usual Gross-Pitaevskii equation.

Since the velocity v_{θ_x} is at least of order θ_x (see (3.8)), adding the term $\frac{m}{2} v_{\theta_x}^2\,\chi_{\theta_x}$ to the Gross-Pitaevskii equation will lead to a correction $\delta\chi_{\theta_x}$ on the amplitude of the wavefunction to be at least of order θ_x^2. Thus, at the lowest order in θ_x[3], only the term $\int_0^L \int_0^L \mathrm{d}x\,\mathrm{d}y\, \frac{m}{2} v_{\theta_x}^2\, n_0$ enters the expression of the energy difference ΔE:

$$\Delta E = \int_0^L \int_0^L \mathrm{d}x\,\mathrm{d}y\, \frac{m}{2} v_{\theta_x}^2\, n_0 + \mathcal{O}(\theta_x^4) = \frac{\hbar^2 \theta_x^2 L}{2m} \frac{1}{\int \frac{1}{n_0}\,\mathrm{d}x} + \mathcal{O}(\theta_x^4) \tag{3.10}$$

where we also took the lowest order in θ_x in the expression of the velocity field (3.8) (*i.e.* $n_{\theta_x} \simeq n_0$).

[3] Obviously, the lowest order in θ_x of the energy difference is at least order 2, since twisting the boundary conditions (or, more practically, trying to move a superfluid by moving the container) should be a problem invariant to changing $\theta_x \to -\theta_x$. Moreover, it should be a positive term, regardless of θ_x, as this costs energy to the fluid.

Identifying (3.10) with (3.9) thus gives an expression for the superfluid fraction along the modulated axis as a function of the modulated density:

$$f_{s,x} = \frac{L^3}{N} \frac{1}{\int \frac{1}{n_0}\,\mathrm{d}x} = \frac{1}{\langle n_0 \rangle \left\langle \frac{1}{n_0} \right\rangle} \tag{3.11}$$

with $\langle n_0 \rangle = \frac{N}{L^2} = \frac{1}{L}\int_0^L n_0(x)\,\mathrm{d}x$ and $\left\langle \frac{1}{n_0} \right\rangle = \frac{1}{L}\int_0^L \frac{1}{n_0(x)}\,\mathrm{d}x$.

Therefore, we demonstrated that in the case of a 2D Bose gas described by Gross-Pitaevskii theory, and for which the potential is separable, the superfluid fraction is equal to the upper bound found by Leggett (3.1). This is a noteworthy outcome as it connects a transport quantity, the superfluid fraction, to a purely static quantity, which is the knowledge of the stationary modulated density profile.

The saturation of Leggett's inequality in this context can also be derived through an alternative definition of the superfluid fraction, which relies on the fluid's momentum response to a linear perturbation [66]. This can also be obtained through techniques of homogeneization applied to the GPE [139] or through sum-rules derivations [140].

The above calculation is based on the applicability of Gross-Pitaevskii theory and the separability of the potential. A natural extension of this study involves a non separable 2D modulated potential. Leggett also explored this problem in his paper of 1998 [66]. For a modulated system of density $n(x, y)$, he showed that the superfluid fraction is bounded not only from above by a quantity analogous to what was seen in the 1D case, but also from below. The following inequalities were obtained:

$$f^- = \frac{1}{\bar{n}} \int \mathrm{d}y \left[\int \frac{\mathrm{d}x}{n(x,y)} \right]^{-1} \leq f_s \leq \frac{1}{\bar{n}} \left[\int \frac{\mathrm{d}x}{\int \mathrm{d}y\, n(x,y)} \right]^{-1} = f^+ \tag{3.12}$$

where $\bar{n} = \int n(x, y)\,\mathrm{d}x\,\mathrm{d}y$ is the mean density. According to this work, this set of inequalities is valid regardless of the statistics obeyed by the particles, bosons or fermions, and regardless of the strength of the interactions[4]. The last section of this chapter will also deal with a discussion of Leggett's bounds in more details.

3.2.2 Sound propagation in a 2D modulated system

We will now discuss a method for describing the propagation of sound in a 2D modulated system, which is a useful tool for assessing the superfluid fraction of a sample.

As previously stated in Chapter 2, a unique feature of a superfluid is the existence of two sound modes for the low energy elementary excitations. This is a consequence of Landau's two-fluid model, where the two degrees of freedom, related to the normal and superfluid components of the gas, give rise to these two sound modes. Landau's two fluid model allows one to express their variations with temperature and, under certain approximations (mainly a low value of the compressibility of the fluid [141, 89, 142]), sound oscillations can be decoupled into isoentropic (first sound) and isobaric (second sound) oscillations. However, in the case of dilute Bose gases, the assumption of low compressibility is not valid and the two sound velocities hybridize at low temperature. Moreover, for weakly-interacting Bose gases, the first sound (the one propagating at the highest velocity) appears to be more difficult to access experimentally than the

[4]However, it seems that the applicability of Gross-Pitaevskii theory is a hidden assumption of the lower-bound expression (see section 3.6).

second sound, due to its weak coupling to density excitations in the system [142, 24]. Hadzibabic's group in Cambridge managed to observe the two sound modes [25] by looking at the absorptive response of the center of mass displacement after driving the system with a weak sinusoidal force. From the second sound measurement, they were able to deduce the superfluid fraction of their uniform system through the thermodynamic formula $c^2 = f_s \frac{1}{m\kappa}$, which gives, in good approximation for a 2D weakly-interacting Bose gas, a connection between the superfluid fraction and the second sound velocity c [89, 142], through $\kappa = \frac{1}{n\left(\frac{\partial \mu_0}{\partial n}\right)}$ the compressibility of the gas.

It can be rigorously justified, by introducing the effective mass along the modulated axis (see for example [143, 83]), that this formula can be extended to anisotropic periodically modulated systems where the superfluid fraction is a tensor. The sound[5] then propagates with different values along the two non-equivalent axes:

$$\begin{cases} c_x^2 = f_{s,x} \frac{1}{m\kappa} \\ c_y^2 = \frac{1}{m\kappa} \end{cases} \tag{3.13}$$

where we used that along the unmodulated axis, the system is fully superfluid *i.e.* $f_{s,y} = 1$. Thus, the superfluid fraction along the modulated axis $f_{s,x}$ can be calculated by taking the ratio of these two equations:

$$f_{s,x} = \frac{c_x^2}{c_y^2} \tag{3.14}$$

The result (3.14) for the superfluid fraction has the key advantage that it does not depend on the compressibility of the gas, which can be difficult to access experimentally. However, each individual sound velocity depends on the compressibility which changes as the modulation depth of the potential is varied. Therefore, we predict that the speed of sound along the unmodulated axis depends on the modulation through the modification of the compressibility and that c_x has two sources of variation, the compressibility and the superfluid fraction, which also varies as the modulation is changed. We will discuss these two sources of variation more quantitatively in the next subsection.

The formula (3.14) provides a direct link between the sound velocities in the system and the superfluid fraction along the modulated axis. It is valid as soon as the low momentum excitation spectrum can be described by a single phononic branch. In particular, this should be a valid way to measure the superfluid fraction in a superfluid Fermi gas, while the Leggett's bound may not be saturated for all values of momenta, especially near unitarity (see [140] for a recent study). Conversely, the sound formula written above does not directly apply to supersolids (especially dipolar supersolids) where there is no single gapless sound branch at low momenta.

3.2.3 Limiting cases and analytical estimations

The results (3.11) and (3.14) are exact results in the case of a weakly-interacting Bose gas described by a single wavefunction and placed in a separable potential. We now consider some limiting cases in which we can estimate the superfluid fraction and the compressibility in terms of the relevant energy scales of the problem. In the case of a weakly-interacting Bose gas, we have already introduced the *chemical potential* μ_0, the energy scale associated with the interactions. The periodic potential

[5] In the following, when talking about sound, it will implicitly refer to the second sound.

$V(x) = V_0 \cos(qx)$ brings two other energy scales into the problem, namely its amplitude V_0, which is also called the *modulation depth*, and the *recoil energy* associated with the wavevector of the potential $\epsilon_q = \frac{\hbar^2 q^2}{2m}$.

According to Leggett's formula (3.11), the spatial density is a crucial quantity for determining the superfluid fraction. It can be expressed as a sum of its Fourier modes:

$$n(x) = n_0 - \sum_{i \geq 1} n_i \cos(iqx) \tag{3.15}$$

n_0 represents the mean density, while n_i is the amplitude of the i-th harmonic.

Comparing ϵ_q with μ_0 allows to write simplified equations for the relevant quantities. First, when $\epsilon_q \ll \mu_0$, or in other words, when the period of the potential is much larger than the healing length, the system can be described by the Local Density Approximation, since the potential varies smoothly enough. In this regime the kinetic energy is negligible and analytical estimations can be derived using the saturation of Leggett's formula:

$$\frac{n_1}{n_0} = \frac{V_0}{\mu_0}, \qquad \frac{n_i}{n_0} = 0 \ \ \forall i \geq 2 \tag{3.16}$$

$$\begin{cases} f_{s,x} = \left(1 - \frac{V_0^2}{\mu_0^2}\right)^{\frac{1}{2}} & \text{when } V_0 < \mu_0 \\ f_{s,x} = 0 & \text{when } V_0 \geq \mu_0 \end{cases} \tag{3.17}$$

Even though $\mu_0 \simeq 7\epsilon_q$ in our setup, we will see that these expressions are not sufficient to explain our results for all values of V_0. To go further, we examine the case of small modulation depths, for which we can expand the solution of the Gross-Pitaevskii equation $\sqrt{n(x)}$ in powers of V_0 (see Appendix C). It leads to the following expressions for the first Fourier component and the compressibility at the lowest order in V_0:

$$\begin{cases} \frac{n_1}{n_0} = \frac{2V_0}{2\mu_0 + \epsilon_q} + \mathcal{O}(V_0^3) \\ \kappa = \mu_0^{-1}\left[1 - \frac{2V_0^2 \epsilon_q}{(2\mu_0 + \epsilon_q)^3}\right] + \mathcal{O}(V_0^4) \end{cases} \tag{3.18}$$

At lowest order in V_0, the saturation of Leggett's inequality then yields to:

$$f_{s,x} = 1 - \frac{2V_0^2}{(2\mu_0 + \epsilon_q)^2} + \mathcal{O}(V_0^4) \tag{3.19}$$

The only condition for these estimations to be relevant is that V_0 should be sufficiently small. In addition, if one takes the limit $\mu_0 \gg \epsilon_q$, one falls into the LDA regime and the equations (3.16) and (3.17) are recovered in the limit of small V_0.

From the expression of the compressibility (3.18) we can deduce that in the LDA regime of small ϵ_q, the correction of κ is at least of order V_0^4, while the correction of the superfluid fraction is of order V_0^2. Thus we predict from the sound velocities (3.13) that c_y^2 is at least of order V_0^4, while c_x^2 is of order V_0^2 and decreases with V_0, varying more rapidly with the modulation depth.

Finally, we mention the quasi non-interacting regime, the opposite regime compared to the LDA, of $\epsilon_q \gg \mu_0$. From (3.19), we can get an estimate of the superfluid fraction at small V_0 in this case: $f_{s,x} = 1 - \frac{2V_0^2}{\epsilon_q^2} + \mathcal{O}(V_0^4)$. Since in this regime the Gross-Pitaevskii equation (which coincides with the Schrödinger equation in this context) is linear, we can extract the evolution of the superfluid fraction over the

whole range of V_0 by a numerical diagonalization of the Hamiltonian and by using the relation between the effective mass and the superfluid fraction (see [67]). The result is plotted in Figure 3.1, together with the limits discussed earlier for two different lattice periods. The consideration of a modulation potential allows to discuss the controversial question of superfluidity in the non-interacting regime. Indeed, we already mentioned in Chapter 2 that Landau's criterion (or metastability criterion) predicts a non superfluid character for the ideal uniform gas, while it possesses the phase stiffness characteristic. Depending on which limit $V_0 \to 0$ (cancellation of the modulation) or $\mu_0 \to 0$ (cancellation of the interactions) is taken first, this results in respectively $f_s \to 1$ (see low expansion in V_0 in (3.19)) or a zero superfluid fraction for the ideal uniform gas (see Figure 3.1(b)). In our opinion, it is more legitimate to take the limit $\mu_0 \to 0$ first and then $V_0 \to 0$, as this allows to account for any residual modulations in the gas.

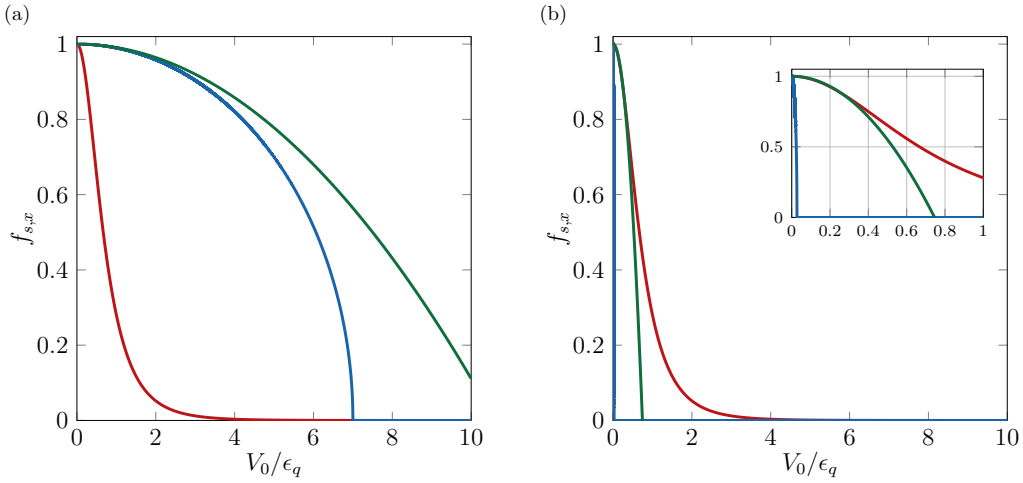

FIGURE 3.1: Superfluid fraction in the limiting regimes. The two plots are obtained for a fixed value of $\mu_0 \simeq k_B \times 50\,\mathrm{nK}$, our experimental value, and correspond to a lattice of period $d = 4\,\mu\mathrm{m}$ (a) and $d = 0.25\,\mu\mathrm{m}$ (b), respectively. The former corresponds to our experimental case where $\epsilon_q \simeq k_B \times 7\,\mathrm{nK} \simeq \mu_0/7$, while the latter would correspond to a retroreflected lattice at 532 nm (as in the recent related work performed in the group of Spielmann [144][6]) yielding $\epsilon_q \simeq 37\mu_0$. In both graphs, we represent the LDA limit in blue (3.17), the non-interacting limit (which does not change between the two plots since the horizontal axis is renormalized by ϵ_q) in red, and the small V_0 expansion at second order in V_0 (3.19) in green. In our work (a), where the LDA regime is more relevant than the non-interacting regime, the small V_0 limit coincides with the LDA. Conversely, in (b), the small V_0 limit approaches well the non-interacting regime, which is a good approximation in this system. The inset of (b) is a zoom for $V_0/\epsilon_q < 1$. This figure emphasizes that the presence of interactions in (a) allows one to have a smoother variation of f_s with respect to the modulation depth and is crucial to provide robustness of the superfluid fraction under the effect of the external modulation potential.

In this section, we have shown how to describe the superfluidity in a 2D modulated system. We demonstrated that for a weakly-interacting Bose gas in a separable potential, Leggett's inequality is saturated. We presented this remarkable result because it opens up a *static* way to measure the superfluid fraction, provided that we have accurate access to the density profile of the modulated gas. We will discuss it later

[6] Their definition of ϵ_q differs by a factor of 4 from ours.

in this chapter. We have also obtained expressions for the sound velocities that we can measure experimentally by exciting the phonons in the modulated system. This is the subject of the next section.

3.3 Dynamical determination of the superfluid fraction

Numerical simulations and experiments are presented here to extract sound velocities in the 2D Bose gas, spatially modulated along one direction, and deduce the superfluid fraction using the formula (3.14).

The spatial modulation is fixed along the x axis and we vary the direction of excitation (x or y) to extract the speed of sound along x or y. The excitation is done by preparing the bidimensional cloud of size $L \times L$, subjected to a uniform force along x (resp. y) (in our case induced by a magnetic gradient) and removing the force at time $t = 0$. It excites the longest wavelength sound mode with a wavelength of $2L$ and after measuring the oscillation frequency of the sound mode ν_x (resp. ν_y), we can deduce the sound velocity $c_x = 2L \times \nu_x$ (resp. $c_y = 2L \times \nu_y$)[7]. This is similar to the technique employed in [25] to measure the two sound velocities but here the system is not driven by the force. Instead, we look at the impulse response after the force is removed. This is a valid protocol to extract the excitation modes of the system as long as the working regime is perturbative. Typically, the energy associated with the magnetic gradient b': $E_{\text{mag}} = g_F m_F \mu_B b' L$ should be small compared to the chemical potential (g_F is the hyperfine Landé factor, m_F is the hyperfine magnetic moment and μ_B is the Bohr magneton).

3.3.1 Numerical simulations

We first apply this protocol to the numerical resolution of the Gross-Pitaevskii equation (see Appendix B for details). Despite the presence of modulation, we assume that the condensate fraction remains unaltered, allowing for the description of the many-body system in a mean-field regime with a single wavefunction at $T = 0$.

First, we compute the ground state (the initial state of the excitation protocol) of the system in presence of a magnetic gradient b' of order $\lesssim 10\,\text{G/m}$ remaining in the regime $E_{\text{mag}} \lesssim \mu_0/4$, and a sinusoidal modulation of amplitude V_0 and wavevector q. In the LDA framework, we anticipate the stationary density profile to exhibit the sinusoidal (due to the modulation) and the linear (due to the force) perturbations, and to be expressed as follows:

$$n(x) = n_0 + \frac{V_0}{g}\cos(qx) + \frac{g_F m_F \mu_B b'}{g} x \tag{3.20}$$

where $g = \frac{\hbar^2}{m}\tilde{g}$. We check that this is a good approximation for a lattice of period $4\,\mu\text{m}$, but no longer as the lattice period decreases or as the modulation depth increases (Figure 3.2(b)). We will look at these deviations in more details in section 3.4 when no force is applied.

In the LDA regime, we can compute the center of mass of the cloud. Since L is commensurable with the lattice spacing, we found the following formula:

$$x_{\text{COM}} = \frac{1}{N}\int_{-L/2}^{L/2}\int_{-L/2}^{L/2} \mathrm{d}x\,\mathrm{d}y\, x n(x) = \frac{g_F m_F \mu_B b' L^4}{12 N g} \tag{3.21}$$

[7] This is valid because the phonon wavelength $2L$ is much larger than the other relevant length scales of the problem, the healing length and the period of the lattice.

where N is the atom number.

We check this formula in Figure 3.2 for the lattice spacing used in our experiment $d = 4\,\mu\text{m}$ and with a small modulation. For $b' \simeq 10\,\text{G/m}$, we calculate a center of mass displacement of the order of $1\,\mu\text{m}$, which should be sufficiently high to be resolved on the experiment.

When V_0 is not negligible compared to μ_0, the LDA formula (3.21) is no longer valid. The evolution of the center of mass with the magnetic gradient remains linear, but the slope given by the compressibility decreases (Figure 3.2(d)). We will discuss this in more details in section 3.6.

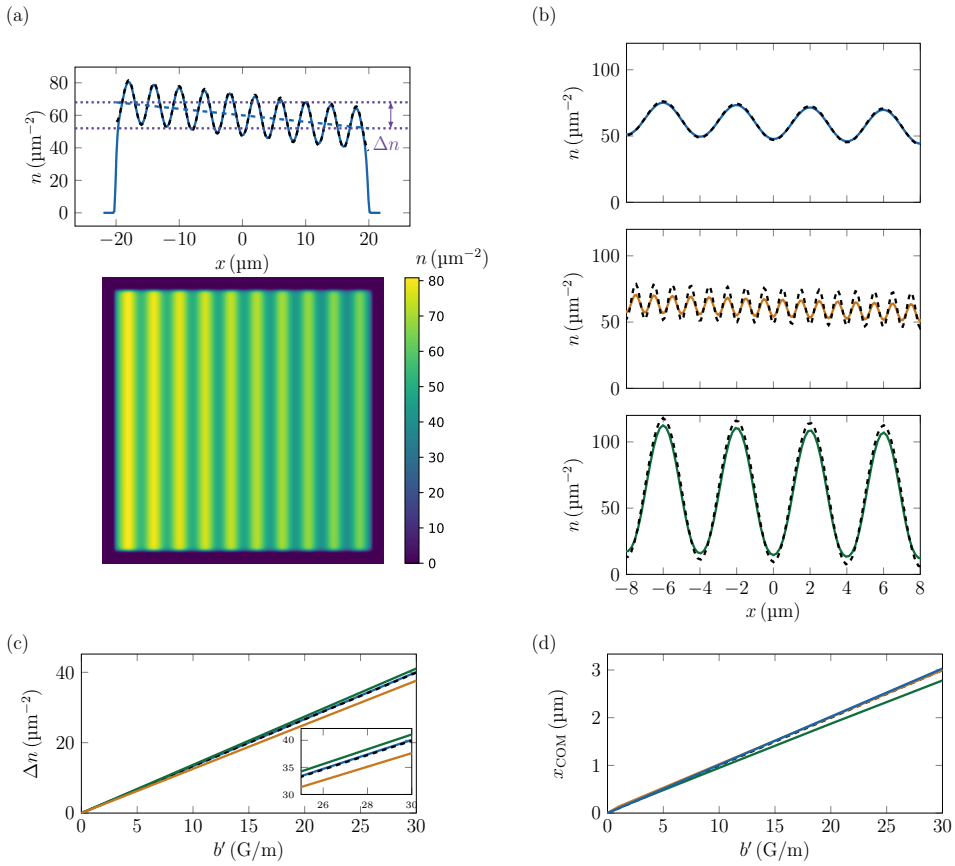

FIGURE 3.2: Numerical stationary state with linear and sinusoidal potentials. In (a), we show an example of stationary state obtained with GP simulations for a gradient of $b' = 10\,\text{G/m}$, a lattice period $d = 4\,\mu\text{m}$ and a modulation potential of $V_0 = k_B \times 10\,\text{nK}$ together with a cut along the modulated direction. The chemical potential is $\mu_0 \simeq k_B \times 50\,\text{nK}$. The dashed blue line is the effect of the magnetic force, which causes a variation of density Δn across the cloud. The LDA result (3.20) is the black dashed line. A zoom of this density cut is represented in Figure (b) top. The other two cuts are obtained respectively for a shorter lattice spacing $d = 1\,\mu\text{m}$ but same modulation depth (orange curve) and for a potential $V_0 = k_B \times 50\,\text{nK} \simeq \mu_0$ but same lattice period (green curve), showing in both cases deviations to the LDA still plotted with a black dashed line (more details in section 3.4). In (c) and (d), we vary the magnetic gradient and look respectively at Δn and x_{COM}. For $d = 4\,\mu\text{m}$ and with a modulation $V_0 = k_B \times 10\,\text{nK}$, the LDA results, still in black dashed lines, are good approximations of the steady state. For $d = 4\,\mu\text{m}$ and $V_0 = k_B \times 50\,\text{nK}$, the result is in green and for $d = 1\,\mu\text{m}$ and $V_0 = k_B \times 10\,\text{nK}$ the result is in orange and we see some deviations from the LDA (more details in section 3.6).

In this section, we investigate the dynamics of the spatially modulated Bose gas after abruptly removing the force on the stationary state discussed just above. We monitor the center of mass's evolution over time for an excitation applied along the modulated axis x (as shown in Figure 3.2) or the unmodulated axis y. The evolution is sinusoidal and we extract a frequency ν_x (or ν_y). While the oscillations along the two axes are identical when the modulation is turned off, we measure a significant difference between them as soon as translational invariance is broken (Figure 3.3).

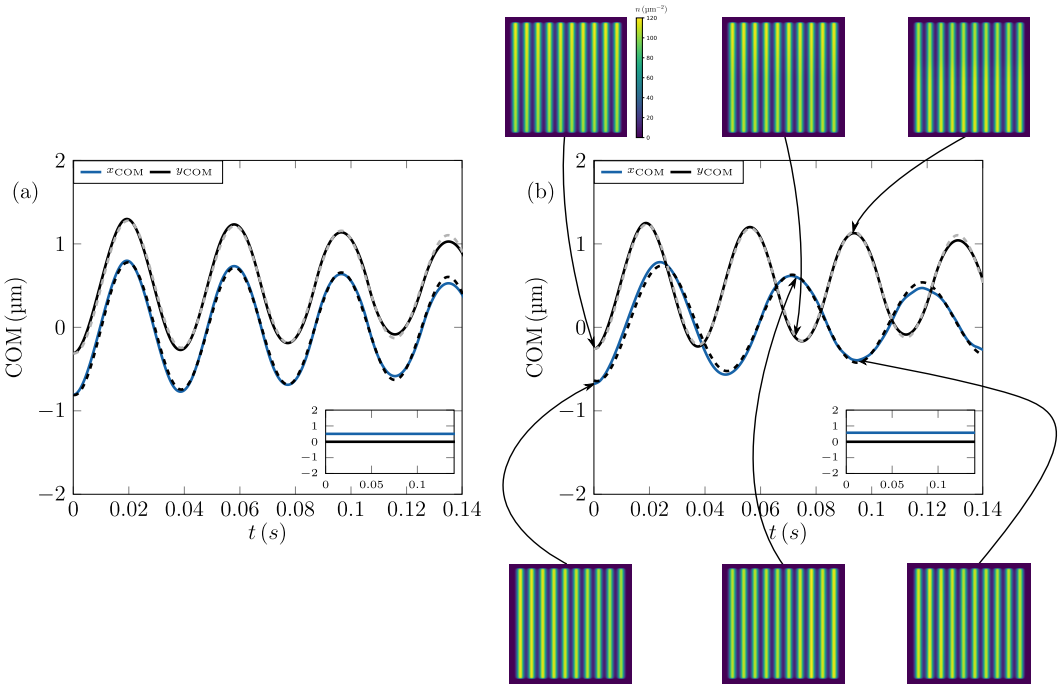

FIGURE 3.3: Numerical evolutions of the center of mass with and without a modulation potential for $b' = 8\,\mathrm{G/m}$ and $d = 4\,\mu\mathrm{m}$. We excite the cloud along x (resp. y) with a magnetic gradient and we look at the center of mass evolution along x (resp. y) in blue (resp. black) after removing the gradient. We check that the cloud does not move along the axis perpendicular to the excitation (insets). The graphs for the excitations along y are shifted by $0.5\,\mu\mathrm{m}$ for clarity. Sinuosoidal damped fits are shown as black dashed (or grey dashed) lines. (a): $V_0 = 0$, the evolutions are isotropic. (b): $V_0 = k_B \times 40\,\mathrm{nK}$. For an excitation along the modulation (blue curve and lower panels), the oscillation frequency is lower than in the unmodulated case, while for an excitation perpendicular to the modulation, the oscillation frequency is slightly higher (black curve and upper panels). The colorbar is the same for all density plots. We can hardly see the center of mass displacement on the density plots, since its maximal value is $\sim 1\,\mu\mathrm{m}$ in the perturbative regime $E_{\mathrm{mag}} \lesssim \mu_0$.

The oscillations are fitted[8] with a sinusoidal damped function whose parameters are defined as follows [24]:

$$x, y_{\mathrm{COM}} = A_{x,y} \exp\left(-\frac{\Gamma_{x,y} t}{2}\right)\left(\frac{\Gamma_{x,y}}{4\pi\nu_{x,y}} \sin(2\pi\nu_{x,y} t) + \cos(2\pi\nu_{x,y} t)\right) + C_{x,y} \qquad (3.22)$$

From the frequency of the center of mass oscillations, triggered by the excitation of the longest wavelength phonon modes, we derive the sound velocities: $c_{x,y} = 2L\,\nu_{x,y}$.

[8] We check that a Fourier analysis gives the same results for the frequency extraction.

We repeat the same procedure for different modulation depths and we summarize the results in Figure 3.4. We also plot the lowest order development in V_0 obtained from the equations (3.18) and (3.19).

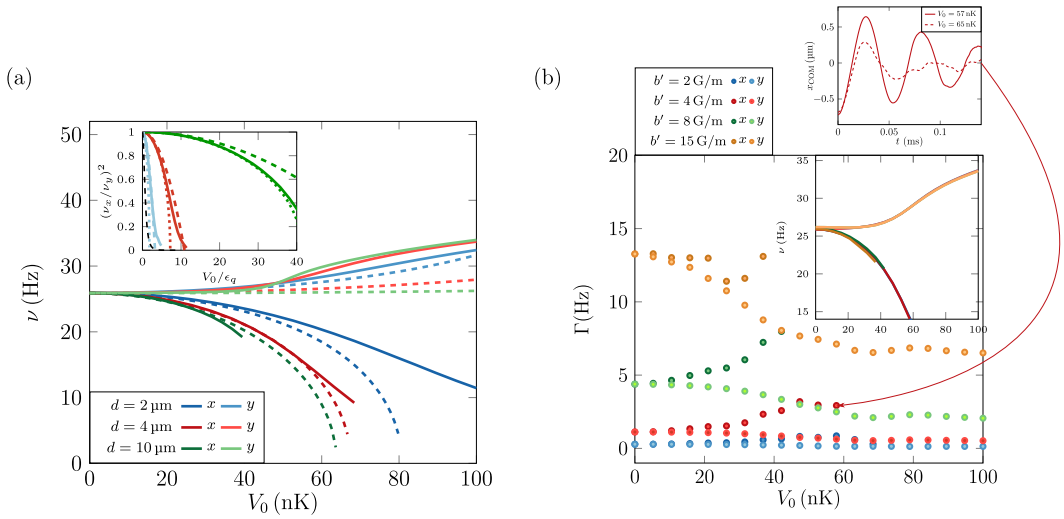

FIGURE 3.4: Simulations to extract sound frequencies. (a): We fix the magnetic gradient $b' = 4\,\mathrm{G/m}$ and we look at the influence of the lattice spacing d on the sound velocities in the same direction as the modulation (x) or in the perpendicular direction (y). The ratio $(\nu_x/\nu_y)^2$ is also plotted in the inset. The dashed colored lines are the low V_0 analytical limits obtained from (3.18) and (3.19), while the dotted lines are the LDA limits (3.17). The dashed black line is the non-interacting limit discussed in section 3.2.3. (b): We plot the damping evolution as a function of the modulation depth for different excitation strengths b' at a fixed lattice spacing: $d = 4\,\mu$m. The larger b', the larger the damping. As a function of the modulation depth V_0, it increases (respectively decreases) when the excitation is parallel (resp. perpendicular) to the modulation. We have to stop the simulations at a certain value of V_0, depending on b', because beyond that the evolution of the center of mass position can no longer be easily fitted with a damped sinusoid (refer to the graph in the upper right part of the figure for an example of evolutions for $b' = 4\,\mathrm{G/m}$: the evolution at $V_0 = k_B \times 65\,\mathrm{nK}$, represented with a dashed red line, is too damped to be considered). We check in the inset that the frequency values do not depend on the excitation for the explored range of b'. This is an essential requirement for this work performed in the perturbative regime.

In Figure 3.4(a), we vary the lattice spacing and see how it modifies the sound velocities and the superfluid fraction. Along the modulated axis, increasing the lattice spacing leads to a larger sound velocity for the same modulation depth. Along the non modulated axis, the behaviour as a function of the lattice spacing is not monotonic. Then we extract the superfluid fraction along the modulated axis $f_{s,x}$ from the ratio squared of the sound velocities (inset of figure 3.4(a), note that the horizontal axis is rescaled by ϵ_q). We see that working with a long wavelength lattice allows to maintain a high superfluid fraction in the system for a same modulation depth. The case of $d = 2\,\mu$m approaches the non-interacting limit ($\epsilon_q \gg \mu_0$), while the superfluid fraction evolution for the $d = 10\,\mu$m lattice is well described by the LDA. For the $d = 4\,\mu$m lattice studied experimentally, the regime is intermediate: the presence of weak interactions maintains a significant superfluid fraction in the system for $V_0/\epsilon_q \lesssim 10$, and the physics deviates quite rapidly from the LDA.

Finally, we briefly discuss the effect of the amplitude of the magnetic field gradient. We see that the less important the magnetic gradient is, the less damping, which is

quantified by the parameter $\Gamma_{x,y}$, we get (Figure 3.4(b)). There is no strong effect on the sound velocities (the curves are superimposed in the inset) as long as we work in the perturbative regime: $E_{\text{mag}} \lesssim \mu_0$. It seems that when the magnetic gradient is increased, more than one phonon mode is excited and this can lead to decoherence of the oscillations over time. At zero modulation ($V_0 = 0$), we numerically found a numerical scaling of the damping coefficient that is compatible with a power law of exponent 2: $\Gamma \propto b'^2$. Since the phonon mode considered has the lowest energy (longest wavelength), it is expected that the damping mechanism is not linear (not Beliaev-like linear behaviour [145]). Recently, Zhang et al. [146] experimentally demonstrated a non-linear damping mechanism in a BEC whereby two low-energy excitations merge into a higher-energy one. The evolution with the modulation seems to be less trivial, as the damping along the non modulated axis is predicted to decrease with V_0.

3.3.2 Experimental implementation

This section presents our experimental study on sound propagation in a 2D modulated Bose gas. The protocol involves two key ingredients: spatial modulation, imprinted with a DMD, and the application of a magnetic gradient for sound measurement. Figure 3.5 illustrates the setup used. We first explain how we calibrate the modulation depth and the magnetic gradient before discussing the experimental procedure.

Calibration of the modulation depth

Regarding the presence of a modulated potential, we already discussed in Chapter 1 our ability to precisely control the potential felt by the atoms with DMD1 and DMD2, working with blue-detuned light. Here, we take advantage of this feature to imprint on DMD2 the following pattern, which we dither[9]:

$$\mathcal{A}(x, y) = \mathcal{A}_0 \sqrt{\alpha + \beta \cos(qx)} \tag{3.23}$$

where we choose $\alpha = 0.5$ and $\beta = 0.4$. With this choice, we avoid defects of impression with the dithering technique at minima of the intensity profile, which would be more important for a fully contrasted modulation. Having a non-vanishing intensity at the minima of the profiles is not an issue, since spontaneous emission is negligible for 532 nm light. The intensity modulation of the light send to the atoms is then sinusoidal with an expected contrast of $\beta/\alpha = 0.8$, as can be seen in Figure 3.6.

The modulation depth can be adjusted by changing the intensity of the 532 nm light sent to the DMD. We could calibrate the resulting potential felt by the atoms as a function of this light intensity, if the beam were perfectly Gaussian and provided we could accurately measure its waist and power on the atoms, using the following formula [147]:

$$V_0 = \frac{3\pi c_{\text{light}}^2 \Gamma}{2\omega_0^3} \left(\frac{1}{\omega - \omega_0} - \frac{1}{\omega + \omega_0} \right) I \equiv \gamma I \tag{3.24}$$

where c_{light} is the speed of light, Γ is the natural linewidth of the first excited level $5P_{3/2}$, ω_0 is the frequency of the D2 line, ω is the frequency of the green light, and I is the intensity of the green Gaussian beam in the atomic plane. γ is the proportionality factor between the modulation depth and the intensity that we want to calibrate. With a power $P \sim 10$ mW and a waist $w \simeq 85$ µm in the atomic plane, we calculate

[9] We recall that the square root comes from the fact that the DMD is an amplitude modulator.

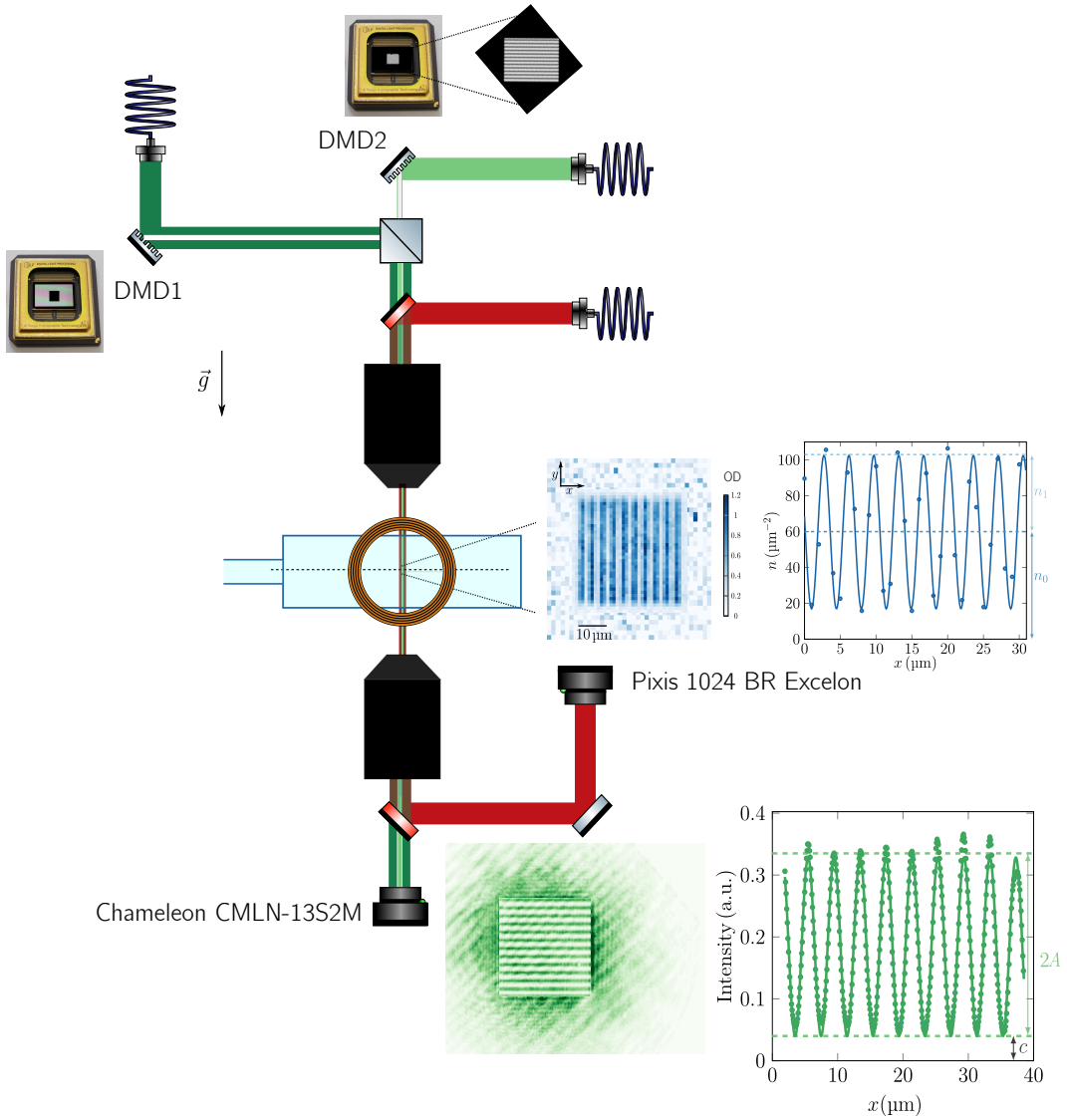

FIGURE 3.5: Scheme of the experimental setup to study the superfluid fraction in a modulated system. The sinusoidal modulation of the light is shaped by shining 532 nm light on DMD2, which is then imaged onto the atoms through a microscope objective, together with the light coming from DMD1, which provides the box potential. An absorption imaging system with 780 nm light is used to image the cloud and is captured on a Pixis camera. An auxiliary imaging system photographs the green light sent to the atoms, and an example of the resulting image is shown near the corresponding Chameleon camera. The diagonal fringes are defects from the imaging setup, while the central fringes are those imprinted with the DMD2. A cut and a sinusoidal fit are plotted. We also depict a MOT coil used in the sound propagation measurement in order to apply a magnetic gradient (we have not shown the bias coils that allow to shift the center of the quadrupolar field).

a potential $V_0 \sim k_B \times 200\,\mathrm{nK}$. We thus estimate that this order of magnitude should allow us to explore the physics seen in the GP simulations (Figure 3.4). However, this is obviously a rough estimate and we need a more precise calibration. For this we use the atomic response directly.

We use long wavelength lattices for which we are confident that our finite resolution imaging system, which acts as a filter for the fast spatial variations, does not have any impact. We measure the relationship between the atomic density modulation n_1

at a certain wavevector of the lattice q[10] and the light intensity. At low modulation depths, the two quantities are proportional with a coefficient called $\alpha(q)$. This is also the case for V_0 and n_1, as we demonstrated in section 3.2.3. The relation is given by (3.18):

$$V_0 = \left(\mu_0 + \frac{\epsilon_q}{2}\right)\frac{n_1}{n_0} = g\, l(q)\, n_1 \tag{3.25}$$

with $l(q) = 1 + \frac{\epsilon_q}{2\mu_0}$. From the measurement of $n_1(I)$ (Figure 3.6(a)) and the formula (3.25), we thus get the desired calibration $V_0 = \gamma I$. For long wavelength lattices $d \geq 8\,\mu$m, the calibration is independent of the lattice spacing (proportionality coefficient γ_∞), which validates this procedure.

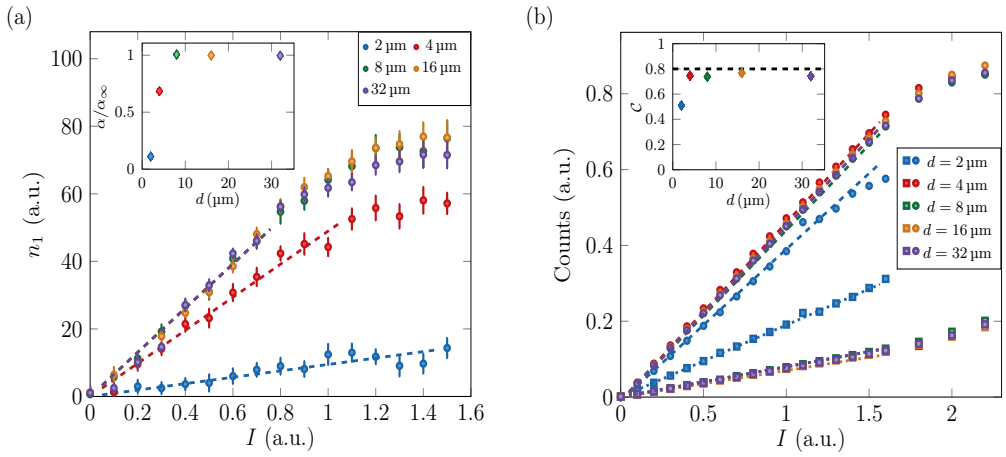

FIGURE 3.6: Calibration of the modulation depth and contrast reduction due to finite resolution imaging. (a): On the atomic signal. Amplitude of the first harmonic, obtained by fitting a sinusoid to the absorption images as a function of the light intensity sent to the DMD. For lattice spacings $d \geq 8\,\mu$m the curves overlap, while the atomic modulation is reduced by $\sim 30\%$ for $d = 4\,\mu$m and by $\sim 90\%$ for $d = 2\,\mu$m. Dashed lines are linear fits for low light intensities. Inset: proportionality coefficient obtained from the linear fits normalized by the long wavelength lattice value. (b): On the light signal. The peak-to-peak amplitude $2A$ (respectively minimum c) of the sinusoidal modulation of light seen on the control camera is represented by circles (resp. squares) as a function of light intensity. Dashed lines are linear fits at low light intensities. The contrast $\mathcal{C}$, defined as $\frac{2A}{2A+c}$, is plotted in the inset. There is no decrease in contrast for the $d = 4\,\mu$m lattice, while there is a $\sim 50\%$ drop for the $d = 2\,\mu$m lattice. The dashed horizontal black line represents the desired imprinted contrast from (3.23).

For a lattice of period $d = 4\,\mu$m, the modulation seen on the atoms is smaller for the same intensity sent to the DMD (Figure 3.6(a)), so how can we be convinced that the above calibration $V_0 = \gamma I$, determined for $d \geq 8\,\mu$m, still holds for the lattice $d = 4\,\mu$m? To do this, we use a side camera to control the intensity of the light sent to the atoms, thus working at 532 nm. We measure the maxima and the minima of the intensity profile for different lattice spacings and extract a contrast at low light intensities where the counts are proportional to the light intensity. This contrast is independent of the lattice spacing for $d \geq 4\,\mu$m, thus confirming that the decrease of

[10] The notation $n_{\mathrm{meas}}(q)$ is also used to distinguish between the expected and measured density modulations for the small lattice spacings.

the modulation depth seen on the atoms is due to a limitation in the detection of the density modulation and not to the imprinting of the modulation potential.

To further explain the decrease in atomic contrast at low lattice periods, we describe the observed density modulation signal as a convolution between the true atomic signal and a Gaussian of standard deviation $\sigma \simeq 0.5\,\mu\text{m}$[11], a value which is compatible with the specifications of our microscope objective at 780 nm. This reduction, combined with a further reduction in contrast due to a pixelization effect on the Pixis camera, explains the measured density modulation at 4 µm.

The modulation depth is still calibrated with $V_0 = \gamma_\infty I$ at 4 µm but when we will try to measure the density profile accurately, we will have to take into account the observed difference between the measured and expected density modulation and calibrate a correction factor (see section 3.4). We summarize the different sources of contrast reduction with the diagram in Figure 3.7 for the 4 µm lattice where the transfer function between the DMD and the atoms is unity (no contrast reduction seen with the Chameleon camera). For the 2 µm lattice this last point is not verified and the diagram is more complicated (see Appendix D).

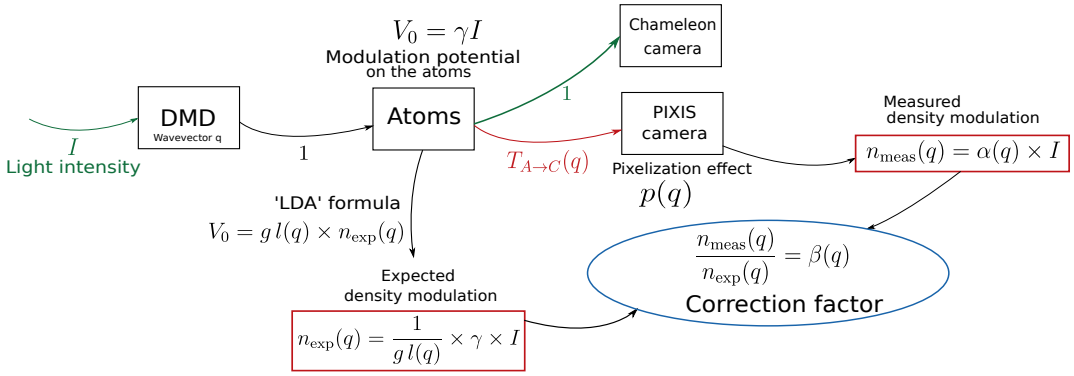

FIGURE 3.7: Contrast reduction for the 4 µm lattice. The DMD shapes the 532 nm light intensity with a sinusoidal intensity modulation of modulation depth $V_0 = \gamma I$. The expected density modulation in the LDA regime at low modulation depths is given by (3.25). However, the point spread function for the absorption imaging scheme, modeled with a transfer function $T_{A\to C}(q)$, and a pixelization effect on the Pixis camera for the 4 µm lattice leads to a reduction of the atomic contrast for this lattice spacing. The slope $\alpha(q)$ takes these two technical limitations into account. The correction factors $\beta(q)$ are used in section 3.4 to accurately calculate the density modulation for the small lattice spacings. For the larger lattice spacings, we have $\gamma = g\alpha_\infty$, which we use for the calibration $V_0(I)$. This is true for three reasons: $l(q) \simeq 1$ for the small q lattices, our imaging system does not filter out the slowly varying lattices (*i.e.* the transfer function $T_{A\to C}(q) = 1$), and the pixelization effect is negligible for the large lattice spacings.

Calibration of the magnetic field gradient

To introduce an excitation of the cloud, we use a quadrupolar magnetic field generated by the MOT coils, shown in Figure 3.5, on an atomic cloud polarized in the

[11] This Gaussian function, which describes the efficiency of our detection method, is called a point spread function (PSF) in this context, and its convolution with a sinusoidal function $n_0 + n_{\text{exp}} \cos(qx)$ leads to:

$$n(x) = n_0 + n_{\text{exp}} \exp\left(-\frac{q^2\sigma^2}{2}\right) \cos(qx) \tag{3.26}$$

So in this simple model, the contrast reduction is the term $\exp\left(-q^2\sigma^2/2\right)$.

magnetically sensitive state $|1,-1\rangle$ (the state in which we end up after the cooling steps, see Chapter 1). It is superimposed upon a magnetic field directed along z of $\simeq 3\,\mathrm{G}$, which sets the quantization axis. Near the center of the quadrupole trap, the norm of the total magnetic field is at first order quadratic with respect to the position coordinates, the curvature being determined by the current flowing in the MOT coils. We might naively think that this is enough to apply a magnetic excitation to the atomic cloud. This is incorrect for at least two reasons. First, the excitation of the cloud depends on the difference in magnetic field norms across it: $E_{\mathrm{mag}} = m_F g_F \mu_B \Delta ||\mathbf{B}_{\mathrm{tot}}||$. However, with a cloud centered on the nearly harmonic quadrupole trap, there is no magnetic field difference across the cloud and thus no excitation. Secondly, it should not be forgotten that the quadrupolar field also produces a magnetic gradient along the other two axes, though twice smaller, while the direction of the excitation should be controllable and alternatively directed only along y (the strong axis of the MOT coils) or x.

In addition to this quadrupolar field centered in (x_0,y_0,z_0), we thus add a small static magnetic field along x (respectively y) to shift the mimimum of the magnetic field curve along x (resp. y). We write the total magnetic field acting on the atoms as:

$$\mathbf{B}_{\mathrm{tot}} = \underbrace{B_0 \mathbf{e_z}}_{\text{quantization field}} \underbrace{+ b'_0 \left(-\frac{x-x_0}{2}\mathbf{e_x} + (y-y_0)\mathbf{e_y} - \frac{z-z_0}{2}\mathbf{e_z} \right)}_{\text{quadrupolar field, strong axis: } y} + \underbrace{B_{b,x}\mathbf{e_x} + B_{b,y}\mathbf{e_y}}_{\text{bias fields}} \tag{3.27}$$

Defining $B_{\mathrm{cent}} = \sqrt{B_0^2 + B_{b,x}^2 + B_{b,y}^2}$ the norm of the magnetic field at the positions (x_0,y_0,z_0), the norm $\mathbf{B}_{\mathrm{tot}}$ at order 2 in the coordinates positions can be written in the more general case as:

$$\begin{aligned} ||\mathbf{B}_{\mathrm{tot}}|| = B_{\mathrm{cent}} \Bigg[& 1 - \frac{b'_0 B_{b,x}}{2B_{\mathrm{cent}}^2}(x-x_0) + \frac{{b'_0}^2}{8B_{\mathrm{cent}}^2}\left(1 - \frac{B_{b,x}^2}{B_{\mathrm{cent}}^2}\right)(x-x_0)^2 + \mathcal{O}(x-x_0)^3 \\ & + \frac{b'_0 B_{b,y}}{B_{\mathrm{cent}}^2}(y-y_0) + \frac{{b'_0}^2}{2B_{\mathrm{cent}}^2}\left(1 - \frac{B_{b,y}^2}{B_{\mathrm{cent}}^2}\right)(y-y_0)^2 + \mathcal{O}(y-y_0)^3 \\ & - \frac{b'_0 B_0}{2B_{\mathrm{cent}}^2}(z-z_0) + \frac{{b'_0}^2}{8B_{\mathrm{cent}}^2}\left(1 - \frac{B_0^2}{B_{\mathrm{cent}}^2}\right)(z-z_0)^2 + \mathcal{O}(z-z_0)^3 \Bigg] \end{aligned} \tag{3.28}$$

Thus, across the atomic cloud, which has not moved due to the box confinement, there is a magnetic field difference along x (resp. y) as soon as $B_{b,x} \neq 0$ (resp. $B_{b,y} \neq 0$). Strictly speaking, the difference of magnetic field norms has terms of order 3, 5, etc. in the position coordinates (see Figure 3.8(a)). Across the atomic cloud of a few tens of µm, however, this curvature effect is negligible and the difference of magnetic field norms evolves linearly, resulting in a uniform magnetic field gradient $b' \simeq \frac{b'_0 B_{b,x}}{2B_{\mathrm{cent}}}$ (resp. $b' \simeq \frac{b'_0 B_{b,y}}{B_{\mathrm{cent}}}$) of the order of a few G/m and an associated energy difference across the cloud $E_{\mathrm{mag}} \simeq m_F g_F \mu_B b' L$ (see Figure 3.8).

The natural question that arises is how to calibrate this (small) magnetic gradient (0.03% of the gravity). To access it, we use Ramsey interferometry between the states $|1,-1\rangle$ and $|2,-2\rangle$, for which the product $g_F m_F$ is different. Indeed, the energy difference associated with the magnetic excitation between two points separated by x is linear in x at first order, as seen just above. Thus, the probability transfer to $|2,-2\rangle$

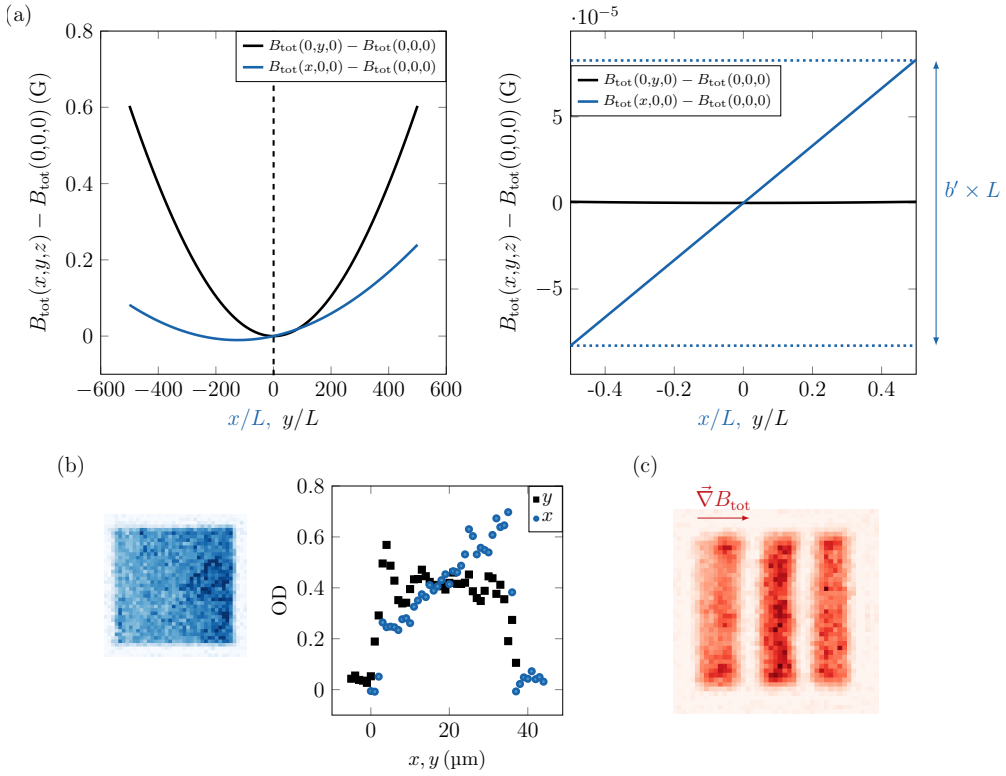

FIGURE 3.8: Magnetic gradient. Experimental implementation and measurement. (a): Spatial variation of the norm of the total magnetic field $B_{\rm tot} \equiv ||\mathbf{B}_{\rm tot}||$ given by (3.28) with $B_{b,x} = 0.25\,\mathrm{G}$ and $B_{b,y} = 0\,\mathrm{G}$. We use (x_0,y_0,z_0)=(0,0,0), $b'_0 = 100\,\mathrm{G/m}$, and $B_0 = 3\,\mathrm{G}$. The center of the quadrupole trap did not move along the y axis (black curve), while it did move along the x axis (blue curve). The left curve range is $1200\,L$, while the right curve is a zoom on the box range $L = 40\,\mu\mathrm{m}$. These bias fields result in an almost linear gradient b' along x ($b' \simeq 5\,\mathrm{G/m}$ here), while no gradient is observed along y. (b): Absorption image and central cuts of the cloud when applying a magnetic gradient of $20\,\mathrm{G/m}$ (in the experiment we apply $b' \sim 5\,\mathrm{G/m}$ and the effect on the density variation over the cloud is barely visible. We choose a higher gradient here for a clearer visualization). (c): Measurement of the magnetic gradient amplitude and direction with a Ramsey sequence, consisting of two $\pi/2$ MW pulses separated by $t_W \sim 5\,\mathrm{ms}$. This leads to interference fringes separated by a distance which is inversely proportional to the magnetic gradient amplitude (3.29). The direction (towards negative x or positive x) of the magnetic gradient is not accessible from this measurement, we infer it here from the density variation of (b). We choose a different colormap from the usual blue one to emphasize the difference between the Ramsey fringes and the atomic profiles in presence of the periodic lattice of Figure 3.10. We can do the same excitation protocol along the y axis by applying a bias field $B_{b,y} \neq 0$ and $B_{b,x} = 0$.

at position x, after two MW pulses, separated by an adjustable waiting time t_W, can be written as $\cos^2(\Delta E_{\rm mag} t_W/2\hbar) = \cos^2(\Delta(m_F g_F)\mu_B b' x t_W/2\hbar)$ where $\Delta(m_F g_F)$ is the difference of the product $g_F m_F$ of the two considered states. We then expect a spatial sinusoidal interference pattern which, for a waiting time of $t_W \sim 10\,\mathrm{ms}$ and $b' \sim 10\,\mathrm{G/m}$, has typically a fringe spacing of $\sim 7\,\mu\mathrm{m}$, accessible with our absorption imaging system. Measuring the direction and the fringe spacing i of the sinusoidal pattern gives access to the axis where there is a magnetic field difference across the

atomic cloud (perpendicular to the fringes) and the magnitude of the magnetic field gradient by the relation:

$$b' = \frac{h}{\Delta(m_F g_F)\mu_B t_W i} \tag{3.29}$$

The sensitivity of this result grows with the product $\Delta(m_F g_F)$, hence the choice to make this measurement for the states $|1,-1\rangle$ and $|2,-2\rangle$[12]. Figure 3.8 shows an example of an atomic profile in the presence of a magnetic field gradient. Its measurement by Ramsey interferometry is also depicted in this figure.

Experimental measurements of sound velocities

The following part describes the experimental protocol for measuring sound velocities in a density modulated gas. We prepare the atomic cloud in the state $|1,-1\rangle$ in the presence of the modulation potential of height V_0 with a fixed mean atomic density $n_0 \simeq 60$ atoms/µm^2 (we discussed in Chapter 1 how to control the density of the cloud) for all measurements. We then adiabatically turn on the coils in 100 ms (MOT coils and bias coils) to create the linear magnetic field difference along the desired direction. After letting the cloud reach equilibrium in the presence of this gradient (again during $\simeq 100$ ms), we abruptly turn it off (via both the bias and MOT coils), setting the time $t = 0$ of the experiment. We then record the triggered evolution of the center of mass position up to times $t \sim 200$ ms. This gives access to the speed at which phonons propagate in the system along the excited direction. For a given modulation depth, we measure the center of mass displacements over time along the two directions for an excitation along x. We repeat this procedure for an excitation along y, but keeping the modulation potential along x. We check that when the cloud is excited along x (respectively along y), the center of mass motion along y (resp. x) is small (< 0.5 µm) and random, while it follows a sinusoidal damped function along x (resp. y) (Figure 3.9).

As in the GP simulations, we interpret the finite damping to the finite magnetic gradient required for this measurement[13], even though we did not manage to extract quantitative evolutions. The damping appears to depend significantly on the homogeneity of the cloud and thus varies from day to day. Additionally, the observed damping is often stronger than the predictions from GP simulations. Still, we checked that the sound frequencies do not depend on the excitation strength, which confirms the validity of this protocol. Further experimental efforts would be required to study the damping in triggered oscillations, which could be an interesting subject to explore.

Figure 3.9 shows the experimental evolution of the oscillation frequencies ν_x and ν_y for an excitation of the system along x and y, respectively.

As predicted and as seen in the GP simulations, the sound velocity along the non modulated axis varies less when changing the modulation depth compared to the sound velocity along the modulated axis. This highlights the anisotropy of sound propagation in the system and the decrease of the superfluid fraction. The variations of these velocities are opposite with respect to the modulation depth: c_y increases due to the evolution of the compressibility, while c_x diminishes due to the variation

[12] We do not need a precise calibration of the magnetic gradient in this project. We simply want to check that we are working in the perturbative regime. However, for the project discussed in Chapter 6, a precise calibration is crucial for the comparison with the theoretical predictions.

[13] The choice of this magnetic gradient $b' \simeq 8$ G/m results from a trade-off between a sufficient signal-to-noise ratio for the center of mass evolution and the strength of the damping.

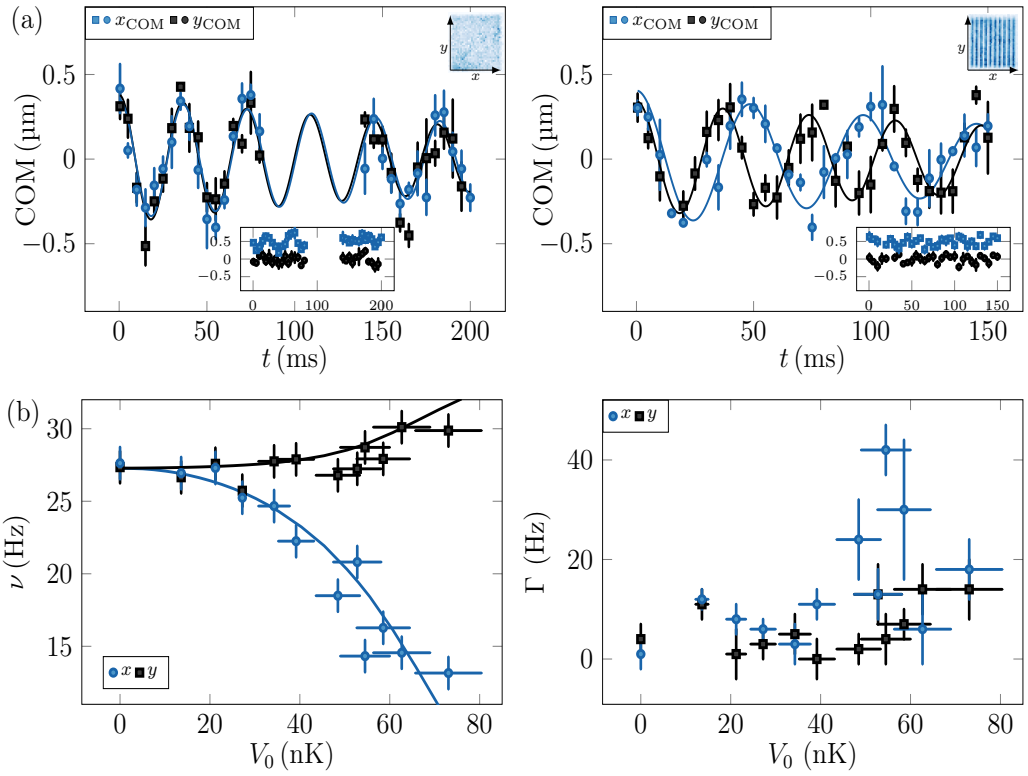

FIGURE 3.9: Sound velocity measurements using center of mass (COM) excitations. (a): COM motions in a uniform cloud (left panel) and modulated along x with $V_0 = k_B \times 40\,\mathrm{nK}$ (right panel). The square (respectively circle) points correspond to the COM motions when exciting the cloud along y (resp. x). The blue (resp. black) points correspond to the COM motion along x (resp. y). Solid lines are damped sinusoidal fits. The insets show the COM motions in the direction perpendicular to the excitation (along x we add an offset of 0.5 µm to make the data more visible). (b): Frequencies and dampings extracted from the sinusoidally damped fits along the x and y directions with the formula (3.22). The solid lines are the results of GP simulations corresponding to the same parameters: $b' = 8\,\mathrm{G/m}$, $d = 4\,\mu\mathrm{m}$, $n = 60\,\mathrm{atoms}/\mu\mathrm{m}^2$.

of the superfluid fraction. The agreement with the GP simulations is excellent over the range of explored modulation depths.

In a recent work, Tao et al. [144] also measured an anisotropic speed of sound in a 3D system by breaking the translational invariance along one axis. They used a retroreflected optical lattice at 532 nm, which yielded a modulation potential of period $d = 256\,\mathrm{nm}$, and confined their gas in a harmonic trap. The sound velocities in their system were extracted via Bragg scattering. More precisely, they added a weak sinusoidal lattice with a much larger period $\simeq 5\,\mu\mathrm{m}$ using a DMD, similar to our experiment. However, they made it move at a speed v in a specific direction. A resonance of transferred atoms was observed after a time of flight when the speed v corresponded to the speed of sound in the system. The study demonstrated an anisotropic variation in the speed of sound when the excitation was applied along the modulated or unmodulated axis. The results were compared with GP simulations. They then extracted the superfluid fraction using the same hydrodynamic formula (3.14) as us. Because they used a lattice of small period, the recoil energy associated to the wavevector q is much larger than the chemical potential, the energy associated to the interactions. Thus,

the interaction energy scale can be neglected compared to the other energy scales in their system. As a result, the evolution of the superfluid fraction approaches that of a non-interacting gas (see Figure 3.1). In addition to this measurement, the authors also extracted a key quantity related to superfluids, which was briefly discussed in Chapter 2: the moment of inertia in a scissors mode experiment.

In this experiment, the researchers checked that the superfluid fraction obtained from the sound velocities was consistent with Leggett's bound. However, due to the small lattice spacing used, they were unable to extract an *in situ* density profile and therefore could not calculate Leggett's integral to obtain another measurement of the superfluid fraction in their system. Our experiment will address this challenge using a 4 µm lattice.

3.4 Static determination of the superfluid fraction

In this section, we present a static determination of the superfluid fraction in a density modulated cloud. We take advantage of the saturation of Leggett's inequality in our separable system, which is well described by Gross-Pitaevskii physics. This measurement of the superfluid fraction is unusual as it is directly obtained from the density profiles, rather than through transport properties. We present the experimental results alongside GP simulations, as in the previous section.

How can we experimentally extract the density profile in our system? In an ideal scenario, we could obtain an absorption image of the cloud and measure its various harmonics (3.15). However, two main limitations prevent us from accessing all the harmonics: our imaging system has a finite resolution, and the camera used for absorption imaging has a finite effective pixel size. We describe these effects as a *filtering* of the harmonics. We introduce *correction factors* β_i for the i-th harmonic and write the measured density profile as:

$$n_{\text{meas}}(x, y) = n_0 - \sum_{i \geq 1} \beta_i n_i \cos(iqx) \tag{3.30}$$

As this is an ambitious project to measure the various harmonics, we will proceed step by step by introducing the measurement of one harmonic at a time.

3.4.1 "Naive" measurements

First, let us consider only the first harmonic n_1. This means that when a sinusoidal modulation potential is applied, the gas is assumed to respond with a sinusoidal modulation of the density. This corresponds to the LDA regime, which is a good approximation of our system at low V_0.

However, the LDA equation (3.16): $\frac{n_1}{n_0} = \frac{V_0}{\mu_0}$ does not give the correct slope at the origin of the evolution of $\frac{n_1}{n_0}(V_0)$. This is due to the non-negligible value of $\epsilon_q/\mu_0 \simeq 0.14$ in our system. The exact behavior at low V_0 is given by the previously discussed expansion (3.18): $\frac{n_1}{n_0} = \frac{2V_0}{2\mu_0+\epsilon_q}$. We verify this statement in Figure 3.10(b).

Nevertheless, mainly due to the filtering of the harmonics by our imaging system of optical resolution $\simeq 1$ µm, already seen in Figure 3.6, the measured density modulation n_1, with a sinusoidal fit to the atomic profiles, cannot be trusted for lattices of spacing $d < 8$ µm. Indeed, we saw a significant reduction in the density modulation for these short-spacing lattices. To account for this reduction in contrast, we correct the measured n_1 by the factor $\beta_1 \equiv \beta(q = \frac{2\pi}{4}\text{µm}^{-1})$ to obtain the data in Figure 3.10.

The calibration of β_1 requires some care and a detailed explanation is given in Appendix D. It takes into account not only the reduction in contrast due to the limited

resolution of our imaging system, but also pixelization effects on the Pixis camera. Indeed, the effective pixelsize on the atoms is 1.15 µm, and is thus not negligible in front of the 4 µm lattice. It leads to a reduction of the measured modulation density of $\simeq 13\%$ (see Appendix D).

These effects contribute to a filtering of the first harmonic and the evaluation of their contributions allows to extract the coefficient β_1: $\beta_1 = 0.73(2)$.

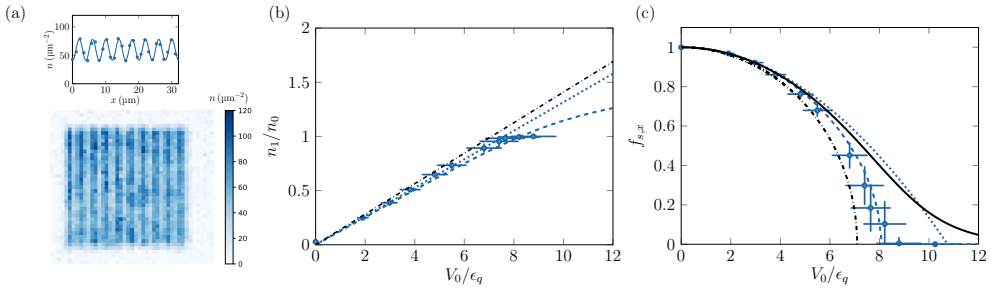

FIGURE 3.10: Limitation to the first harmonic. (a): Experimental *in situ* absorption image for $V_0 = k_B \times 20\,\mathrm{nK}$ ($V_0/\epsilon_q \simeq 3$) together with a mean density profile along the modulated axis (blue circles). A sinusoidal fit of amplitude n_1 and mean value n_0 is represented by a blue solid line. (b): n_1/n_0 as a function of the modulation depth. n_1 is corrected by β_1. The dashed blue line is the GP simulation prediction fitting the profiles with a sinusoid. The dotted blue line is the small V_0 expansion (3.18) and the black dash-dotted line is the LDA prediction (3.16). (c): Superfluid fraction extracted from Leggett's formula. Restricting to the first harmonic, we have $f_{s,x} = \sqrt{1 - \left(\frac{n_1}{n_0}\right)^2}$. The plotting conventions are the same as in (b). For the values of $V_0/\epsilon_q \gtrsim 8$, the value of n_1/n_0 is greater than 1, and since Leggett's integral is ill-defined, we manually set the superfluid fraction points to 0. The solid black line is the GP prediction including all harmonics in the density profile.

Once n_1/n_0 has been carefully evaluated, we can extract the superfluid fraction using the saturation of Leggett's formula. In this subsection, where the density is assumed to be sinusoidal, the connection between the superfluid fraction and the density modulation is simple and given by (3.17): $f_{s,x} = \sqrt{1 - \left(\frac{n_1}{n_0}\right)^2}$. We obtain the result shown in Figure 3.10(c). The comparison with the numerical results obtained by limiting the knowledge of the density profile to its first harmonic is satisfactory. The solid black line represents the numerical result obtained from the knowledge of the full density profile. Not surprisingly, we see that the data deviate from the numerical results as soon as $V_0/\epsilon_q \gtrsim 6$. Can we do a little bit better?

3.4.2 Going further

We now take into account the presence of a second harmonic in the Fourier expansion of the density (3.30), creating a modulation at 2 µm.

As with the first harmonic, the second Fourier mode is affected by the various limitations of the measurement procedure. We extract $\beta_2 \equiv \beta(q = \frac{2\pi}{2}\,\mu\mathrm{m}^{-1})$ from a careful evaluation of these limitations at $d = 2\,\mu\mathrm{m}$[14]. We obtain a factor $\beta_2 = 0.27(6)$ (see Appendix D). The amplitudes of the measured harmonics extracted from the two

[14]For the 2 µm lattice, we must also take into account the filtering seen on the control camera (see Figure 3.6 and Appendix D).

harmonic fits[15] are then corrected by the β_i coefficients to obtain Figure 3.11(b). Since the second harmonic tends to increase the density around minima compared to the first harmonic (see Figure 3.11(a)), the sign of n_2 is opposite to the sign of n_1. Even though the second harmonic is a small corrective effect around the density minima ($n_2 \ll n_1$), it is sufficient to modify significantly the derived value of the superfluid fraction at large V_0. Indeed, it affects the density minima and since Leggett's integral has a $\left\langle \frac{1}{n_0} \right\rangle$ term, the second harmonic can play a non-negligible role. As with the first harmonic in the previous subsection, the results are compatible with the GP prediction restricting the density knowledge to the first two harmonics, and the points follow the full GP numerical simulation up to $V_0/\epsilon_q \simeq 8$, a higher number compared to when we fit the profiles with only the first harmonic.

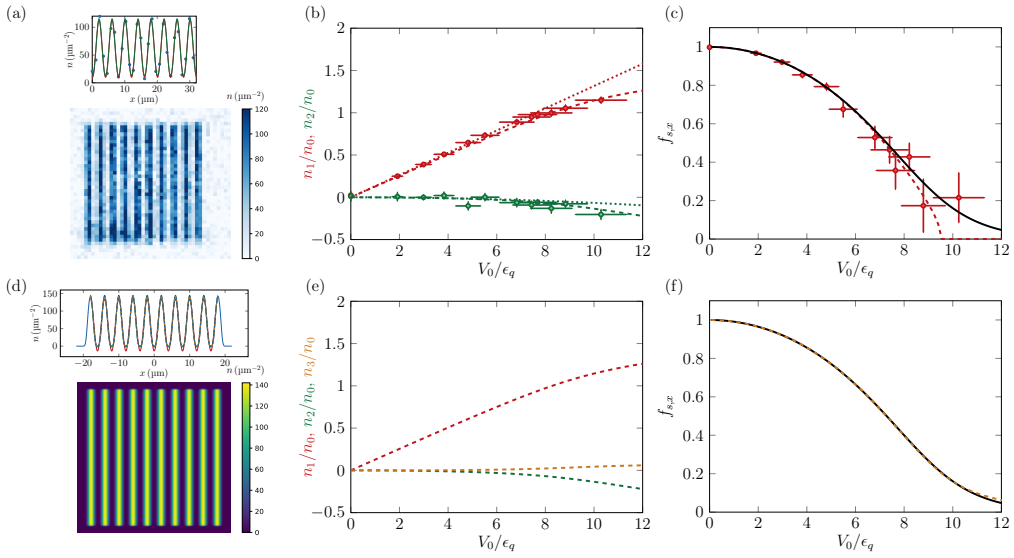

FIGURE 3.11: Superfluid fraction from the density profiles. For the figures in the top row, we include the first two harmonics. (a): Absorption image for $V_0 = k_B \times 72\,\mathrm{nK}$ ($V_0/\epsilon_q \simeq 10$) together with a mean profile along the modulated axis. The red line represents a sinusoidal fit (only one harmonic), while the green line is a fit that includes the first two harmonics. From these fits, we extract the amplitudes of the first two harmonics, n_1 and n_2, which we then correct by the β_1 and β_2 factors (b). Once this is done, we can reconstruct the truncated density profile and calculate the superfluid fraction using Leggett's formula (red points in (c)). The dashed lines are the predictions from GP simulations truncating the density to the first two harmonics, while the dotted lines are the low V_0 analytical expansions. The black solid line is the full GP prediction. The second row of figures includes the first three harmonics. These are numerical results only. The fit for the first three (respectively two, first) harmonics is plotted in orange (resp. green, red) in (d) in the case of $V_0 = k_B \times 80\,\mathrm{nK}$ ($V_0/\epsilon_q \simeq 11$). The dashed lines in (e) are the GP predictions of the amplitude of the first three harmonics. When the density signal is reconstructed, this leads to the superfluid fraction shown with the dashed orange line in (f) using Leggett's formula. The discrepancy with the full GP result in black is now barely visible for the explored range of modulation depths.

[15] The fit of the two harmonics also requires some care. Indeed, naively attempting to fit the signal by the sum of the two harmonics will give no signal for the second harmonic. Instead, we first fit only the first harmonic with the amplitude and the phase ϕ as free parameters. We then fit the residue of the previous fit with a $\sin(2qx + 2\phi)$ function where the only free parameter is the amplitude. An example of fit is plotted in Figure 3.11(a).

Can we do better than that? Numerically, of course, we can always go further by including the third harmonic. This is the subject of the second row in Figure 3.11. We see in Figure 3.11(f) that the superfluid fraction when including the first three harmonics (orange dashed curve) is an extremely good approximation of the full result, plotted in black, up to $V_0/\epsilon_q \simeq 10$[16]. Experimentally, however, the third harmonic, which leads to a density modulation at 1.33 µm, is completely filtered out by our imaging system ($\beta_3 \simeq 0$ and $\beta_{i\geq 3} \simeq 0$). Therefore, we will limit our experimental analysis to the second harmonic, knowing that we can obtain a reliable estimate of the superfluid fraction from the density profile measurements within the explored range of modulation depths of $V_0/\epsilon_q \lesssim 10$.

3.5 Comparison of the two methods

In this section, we compare the two different methods for extracting the superfluid fraction, both numerically and experimentally.

The first method exploiting the anisotropy of sound propagation when a modulation is added, leads to the purple squares in Figure 3.12. These points are obtained from the ratio squared of the sound velocities plotted in Figure 3.9. The corresponding numerical results are represented by a blue dashed line (they were already shown in the inset of Figure 3.4).

The second method uses the saturation of Leggett's formula and the knowledge of the *in situ* density profile. The resulting red circles should be compared to the GP estimation shown as a black solid line.

Overall, the results are in good agreement in the range of V_0/ϵ_q studied. The choice of the lattice at $d = 4$ µm allows to measure the *in situ* profiles with good accuracy, while the physics involved deviates significantly from the LDA regime at sufficiently high modulation depths.

It can be seen that the vertical errorbars are similar between the two methods. The sound velocity errorbars are obtained with a bootstrap analysis on the center of mass fits. We are limited by the damping of the oscillations to achieve higher modulation depths. For the stationary density profile measurements, the vertical errorbars take into account the error in the calibration of the correction factors β_1 and β_2 and in the fits of the density profiles. They increase with V_0/ϵ_q.

In this work, which has been the subject of an article [67], we have shown two different ways to measure the superfluid fraction in our density modulated gas. Apart from the natural extension of this work to the study of the quenching of the superfluid fraction in supersolids, Fermi gases or 2D modulated potentials, there is a connection with astrophysics and neutron stars. Indeed, in neutron stars the periodic lattice of the nuclei influences the superfluidity in the inner crust [148]. Despite the inevitable quenching of the superfluid fraction, its value is kept high even for large density modulations [149]. This is due to the strong interactions present in the inner crust of these neutron stars. Similarly, when comparing the superfluid fraction value in our system to that, for example, of Tao et al. [144], we can argue that our large period lattice allows us to stay far away from the non-interacting regime and to maintain a non-zero superfluid fraction over a wide range of modulation depths (see Figure 3.1).

[16] The relative error in the superfluid fraction estimation by taking only the first three harmonics is $\simeq 10\%$ for $V_0/\epsilon_q = 11$.

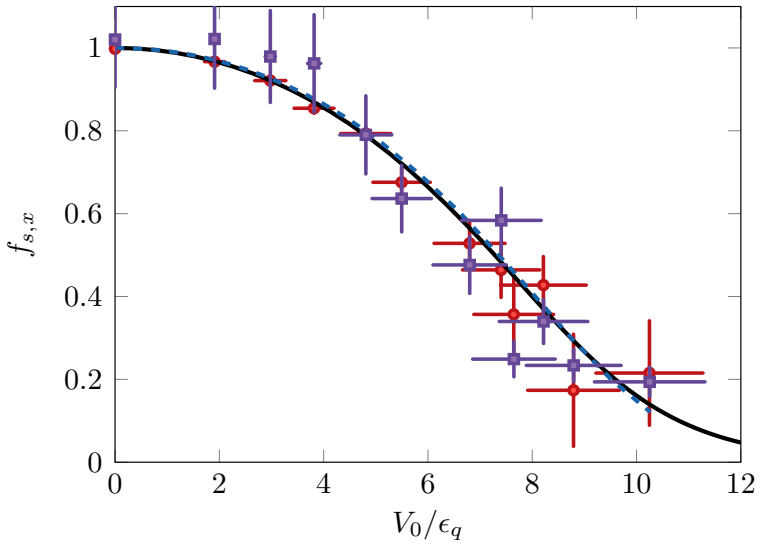

FIGURE 3.12: Comparison of the two methods for extracting the superfluid fraction. The purple squares are obtained with sound velocity measurements, while the red circles are extracted from the *in situ* density profiles and the Leggett's formula. The dashed blue line and the solid black line are the numerical predictions from the sound measurements and from the application of the Leggett's formula on the full density profile, respectively. We stop the dashed blue line at $V_0/\epsilon_q \simeq 10$ because further the damping is too large to accurately measure the oscillation frequency for $b' = 8\,\mathrm{G/m}$.

3.6 Extension of this work to 2D modulated potentials

As previously mentioned, this work focused on studying the superfluid fraction in a weakly-interacting Bose gas with a separable wavefunction. In this particular case, the two Leggett's bounds (3.12) are valid and coincide. We now extend the question of superfluidity in modulated systems to more complicated 2D cases than the one considered in this chapter.

3.6.1 A sufficient condition to saturate Leggett's inequalities?

We start by exploring the possibility of identifying sufficient conditions for the two bounds to be equal. We pick up the possible requirements among the two used in our previous study *i.e.* the mean-field treatment and the separability of the wavefunction.

First, is the separability of the many-body wavefunction sufficient to saturate Leggett's inequalities? While Leggett gave a positive answer in his 1998 paper [66], it seems that he had in mind the applicability of Gross-Pitaevskii theory. Indeed, the example of a quasi-1D Bose gas, a separable system, placed in an optical lattice of on-site interaction U and nearest-neighbor tunneling constant J, brought to the Mott-insulator regime of $U \sim J$, provides a counterexample. In the superfluid regime, the bounds are saturated, but as U/J increases, the superfluid fraction decreases until it reaches zero in the Mott-insulator phase. However, the written lower bound predicts an increase in the superfluid fraction as the density contrast decreases and the repulsive interactions increase. Therefore, in this beyond mean-field system, Leggett's lower bound is not valid and thus cannot be equal to Leggett's upper bound.

Then, what about the condition of applicability of Gross-Pitaevskii theory? In a recent numerical study [150], the superfluid fraction tensor was investigated in a 2D dipolar supersolid gas described by an extended Gross-Pitaevskii theory. In most lattice angle configurations, the superfluidity is anisotropic, with the exception of the square and triangular lattices, which exhibit isotropic superfluidity. For a triangular lattice, the potential is non-separable. The (unique) superfluid fraction in the system does not strictly coincide either with Leggett's upper bound or lower bound. Therefore, the applicability of Gross-Pitaevskii theory is not a sufficient condition to saturate Leggett's inequalities. Still, the bounds provide a useful estimate of the superfluid fraction in the modulated system.

3.6.2 Calculation of the compressibility and the superfluid fraction in 2D weakly-interacting modulated Bose gases

From the previous subsection, we argue that even when restricting ourselves to mean-field systems in the general 2D modulation case, Leggett's bounds are not saturated. Therefore, we cannot generally use them to calculate the superfluid fraction in the system. What are the other ways to calculate a superfluid fraction?

Blakie's numerical study [150] extracted the superfluid fraction using twisted boundary conditions and effective mass calculations in a unit cell. He also discussed in another paper [151] the evolution of the different sound branches over the transition from a superfluid to a supersolid in the case of a 2D spatial confinement. At the same time, Sindik and collaborators [152] studied the case of an annular spatial confinement and proposed an experimental protocol to excite the different sound modes. As mentioned earlier in this chapter, the existence of multiple sound branches at low momenta in a dipolar supersolid complicates the protocol to extract a superfluid fraction compared to what we used in our experiment (3.14). Sindik et al. showed that they could calculate the different sound velocities together with the compressibility of the system after applying a periodic modulation proportional to $\cos(\phi)$, where ϕ is the azimuthal angle in the ring. Importantly, they related the sound velocities and the compressibility to the superfluid fraction, whose calculated value coincides with Leggett's upper bound as expected (extended GP model and separable potential).

Following the study of Blakie [150], we adapt our Gross-Pitaevskii numerical simulations to the cases of a square or a triangular 2D lattice modulation. From the ground states of the system, we compute upper and lower bounds for the superfluid fraction with the equations (3.12). Furthermore, we calculate the sound frequencies along the two directions x and y using the same protocol as in Figure 3.4. We compute the initial state in the presence of a magnetic gradient either along x or y and turn it off at time $t = 0$ of the evolution. It triggers the phonon modes in the system and the resulting sound frequencies along x or y can be inferred. Once this is done, how can we access the superfluid fraction in the system?

As in Blakie's study, and given that there is no preferential axis in the square or triangular lattices, we obtain identical sound velocities along the two directions of the box (insets of Figure 3.15).

Therefore, in contrast to the case of a 1D modulation, where we were able to get rid of the compressibility dependance, here we have no choice but to calculate the compressibility in the system. Inspired by the works discussed previously [152, 151], and [153], we measure it numerically from the initial state of the excitation protocol, *i.e.* in the presence of the linear potential created by the magnetic gradient. More specifically, we calculate the position of the center of mass of the initial state, shifted

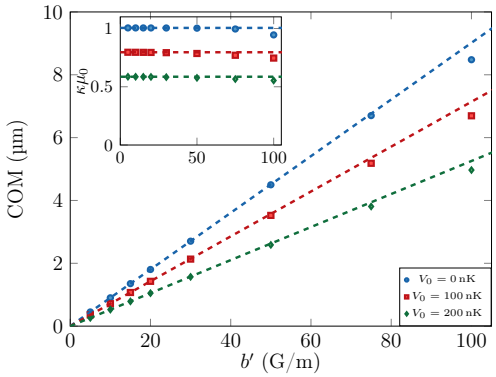

FIGURE 3.13: Compressibility calculation and range of application for the linear relation between the gradient and the center of mass (3.31). We compute numerically the center of mass of the gas under a linear potential (gradient b') and a 2D square potential $V(x, y) = \frac{V_0}{2}[\cos(qx) + \cos(qy)]$ with $q = (2\pi/4)\,\mu\text{m}^{-1}$. The dashed lines are linear fits for $b' < 30\,\text{G/m}$. The inset shows the evolution of the compressibility extracted from the COM values. The dashed lines are the compressibility values obtained from the linear fits.

with respect to the central position due to the magnetic gradient, and we assume that the compressibility can be deduced with the following formula:

$$\kappa = \frac{12}{g_F m_F \mu_B b' L^2} \times x_{\text{COM}}(t = 0) \tag{3.31}$$

In the LDA regime, $\kappa = \frac{1}{\mu_0} = \frac{1}{gn}$ and the expression (3.31) is equivalent to that already given in (3.21). When leaving the LDA regime, the compressibility diminishes slightly causing the slope of the evolution x_{COM} versus b' to decrease (see Figures 3.2 and 3.13)[17]. One can then derive the evolution of the superfluid fraction as a function of the modulation depth by assuming the validity of the hydrodynamic formula:

$$c_{x,y}^2 = \frac{f_{s,(x,y)}}{m\kappa} \tag{3.32}$$

In the simulations we first verify the range of application of the linear relation (3.31) for different modulation depths. Typically, the linearity is checked for linear excitations of gradient $b' < 50\,\text{G/m}$, *i.e.* as long as the magnetic excitation energy is smaller than the chemical potential: $E_{\text{mag}} \lesssim \mu$ (Figure 3.13). We then choose $b' = 5\,\text{G/m}$ in the simulations, both for the calculation of the stationary profile and the extraction of κ with (3.31), and for the measurement of the sound velocities with the time-dependent simulation.

The validity of this protocol and the formula (3.31) are benchmarked in the 1D modulated lattice used throughout this chapter, for which we have shown that the hydrodynamic formula (3.32) is correct (see [67] and [83]) (Figure 3.14).

2D square or triangular lattices were then used as in Blakie's study. The two effects of decrease of the sound velocities and decrease of the compressibility go in the same direction and result in an overall decrease of the superfluid fraction as the modulation is increased (see (3.32)).

[17] This was also the case in the 1D modulation case: the sound velocity along the non modulated direction increased due to the slight decrease in compressibility.

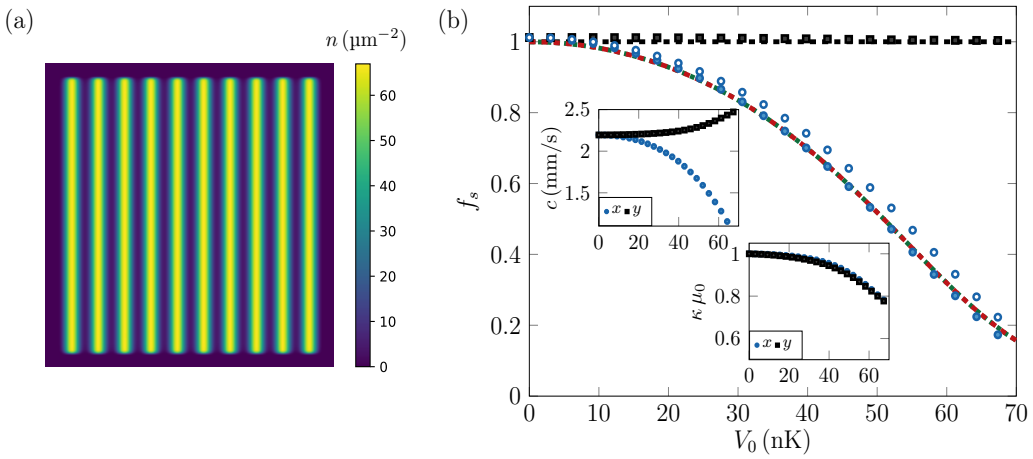

FIGURE 3.14: Superfluid fraction from the compressibility calculation in the 1D sinusoidal lattice case. (a): Example of profile for $V_0 = k_B \times 50\,\mathrm{nK}$. We define it as $V(x, y) = V_0 \cos(qx)$ with $q = (2\pi/4)\,\mu\mathrm{m}^{-1}$. (b): 1D sinusoidal lattice case for $b' = 5\,\mathrm{G/m}$. The dashed red line (respectively dotted green line) is the upper (resp. lower) bound given by Leggett, which coincide in this separable system. The filled blue circles (respectively black squares) are the superfluid fractions extracted from the sound velocity and the compressibility calculation along the modulated axis (resp. non modulated axis) (3.32). In contrast to what was plotted in Figure 3.12, we emphasize that here the blue circles are not obtained by taking the squared ratio of the sound velocities. The empty circles represent the case where the variation of the compressibility is neglected and $\kappa = 1/\mu_0$ is taken. The black dashed line corresponds to $f_s = 1$. The insets show the variation of κ and the sound velocities along both axes.

In the case of a square lattice, plotted in Figure 3.15(a), we found almost equal upper and lower bounds for the superfluid fraction, as expected in this nearly separable system[18], and the superfluid fraction calculated with sound and compressibility measurements is compatible with both bounds. Regarding the triangular lattice, the bounds significantly deviate from each other, as also seen in Blakie's study, and the superfluid fraction extracted from the sound and compressibility measurements lies in between the two bounds. It seems that the superfluid fraction is closer to the lower bound than to the upper bound, as also calculated by Blakie in the dipolar supersolid case.

The superfluid fraction can also be extracted numerically for other 2D lattice arrangements, such as hexagonal, Kagomé, or checkerboard lattices.

The calculation of the superfluid fraction in this case relies on the hydrodynamic formula (3.32) and on the compressibility formula (3.31). However, we are not aware of any rigorous theoretical justification for these formula in 2D lattices. Another measurement of the superfluid fraction, via the application of twisted boundary conditions in an elementary cell of the lattice (method used by Blakie et al. [150] for instance), could be performed to confirm these calculations.

Finally, the question of superfludity in modulated disordered systems is also of interest. This topic was recently explored in Daniel Pérez Cruz's master's thesis [154], where he studied the quench of the superfluid fraction in a 2D speckle potential. It is also possible to consider an Aubry-André potential, which could simulate disorder.

[18] Even though the potential is separable, the density is not exactly separable, since the GP equation is nonlinear.

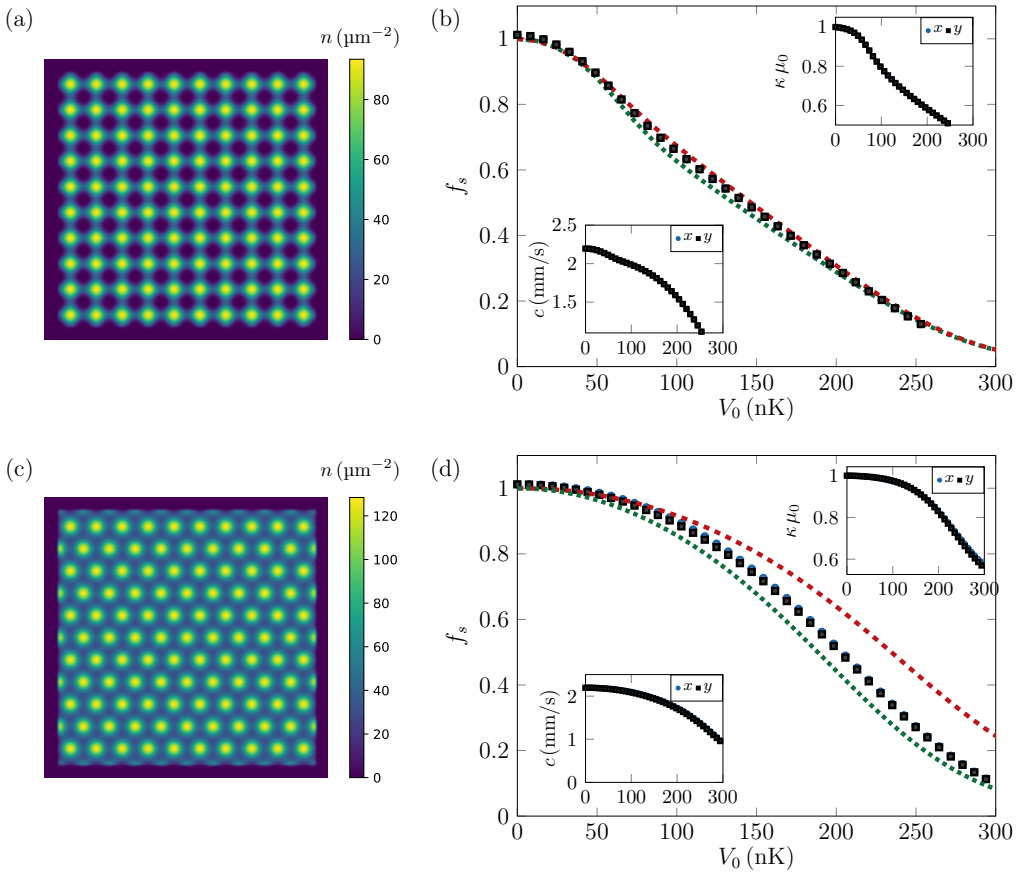

FIGURE 3.15: Numerical simulations of the superfluid fraction measurement in a weakly-interacting Bose gas in a 2D square and triangular lattice via compressibility calculations. (a): Ground state with a square lattice of $V_0 = k_B \times 100\,\mathrm{nK}$. The modulation depth is defined as the maximum value of the square potential $V(x, y) = \frac{V_0}{2}[\cos(qx) + \cos(qy)]$ with $q = (2\pi/4)\,\mu\mathrm{m}^{-1}$. (b): Evolution of the superfluid fraction in a 2D square lattice. The dashed red line (respectively dotted green line) is the upper (resp. lower) bound given by Leggett's formula (3.12). The black square points are obtained from the combination of the calculation of the compressibility of the system and the sound velocity measurements (shown in the inset) along the y axis. Since there is no preferential axis in the system, they are superimposed with the blue circle points obtained from the calculation of the compressibility and the sound velocity along the x axis. (c): Ground state in a triangular lattice of $V_0 = k_B \times 100\,\mathrm{nK}$. The modulation depth is defined as the maximum value of the triangular potential $V(x, y) = \frac{V_0}{9}\left[1 + 4\cos^2\left(\frac{\sqrt{3}q}{2}x\right) + 4\cos\left(\frac{\sqrt{3}q}{2}x\right)\cos\left(\frac{3q}{2}y\right)\right]$ with $q = (2\pi/6)\,\mu\mathrm{m}^{-1}$. (d): Superfluid fraction in the triangular lattice. The two bounds do not coincide and the superfluid fraction extracted with sound measurements and compressibility lies between the two curves. The conventions are the same as for the square lattice.

In our experimental setup, we plan to measure the superfluid fraction in a previous case of non-equality of Leggett's bounds. We will measure the compressibility via center of mass deviations for large gradients (but still remaining in the linear regime of Figure 3.13) and sound velocities for reasonable gradients to determine the superfluid fraction.

3.7 Conclusion

In this chapter, we examined the modification of the notion of superfluidity in a 2D density-modulated system at $T = 0$. First, we demonstrated analytically that Leggett's upper bound is saturated in a system described within mean-field theory and separable along the two directions of space. This equality, rather than an inequality in the general case, has significant implications. The knowledge of the *stationary* density profile provides all the information on the superfluid fraction, an intrinsic *transport* quantity. The properties of the stationary state can be used to predict the dynamics of the superfluid system. Analytical expressions for low modulation depths were also developed.

To explore the validity range of Leggett's equality in our system, we then performed two distinct numerical and experimental protocols. The first relied on anisotropic measurements of sound modes propagating in the system after a weak excitation. Previous studies have extracted sound velocities, particularly their temperature dependence, using Landau's two-fluid model [25, 118, 24]. Our study revealed an anisotropic variation of sound velocities at zero temperature, solely due to the presence of a one-dimensional modulated potential.

Additionally, we described the first stationary determination of the superfluid fraction using the saturation of Leggett's inequality in the case of a weakly-interacting Bose gas. The atomic density modulation was accurately measured. It was demonstrated that the limitations of imaging fast-varying spatial modulations can be assessed and overcome.

The agreement between both methods is satisfactory for the explored range of modulation depths, both numerically and experimentally.

In the general 2D case, if either the validity of the GP treatment or the separability of the wavefunction, the two key ingredients for the use of Leggett's equality, do not hold, then Leggett's bounds are not saturated. As a result, the superfluid fraction cannot be measured using the stationary profile. Instead, one must rely on other methods, such as compressibility calculation or twisted boundary conditions consideration. In the last section, we presented a numerical analysis of the superfluid fraction in 2D modulated lattices. Our findings suggest potential for future experimental investigations in regimes where the two bounds can be distinguished.

This work is related to other spatially modulated systems, such as dipolar supersolids, where the density modulation occurs spontaneously. Recently, the group of Giovanni Modugno in Florence conducted a remarkable study that quantitatively measured the superfluid fraction in a quasi-1D dipolar Bose gas [155]. They obtained this measurement via Josephson oscillations instead of sound oscillations. In addition to the spontaneous spatial modulation that arises in the supersolid phase, a weak optical lattice was introduced, which triggered a sinusoidal oscillation of the phase difference between two adjacent clusters of the supersolid lattice. This work illustrates that the supersolid can be viewed as consisting of multiple lattice cells that act as self-induced Josephson junctions. The measured superfluid fraction agrees well with numerical results and falls between the two calculated Leggett's bounds. These bounds do not coincide in this non-perfectly separable system (density not separable in the transverse directions).

Part III

Magnetic solitons and Bloch-like oscillations in a weakly immiscible mixture

Chapter 4

Introduction to the physics of 1D magnetic solitons

This chapter and the two following ones discuss some properties of the magnetic soliton. This soliton corresponds to the appearance of spatially localized magnetic excitations in a 1D ferromagnetic spin chain, hence the name *magnetic*. The nonlinear equation governing its dynamics is the Landau-Lifschitz equation (LLE). Remarkably, in a specific limit, this soliton can be mapped to a vector soliton of the NonLinear Schrödinger Equation (NLSE). As discussed in the previous chapters, the NLSE equation is commonly used to describe the mean-field physics of weakly-interacting Bose gases, which are a priori fundamentally different systems compared to ferromagnetic spin chains. We thus begin this chapter by introducing various types of solitons of the NLSE encountered in different fields of physics. Then, the magnetic soliton is introduced and its form is computed analytically. Finally, the connection between the ferromagnetic spin chain and the immiscible mixture of BECs in a certain limit is discussed. Conserved quantities associated with the magnetic soliton, which will play a crucial role when a linear potential is added (Chapter 5), are then derived.

4.1 1D solitons of the Gross-Pitaevskii equation

Solitons are localized wavepackets that maintain their shape while propagating. Their shape is also preserved in collisions with other solitons. They are present in physical systems that exhibit nonlinear phenomena. Therefore, they are found in various fields, including fiber optics (see [156] for a recent review), hydrodynamics, condensed matter and high-energy physics [30]. Solitons are also popular in mathematics as they are solutions of partial differential nonlinear equations, such as the Korteweg-de Vries equation, the sine-Gordon equation or the nonlinear Schrödinger equation (NLSE). The solitons are said to be *integrable* objects. In other words, their dynamics are confined to a small portion of the entire phase space due to the presence of certain conserved quantities. As a result of these constraints, these non-ergodic systems never reach thermal equilibrium. The integrability property provides them with a unique stability against perturbations of the initial state, unlike chaotic systems. Their study led to a fruitful approach to solve the dynamics of such integrable systems, namely the inverse scattering method, discovered in 1967 [157], which generalises local linear methods, such as Fourier transforms, to nonlocal linearisation[1].

[1] A quantized (or discretized) version of the inverse scattering method is used to solve many-body problems, such as spin chains. For instance, the Bethe ansatz is used to express the eigenstates of the Lieb-Liniger model [158].

4.1.1 The 1D regime

This chapter focuses on 1D physics and employs a mean-field approach, similar to Chapter 2 when deriving the 2D Gross-Pitaevskii equation. The 3D wavefunction is written as a separable wavefunction: $\phi(\mathbf{r}) = \psi(x)\varphi(y)\chi(z)$. Assuming harmonic confinements along the transverse directions y and z, we consider the states of the atoms along these directions to be the ground states of the corresponding harmonic oscillators with angular frequencies $\omega_{y,z}$, *i.e.* $\varphi(y) = \left(\pi l_y^2\right)^{-1/4} \mathrm{e}^{-y^2/2l_y^2}$ and $\chi(z) = \left(\pi l_z^2\right)^{-1/4} \mathrm{e}^{-z^2/2l_z^2}$, with $l_{y,z} = \sqrt{\frac{\hbar}{m\omega_{y,z}}}$.

As we did in the 2D case in Chapter 2, we insert this separable wavefunction into the GP energy functional (2.9) where $g = \frac{4\pi\hbar^2}{m}a$ is the 3D interaction parameter:

$$E[\phi] = \int \mathrm{d}^3 r \left[\frac{\hbar^2}{2m}\left|\nabla\phi\right|^2 + V(\mathbf{r})\left|\phi(\mathbf{r})\right|^2 + \frac{g}{2}\left|\phi(\mathbf{r})\right|^4\right] \tag{4.1}$$

It yields the following 1D Gross-Pitaevskii equation for a homogeneous gas:

$$-\frac{\hbar^2}{2m}\frac{\partial^2\psi}{\partial x^2} + g_{1\mathrm{D}}\left|\psi\right|^2\psi = \mathrm{i}\hbar\frac{\partial\psi}{\partial t} \tag{4.2}$$

The wavefunction ψ is normalized to the atom number. The parameter $g_{1\mathrm{D}}$ is the 1D interaction parameter and is related to the harmonic confinement parameters by $g_{1\mathrm{D}} = 2\hbar\omega_\perp a$, where $\omega_\perp = \sqrt{\omega_y\omega_z}$ is the geometric mean of the transverse confinements.

We recall that this is a valid approach as long as we work in the mean-field regime for a sample of density $n = |\psi|^2$ and provided that the transverse confinement energy scale is larger than the other relevant energy scales: $\hbar\omega_\perp \gg k_B T, \mu$. The Lieb-Liniger parameter $\gamma = \frac{g_{1\mathrm{D}}m}{n\hbar^2}$ quantifies the validity of this approach. It can also be written: $\gamma = \frac{1}{(n\xi)^2}$, where $\xi = \frac{\hbar}{\sqrt{n g_{1\mathrm{D}} m}}$ is the 1D healing length. The mean-field approach gives a good approximation to the dynamics of the system if there are a sufficient number of atoms per length scale ξ *i.e.* if $\gamma \ll 1$ [159]. We note that unlike in 2D and 3D gases, the 1D Bose gas becomes more interacting as the density decreases [99]. A brief discussion of the non-weakly interacting 1D Bose gas will be deferred to the section 5.2.1.

4.1.2 Soliton background

The 1D Gross-Pitaevskii equation (4.2), also called the nonlinear Schrödinger equation, is an example of an equation that holds solitons. The discovery of solitons is attributed to John Scott Russell in 1834. While he was conducting experiments on the most efficient design for canal boats, he saw what he called a "wave of translation" which "continued its course along the channel apparently without change of form or diminution of speed" [31]. The existence of solitons was controversial at the time, as Russell's observations seemed to contradict established hydrodynamic theories. A few years later, Korteweg and de Vries, following the work of Boussinesq, provided a nonlinear wave equation describing the evolution of the height of the fluid on shallow surfaces $\eta(x,t)$ with respect to its resting value h [32]:

$$\frac{1}{c}\frac{\partial\eta}{\partial t} + \frac{\partial\eta}{\partial x} + \frac{3}{2h}\eta\frac{\partial\eta}{\partial x} + \frac{h^2}{6}\frac{\partial^3\eta}{\partial x^3} = 0 \tag{4.3}$$

with $c = \sqrt{gh}$ the celerity of gravity waves (g is the gravity acceleration). Remarkably, the Korteweg-de Vries (KdV) equation (4.3) admits a solution that propagates with a celerity (the soliton celerity) $v = c\left(1 + \frac{\eta_0}{2h}\right)$ greater than c:

$$\eta(x,t) = \eta(x - vt) = \eta_0 \frac{1}{\cosh^2\left(\sqrt{\frac{3\eta_0}{h}}\frac{x-vt}{2h}\right)} \tag{4.4}$$

with η_0 the maximum height of the wave. This explained Russell's observations. The long wavelength tsunami waves are concrete examples of solitonic solutions of the KdV equation, which are among the most deadly natural disasters. Zabusky and Kruskal solved the KdV equation numerically in 1965 [33] and the term "soliton" was coined by Gardner et al. [157], the inventors of the inverse scattering method, for their particle-like behaviour in collisions of such solitary waves.

Since then, soliton theory has been further developed, particularly in the field of photonics. A distinction is made between *temporal* and *spatial* solitons, depending on whether the confinement of light during propagation occurs in time or in space: temporal solitons are optical pulses that retain their shape in time, while spatial solitons are self-guided beams that remain confined in the transverse directions (orthogonal to the direction of propagation) during propagation. Temporal solitons result from a balance between dispersion (the group velocity v_g depends on the frequencies of the beam ω) and a nonlinear term due to the Kerr effect[2]. Spatial solitons arise from balancing diffraction and refractive index dependence. Figure 4.1 gives a summary of how optical solitons can emerge in nonlinear media.

The possibility of observing them arose together with the invention of the lasers in the 1960s. Hasegawa and Tapert showed in 1973 [160] that pulse propagation in an optical fiber can be described by a nonlinear Schrödinger equation of the type (4.2), predicting the existence of stable temporal solitons. Their first experimental realization followed in 1980 [34]. Figure 4.1 also presents early experimental demonstrations of optical solitons. Since then, proposals have been made to use optical solitons as information carriers which would not be affected by dispersive broadening [161, 156].

Finally, it is worth mentioning that the NLSE can also be used to describe Langmuir waves of small amplitude in plasmas [30, 162].

We have described here how solitons arise as stationary solutions of nonlinear equations. In the following, we will focus on the solitons of the 1D NLSE, which can take various forms.

4.1.3 Various classes of solitons of the 1D NLSE

Bright solitons

The first natural class of solitons concerns the so-called bright solitons. They are localized wavepackets solutions of (4.2) with a negative interaction parameter g_{1D}. In photonics, the bright temporal soliton is obtained in the anomalous dispersion regime *i.e.* $\frac{\partial(1/v_g)}{\partial\omega} < 0$ while the spatial bright soliton propagates in a self-focusing medium *i.e.* the refractive index increases with light intensity. Zakharov and Shabat [164] generalized the inverse scattering method[3] to the case of the 1D attractive NLSE and analytically expressed a family of solutions of (4.2), whose simplest representative is the following bright soliton:

[2]The refractive index depends on the light intensity and thus the frequency of the pulse depends on the time derivative of the light intensity. This is called the *self-phase modulation* effect.

[3]Introduced by Gardner et al. [157], this method provides a systematic procedure to obtain *all* solutions of an integrable 1D nonlinear equation. It can be seen as a Fourier analysis for non-linear problems, where the solitons play the role of normal modes [30].

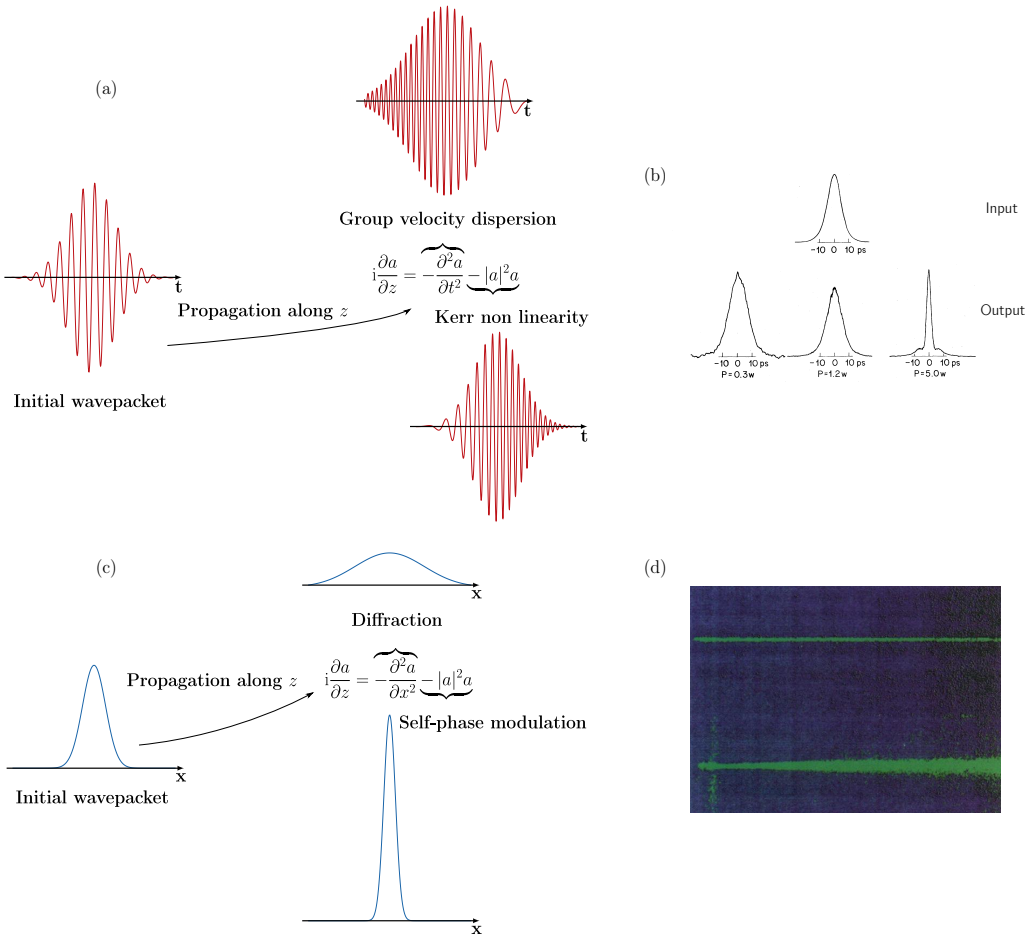

FIGURE 4.1: Optical (bright) solitons. (a): A (bright) temporal soliton arises in a nonlinear medium when the group velocity dispersion effect counteracts the Kerr non-linearity effect. The former makes the higher frequencies propagate faster in the anomalous dispersion regime ("chirp") on top of a global spreading of the wavepacket, while the latter causes the higher frequencies to propagate slower. The adimensionalized equation for the envelope of the field is written with these two terms. (b): The first realization of a temporal soliton. The figure is adapted from [34]. The lower curves are autocorrelation curves of a beam at the output of a fiber of length 700 m, which should be compared with the one at the fiber input (upper curve). If the power at the fiber input is too low, the diffraction dominates (lower left curve) while if it is too high, non-linearity shortens the pulse. For intermediate powers, a temporal soliton is obtained. Solitons of higher energies, called higher-order solitons, were also observed but are not shown here. (c): A spatial soliton results from the competition between the diffraction effect, which tends to spread the initial wavepacket, and the self-phase modulation effect. Here we show the example of a bright spatial soliton for which the self-focusing effect (negative nonlinear term in the NLSE) allows a localized wavepacket. The adimensionalized equation of the field amplitude evolution is also shown. (d): An example of a 2D spatial soliton. Figure taken from [163]. Photographs of a beam propagating in a photorefractive crystal over 6 mm with the nonlinearity on (top) and off (bottom), showing respectively the formation of a spatial soliton and a diffracted beam.

$$\psi(x,t) = \frac{\psi_0}{\cosh(\kappa x)}\, \mathrm{e}^{\mathrm{i}\Omega t} \tag{4.5}$$

with $\kappa = \frac{mN|g_{1D}|}{2\hbar^2}$ the typical inverse size of the localized wavepacket, $\psi_0 = \sqrt{\frac{\kappa N}{2}}$ its amplitude, N its norm, and $\hbar\Omega = \frac{mg_{1D}^2 N^2}{8\hbar^2}$ a quantity analogous to a chemical potential. To describe moving bright solitons with velocity v, one can use Galilean invariance in the system (see [111] and Chapter 2) and write the wavefunction in the moving frame as:

$$\psi_v(x,t) = \mathrm{e}^{\mathrm{i}m(xv - v^2 t/2)/\hbar}\,\psi(x - vt, t) \tag{4.6}$$

We note the strong similarity between the KdV soliton (4.4) and the bright soliton of the NLSE (4.5). We emphasize that the family of solutions of the 1D attractive NLSE is infinite and we can express higher-order solitons (also called multisolitons of order p) whose shape is not constant but rather varies periodically during propagation [165] (see [166] for an experimental realization of a $p = 13$ optical multisoliton).

The first bright temporal soliton was obtained in 1980 [34], propagating light at $\lambda \simeq 1.55\,\mu\mathrm{m}$ in a silica-glass fiber for which the anomalous dispersion regime is reached at this wavelength. Regarding the spatial soliton, the first experiment was performed by Ashkin and Bjorkholm [167] in a sodium vapor cell. In a 1D configuration, their first realization was made in Limoges using liquid carbon disulphide [35]. Because 1D solitons are unstable in a 3D bulk, the inhibition of diffraction along the transverse directions was needed to obtain a stable soliton.

In matter-wave solitons, where the nonlinearity arises from the interaction between atoms, the first quasi-1D bright soliton was reported in [36]. The attractive interactions were obtained thanks to the use of a Feshbach resonance on a BEC cloud of ^{7}Li atoms with initially repulsive interactions. Bright multisolitons propagating under a force were reported shortly after in [168][4].

Dark solitons

The bright soliton is the most "natural" soliton that emerges from the nonlinear Schrödinger equation as a localized pulse either in space or in time. However, there are other types of solutions, such as the dark soliton. It is a solution of the repulsive NLSE (4.2), *i.e.* with $g_{1D} > 0$. At rest, it takes the following stationary form:

$$\psi(x,t) = \sqrt{\frac{\mu}{g_{1D}}}\tanh(\kappa x)\,\mathrm{e}^{-\mathrm{i}\mu t/\hbar} \tag{4.7}$$

with $\kappa = \frac{1}{\hbar}\sqrt{\mu/m}$. This type of solution cannot be normalized but it still corresponds to a localized excitation. To describe such a moving defect in a resting bath, we cannot use the Galilean invariance as we did for the bright soliton because it would not describe a bath at rest. The density minimum of the dark soliton moving at velocity v is no longer zero. A moving dark soliton is thus called a *grey* soliton, which takes the following form [171]:

$$\psi_v(x - vt, t) = \sqrt{\frac{\mu}{g_{1D}}}\left[\mathrm{i}\frac{v}{c_B} + \sqrt{1 - \frac{v^2}{c_B^2}}\tanh\left(\kappa\sqrt{1 - \frac{v^2}{c_B^2}}(x - vt)\right)\right]\mathrm{e}^{-\mathrm{i}\mu t/\hbar} \tag{4.8}$$

[4] In contrast to the experiment of Khaykovic et al. [36], the atom number in the condensate is an order of magnitude larger in Strecker et al.'s experiment, which triggers a so-called *modulational instability* and leads to the formation and propagation of bright multisolitons of typical order $p = 4$ [169].

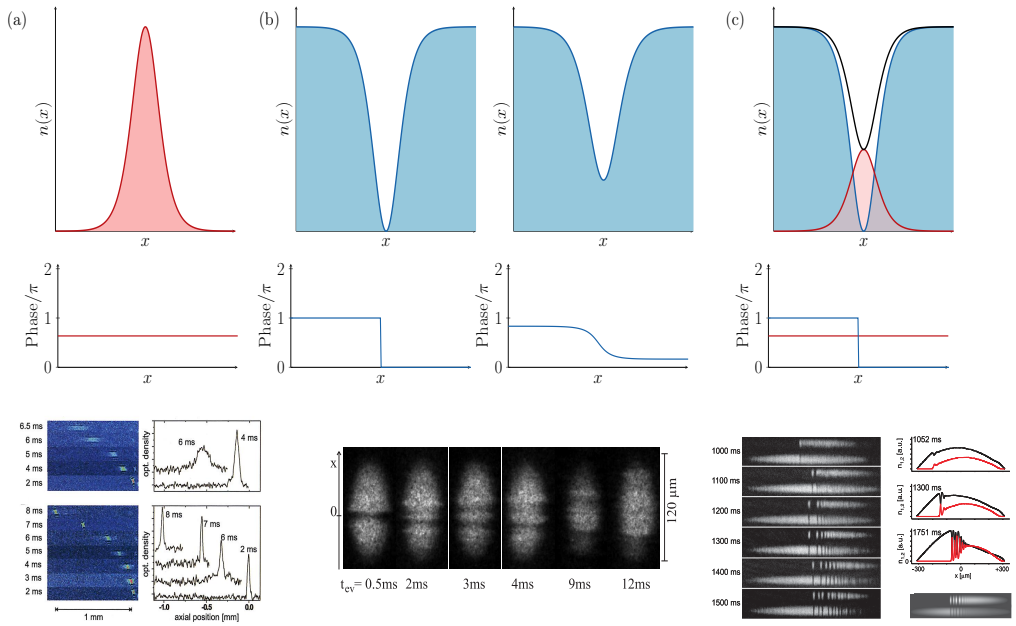

FIGURE 4.2: Different types of solitons of the 1D NLSE and examples from matter wave experiments. (a): A sketch of a bright soliton. The density is localized and the phase of the wavefunction is constant over the soliton. Experimental results from Salomon's group are reproduced [36]. Absorption images after removal of confinement are shown in a 1D waveguide. Top panel: ideal gas (interactions switched off), the gas expands. Bottom image: attractive gas, the cloud keeps its shape over time during propagation for a specific range of atom number in the condensate. It is a bright soliton. (b): Dark/grey soliton. For a dark soliton, the density vanishes and the phase undergoes a sharp π phase shift at the hole position while for a grey soliton, the density is never zero and the phase evolution is smoother. Experimental absorption images of an elongated BEC from [170] are shown. A phase imprinting method produces a dark soliton propagating along $-x$, accompanied by a density wave propagating along $+x$. (c): Dark-bright soliton. A bright soliton is trapped in the hole of a dark soliton. The total density is represented by a black solid line. The bottom figure, taken from [40], shows experimental results (left) compared with numerical simulations (right) of the generation and propagation of dark-bright multisolitons trapped in a cigar-shaped potential. They are formed by the counterpropagation of two superfluids.

c_B is the Bogoliubov speed of sound (see Chapter 2). The velocity v of the grey soliton cannot exceed c_B, as we can see from its expression. On top of this density hole, a dark soliton is associated with a phase jump, which is sharp for a stationary dark soliton and smoother for a moving one (see Figure 4.2). We can then explain the existence of a dark soliton: minimizing the 1D repulsive interparticle interaction energy would tend to reduce the density minimum (see section 4.1.1) while the kinetic energy associated to the phase gradient is minimized when the density minimum is increased [170]. The balance between the two creates a dark/grey soliton[5].

The first observations of (temporal) dark solitons in optical fibers are attributed to Weiner et al. [173]. This required to be in the normal dispersion regime $\left(\frac{\partial(1/v_g)}{\partial\omega} > 0\right)$. Regarding Bose-Einstein condensates, they were first demonstrated in [170] with a phase imprinting method (quickly followed by [37]). A dipole potential created by a

[5]The higher-order dark solitons are not stable [172].

blue-detuned beam is applied to half of the BEC for a duration corresponding to the addition of a π phase shift. The density is initially unperturbed but after a certain time, the potential gradient transfers momentum to the wavefunction and two density minima travelling in opposite directions appear. The one that moves in the same direction as the force created by flashing the dipolar potential (see Appendix E) is a dark soliton. They verified that the speed of the soliton is significantly less than the Bogoliubov speed of sound c_B and therefore cannot be a density wave.

Vector solitons

Not only the scalar NLSE but also coupled NLSEs admit solitonic solutions, called "vector" solitons, which are solitary waves consisting of two components. Depending on the nature of the scalar soliton components, bright or dark, the composite object is called a bright-bright, a dark-dark, or a dark-bright soliton. In the photonic framework of light propagation in birefringent fibers, bright-bright, dark-dark or dark-bright solitons can be formed due to cross-phase modulation coupling [174]. They have recently been observed experimentally [175, 176, 177]. In particular, dark-bright solitons show enhanced dynamical stability compared to dark solitons. They appear as a bright pulse in a system trapped within a copropagating dark soliton. In the context of two-component BECs denoted by the states $|1\rangle$ and $|2\rangle$ of interaction intra-component parameters g_{11}[6] and g_{22} and inter-component parameter g_{12}, the two coupled equations for the wavefunctions ψ_1 and ψ_2 are written as follows:

$$\begin{cases} -\frac{\hbar^2}{2m}\nabla^2\psi_1 + g_{11}\left|\psi_1\right|^2\psi_1 + g_{12}\left|\psi_2\right|^2\psi_1 = \mathrm{i}\hbar\,\frac{\partial\psi_1}{\partial t} \\ -\frac{\hbar^2}{2m}\nabla^2\psi_2 + g_{22}\left|\psi_2\right|^2\psi_2 + g_{12}\left|\psi_1\right|^2\psi_2 = \mathrm{i}\hbar\,\frac{\partial\psi_2}{\partial t} \end{cases} \tag{4.9}$$

Even if all the interaction parameters g_{ij} are positive, a bright component can exist if it is trapped within a dark component, forming a dark-bright soliton, which can thus be seen as a "symbiotic" system.

The stationary dark-bright soliton emerges when one takes all the g_{ij} equal to a value g (or sufficiently close to each other [38]). It is called the Manakov limit [178][7]. The stationary dark-bright soliton is obtained by imposing a dark soliton for ψ_1 of background density n_0 and a bright soliton for ψ_2 normalized to N_2:

$$\begin{cases} \psi_1(x) = \sqrt{n_0}\tanh(\kappa x)\,\mathrm{e}^{-\mathrm{i}\mu_1 t/\hbar} \\ \psi_2(x) = \frac{\sqrt{\kappa N_2/2}}{\cosh(\kappa x)}\,\mathrm{e}^{-\mathrm{i}\mu_2 t/\hbar} \end{cases} \tag{4.10}$$

The verification of the coupled NLSEs (4.9) for this set of solutions links the parameters as $\mu_1 = gn_0$, $\mu_2 = \mu_1 - \frac{\hbar^2\kappa^2}{2m}$ and $\frac{\hbar^2\kappa^2}{m} = g\left(n_0 - \kappa N_2/2\right)$. Note that depending on the atom number chosen for the minority component, the total density $|\psi_1|^2 + |\psi_2|^2$ can vary significantly over the system size.

The expression for a moving dark-bright soliton with velocity v when the bright component is subjected to a potential $V_2(x)$ can also be found in [38]:

$$\begin{cases} \psi_{1,v}(x,t) = \sqrt{n_0}\left\{\mathrm{i}\sin(\alpha) + \cos(\alpha)\tanh\left[\kappa(x-vt)\right]\right\} \\ \psi_{2,v}(x,t) = \frac{\sqrt{\kappa N_2/2}}{\cosh[\kappa(x-vt)]}\,\mathrm{e}^{\mathrm{i}mvx/\hbar}\,\mathrm{e}^{-\mathrm{i}\omega t}\,\mathrm{e}^{-\mathrm{i}V_2 t/\hbar} \end{cases} \tag{4.11}$$

[6] We will omit the "1D" indexes in the following.

[7] Deviations from the Manakov limit have been studied in [179, 180].

The parameters are linked to the velocity v as: $\frac{v}{c_B} = \kappa\xi\tan(\alpha)$ with $\xi = \hbar/\sqrt{mgn_0}$[8]. Besides, we have $\hbar\omega = \frac{1}{2}mv^2 - \frac{\hbar^2\kappa^2}{2m}$.

The dark-bright matter-wave soliton was first demonstrated in 2001 by Anderson et al. [181], where a bright soliton was trapped in a dark pulse. Becker et al. [39] combined the use of a Spatial Light Modulator and Raman beams to first create a dark soliton and then fill the density hole with atoms in a different hyperfine state. They were also able to study the collision between a dark and a dark-bright soliton. Dark-bright multisolitons emerging from the counterflow of two superfluids have been observed in [40]. Dark-dark solitons were similarly identified in Engels' group [182].

The list goes on

We continue this subsection by briefly mentioning other types of solitons of the 1D NLSE. This equation admits other classes of solutions, such as spatio-temporal breather solutions, which undergo periodic evolution. Kuznetsov-Ma breathers [183] are localized in space and are periodic in time. They were observed experimentally in photonics in 2012 [184]. Conversely, Akhmediev breathers are localized in time and periodic in space. The Peregrine soliton is a limit of this class of breather solitons, a structure localized in both space and time, solution of the attractive (*i.e.* $g_{1D} < 0$) NLSE (4.2). It is reminiscent of the unpredictable and suddenly appearing *rogue waves*. It was first observed in optical fibers [185], 25 years after it was predicted [186]. In a very recent work, Romero-Ros et al. [187] demonstrated a Peregrine soliton in an immiscible repulsive two-component BEC, following a theoretical proposal [188]. The emerging effective attractive dynamics for the minority component, studied in [189] and first used experimentally in our group [190], and the seeding of its modulational instability with a potential well, were the two key ingredients for the formation of this soliton.

Finally, let us say a few words about higher-dimensional solitons. Actually, in 2D and 3D, the integrability and thus the stability properties of solitons are most often lost. We therefore prefer to call the 2D and 3D stationary waves *solitary waves*, which do not necessarily share the stability property of solitons. 1D solitons placed in a higher dimensional geometry develop transverse instabilities, called *snake instabilities*. Nevertheless, 2D solitary waves have been observed both in optical media [167] and recently studied experimentally in our group [77, 190] in the case of the 2D attractive NLSE, realizing the celebrated *Townes soliton*. A 3D solitary wave is expected to be metastable from scale analysis (see for example [77]). Nevertheless, its dynamics have been observed in [191]. Regarding 2D or 3D dark solitons, the so-called *Jones-Roberts solitons* have been experimentally realized in BECs in [192]. Several ideas have been proposed to stabilize 2D or 3D solitons. Among them, the addition of a spatial lattice or the periodic modulation of the nonlinear term of the NLSE equation have been shown to stabilize the so-called *lattice soliton* (see [193, 194, 195]).

Other categories of multidimensional self-bound states are *quantum droplets* [55]. Although the nature of droplets, resulting from a balance between a mean-field attractive term and a beyond mean-field term, is fundamentally different from that of solitons, stationary solutions of a mean-field equation, the equilibrium state, with a

[8] The verification of the coupled GPEs leads to:

$$\kappa\xi = -\frac{\bar{N}_2}{4} + \sqrt{\cos^2\alpha + \frac{\bar{N}_2^2}{16}} \tag{4.12}$$

with $\bar{N}_2 = \frac{N_2}{n_0\xi}$.

size that depends on the number of particles, is reminiscent of a soliton. Initially proposed by Petrov [55], they were demonstrated shortly after [56, 57, 58]. The term "droplet" comes from the liquid-like properties of these self-bound objects. The connection between 3D droplets and 1D solitons has been studied experimentally in [59] and a recent numerical exploration of the cross-over between Townes solitons and droplets in a 2D Bose mixture can be found in [196].

4.2 Stationary magnetic solitons

In the previous section, we provided an overview of some classes of 1D solitons of the NLSE. This section will focus on magnetic solitons, which will be experimentally studied in Chapter 6. Although the magnetic soliton was not initially introduced as a solution of the NLSE, we will connect it to the NLSE in a specific limit. We focus first on *stationary* solitons, static or not, whose form does not evolve in time.

4.2.1 Magnetization vector in a ferromagnet

The term magnetic soliton first appeared in a 1990 paper by Kosevich et al. [43]. It is a solution of the nonlinear Landau-Lifshitz equation (LLE) [197]. The system under consideration is a 1D ferromagnetic spin chain in which each spin can be described as a 3D vector (see Figure 4.3). From a quantum mechanical point of view, we associate a spin operator $\hat{\mathbf{S}}_i = \frac{\hbar}{2}\hat{\boldsymbol{\sigma}}_i$ to each spin i where $\hat{\boldsymbol{\sigma}}_i$ is the vector of the Pauli matrices. The Heisenberg Hamiltonian is used to describe a 1D spin chain with an exchange interaction quantity J, assumed constant and positive to describe an isotropic ferromagnet. It is defined as follows:

$$\hat{H} = -J \sum_{i \neq j} \hat{\mathbf{S}}_i \cdot \hat{\mathbf{S}}_j \tag{4.13}$$

where the sum over j accounts for the nearest neighbors of the spin i. For dimensionality reasons, we introduce a parameter γ (it does not have any connection with the Lieb-Liniger parameter) and write the Heisenberg Hamiltonian as $\hat{H} = \gamma \sum_i \hat{\mathbf{S}}_i \cdot \hat{\mathbf{H}}_{\text{eff},i}$ with $\hat{\mathbf{H}}_{\text{eff},i}$ the effective magnetic field created by the neighboring spins: $\hat{\mathbf{H}}_{\text{eff},i} = -\frac{J}{\gamma}\left(\hat{\mathbf{S}}_{i-1} + \hat{\mathbf{S}}_{i+1}\right)$.

Using the Heisenberg equations of motion: $\mathrm{i}\hbar\frac{\partial \hat{S}_i^k}{\partial t} = \left[\hat{S}_i^k, \hat{H}\right]$ and the commutation rules of the spin operators: $\left[\hat{S}_i^k, \hat{S}_j^{k'}\right] = \mathrm{i}\hbar\,\delta_{i,j}\epsilon_{k,k',k"}\hat{S}_i^{k"}$ with $k, k', k" = x, y, z$; i, j the spin indexes in the chain, $\delta_{i,j}$ the Kronecker symbol and $\epsilon_{k,k',k"}$ the Levi-Civita symbol, we obtain the equation of motion for the spin i:

$$\frac{\partial \hat{\mathbf{S}}_i}{\partial t} = -\gamma \hat{\mathbf{S}}_i \times \hat{\mathbf{H}}_{\text{eff},i} \tag{4.14}$$

The LLE describes phenomenologically the evolution of the magnetization vector $\mathbf{M}(x,t)$ which is defined as the magnetic moment per unit of volume of the spin chain. Its value for the i-th site of the chain is proportional to the average of the spin operator $\hat{\mathbf{S}}_i$. If the angle between the adjacent spin vectors is small, one can take a continuous limit and ignore the discrete nature of the spin positions. The nonlinear equation

obtained for the evolution of the magnetization vector, the so-called Landau-Lifshitz equation, then takes the form[9]:

$$\frac{\partial \mathbf{M}}{\partial t} = -\gamma \mathbf{M} \times \mathbf{H}_{\text{eff}} \tag{4.16}$$

This equation describes a precessional motion of the magnetization vector around the axis defined by the effective magnetic field. Thus, the notation for the parameter γ is not fortuitous, it is the electron gyromagnetic ratio: $\gamma = \mu_B/\hbar$[10]. From (4.16), it can be seen that the norm of the magnetization vector is conserved during the movement and is equal to its saturation value, as it should be in a ferromagnetic material.

For the sake of simplicity, the previous link between the LLE and the Heisenberg Hamiltonian was derived assuming an isotropic ferromagnet and an exchange interaction quantity J that does not depend on the spatial direction. Actually, this is not general as there are several causes of anisotropy in a ferromagnet. The anisotropy may be due to an intrinsic anisotropic crystalline order, or it may occur in an asymmetric material where the demagnetizing field (the magnetic field generated by the magnetization) is not the same in all directions. Anisotropy can also be externally imposed, for example by a mechanical constraint. We now discuss different cases depending on the relative values of J_x, J_y and J_z. We treat the case of weakly anisotropic ferromagnets for which the values of the exchange constants J_x, J_y and J_z are close to each other [43]. We express the effective magnetic field as (minus) the functional derivative of the magnetic energy with respect to the magnetization vector: $\mathbf{H}_{\text{eff}} = -\frac{\delta E}{\delta \mathbf{M}}$. For the moment, we do not consider an external magnetic field and the magnetic energy has only two contributions: $E = E_{\text{ex}} + E_{\text{ani}}$. The first one is an exchange energy term E_{ex} which tends to align locally the different neighboring spins. It corresponds to a continuous description of the exchange interaction of the Heisenberg Hamiltonian. This term favors a uniform magnetization. The second term is an anisotropic energy term E_{ani} which accounts for the (small) differences between J_x, J_y and J_z. In a 1D ferromagnetic spin chain directed along x, we write them at lowest order in the difference between the different exchange constants as:

$$\begin{cases} E_{\text{ex}} = \alpha \int \mathrm{d}x \left| \frac{\partial \mathbf{M}}{\partial x} \right|^2 \\ E_{\text{ani}} = -\frac{1}{2} \int \mathrm{d}x \left(J_x M_x^2 + J_y M_y^2 + J_z M_z^2 \right) \end{cases} \tag{4.17}$$

with α a positive (ferromagnet) constant and $\mathbf{M} = M_x \mathbf{u_x} + M_y \mathbf{u_y} + M_z \mathbf{u_z}$ decomposed in an orthonormal basis. Because the magnetization vector $\mathbf{M}$ is a constant of motion, we can express M_y as a function of M_x and M_z. Introducing the $\beta_x \equiv J_x - J_y$ and $\beta_z \equiv J_z - J_y$ coefficients, we can express the anisotropic energy as $E_{\text{ani}} = -\frac{1}{2} \int \mathrm{d}x \left(\beta_x M_x^2 + \beta_z M_z^2 \right)$ up to a constant. Therefore, by taking (minus) the functional derivative of the total energy with respect to the magnetization vector, we obtain the expression for the effective magnetic field:

[9] A damping term is included in a more general form of this equation:

$$\frac{\partial \mathbf{M}}{\partial t} = -\gamma \mathbf{M} \times \mathbf{H}_{\text{eff}} - \lambda \mathbf{M} \times (\mathbf{M} \times \mathbf{H}_{\text{eff}}) \tag{4.15}$$

taking into account dissipation phenomena with λ a phenomenological damping parameter. In the following, we will consider the undamped Landau-Lifshitz equation.

[10] We neglect the orbital kinetic moment of the electrons. The magnetism involved here comes only from the spin of the electrons. This equation can also be phenomenologically found by treating the classical motion of an electron in a magnetic field and using the angular momentum theorem.

$$\mathbf{H}_{\text{eff}} = \alpha \frac{\partial^2 \mathbf{M}}{\partial x^2} + \beta_x M_x \mathbf{u_x} + \beta_z M_z \mathbf{u_z} \tag{4.18}$$

Now let us explore various possibilities. When $J_x \neq J_y$, the ferromagnet is called *biaxial* [43]. In the following, we will assume $J_x = J_y$ (*i.e.* $\beta_x = 0$). The ferromagnet is then referred to as *uniaxial* because the anisotropy axis aligns with the z axis. In the uniaxial case, if $J_z > J_y$ ($\beta_z > 0$), the anisotropy is of the *easy-axis* type as the magnetization vector of the ground state aligns with the z axis. On the contrary, if $J_z < J_y$ (*i.e.* $\beta_z < 0$), the anisotropy is of the *easy-plane* type. The ground state magnetization vector lies in the plane (x,y) with an arbitrary direction (as $J_x = J_y$).

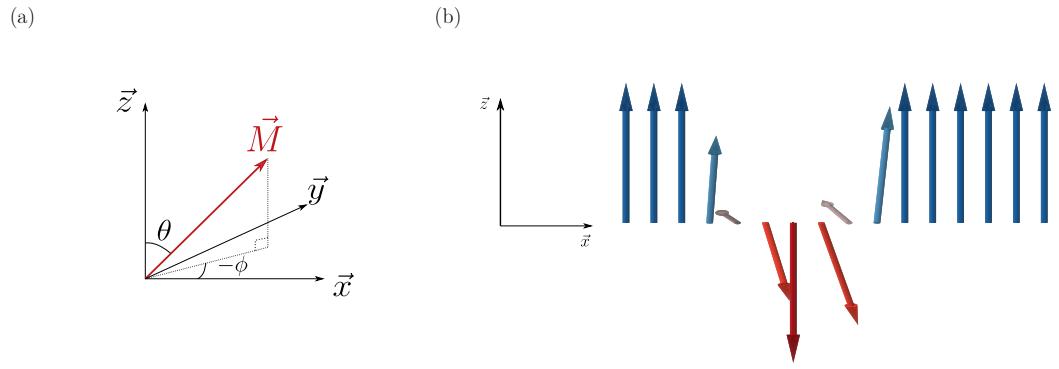

FIGURE 4.3: Magnetization vector in a 1D spin chain. (a): Parametrization of the angles of the magnetization vector. (b): 1D spin chain. On each site, the magnetization vector is represented by an arrow. The direction of the vector provides insight into the angles θ and ϕ as in (a). Its color also indicates the angle θ with respect to the z axis. We plot the case of an easy-axis ferromagnet for which the ground state magnetization vector is oriented along the z axis. Around the position of the localized magnetic excitation, the magnetization vector is reversed to $\theta = \pi$.

Plugging the expression of the effective magnetic field (4.18) into the LLE (4.16), one obtains a nonlinear equation written for an uniaxial ferromagnet:

$$\frac{\partial \mathbf{M}}{\partial t} = -\gamma \mathbf{M} \times \left(\alpha \frac{\partial^2 \mathbf{M}}{\partial x^2} + \beta_z M_z \mathbf{u_z} \right) \tag{4.19}$$

In the description of the weakly-interacting Bose gas, we saw in Chapter 2 the importance to consider its weakly-excited states, called elementary excitations. In a ferromagnet, these excitations are characterized by a small deviation of the magnetization vector from its equilibrium value. In classical terms, the wave associated to the small deviation is characterized by a wavevector k and a frequency ω, and is called a *spin wave*. In quantum mechanical terms, these excitations are associated to quasi-particles, called *magnons*, with an energy spectrum $\hbar\omega(k)$[11]. It can be shown [43] that the interactions between magnons in an easy-axis (respectively easy-plane) ferromagnet are attractive (resp. repulsive). They are responsible for the appearance of localized magnetic excitations, which we call magnetic solitons.

To parametrize the magnetization vector $\mathbf{M}$, we only need two angles (θ,$-\phi$), since its amplitude is a constant of motion, which we set to 1 for simplicity (see Figure 4.3):

[11] It is reminiscent of the description of the elementary excitations of a 2D Bose gas, which propagate as *sound waves*, and whose quasi-particles are called *phonons* in the low-k regime. In the same way as the Bogoliubov spectrum (2.25), the energy spectrum of the magnons can be obtained with a diagonalization of the Hamiltonian under some approximations [43].

$$\begin{cases} M_x = \sin\theta\cos\phi \\ M_y = -\sin\theta\sin\phi \\ M_z = \cos\theta \end{cases} \tag{4.20}$$

The amplitude of the magnetization vector in the plane $\sqrt{|M_x|^2 + |M_y|^2}$ is given by $|\sin\theta|$ while its projection along z is given by $|\cos\theta|$.

From the LLE equation (4.19), we identify a natural frequency scale $\omega_0 = \gamma\beta_z$ which is a Larmor precession frequency and a natural length scale as $l_0 = \sqrt{\alpha/|\beta_z|}$, a characteristic magnetic length. Plugging (4.20) into the LLE (4.19), we obtain (after a few lines of calculation) the pair of equations for ϕ and θ:

$$\begin{cases} \frac{\partial\theta}{\partial t} = -l_0^2\omega_0\left[\sin\theta\left(\frac{\partial^2\phi}{\partial x^2}\right) + 2\cos\theta\frac{\partial\theta}{\partial x}\frac{\partial\phi}{\partial x}\right] \\ \frac{\partial\phi}{\partial t} = \omega_0\left[-\cos\theta\left(1 + l_0^2\left(\frac{\partial\phi}{\partial x}\right)^2\right) + \frac{l_0^2}{\sin\theta}\frac{\partial^2\theta}{\partial x^2}\right] \end{cases} \tag{4.21}$$

To pursue the resolution, we introduce adimensionalized variables: $t' = \omega_0 t$ and $x' = x/l_0$. Depending on whether we consider an easy-axis or an easy-plane ferromagnet, we obtain different sets of equations because the β_z factor enters the adimensionalization. Omitting the prime indexes, we write the adimensionalized equations as:

$$\begin{cases} \frac{\partial\theta}{\partial t} = -\left[\sin\theta\left(\frac{\partial^2\phi}{\partial x^2}\right) + 2\cos\theta\frac{\partial\theta}{\partial x}\frac{\partial\phi}{\partial x}\right] \\ \frac{\partial\phi}{\partial t} = -\cos\theta\left(\pm 1 + \left(\frac{\partial\phi}{\partial x}\right)^2\right) + \frac{1}{\sin\theta}\frac{\partial^2\theta}{\partial x^2} \end{cases} \tag{4.22}$$

where the $+$ sign represents the case of an easy-axis ferromagnet ($\beta_z > 0$) and the $-$ sign accounts for the easy-plane ferromagnet ($\beta_z < 0$). This sign change has a significant impact on the observed physics as we will see in the following.

4.2.2 Stationary magnetic solitons - Easy-plane

We first consider the stationary solutions of (4.22) in the easy-plane case (sign $-$). We look for travelling solitonic solutions and introduce the quantity v describing the velocity of the soliton and Ω a pulsation. Therefore, we consider solutions written as $\theta(x,t) = \theta(x - vt)$ and $\phi(x,t) = \tilde{\phi}(x - vt) + \Omega t$. In this chapter, we focus on stationary solitons, meaning that the soliton's form does not change over time. In other words, v and Ω remain constant over time.

The equations (4.22) then write:

$$\begin{cases} -v\theta' = -\sin\theta\,\tilde{\phi}'' - 2\cos\theta\,\theta'\tilde{\phi}' \\ \Omega - v\tilde{\phi}' = -\cos\theta(-1 + \tilde{\phi}'^2) + \frac{\theta''}{\sin\theta} \end{cases} \tag{4.23}$$

the symbol $'$ meaning the derivative with respect to $\chi = x - vt$. The first equation can be written: $\frac{\mathrm{d}}{\mathrm{d}\chi}\left(v\cos\theta + \sin^2\theta\,\tilde{\phi}'\right) = 0$. We can integrate it assuming $\tilde{\phi}'(\chi \to \infty) = 0$ (see [41]). Because we are dealing with an easy-plane ferromagnet, the magnetization vector at infinity lies in the plane *i.e.* $\theta \to \pm\pi/2$ as $\chi \to \infty$. Thus the integration constant is equal to zero and we obtain: $\tilde{\phi}' = -v\frac{\cos\theta}{\sin^2\theta}$. Plugging this result into (4.23), we get an equation that only involves θ:

$$\theta'' - v^2\frac{\cos\theta}{\sin^3\theta} - \Omega\sin\theta + \cos\theta\sin\theta = 0 \tag{4.24}$$

We recognize a total derivative:

$$\frac{\mathrm{d}}{\mathrm{d}\chi}\left(\frac{\theta'^2}{2}+\frac{v^2}{2}\frac{1}{\sin^2\theta}+\Omega\cos\theta-\frac{1}{2}\cos^2\theta\right)=0 \tag{4.25}$$

We can integrate it by evaluating the integration constant in $\chi\to\infty$ (we assume $\theta'(\chi\to\infty)=0$ and the integration constant is thus equal to $v^2/2$). Introducing $C(\chi)=\cos\left[\theta(\chi)\right]$, the equation on θ simplifies to:

$$(C')^2=P(C)\,,\quad \text{with } P(C)=-C\left[C^3-2\Omega C^2+(v^2-1)C+2\Omega\right] \tag{4.26}$$

The general solution of (4.26) can be expressed in terms of Jacobi elliptic functions [42] and can be seen as a limited case of the biaxial ferromagnet [43]. Kosevich et al. [43] give a restricted plane (v, Ω) for the possible solutions of (4.26).

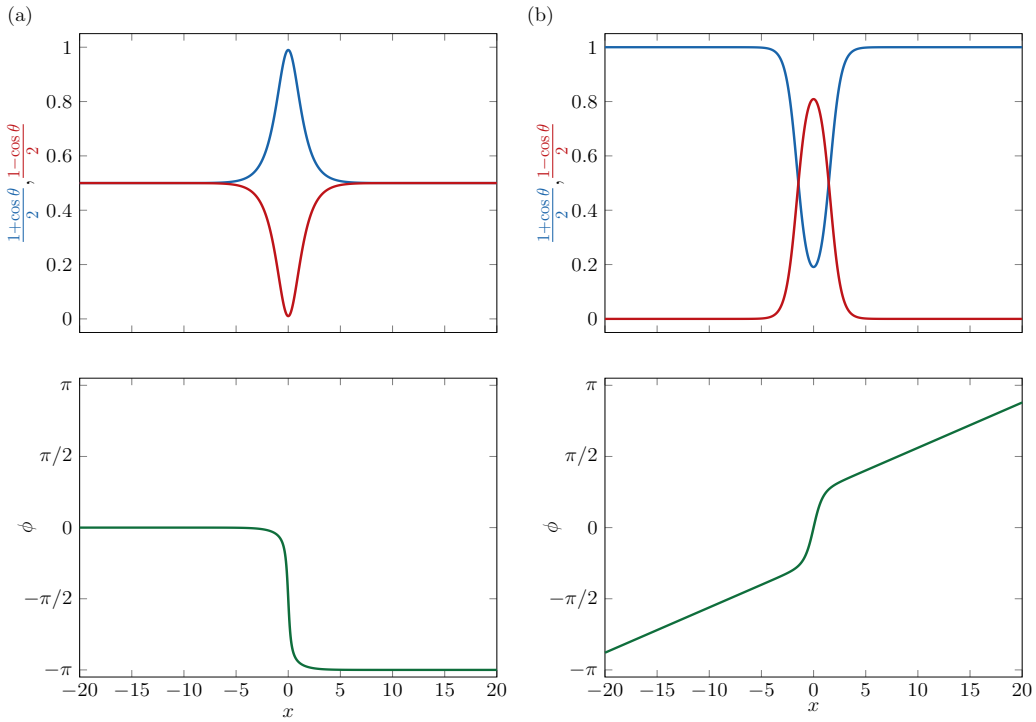

FIGURE 4.4: Example of stationary solutions of the LLE equation characterized by the angles θ (upper panels)[12] and ϕ (lower panels). We obtain them from the formula (4.27) and (4.34). (a): Easy-plane ferromagnet case for $\Omega=0$ and $v=0.2$. At $x\to\infty$, the magnetization vector lies in the plane, *i.e.* $\theta=\pi/2$. The lower v the thinner the localized magnetic excitation and the thinner the zone of relative jump from 0 to π. The phase jump becomes a step function for the static soliton. (b): Easy-axis ferromagnet ground state for $\Omega=-0.1$ and $v=0.2$. At $x\to\infty$, the magnetization vector lies along the vertical axis, *i.e.* $\theta=0$. The velocity has two effects on the phase: the linear slope outside the central zone increases with v and the lower the velocity the steeper the phase jump at the soliton position. The larger Ω the thinner the soliton size and the larger the value of $(1+\cos\theta)/2$ at $x=0$.

[12] The reason for plotting $\frac{1+\cos\theta}{2}$ and $\frac{1-\cos\theta}{2}$ instead of $\cos\theta$ and $\sin\theta$ will become clear after the mapping with the coupled GPEs is accomplished.

We particularize the set of solutions to the case $\Omega = 0$ as considered in [41][13]. In this case, $P(C) = -C^2\left[C^2 - (1-v^2)\right]$. We see that (4.26) admits solutions only if $|v| < 1$. In this case, one can check that the solutions are as follows:

$$\begin{cases} C(x-vt,t) = \cos\left[\theta(x-vt,t)\right] = \frac{\sqrt{1-v^2}}{\cosh\left[\sqrt{1-v^2}(x-vt)\right]} \\ \cot\left[\phi(x-vt,t)\right] = \frac{1}{v}\sinh\left[\sqrt{1-v^2}(x-vt)\right] \end{cases} \tag{4.27}$$

$C(x,t)$ gives the projection of the magnetization vector along the uniaxial axis z. The velocity v influences the slope of the phase at the center: the slower the soliton, the steeper the phase jump [41] (see Figure 4.4).

4.2.3 Stationary magnetic solitons - Easy-axis

We now turn to the case of an easy-axis ferromagnet which will be the focus of the rest of this chapter and whose experimental realization will be the object of Chapter 6. To find the stationary solution, we follow the same procedure as for the easy-plane magnetic soliton: we search for solutions written as $\theta(x,t) = \theta(x-vt)$ and $\phi(x,t) = \tilde{\phi}(x-vt) + \Omega t$. The equations (4.22) write:

$$\begin{cases} -v\theta' = -\sin\theta\,\tilde{\phi}'' - 2\cos\theta\,\theta'\tilde{\phi}' \\ \Omega - v\tilde{\phi}' = -\cos\theta(1+\tilde{\phi}'^2) + \frac{\theta''}{\sin\theta} \end{cases} \tag{4.28}$$

The first equation is identical to the easy-plane first equation and leads to $\frac{\mathrm{d}}{\mathrm{d}\chi}\left(v\cos\theta + \sin^2\theta\,\tilde{\phi}'\right) = 0$. However, the difference will be the integration constant. For the easy-axis ferromagnet, $\theta(\chi\to\infty) = 0$ because the magnetization vector at infinity is aligned along the z axis. Assuming that $\tilde{\phi}'(\chi\to\infty)$ remains finite, the integration constant is equal to v and we get: $\tilde{\phi}' = v\frac{1-\cos\theta}{\sin^2\theta} = v\frac{1}{1+\cos\theta}$. The strategy is the same as for the easy-plane ferromagnet: plug this expression into the second equation of (4.28) and identify a total derivative. The differential equation on θ is:

$$\theta'' + v^2\frac{\sin\theta}{(1+\cos\theta)^2} - \Omega\sin\theta - \cos\theta\sin\theta = 0 \tag{4.29}$$

from which we identify:

$$\frac{\mathrm{d}}{\mathrm{d}\chi}\left(\frac{\theta'^2}{2} + v^2\frac{1}{1+\cos\theta} + \Omega\cos\theta + \frac{1}{2}\cos^2\theta\right) = 0 \tag{4.30}$$

We still assume $\theta'(\chi\to\infty) = 0$ and introduce $C(\chi) = \cos\left[\theta(\chi)\right]$. The integration constant is $v^2/2 + \Omega + 1/2$ and multiplying both sides of the equation (4.30) by $\sin\theta$, the equation is written in the form:

$$(C')^2 = P(C)\,, \quad \text{with } P(C) = -v^2(1-C)^2 + (1-C)(1-C^2)(2\Omega+1+C) \tag{4.31}$$

As we consider an easy-axis soliton, the magnetization vector at infinity should be aligned along the z axis, *i.e.* $C(\chi\to\infty) = 1$. Thus, a positive value of the polynomial (4.31) near $C = 1$ is a necessary condition for identifying a magnetic soliton. This requires[14]:

$$\Omega > \frac{v^2}{4} - 1 \tag{4.32}$$

[13] Their definition of the relative phase is opposite to ours.

[14] It is the same condition as in [43] but their definition of Ω is opposite to ours.

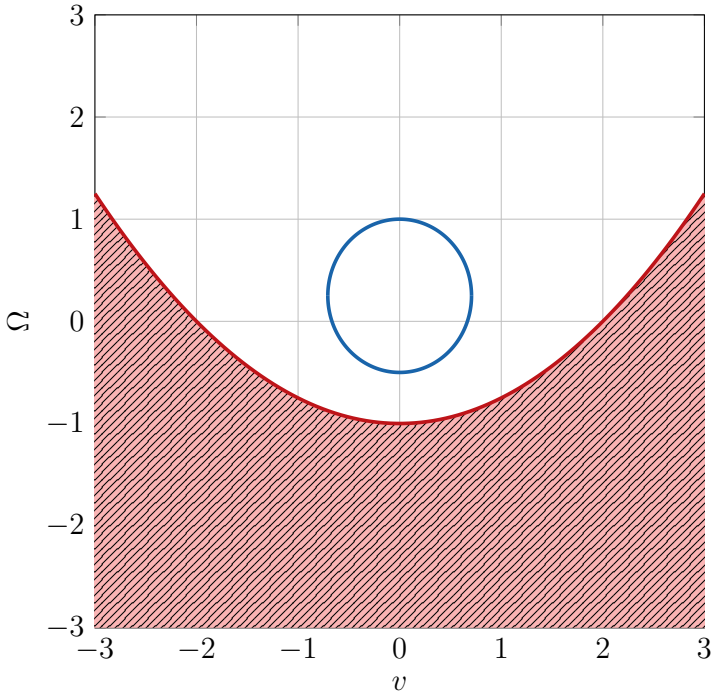

FIGURE 4.5: Map (v, Ω) for the easy-axis magnetic soliton. No solutions exist for $\Omega < (v^2/4 - 1)$ (4.32). The forbidden zone is represented with red hatches. The point (0,0) should also be excluded because it does not represent a localized magnetic excitation. A similar figure with the opposite definition for Ω is given in [43]. Several (v, Ω) correspond to a same magnetization N. The curve $N = \text{const.}$ is an ellipse in the plane (v, Ω). It follows the equation $\cosh(N/2) = \frac{2+\Omega}{\sqrt{\Omega^2+v^2}}$. With a blue solid line, we represent the case $N = 3$ which is a typical number realized in the experiment described in Chapter 6.

This defines the interior of a parabola in the plane (v, Ω) (Figure 4.5). The polynomial P can be factorized into: $P(C) = (1 - C)^2 \left(C^2 + 2(\Omega + 1)C - v^2 + 1 + 2\Omega\right)$. We identify $C = 1$ as a root of order 2 and denote C_+ and C_- the two other roots: $C_\pm = -(\Omega + 1) \pm \sqrt{\Omega^2 + v^2}$. The condition (4.32) implies that the roots satisfy $C_- < C_+ < 1$. We can therefore set $\kappa = \frac{1}{2}\sqrt{(1 - C_+)(1 - C_-)}$. One can check that the following expression is a solution of (4.31) [198, 43]:

$$C(x - vt) = 1 - \frac{(1 - C_+)(1 - C_-)}{1 - \frac{C_+ + C_-}{2} + \frac{C_+ - C_-}{2} \cosh\left[2\kappa(x - vt)\right]} \tag{4.33}$$

Replacing the expressions of C_+ and C_- in (4.33), we can obtain the solution for θ. The angle ϕ can then be calculated from the integration of the above formula: $\tilde{\phi}' = v\frac{1}{1+v\cos\theta}$. The solutions for the easy-axis soliton are:

$$\begin{cases} C(x - vt) = \cos\left[\theta(x - vt)\right] = 1 - \frac{4\kappa^2}{2+\Omega+\sqrt{\Omega^2+v^2}\cosh[2\kappa(x-vt)]} \\ \tilde{\phi}(x - vt, t) = \frac{1}{2}v(x - vt) + \arctan\left\{\frac{2\Omega - v^2 + 2\sqrt{\Omega^2+v^2}}{2\kappa v} \tanh\left[\kappa(x - vt)\right]\right\} \end{cases} \tag{4.34}$$

with $\kappa = \sqrt{1 + \Omega - v^2/4}$. Note that, unlike the easy-plane ferromagnet, there is no restriction on the absolute value of v. We show in Figure 4.4 an example of

magnetization profile.

We see in Figure 4.4 that the density and phase profiles are reminiscent of those discussed in section 4.1.3, especially that of the dark-bright soliton of the 1D NLSEs. What is the exact connection between a vector soliton of the coupled NLSEs and the magnetic soliton of the LLE?

4.2.4 Connection with BEC mixtures

We consider a mixture of two BECs fully described by the matter waves denoted ψ_1 and ψ_2. As we did in 4.1.3, we write g_{12} the inter-component interaction parameter and g_{11}, g_{22} the intra-component interaction parameters. Let us take the symmetric case and define $g \equiv g_{11} = g_{22}$. We rewrite the equations (4.9) as:

$$\begin{cases} -\frac{\hbar^2}{2m}\nabla^2\psi_1 + g\,n_1\,\psi_1 + g_{12}\,n_2\,\psi_1 = \mathrm{i}\hbar\,\frac{\partial\psi_1}{\partial t} \\ -\frac{\hbar^2}{2m}\nabla^2\psi_2 + g\,n_2\,\psi_2 + g_{12}\,n_1\,\psi_2 = \mathrm{i}\hbar\,\frac{\partial\psi_2}{\partial t} \end{cases} \tag{4.35}$$

with $n_{1,2} = |\psi_{1,2}|^2$. The total density $n = n_1 + n_2$ depends a priori on the spatial position and can vary significantly as we saw in Figure 4.2. However, in the experimentally relevant case where $|\delta g = g_{12} - g| \ll g$, one can assume (see for example [42]) that the total density of the gas remains uniform across the soliton. This ensures that the spin dynamics are decoupled from the density dynamics [41, 42] and is a crucial hypothesis for the following derivation[15]. The limit $\delta g \to 0$ is called the Manakov limit [178], which we encountered in section 4.1.3 in the dark-bright soliton discussion. Since the total density, denoted n_0, is constant over the size of the system, the two complex numbers (ψ_1,ψ_2) can be parametrized with only three real numbers called θ, ϕ and Ψ with the following definition:

$$\begin{cases} \psi_1 = \sqrt{n_0}\,\mathrm{e}^{\mathrm{i}\Psi/2}\,\cos(\theta/2)\,\mathrm{e}^{-\mathrm{i}\phi/2} \\ \psi_2 = \sqrt{n_0}\,\mathrm{e}^{\mathrm{i}\Psi/2}\,\sin(\theta/2)\,\mathrm{e}^{+\mathrm{i}\phi/2} \end{cases} \tag{4.36}$$

where Ψ, θ and ϕ depend implicitly on (x,t). The angle θ gives the relative density weight of component 1 (or 2) with respect to the total density: $n_1/n_0 = \frac{1+\cos\theta}{2}$. The angle ϕ represents the relative phase of the two component wavefunctions.

We now have two equations (4.35) for three variables. The variable Ψ can be eliminated by considering the total particle flux:

$$J(x,t) = \frac{\hbar}{m}\left(n_1\frac{\partial\psi_1}{\partial x} + n_2\frac{\partial\psi_2}{\partial x}\right) \tag{4.37}$$

It is equal to: $J(x,t) = \frac{\hbar n_0}{2m}\left(\frac{\partial\Psi}{\partial x} - \cos\theta\frac{\partial\phi}{\partial x}\right)$. Its spatial derivative is zero because n is constant: $\frac{\partial J}{\partial x} = -\frac{\partial n}{\partial t} = 0$. We now assume that we can find a Galilean reference frame in which the particle flux is zero. If one works in this reference frame, one gets:

$$\frac{\partial\Psi}{\partial x} = \cos\theta\frac{\partial\phi}{\partial x} \tag{4.38}$$

Once the variable Ψ is expressed as a function of the other two, we can write two equations for the two variables θ and ϕ. After isolating real and imaginary terms in the equations (4.35), and using (4.38), we obtain:

[15] More precisely, in this type of system, we usually call *density waves* the excitations propagating at the velocity $c = \sqrt{n_0 g/(2m)}$. The *spin waves* characterize the relative motion of the two components and they propagate at the velocity $c_s = \sqrt{n_0|\delta g|/(2m)}$. The characteristic time scale of the spin dynamics is $\hbar/(n_0|\delta g|)$ while for the density dynamics it is $\hbar/(n_0 g)$. When $|\delta g| \ll g$, the two dynamics are decoupled, the spin dynamics being much slower than the density dynamics.

$$\begin{cases} \frac{\hbar}{2}\frac{\partial\theta}{\partial t} = -\frac{\hbar^2}{4m}\left(\sin\theta\frac{\partial^2\phi}{\partial x^2} + 2\cos\theta\frac{\partial\theta}{\partial x}\frac{\partial\phi}{\partial x}\right) \\ \frac{\hbar}{2}\frac{\partial\phi}{\partial t} = \frac{\hbar^2}{4m}\frac{1}{\sin\theta}\frac{\partial^2\theta}{\partial x^2} - \frac{\hbar^2}{4m}\cos\theta\left(\frac{\partial\phi}{\partial x}\right)^2 - n_0\frac{\delta g}{2}\cos\theta \end{cases} \tag{4.39}$$

The problem is now adimensionalized. A natural length scale in the problem, which was not present in the dark-bright soliton case at $\delta g = 0$, is the spin healing length defined as $\xi_s = \frac{\hbar}{\sqrt{2mn_0|\delta g|}}$. Concerning the time scale, we introduce $\tau_s = \frac{\hbar}{n_0|\delta g|}$ the time scale governing the spin dynamics. Defining $x' = x/\xi_s$ and $t' = t/\tau_s$, we get (omitting the prime indexes):

$$\begin{cases} \frac{\partial\theta}{\partial t} = -\left[\sin\theta\left(\frac{\partial^2\phi}{\partial x^2}\right) + 2\cos\theta\frac{\partial\theta}{\partial x}\frac{\partial\phi}{\partial x}\right] \\ \frac{\partial\phi}{\partial t} = -\cos\theta\left(\pm 1 + \left(\frac{\partial\phi}{\partial x}\right)^2\right) + \frac{1}{\sin\theta}\frac{\partial^2\theta}{\partial x^2} \end{cases} \tag{4.40}$$

the $\pm$ sign depends on the sign of δg: a $+$ sign for $\delta g > 0$ and a $-$ sign for $\delta g < 0$. The equations (4.40) are identical to those obtained in the 1D ferromagnetic chain of spins (4.22). The easy-plane ferromagnet is then equivalent to the miscible mixture ($\delta g < 0$), while the easy-axis ferromagnet obeys the same equations as the immiscible mixture ($\delta g > 0$)[16].

Thus, the stationary solutions (4.27) (respectively (4.34)) of the easy-plane (resp. easy-axis) ferromagnets are valid for the case of miscible (resp. immiscible) mixtures close to the Manakov limit. In the following, we simulate the physics of magnetic solitons with the immiscible mixture system and the coupled GPEs (Figure 4.6) but we could also have studied the resolution of the LLE directly. Figure 4.6 confirms that the numerical ground state given by the coupled GPEs for an immiscible mixture is well approximated by the solution derived in the magnetic spin chain context (4.34), close to the Manakov limit.

In the context of BEC mixtures, these equations have been derived and studied in the miscible case in [42, 41, 200] (with an opposite definition for the sign of δg). The immiscible case was studied in the special regime where $g_{12} = \frac{g_{11}+g_{22}}{2}$ in [46]. The general immiscible regime was treated in [47], however, they restricted the set of solutions to $\Omega = 0$.

In conclusion, we have shown here that the coupled NLSEs can be mapped onto the LLE near the Manakov limit. This allowed us to identify a special class of dark-bright solitons of the NLSE, the matter-wave magnetic solitons. We will discuss their experimental realization in Chapter 6. The stability of the magnetic soliton, as of any other solitary wave, is ensured by the existence of some conservation laws. Among them, we will emphasize some conserved quantities during the motion.

4.2.5 Conserved quantities associated to the magnetic soliton

For now, we will focus on the easy-axis magnetic soliton (or immiscible mixture). Discussions of the easy-plane magnetic soliton (or miscible mixture) can be found in [43, 41, 48].

The first quantity of interest is linked to the magnetization vector whose conservation over time under an evolution governed by the (4.19) was established. We will

[16] It can be rigorously justified that an immiscible mixture is characterized by $g_{12}^2 > g_{11}g_{22}$ (see [199]). Here we can simply say that if it costs the system more energy to have the components 1 and 2 together than apart, *i.e.* $g_{12} > g$, then the system will be immiscible.

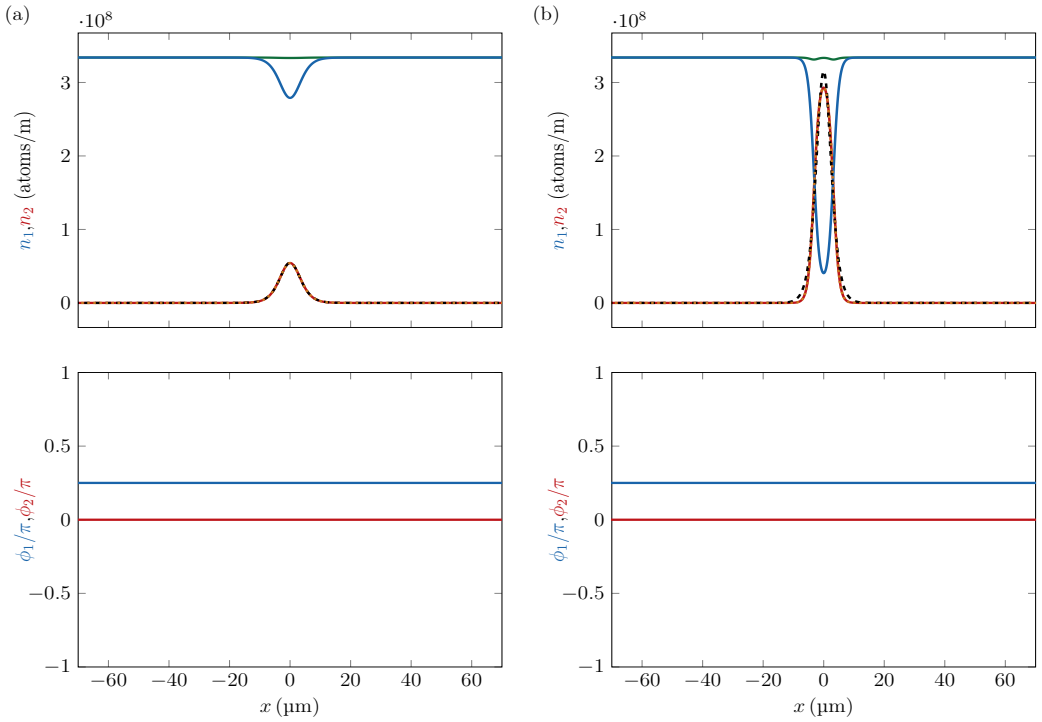

FIGURE 4.6: Numerical steady state solutions of the coupled GPEs for a 1D immiscible mixture with strict boundary conditions. The parameters used are $n_0 = 3.3 \times 10^8$ atoms/m; $\delta g/g = 0.013$; $L = 150\,\mu$m and the plot is restricted between -70 and $+70\,\mu$m to exclude the borders of the box. The upper plots are density graphs for the majority component (respectively the minority component) in blue (resp. red). The green solid line is the total density of the mixture. The lower plots are phase plots of each component with the same color convention. A $\pi/4$ offset phase is added for the minority component for clearer visualization. We plot a fit of the minority component density profile with a $1/\cosh^2(\kappa x)$ function with a dashed black line. The anaytical expression of the easy-axis magnetic soliton $(1+\cos\theta)/2$ given by equation (4.34) with the parameters $v = 0$ (static soliton) and $\Omega \simeq -0.84$ (a), $\Omega \simeq -0.12$ (b), is plotted with a dotted orange line. The Ω values are obtained from the magnetization (4.42). (a): $N_2 = 500$: the depletion is $\sim 20\%$ and the $1/\cosh^2$ fit approximates the steady state well (see Chapter 6 for a justification of this fit). (b): $N_2 = 2000$: the depletion is $\sim 85\%$. The $1/\cosh^2$ fit is not sufficient and the minority component density profite is well approximated with the solution found in the easy-axis magnetic soliton case. The total density is approximately constant regardless of the atom number, contrary to the general dark-bright soliton study (see Figure 4.2). The phase of each component is mostly zero over the box size.

consider the average over the spins of the deviation of its projection along the easy-axis z (*i.e.* $\cos\theta$) from its rest value ($\theta = 0$ in the easy-axis case). We denote it N and call it *magnetization*. It is thus given by:

$$N = \int_{-\infty}^{+\infty} [1 - \cos\theta(x)]\,\mathrm{d}x \tag{4.41}$$

It is also referred to as the number of spin deviations or, from the perspective of elementary particles, as the number of magnons that constitute the localized magnetic

excitation [43]. From the equations (4.40), one can check its conservation over time[17]. Using the expression for the easy-axis magnetic soliton (4.34), we can calculate[18] its expression as a function of Ω and v:

$$N = 2 \ln\left(\frac{2+\Omega+2\kappa}{\sqrt{\Omega^2+v^2}}\right) \tag{4.42}$$

It can also be written as $\tanh(N/4) = \frac{2+\Omega-\sqrt{\Omega^2+v^2}}{2\kappa}$. From the BEC mixture point of view, we can relate N to the number of atoms in the minority component, which we call component 2: N_2. In fact, the definition of ψ_2 (4.36) leads to: $N_2 = \frac{1}{2}n_0\xi_s N$.

The total momentum P of the soliton is also a constant of motion when no external force is applied. We expect it to be proportional to the phase gradient $\frac{\partial\phi}{\partial x}$ (see 2.1.5) and to the magnon density $1-\cos\theta$. Indeed, the definition is:

$$P = \int_{-\infty}^{+\infty} [1-\cos\theta(x)]\,\frac{\partial\phi}{\partial x}\,\mathrm{d}x \tag{4.43}$$

Again, its conservation over time can be checked with (4.40). We emphasize that the conservation is obtained thanks to the following boundary conditions:
$\frac{\partial\theta}{\partial x}(\pm\infty) = \theta(\pm\infty) = 0$. If these conditions are not checked, the total momentum P as defined here is not a conserved quantity.

P is directly related to the phase of the majority component. Indeed, the latter is written (4.36): $\phi_1 = \frac{1}{2}[\Psi(x)-\phi(x)]$. Therefore, using (4.38), we get:
$\frac{\partial\phi_1}{\partial x} = -\frac{1}{2}(1-\cos\theta)\frac{\partial\phi}{\partial x}$. An integration of this equation yields:

$$P = 2\Delta\phi_1 \equiv 2\,[\phi_1(-\infty)-\phi_1(+\infty)] \tag{4.44}$$

It is an important expression for interpreting the oscillations of the magnetic soliton, which we will discuss in Chapter 5. From the analytical solutions (4.34), one can calculate[19]:

$$P = 4\arctan\left(\frac{\kappa v}{\sqrt{\Omega^2+v^2}-\Omega+\frac{v^2}{2}}\right) \tag{4.45}$$

This result can be written as $\sin(P/2) = \frac{v}{2}\sinh(N/2)$ or as
$\sin^2(P/4) = \frac{1}{2}\left(1+\frac{\Omega-v^2/2}{\sqrt{\Omega^2+v^2}}\right)$. A soliton of momentum $P=0$ is thus characterized by $v=0$, as expected, and $\Omega<0$ to satisfy the second equality.

Two key properties of the immobile magnetic soliton can be expressed solely as a function of the magnetization N: the depletion $n_2^{(\max)}/n_0$, which gives the maximal density of the minority component (*i.e.* at the center of the minority wavepacket) with respect to the total density n_0, and the typical inverse size of the wavepacket κ. Indeed, the magnetization expression (4.42) evaluated at $P=0$ (and thus $\Omega<0$ as justified above) gives:

$$\kappa = \tanh(N/4) \tag{4.46}$$

Furthermore, the expression (4.34) for $v=0$ and $\Omega<0$ leads to:

[17] One uses $\frac{\partial\phi}{\partial x}(+\infty) = \frac{\partial\phi}{\partial x}(-\infty) = 0$ and $\theta(+\infty) = \theta(-\infty) = 0$ for an easy-axis ferromagnet.

[18] The value of the integral: $\int_{-\infty}^{+\infty}\frac{\mathrm{d}x}{a+b\cosh x} = \frac{1}{\sqrt{a^2-b^2}}\ln\left(\frac{a+\sqrt{a^2-b^2}}{b}\right)$ if $0<b<a$ is used [201].

[19] The integral $\int_{-\infty}^{+\infty}\frac{\mathrm{d}x}{a+b\cosh x} = \frac{2}{\sqrt{b^2-a^2}}\arctan\left(\frac{\sqrt{b^2-a^2}}{a+b}\right)$ if $a^2<b^2$ is used [201].

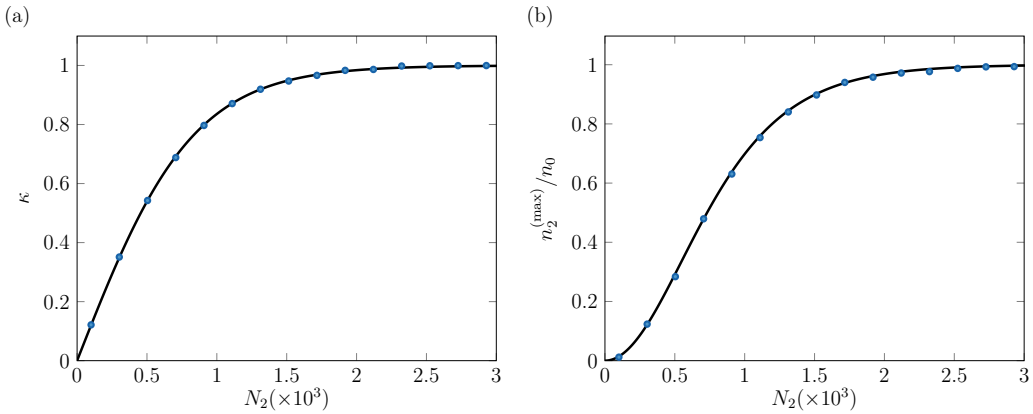

FIGURE 4.7: Stationary immobile solitons: size and depletion. From the numerical stationary solutions obtained from the coupled GPEs (see Appendix B) with $\delta g/g = 0.013$ and $n_0 = 3.3\times10^8$ atoms/m, we extract the depletion $n_2^{(\max)}/n_0$ at the center. No linear potentials are applied on the mixture for the moment. From a fit to the expected solution (4.34), as done in Figure 4.6, we calculate the typical inverse size κ of the wavepacket. We plot it as a function of the atom number in the minority component N_2. These static solutions correspond to $v = 0$ and $\Omega < 0$. In this case, the links between these two quantities and N are given by (4.46) and (4.47). We plot these two predictions with a black solid line. The numerical agreements are convincing.

$$\frac{n_2^{(\max)}}{n_0} = \sin^2\left[\frac{\theta(x)}{2}\right] = \frac{1-\cos\left[\theta(x)\right]}{2} = \kappa^2 = \tanh^2(N/4) \tag{4.47}$$

The evolution of these two quantities as a function of the atom number in the minority component N_2 (proportional to N as we saw above) is verified numerically in Figure 4.7. The agreements with the formula (4.46) and (4.47) are satisfactory, confirming once again that the magnetic spin chain formalism is adequate to treat the immiscible mixture close to the Manakov limit.

The soliton energy is another conserved quantity. Referring to the expressions of the exchange and anisotropic energies (4.17) and the parametrization (4.20), it is naturally defined as [49]:

$$E = \int_{-\infty}^{+\infty} \frac{1}{2}\left\{\left(\frac{\partial\theta}{\partial x}\right)^2 + \sin^2\theta\left[1+\left(\frac{\partial\phi}{\partial x}\right)^2\right]\right\}\mathrm{d}x \tag{4.48}$$

The expression of the stationary solution given in (4.34) leads to the simple equation: $E = 4\kappa$. In terms of the conserved quantities discussed above, one gets [43]:

$$E(N,P) = 4\tanh(N/4) + 8\frac{\sin^2(P/4)}{\sinh(N/2)} \tag{4.49}$$

The energy E thus evolves periodically with P. This expression was also given in a recent study [48], which inspired the experimental work described in Chapter 6.

The variables v and Ω, the rate of variation of the soliton position and a quantity linked to the rate of variation of its phase, are related to partial derivatives of E with respect to the conserved quantities as follows:

$$\begin{cases} \Omega = -\left(\frac{\partial E}{\partial N}\right)_P \\ v = \left(\frac{\partial E}{\partial P}\right)_N \end{cases} \tag{4.50}$$

The problem of finding the solutions of the Landau-Lifshitz equation can be reformulated using a thermodynamic approach. The variables v and $-\Omega$ can be seen as two conjugated variables associated with the thermodynamic variables P and N, respectively [49]. Minimizing the free energy state function: $E + \Omega N - vP$ over all possible values of θ and ϕ leads to the equations (4.28).

4.3 Conclusion

In this chapter, we introduced the magnetic soliton within the rich nonlinear physics of solitons that we briefly discussed. The magnetic soliton was first defined as a stationary solution of the nonlinear Landau-Lifschitz equation. General solutions for both the easy-plane and easy-axis magnetic solitons were distinguished and expressed following the work of Kosevich [43]. The link with binary Bose mixtures was established close to the Manakov limit, where the spin and density degrees of freedom separate, and the total density is consequently constant. The study then focused on immiscible mixtures, or equivalently, the easy-axis magnetic solitons.

In the stationary case, with no external perturbations, three conserved quantities were identified: the magnetization, the total momentum and the energy. A key feature of the magnetic soliton was highlighted: the total momentum is purely a phase. According to Pitaevskii [202], it gives a "non trivial" character to the magnetic soliton. Morevover, we have demonstrated the periodic dispersion relation of the magnetic soliton.

This suggests that if the momentum evolves linearly in time under the action of a constant force for example, one can obtain a sinusoidal motion, reminiscent of the Bloch oscillation phenomena seen for electrons trapped in the periodic potential created by a crystal and subjected to an electric field. This is the object of the next chapter.

Chapter 5

Magnetic solitons under a constant force

The previous chapter introduced the magnetic soliton. It was shown how it could be connected to the physics of mixtures of weakly-interacting Bose gases with nearly equal interaction parameters. We analytically computed the dispersion relation of the stationary magnetic soliton and linked the velocity of the soliton v to its total momentum P as: $v \propto \sin(P/2)$. If a constant force is applied to the wavepacket, one can expect the momentum to evolve linearly in time. For a classical system, v and P are usually proportional to each other, and the object's position follows an accelerated motion, as we are familiar with. However, in the case of a magnetic soliton, the relationship between v and P suggests that the velocity and thus the position of the soliton follow a periodic evolution over time in this case. After half a period, the wavepacket is expected to propagate in the opposite direction of the force, returning to its initial position! The object of this chapter is the analytical and numerical discussion of these oscillations referred to as *Bloch-like oscillations*, since they are reminiscent of the Bloch oscillations of electrons in the periodic potential created by a crystal when an electric field is applied. The concept of "force" applied on this system is first precised and analytically added to the model. Then the validity of the previous reasoning is discussed. Numerical simulations are used to illustrate this Bloch-like oscillation phenomenon. Finally, we will explain why this system can be considered of broadband interest and how it relates to other striking phenomena observed in physics.

5.1 Application of a constant force on the magnetic soliton

The study aims to investigate the dynamics of an easy-axis magnetic soliton under a constant force. In the 1D ferromagnetic spin chain, any non-homogeneous external magnetic field, not accounted for in the equations for the moment, can result in a small magnetic gradient felt by the spins. This small magnetic gradient acts as a force on the spin chain. The focus of this thesis is on the case of a constant force, or constant magnetic gradient (*i.e.* a linear potential). In the immiscible mixture platform, this translates into a *differential* force acting on the two components rather than a common force, as we will demonstrate.

5.1.1 Modification of the coupled nonlinear equations

First, let us examine the modifications of the equations of motion in the presence of a force acting on one of the two components. It is assumed that this force acts only on the minority component, which is localized in space, and is referred to as

component 2. More precisely, we add the term $V_2(x)\,\psi_2$ to the left side of the second equation of (4.35). We also introduce $\omega_0(x)$, the adimensionalized version of the potential V_2: $\omega_0(x) = V_2(x)/\left(\frac{\hbar^2}{2m\xi_s^2}\right)$. It can be shown that the equations (4.40) are then modified in the following way:

$$\begin{cases} \frac{\partial\theta}{\partial t} = -\left[\sin\theta\left(\frac{\partial^2\phi}{\partial x^2}\right) + 2\cos\theta\frac{\partial\theta}{\partial x}\frac{\partial\phi}{\partial x}\right] \\ \frac{\partial\phi}{\partial t} = -\cos\theta\left(\pm 1 + \left(\frac{\partial\phi}{\partial x}\right)^2\right) + \frac{1}{\sin\theta}\frac{\partial^2\theta}{\partial x^2} - \omega_0(x) \end{cases} \tag{5.1}$$

The first equation is unchanged and the second equation has an additional term $-\omega_0(x)$. Regarding the study of the easy-axis ferromagnet, the equations (5.1) can be written in a "LLE adimensionalized form" as:

$$\frac{\partial\mathbf{M}}{\partial t} = -\mathbf{M}\times\mathbf{H}\ \text{, with}\ \mathbf{H} = \left(\frac{\partial^2\mathbf{M}}{\partial x^2} + [M_z - \omega_0(x)]\,\mathbf{u_z}\right) \tag{5.2}$$

In addition to the effective magnetic field created by the neighboring spins (see (4.18)): $\mathbf{H}_{\text{eff}} = \frac{\partial^2\mathbf{M}}{\partial x^2} + M_z\mathbf{u_z}$, an external magnetic field directed along the anisotropy axis $\mathbf{u_z}$: $\mathbf{H}_{\text{ext}} = -\omega_0(x)\mathbf{u_z}$ enters the equation. Thus, the addition of the term $-\omega_0(x)$ in the second equation of (5.1), *i.e.* the application of a potential $\omega_0(x)$ on the minority component but not on the majority component, accounts for the presence of an external magnetic field applied to the spin chain, as intended.

If ω_0 is spatially constant (constant external magnetic field), it can be reabsorbed in the definition of the angular frequency Ω and the problem remains analytically solvable with the solutions (4.34). If ω_0 depends on x, then in general it is not possible to find analytic solutions. However, in the next subsection, it will be shown that, under certain assumptions, the equation of motion of the magnetic soliton can be derived when a weak constant force, *i.e.* a weak constant magnetic gradient, is considered.

5.1.2 Soliton oscillation

Under the action of a constant force, the equations of motion are modified and written as (5.1). Therefore, it is necessary to re-evaluate the conservation of the quantities, previously defined in sectoin 4.2.5.

Regarding the magnetization, since its knowledge only refers to θ, whose equation of motion is unchanged (5.1), N is still conserved during the motion. However, P is no longer conserved. Let us consider the case of a constant force (or constant magnetic gradient) f. We write $\omega_0(x) = -Fx$ where F is the adimensionalized force: $F = f/\left(\frac{\hbar^2}{2m\xi_s^3}\right)$. From the definition of the momentum (4.43) and the equations (5.1), the evolution of the momentum can be derived. We obtain:

$$\frac{\mathrm{d}P}{\mathrm{d}t} = -\int_{-\infty}^{+\infty}(1-\cos\theta)\frac{\partial\omega_0}{\partial x}\,\mathrm{d}x = NF \tag{5.3}$$

The conservation of P is thus no longer applicable. Instead, considering the soliton as a macro-object, it follows an intuitive equation that could have been written within Newton's formalism[1]. From this formula, it can be deduced that P evolves linearly over time:

[1]For the bright or dark solitons submitted to a constant force, the term analogous to the magnetization which appears in front of the single-particle force is the atom number in the wavepacket (see Appendix E).

$$P(t) = P(0) + NFt \tag{5.4}$$

This equation was originally derived by Kosevich et al. in 1998 [49].

Another important modified quantity to consider is the total energy of the soliton. The addition of the term $\int V_2(x)\, n_2(x)\, \mathrm{d}x$ in the GP energy leads to the following modification for the energy of the magnetic soliton:

$$E_{\omega_0} = \int_{-\infty}^{+\infty} \frac{1}{2} \left\{ \left(\frac{\partial \theta}{\partial x} \right)^2 + \sin^2 \theta \left[1 + \left(\frac{\partial \phi}{\partial x} \right)^2 \right] \right\} + \int_{-\infty}^{+\infty} \omega_0(x)\, (1 - \cos\theta)\, \mathrm{d}x \tag{5.5}$$

The first term remains unchanged compared to (4.48). However, it is important to note that the expressions of θ and ϕ have been altered by the presence of the force. In general, it is not possible to express the energy analytically in terms of N and P as we did in (4.49). However, if the force is sufficiently weak (to be precised later), its presence can be seen as a small perturbation of the magnetic soliton in the absence of the force. It is called the *adiabatic approximation* [49]. Then, the state of the moving wavepacket under the force remains a magnetic soliton characterized by θ and ϕ which follow the same equations as in the absence of a force (4.34). But now, the angles θ and ϕ depend on the center of mass of the soliton $X(t)$ as $\theta = \theta\,[x - X(t)]$ and $\phi = \phi_0(t) + \tilde{\phi}\,[x - X(t)]$. The parameters $v = \frac{\mathrm{d}X}{\mathrm{d}t}$ and $\Omega = \frac{\mathrm{d}\phi_0}{\mathrm{d}t}$, linked to the soliton's shape, now vary with time. In other terms, the adiabatic approximation states that the moving wavepacket can be described at any time as a solitonic wavepacket whose form now evolves with time due to the force. Since in this case the functions of θ and ϕ at any time are the same as without the force, the soliton energy can be written as [49]:

$$E_{\omega_0}(N, P, \omega_0) = E(N, P) + \int_{-\infty}^{+\infty} \omega_0(x)\, (1 - \cos\theta)\, \mathrm{d}x \tag{5.6}$$

with $E(N, P)$ the function of N and P given by (4.49). However, P must be taken as a function linear in time (5.4).

The second integral takes non zero values over the extension size of the soliton located at $X(t)$. In the adiabatic approximation, the force is so weak such that the variation of $\omega_0(x) = -Fx$ over the size of the soliton can be neglected *i.e.* $\int_{-\infty}^{+\infty} \omega_0(x)\, (1 - \cos\theta)\, \mathrm{d}x \simeq \omega_0\,[X(t)] \times \int_{-\infty}^{+\infty} (1 - \cos\theta)\, \mathrm{d}x = \omega_0\,[X(t)]\, N = -NFX(t)$. Therefore, the energy expression for the magnetic soliton subjected to a constant force within the adiabatic approximation is:

$$E_{\omega_0}(N, P, \omega_0) \simeq 4 \tanh(N/4) + 8 \frac{\sin^2(P(t)/4)}{\sinh(N/2)} - NFX(t) \tag{5.7}$$

with $P(t) = P(0) + FNt$. In the adiabatic approximation, since the additional term in the energy expression $-NFX$ does not depend explicitly on the momentum P, v is still a periodic function of the momentum: $v(t) = \left(\frac{\partial E}{\partial P}\right)_N = \frac{2}{\sinh(N/2)} \sin(P(t)/2)$ and its integration over the spatial coordinate gives the center of mass evolution:

$$X(t) = X(0) + 4\, \frac{\cos\left[P(0)/2\right] - \cos\left[\frac{1}{2}(P(0) + FNt)\right]}{FN \sinh(N/2)} \tag{5.8}$$

This result was first derived in 1998 by Kosevich et al. [49]. Recently, in the context of quantum gases mixtures, the oscillation has been studied numerically in

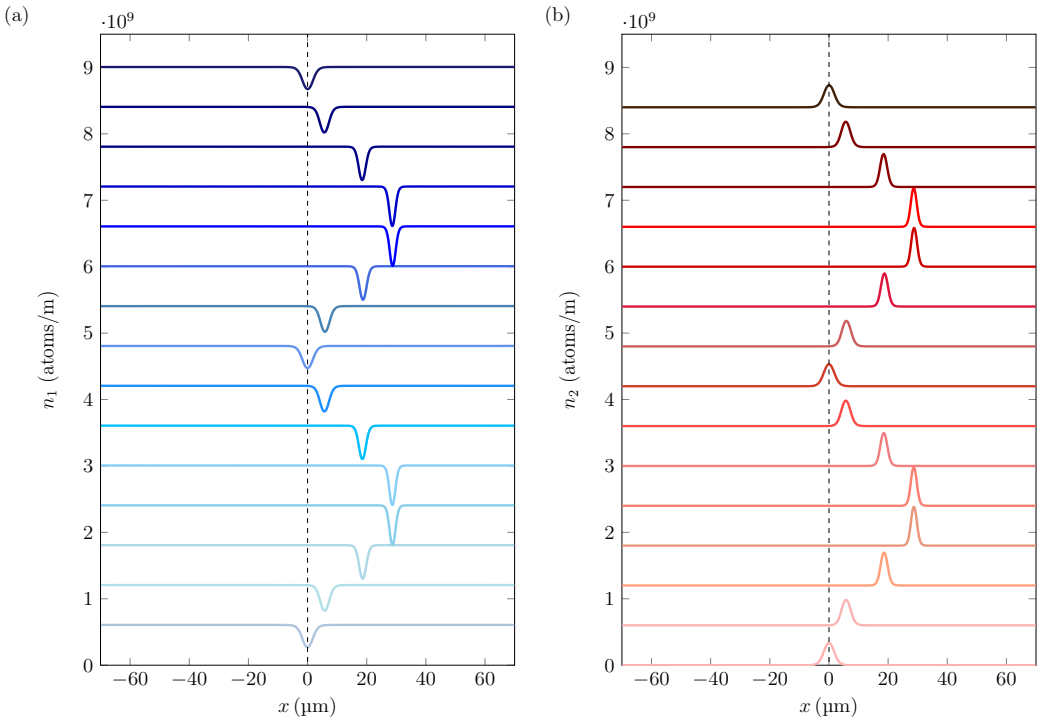

FIGURE 5.1: Numerical simulation of the magnetic soliton oscillation. We solve numerically with imaginary time evolution the coupled GPEs with $\delta g/g = 0.013$, $N_2 = 1500$, $n_0 = 6 \times 10^8$ atoms/m to find the ground state of the system. We then abruptly apply a constant force directed along $+x$ and corresponding to a magnetic gradient $b' = 1\,\mathrm{G/m}$ only to the minority component. We record the evolution of the density profiles in a real time evolution simulation (the phase profiles, which are also of interest, are discussed in section 5.2.2) for the majority component in blue (a) and the minority component in red (b). We plot the profiles every $t_0 = 81.4\,\mathrm{ms}$. The time grows from bottom to top and the darker the color the longer the time. The i-th profile is shifted by $i \times n_0$ for more clarity. The profiles at $t \simeq 3\,t_0$ and $t \simeq 10\,t_0$ are completely depleted while the profiles at $t \simeq 7\,t_0$ and $t \simeq 14\,t_0$ are strongly similar to the initial profile.

the particular case of $g_{12} = \frac{1}{2}(g_{11} + g_{22})$ in [46] and in the general case by Bresolin et al. [48]. In the following, we will describe numerical simulations of the coupled GPEs which reproduce their results with a focus on the $|1, -1\rangle/|1, +1\rangle$ immiscible mixture of Rubidium atoms.

To continue this subsection, we will precise the adiabaticity criterion to clarify the statement of "low force" or weak magnetic gradient. We evaluate the work of the constant force over the soliton size which is typically given by ξ_s: $W = f \times \xi_s$. According to a "basic" adiabatic criterion, this work must be significantly smaller than the other relevant energy scales in the problem. In particular, it should be much smaller than the spin interaction energy $\delta g\, n_0$. Expressed in terms of the adimensionalized force, this condition translates into [48]:

$$f\xi_s \ll \delta g\, n_0 \Longleftrightarrow F \ll 1 \tag{5.9}$$

When this condition is fulfilled, the wavepacket remains a soliton during its motion *i.e.* the variables θ and ϕ are still given by the stationary formula but v and Ω (*i.e.* the shape of the magnetic soliton) change with time. More precisely, let us imagine

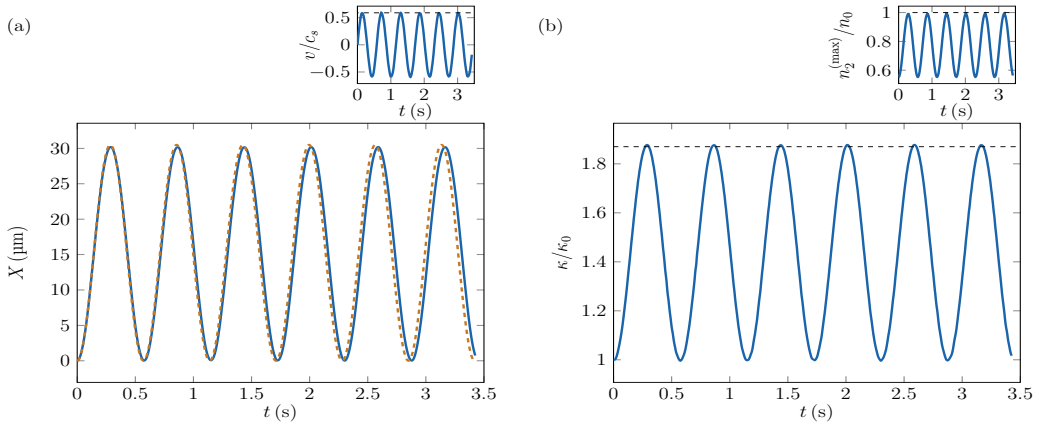

FIGURE 5.2: Numerical evolution of the magnetic soliton characteristics over time under the action of a constant force. The physical parameters are the same as in Figure 5.1: $\delta g/g = 0.013$, $N_2 = 1500$, $n_0 = 6 \times 10^8$ atoms/m and $b' = 1\,\mathrm{G/m}$. (a): Center of mass evolution $X(t)$ and its velocity $v = \frac{\mathrm{d}X}{\mathrm{d}t}$, normalized by the spin sound velocity $c_s = \sqrt{n_0 \delta g/(2m)}$ in inset. The orange dashed line is the analytical prediction (5.8). The black horizontal dashed line in the inset is the predicted maximum velocity: $v = \frac{2}{\sinh(N/2)}$ obtained by taking $P = \pi$ in (4.45). (b): Evolution of κ, the typical inverse size of the soliton, and the depletion of the bath $n_2^{(\max)}/n_0$ with time. The black dashed lines are the predicted maximum values at the turning point: $\kappa = 1/\tanh(N/4)$ and a full depletion: $n_2^{(\max)}/n_0 = 1$. The evolution all follow a sinusoidal pattern and are in agreement with the analytical predictions.

that one starts with a stationary magnetic soliton at rest *i.e.* $v = 0$ and $\Omega < 0$ (point (a) in Figure 5.3). After applying a force $F > 0$, the soliton will begin to move on the ellipsis of constant magnetization N (as N was shown to remain constant) in the same direction as the force (since $v \propto \sin(P/2) > 0$). Once the ellipsis crosses $P = \pi$ (point (b) in Figure 5.3), the velocity of the soliton decreases and reaches $P = 2\pi$, where $v = 0$ (point (c) in Figure 5.3). The soliton then turns around ($v < 0$) and returns to its starting point.

The evolution of the depletion and size of the wavepacket of the minority component can also be deduced from the ellipsis of constant magnetization plotted in Figure 5.3. Indeed, the magnetization (4.42) can also be written as $\sinh(N/2) = \frac{2\kappa}{\sqrt{\Omega^2+v^2}}$. Therefore, the initial κ, which is the typical inverse size of the soliton, is $\kappa_0 = -\Omega_0/2 \sinh(N/2)$, with $\Omega_0 < 0$ being the initial value of Ω. After a time t its value is $\kappa = \frac{1}{2}\sinh(N/2)\sqrt{\Omega^2 + v^2}$. The ratio of the two gives: $\frac{\kappa}{\kappa_0} = \sqrt{\left(\frac{\Omega}{\Omega_0}\right)^2 + \left(\frac{v}{\Omega_0}\right)^2}$. The equation $1 = \sqrt{\left(\frac{\Omega}{\Omega_0}\right)^2 + \left(\frac{v}{\Omega_0}\right)^2}$ defines a circle with radius Ω_0 centered at (0,0) in the plane (v, Ω). Since in Figure 5.3 this circle is always contained in the ellipsis, we conclude that κ is always larger than its initial value during the evolution at constant magnetization. The maximum is reached when $P = 2\pi$ (point (c))[2]. Therefore,

[2] Actually, the extremal values of κ can be computed from the expression of the magnetization (4.42). Calling $\kappa_0 = \tanh(N/4)$ (see (4.46)) and $\kappa_1 > \kappa_0$ the points of $v = 0$, we have:

$$\kappa_1 = \kappa_0 \frac{1}{\tanh^2(N/4)} = \frac{1}{\tanh(N/4)} \tag{5.10}$$

These values are given in [49] and we verify these results in Figures 4.7(a) and 5.2(b).

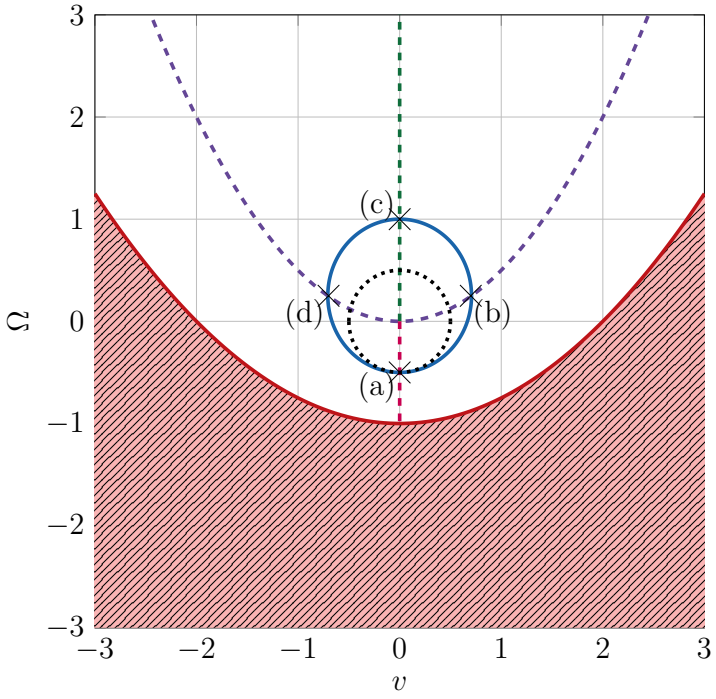

FIGURE 5.3: Map (v, Ω) for the easy-axis soliton submitted to a linear potential. We recall that no stationary solutions exist for $\Omega < (v^2/4-1)$ (4.32). The forbidden zone is represented with red hatches. The blue solid line still represents the points corresponding to a magnetization $N = 3$ which is a typical number realized in the experiment described in Chapter 6. We also plot a few curves of $P = \text{const.}$ following $\sin^2(P/4) = \frac{1}{2}\left(1 + \frac{\Omega - v^2/2}{\sqrt{\Omega^2+v^2}}\right)$: $P = 0$ in dashed pink, $P = \pm\pi$ in dashed violet and $P = \pm 2\pi$ in dashed green lines. We also labelled characteristic points of a trajectory at fixed N. For $F > 0$, the ellipsis is followed in a counter-clockwise direction. (a): starting point at $P = 0$ $(0, \Omega_0)$; (b): $P = \pi$, the velocity starts to decrease; (c): $P = 2\pi$, the velocity is zero, the soliton turns back; (d): $P = 3\pi$ (or $-\pi$ if we take its value modulo 4π). The black dotted line is a circle of radius Ω_0 centered on $(0, 0)$.

the typical size of the wavepacket diminishes when the soliton propagates in the same direction than the force.

In order to maintain a constant magnetization, and thus a constant number of atoms in the minority component N_2, we expect the depletion to increase as the soliton shrinks and vice versa as the soliton turns back. Its initial value is determined by N as $n_2^{(\max)}/n_0 = \tanh^2(N/4)$ (see Figure 4.7) and its maximal value is 1 (for example obtained after half a period for $v = 0$ and $\Omega > 0$ in (4.34)).

We check these evolutions in Figure 5.2 for a low force, which allows us to perform an adiabatic approximation, and interaction parameters that satisfy the condition $\delta g \ll g$.

We obtain the adimensionalized predicted values of the period and amplitude[3] of the motion from the equations (5.4) and (5.8):

$$\begin{cases} T = \frac{4\pi}{NF} \\ \mathcal{A} = \frac{4}{NF\sinh(N/2)} \end{cases} \tag{5.11}$$

[3]We will always call "amplitude" half of the peak-to-peak amplitude.

Putting back the dimensional units (τ_s and ξ_s for T and $\mathcal{A}$, respectively), the period and amplitude are:

$$\begin{cases} T = \frac{2\pi\hbar n_0}{N_2 f} \\ \mathcal{A} = \frac{2n_0^2\,\delta g\,\xi_s}{N_2 f \sinh\left(\frac{N_2}{n_0\xi_s}\right)} \end{cases} \tag{5.12}$$

In the context of BEC mixtures, these equations can be found in [48]. The period expression is remarkably simple and does not depend on the mixture being considered. The observed phenomenon and periodic relation are reminiscent of Bloch oscillations in a lattice, which explains the analogous formula of a period inversely proportional to the force. This similarity will be further discussed in section 5.2.1. The amplitude expression is less universal and less simple, since it depends non-linearly on the physical parameters.

5.1.3 Deviation from adiabaticity

The previous discussions assume the validity of the adiabaticity criterion (5.9). However, what happens when this criterion is not fulfilled? To answer this question, we conduct GP simulations using a wide range of parameters. We vary n_0, f and N_2 keeping fixed the choice of the mixture $\delta g/g = 0.013$. At first, two observables were used to assess the deviation from adiabaticity: the "distance to prediction", which quantifies how far the center of mass evolution deviates from the prediction (5.8), and the scalar product between the minority wavefunction after two periods of oscillations and the initial minority wavefunction. But only the latter was retained as it was more robust and does not depend on the amplitude of the oscillation. We limit the range of parameters to maintain accessible experimental values for the amplitude and period of the oscillation.

If the adiabaticity criterion is not well verified, we observe the emission of another wavepacket after an odd number of turns, when the soliton moves in the same direction as the force before the turning point and in the opposite direction afterwards. We call this phenomenon the *fragmentation* of the soliton. The wavepacket does not maintain its solitonic shape as it moves. Kosevich also referred to these emitted waves as "a small-amplitude spin wave whose frequency corresponds to the frequency of magnetization precession in the soliton" [49]. An example is shown in Figure 5.4(a).

In Figure 5.4, we also plot the value of the squared scalar product of the minority wavefunction at time $t = 0$ and time $t = 2T$. Typically, we consider that the wavepacket oscillates properly, retaining its solitonic shape, when $|\langle\psi_2(0)|\psi_2(2T)\rangle|^2 \gtrsim 0.9$. We verify that the adimensionalized force must indeed be sufficiently small: $F \lesssim 0.3$ to guarantee $|\langle\psi_2(0)|\psi_2(2T)\rangle|^2 \gtrsim 0.9$.

Moreover, it seems that the criterion on F is not sufficient to obtain scalar products close to unity. Indeed, for $F \ll 1$, but $N \lesssim 1$, the soliton also fragments. Although obtaining this regime experimentally can be complicated due to the large amplitude and period of oscillation (see Figure 6.3), we have introduced a second criterion to obtain a proper oscillation. It involves maintaining a sufficiently low maximum velocity for the soliton. Typically, we say that the wavepacket retains its solitonic shape if its maximum velocity (obtained when $P = \pi$ in (4.45)) is less than the spin sound velocity c_s. If this is not the case, the soliton will fragment by emitting a small amplitude sound wave. In the plane (N, F) it translates to a criterion on N:

$$v_{\max}/c_s = \frac{2}{\sinh(N/2)} \lesssim 1 \iff N \gtrsim 2.6 \tag{5.13}$$

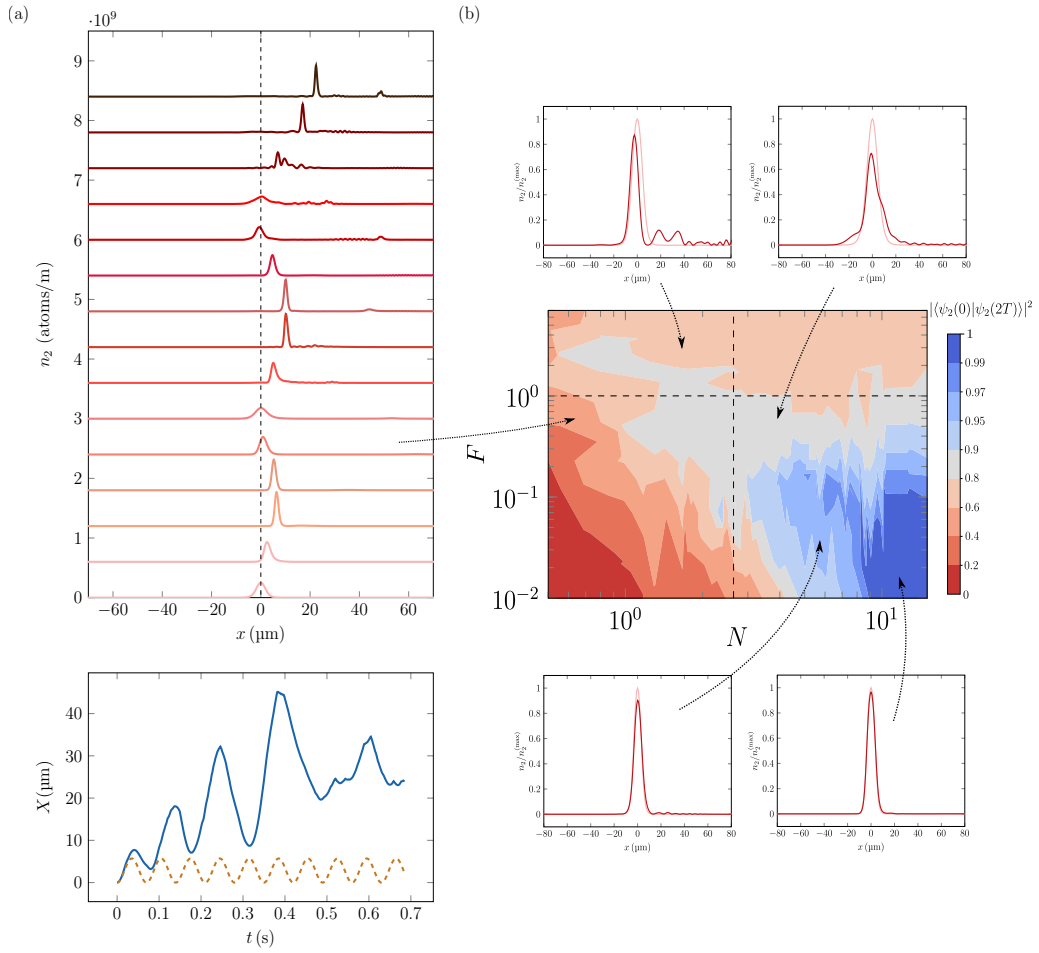

FIGURE 5.4: Numerical study of the deviation from adiabaticity. We examine the survival of the oscillation phenomenon when changing $N = \frac{2N_2}{n_0\xi_s}$ and $F = \frac{f\xi_s}{n_0\delta g}$. (a): We show an example of the profile evolution of the minority component every $t_i = i\frac{T}{5}$, where T is the expected period (upper plot), for $n_0 = 10^8$ atoms/m, $b' = 2\,\mathrm{G/m}$ and $N_2 = 100$, corresponding to $F \simeq 0.4$ and $N \simeq 0.7$. The shape of the soliton is approximately conserved during the first period of oscillation but it deteriorates afterwards: a small amplitude wave is emitted at the turning point position (when the amplitude is maximum) and the wavepacket gets fragmented. This wave bounces off the wall and the oscillation is then blurred. On the bottom graph, we show the center of mass evolution in blue and the analytical prediction assuming an adiabatic evolution with a dashed orange line. (b): For each chosen parameter set, we measure $|\langle\psi_2(0)|\psi_2(2T)\rangle|^2$ the scalar product between the wavefunction of the minority component at $t = 0$ and at $t = 2T$, where T is still the analytical prediction of the period. We show examples of density profiles at $t = 0$ (light red) and $t = 2T$ (dark red) at different positions in the 2D diagram. The vertical dashed line represents the line where the maximum velocity of the magnetic soliton is equal to the spin sound velocity *i.e.* $v_{\max} = \frac{2}{\sinh(N/2)} = 1$. The horizontal line separates the regions $F < 1$ and $F > 1$. Note that the chosen scale of the color map is highly nonlinear in order to better assess the adiabaticity for scalar products near unity.

The agreement between the simulations and the criteria on the chosen figure of merit is only qualitative. However, they strongly suggest that the fragmentation phenomenon can be avoided by aiming for high N and low F.

The experimental requirements to keep in mind for Chapter 6 are thus a small force, a large N_2 and a large n_0[4].

To conclude this section, it is important to note that the oscillation phenomenon is nontrivial and is related to the periodic dispersion relation of the magnetic soliton, a peculiarity of this soliton with respect to the dark or bright solitons for instance. Additionally, the adiabatic assumption is crucial in maintaining the solitonic shape during the motion and achieving sinusoidal oscillation. In the case of the dark-bright soliton of $\delta g = 0$, adiabatic motion is not possible even if its dispersion relation is periodic (see Appendix E). This is because the soliton shape cannot be maintained at the turning point. In Appendix E, we provide numerical simulations of bright, dark, and dark-bright solitons subjected to a constant force to highlight the differences with the easy-axis magnetic soliton studied earlier. Regarding miscible mixtures or easy-plane magnetic solitons close to the Manakov limit, where the mapping between the two systems is applicable, the dispersion relation is also periodic. However, solitons are often unstable under the presence of a constant force and may fragment. For further details, we refer to Bresolin et al.'s study [48].

In the following, we will discuss two complementary interpretations of the observed oscillations. The first interpretation relies on the evolution of the phase of the majority component, which we have not yet discussed. The second interpretation is the link with Bloch oscillations.

5.2 Interpretations of the observed oscillations

The physics discussed above is rich and connected to quantum phenomena in various fields. The discussion begins with the phenomenon of Bloch oscillations.

5.2.1 Bloch oscillations and 1D dynamics

The Bloch oscillations were first predicted in the condensed matter context by Zener in 1934 [50]. He showed that electrons in a crystal submitted to a constant force (induced by an electric field) exhibit a periodic motion. A modern derivation uses the Bloch theorem and can be found for example in [203]. Let us consider the 1D case of a periodic potential $V(x)$ of period a. Félix Bloch, in a 1929 paper [204], expressed the eigenstates of the Hamiltonian of the problem $\hat{H} = \frac{\hat{p}^2}{2m} + V(\hat{x})$ as a product of a plane wave and a periodic function on the considered lattice.

More precisely, the sites of the lattice are given by $a_m = ma$, $m \in \mathbb{Z}$. We introduce the reciprocal lattice associated to the latter one: $b_m = \frac{2\pi}{a}m$, $m \in \mathbb{Z}$. Since the translational operator $\hat{T}_a = \mathrm{e}^{-\mathrm{i}a\hat{p}/\hbar}$ commutes with the Hamiltonian due to the spatial periodicity of V, we can search a common basis of eigenfunctions. The complex eigenvalues of $\hat{T}_a$ are expressed as $\mathrm{e}^{-\mathrm{i}\theta}$, $\theta \in \mathbb{R}$, due to the unitary nature of the operator. The associated eigenfunction is commonly called $\psi_q(x)$ with $q = \theta/a$.

The Bloch's theorem states that for each eigenstate of the problem, denoted by the real number q, one can find a periodic function $u_q(x)$ such that the wavefunction $\psi_q(x)$ can be written as:

$$\psi_q(x) = \mathrm{e}^{\mathrm{i}xq}u_q(x), \quad \text{with } u_q(x-a) = u_q(x) \tag{5.14}$$

Actually, the angle θ is defined modulo 2π and one does not expect the physics to change by this arbitrary choice. In the reciprocal domain, one thus imposes

[4]Indeed, $N \sim \frac{1}{\sqrt{n_0}}$ and $F \sim \frac{1}{{n_0}^{3/2}}$, so it is more favorable to have a larger density even if N is slightly smaller.

$\psi_{q+b_m}(x) = \psi_q(x)$ for any reciprocal vectors b_m. We can thus restrict the variation zone of the quasi-momentum to $]-\pi/a, \pi/a]$, usually called the *first Brillouin zone*.

For a given value of q, there are several solutions to the eigenvalue problem: $\hat{H}\psi_q(x) = E(q)\psi_q(x)$ and thus we denote the different solutions by an integer n, called the *band index*, as $\psi_{n,q}(x)$ of eigenvalue $E_n(q)$. Not only the eigenfunctions $\psi_{n,q}(x)$ are invariant with respect to the variation $q \to q + \frac{2\pi}{a}$, but also the eigenvalues $E_n(q)$, which are thus periodic with respect to the quasi-momentum:

$$E_n\left(q + \frac{2\pi}{a}\right) = E_n(q) \tag{5.15}$$

This is the first requirement for obtaining Bloch oscillations in the presence of a constant force. Under the application of this force, the Hamiltonian expression is modified: $\hat{H}_F = \frac{\hat{p}^2}{2m} + V(\hat{x}) - F\hat{x}$. We can recover the spatial periodicity of the Hamiltonian by applying the unitary transform $\hat{U} = \exp(-\mathrm{i}\hat{x}Q(t))$ to $\hat{H}_F$, with $Q(t) = \frac{1}{\hbar}\int \mathrm{d}t\, F = \frac{1}{\hbar}Ft$ for a constant force. The Hamiltonian is then expressed as $\hat{H}_1 = \frac{(\hat{p}+\hbar Q(t))^2}{2m} + V(\hat{x})$.

If we know the eigenfunction of $\hat{H}_1$, ψ_1, we can obtain the expression of the eigenfunction ψ_F of $\hat{H}_F$ with: $\psi_F = \hat{U}^\dagger\psi_1$. We take $\psi_1(x, t = 0)$ as a Bloch wave of quasi-momentum q_0: $\psi_1(x, t = 0) = \mathrm{e}^{\mathrm{i}q_0x}u(x)$. Since the evolution operator of the spatially periodic Hamiltonian $\hat{H}_1$ also commutes with the translation operator $\hat{T}_a = \mathrm{e}^{-\mathrm{i}a\hat{p}/\hbar}$, the Bloch form is preserved with a constant quasi-momentum q_0. We have $\psi_1(x, t) = \mathrm{e}^{\mathrm{i}q_0x}u(x, t)$. Therefore, we can write the eigenfunctions of $\hat{H}_F$ as $\psi_F(x, t) = \mathrm{e}^{\mathrm{i}q_0x} \times \mathrm{e}^{\mathrm{i}Q(t)x}u(x, t)$. In other words, the Bloch form is preserved during the application of the force, because u enters the equation, but its quasi-momentum varies linearly with time:

$$q(t) = q_0 + \frac{1}{\hbar}Ft \tag{5.16}$$

For the moment, we have not specified the form of u. We now choose the initial state (in the presence of the force) to be a Bloch function of the Hamiltonian corresponding to no force $\hat{H}_{F=0}$: $u(x, 0) = u_{n,q_0}(x)$ (up to a phase). The last ingredient to obtain Bloch oscillations is the adiabatic approximation. We assume that at any time of the evolution, $u(x, t)$ will be proportional to the Bloch function $u_{n,q(t)}(x)$ with the quasi-momentum $q(t)$. In other words, the state in the presence of the force ψ_F is written as:

$$\psi_F(x, t) \propto \mathrm{e}^{\mathrm{i}xq(t)}u_{n,q(t)}(x) \tag{5.17}$$

Therefore, we assume that energy bands other than the initial band denoted by n are not populated. This statement is equivalent to the one in the previous section regarding the preservation of the soliton wavepacket when a force is applied. The Bloch function u of the band n plays the role of the angles θ and ϕ of the magnetic soliton and the quasi-momentum q is reminiscent of the total momentum P.

A natural time scale in the problem is the time τ_B it takes the electron to cross a Brillouin zone of length $2\pi/a$ at a constant velocity determined by (5.16). It writes $\tau_B = \frac{2\pi\hbar}{aF}$. Since $\psi_{q+2\pi/a}(x) = \psi_q(x)$ (up to a phase) and $q(t + \tau_b) = q(t) + 2\pi/a$, the wavefunction ψ_F is periodic in time (up to a phase[5]) with a period τ_B.

[5]The geometric phase accumulated during an oscillation is called the Zak phase [205] and plays an important role in systems of non trivial topology.

The first realizations of Bloch oscillations in cold atom platforms were made in 1996 and 1997 in the groups of Christophe Salomon in Paris and Mark Raizen in Austin [131, 206] with a force generated by an accelerated optical lattice. Since then, the Bloch oscillations have become an important tool for various applications, from metrology to the study of collective phenomena. When the force is the gravity itself, the precise measurement of the oscillation period provides direct access to the gravity acceleration g. For example, in Syrte [207], sensitivities up to $\sim 10^{-4}\,g$ in 1 s have been achieved in trapped interferometers. The measurement of weak forces, such as the Casimir-Polder force, is an application of the Bloch oscillation phenomenon. Proposals have been made in this direction [208].

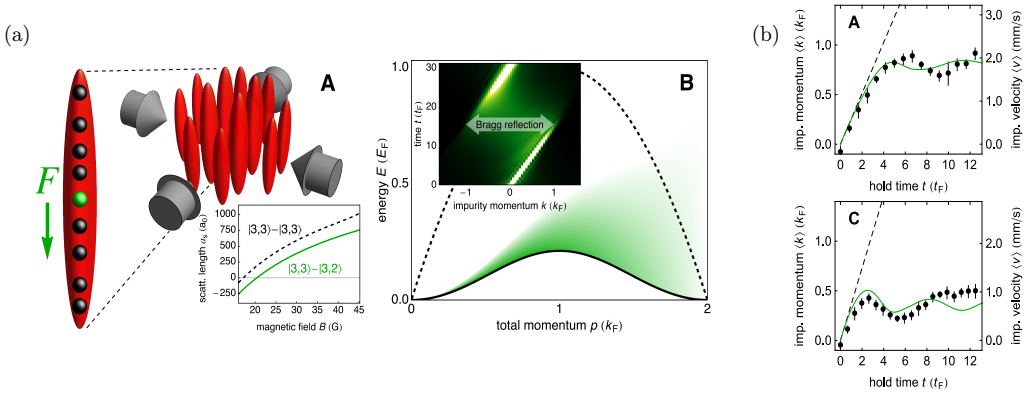

FIGURE 5.5: Example of Bloch oscillations observed in the absence of a lattice. Figures extracted from [54]. (a): Experimental realization of 1D Bose gases of Cesium atoms with a 2D optical lattice. An impurity in the state $|3,3\rangle$ (green dot) is created with a radio-frequency pulse while the bath is in the hyperfine state $|3,2\rangle$ (A). The dispersion relation of an impurity in a 1D Bose gas is periodic. In B, the black solid line is the lower bound of the excitation spectrum of the system bath + impurity, while the dashed line represents the lower bound of the excitation spectrum in the 1D gas without the impurity. The periodicity may result in Bloch oscillations when the impurity is exposed to a constant force, which can be interpreted as Bragg reflections at the edges of the Brillouin zone[6]. The inset of B shows a numerical example of motion under a weak force and large γ ($\gamma = \infty$ for the background gas interactions and $\gamma = 12$ for the impurity-bath interactions). However, in the presence of a finite force, the continuum spectrum is populated and the Brillouin zone crossing is not completely adiabatic (shaded green area). (b): Evolution of the mean impurity momentum (or mean velocity) as a function of time for $\gamma \sim 5$ in A and $\gamma \sim 20$ in C. The dashed lines indicate the free falling impurity case and the green solid line are numerical simulations using the Matrix Product States technique. There is a clear deviation from the free falling case and the results are well captured by the simulations.

The previous discussion outlined the requirements for observing Bloch oscillations: a periodic dispersion relation, linear quasi-momentum evolution, and the ability to adiabatically follow the lowest branch of the dispersion curve. These requirements are naturally met in crystals, where the breaking of translational invariance is accompanied by periodicity in the dispersion relation. However, this periodicity occurs in other systems, in particular *1D quantum liquids* of background density n_∞. These 1D systems, in the case of spinless bosonic gases, are described by the Lieb-Liniger

[6] It is an effective Brillouin zone since there is no underlying lattice in the longitudinal direction. The Brillouin zone extends from $-k_F$ to k_F where $k_F = \pi n_\infty$ and n_∞ is the 1D density.

Hamiltonian [158] and a general solution can be found with a Bethe Ansatz. The Lieb-Liniger parameter, γ, introduced in section 4.1.1, quantifies the strength of the interactions in the 1D gas. For very large γ, the 1D hardcore bosonic gas can be *fermionalized*, *i.e.* mapped onto a non-interacting fermionic system [209]. The gas then realizes a model of a *Luttinger liquid*, which generalizes the notion of Fermi liquid to the 1D case [52]. Its first experimental evidence in the ultracold atom plaform was provided by Kinoshita et al. [210]. Thus, 1D confinement dramatically changes the physics due to the strong correlations that occur in such systems. A moving impurity in such a gas has specific dynamics. It tends to deplete the host fluid, called the bath, as a consequence of the repulsive 1D interactions. The elementary excitations of the fluid at low momenta are called *polarons* [211]. The excitation spectrum becomes more complicated at large momenta or large impurity/bath interactions, giving rise to a new quasiparticle called *depleton* in [51]. The dispersion relation of these quasiparticles is determined by that of the collective excitations of the 1D Bose gas, which is periodic. The argument, valid in the thermodynamic limit for a uniform gas with periodic boundary conditions, states that in a ring of perimeter L with $N = n_\infty L$ atoms, the energy cost of a momentum increase of $2\pi\hbar/L$ for each particle is equal to $N \times (2\pi/L)^2\hbar^2/2m$ and tends to zero in the thermodynamic limit[7]. This is not the case for the total momentum which is increased by $N \times 2\pi\hbar/L$ and thus remains finite in the thermodynamic limit [51]. Thus, this simple argument leads to a periodic dispersion relation for the energy of period $2\pi\hbar n_\infty$. Although the interactions between particles were not considered in the previous reasoning, the final result of the periodic dispersion relation for the collective excitations of the gapless system remains valid in the limit where the bath can be treated as a Luttinger liquid [52]. Thus, applying a force to the impurity may lead to the appearance of Bloch oscillations in the 1D strongly-interacting Bose gas. The discussion of observing these oscillations is presented in [53, 51].

In 2017, Meinert et al. managed to see Bloch oscillations without an underlying lattice structure [54] (see Figure 5.5). Their system was a 1D Bose gas of Cesium atoms in a given hyperfine state in which they transfer an impurity consisting of a Cs atom in another hyperfine state. Their typical Tonks-Girardeau parameters for both impurity-bath and bath-bath interactions are $\gamma \sim 10$. The magnetic gradient was tuned so that only the impurity was sensitive to gravity (*differential force* for the system bath + impurity). After an adjustable time in the 1D trap, a time of flight was performed, and the momentum distribution of the gas was reconstructed. The results showed oscillations of this quantity as a function of time. The authors quantified the finite dissipated energy resulting from the imperfect adiabatic following of the lower sinusoidal branch of the dispersion curve. Additionally, their measurement of the Bloch period is in good agreement with the prediction $t_B = \frac{2\pi\hbar n_\infty}{F}$.

There are similarities between this experiment and the magnetic soliton under consideration, but there are also several differences. Firstly, our immiscible mixture is well described by mean-field theory, whereas the Hamiltonian of the 1D strongly-interacting Bose gas is the full Lieb-Liniger Hamiltonian. Secondly, unlike the single-particle impurity behavior described in [54], the magnetic soliton undergoing the Bloch oscillations is a macro-object with a potentially large value of the atom number in the minority component (or magnetization in the spin chain language). Finally, achieving an adiabatic motion appears to be less challenging in our system compared to the Tonks-Girardeau gas.

[7] We recall that this limit takes $N \to \infty$, $L \to \infty$, keeping $n_\infty = N/L$ constant.

To conclude this subsection, we mention a recent numerical work on the dynamics of polaron formation in a weakly-interacting Bose gas [212] with an approach based on truncated Wigner simulations.

5.2.2 Analogy with Josephson physics

The solitonic oscillations can be interpreted as Bloch-like oscillations, which is natural when considering the periodic dispersion relation of the immiscible mixture near the Manakov limit. However, the existence of this dispersion relation is not trivial, as discussed in this chapter. Is there an alternative interpretation to explain these oscillations?

Bresolin et al.'s paper [48] discusses the Josephson effect as an alternative description. This effect was first discovered in 1962 by Brian Josephson [213] and studied with superconductors separated by a thin weak link insulator, named *Josephson junction*. The DC Josephson effect describes the flow of an electrical current across an insulating junction without the need for any external voltage. This current is carried by Cooper pairs of the superconductors. The AC Josephson effect occurs when an external voltage is applied through the Josephson junction, causing the electrical current to become a sinusoidal function of time. This effect is a remarkable macroscopic manifestation of quantum physics with numerous applications. The existence of the AC Josephson effect is crucial in describing the superconducting quantum interference device (SQUID), which is a highly sensitive detector of magnetic fields. The frequency of the AC Josephson current is directly proportional to the voltage applied across the junction, providing a precise method for voltage measurement. Additionally, the Josephson effect is utilized in superconducting qubits for quantum computing [214].

More quantitatively, two equations describe the Josephson effect. They relate the order parameter difference between the two superconductors φ, the voltage applied across the junction $V(t)$ and the electrical current $I(t)$ as:

$$\begin{cases} \frac{\mathrm{d}\varphi}{\mathrm{d}t} = \frac{2eV(t)}{\hbar} \\ I(t) = I_c \sin\left[\varphi(t)\right] \end{cases} \tag{5.18}$$

where I_c is the maximal current amplitude and e is the elementary charge. For a constant voltage V, we recover the sinusoidal variation of $I(t)$ and the AC Josephson effect.

The Josephson effect has been observed in other platforms described by an order parameter that exhibit superfluidity or Bose-Einstein condensation, such as superfluid ^{4}He [215] or ultracold gases [216, 217, 218], where the flow of electrons is replaced by a flow of atoms[8]. A particular AC Josephson effect occurring between two weakly-coupled ferromagnets is known as the spin Josephson effect [219] and was first observed with the B phase (low temperature and pressure phase) of ^{3}He in 1989 [220]. The "phase difference" is replaced by the difference of the in plane magnetization angle of the two ferromagnets (ϕ in Figure 4.3) and the current is a spin current related the difference in vertical magnetization between the two ferromagnets and how it changes over time [219]. The complementary picture of immiscible mixtures gives the exact expression of these quantities. The phase difference is simply the difference of the phase of the majority component order parameter between the two sides of the barrier that we call x_+ and x_-: $\phi_1(x_+) - \phi_1(x_-)$, and the spin current reads $I_{\mathrm{spin}} = \frac{\mathrm{d}}{\mathrm{d}t}\int_X^\infty \mathrm{d}x\, n_1(x,t)$ with X the position of the localized minority wavepacket. In

[8] Even though there is no true condensate in 1D, in accordance with the Mermin-Wagner theorem [124], one assumes a local superfluid order to introduce an order parameter.

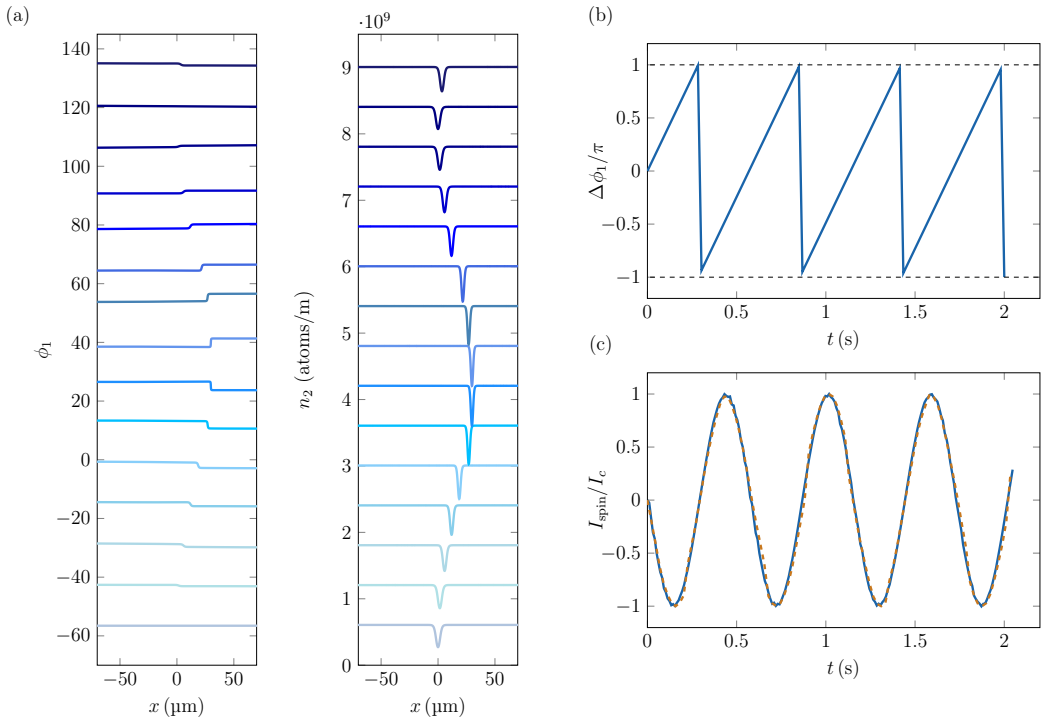

FIGURE 5.6: Numerical phase evolution and AC Josephson effect. (a): Evolution of the phase of the majority component as well as the density over a bit more than one oscillation period for the same parameters as in Figure 5.1. There is a phase jump at the soliton position which increases with time. At the turning point where the bath is completely depleted, the phase difference between each side of the soliton jumps from $+\pi$ to $-\pi$. The phase difference then returns to 0 after one oscillation period. The profiles are shown every $\mathrm{d}t = T/13$. They are vertically shifted for better visualization and should be read from bottom to top. (b): Phase difference of the majority component across the soliton. It increases linearly with time and jumps from $+\pi$ to $-\pi$ at $T/2$, $3T/2$, $5T/2$ and $7T/2$. The dashed horizontal lines represent $\Delta\phi_1 = \pi$ and $\Delta\phi_1 = -\pi$. (c): Spin current evolution calculated from the soliton velocity in blue: $I_{\text{spin}}(t) = -n_0\dot{X}(t)$ and from the sinus of $\Delta\phi_1$: $I_{\text{spin}}(t) = -I_c \sin(\Delta\phi_1)$ in dashed orange. The two curves coincide.

our system, this wavepacket, playing the role of the barrier, moves in time. Therefore, unlike usual *fixed* Josephson junction, the barrier separating the two "ferromagnets" is *mobile* in the immiscible mixture system.

The equivalence between the spin-Josephson junction and the magnetic soliton in an easy-axis ferromagnet is now justified in more detail. The key relation at play is the simple proportionality relation between the total momentum of the soliton and the phase difference of the majority component wavefunction across the soliton[9] (4.44): $P = 2\Delta\phi_1$. Thus, using the equation of motion: $\frac{\mathrm{d}P}{\mathrm{d}t} = NF$, we recover an equation similar to the first one of (5.18):

$$\frac{\mathrm{d}\phi_1}{\mathrm{d}t} = \frac{NF}{2} \tag{5.19}$$

where the force replaces the applied voltage and the magnetization is a substitute for

[9]When we consider open boundary conditions, ϕ_1 is approximately constant outside the soliton position (see Figure 5.6) so we can take the difference of phase between each side of the soliton x_- and x_+ instead of between $-\infty$ and $+\infty$ [48].

the elementary charge. Then, using that the spin current is proportional to the velocity of the soliton which is expressed as $v = \frac{2}{\sinh(N/2)} \sin(P/2)$, we obtain a sinusoidal evolution for the spin current:

$$I_{\text{spin}}(t) = -I_c \sin(\Delta\phi_1) \tag{5.20}$$

with $I_c = 2/\sinh(N/2)$. We thus find the other key equation describing Josephson effect (5.18).

Therefore, we showed that the equations obtained in the magnetic soliton case can be mapped on Josephson-like equations, confirming the interpretation of the oscillations as an AC spin-Josephson effect.

We therefore make the following interpretation of the oscillation of the magnetic soliton as a spin-Josephson effect for the majority component in the presence of a constant force, as done in [48]. As the magnetic soliton moves under the action of a constant force, its momentum, and thus the phase difference of the majority component across the soliton, increases linearly with time. When $P = 2\pi$, the phase difference is equal to π. This causes a change of sign for the spin current (5.20) and thus for the velocity of the soliton. The velocity becomes negative and the soliton moves in the opposite direction of the force, returning to its initial position. The phase still increases with time and reaches 0 again at the initial position (see Figure 5.6). This explains the periodic motion of the soliton position.

We mention that Schecter et al. [221] studied a similar analogy for the motion of an impurity in a 1D Bose gas, which in this case plays the role of a mobile Josephson barrier.

5.2.3 Change of sign for the effective mass

Another complementary description involves the effective mass of the magnetic soliton.

Several definitions of the effective mass exist but we will use the one that relies on the curvature of the dispersion relation in a lattice. We assimilate the total momentum P to a quasi-momentum as we did in the Bloch-oscillations analogy, and write:

$$\frac{1}{m_{\text{eff}}} = \left(\frac{\partial^2 E}{\partial P^2}\right)_N \tag{5.21}$$

From the definition of $v = \left(\frac{\partial E}{\partial P}\right)_N$ and the relation between P and v: $v = \frac{2\sin(P/2)}{\sinh(N/2)}$, we obtain:

$$\frac{1}{m_{\text{eff}}} = \frac{\cos(P/2)}{\sinh(N/2)} = \frac{v^2 - 2\Omega}{4\kappa} \tag{5.22}$$

The following equation of motion can be verified using the effective mass defined above:

$$m_{\text{eff}} \frac{\mathrm{d}v}{\mathrm{d}t} = NF \tag{5.23}$$

To obtain this equation, we use the conservation of the two quantities associated with the soliton in the presence of the force, namely the magnetization and the total energy, to connect the variation of Ω and v with time. We obtain in the adiabatic approximation (see (4.42) and (5.5)):

$$\begin{cases} \frac{\mathrm{d}N}{\mathrm{d}t} = 0 \Rightarrow \frac{\mathrm{d}\Omega}{\mathrm{d}t} = v\frac{\mathrm{d}v}{\mathrm{d}t}\frac{\Omega+2}{v^2-2\Omega} \\ \frac{\mathrm{d}E_{\omega_0}}{\mathrm{d}t} = 0 \Rightarrow \frac{\partial E_{\omega_0}}{\partial \Omega}\frac{\mathrm{d}\Omega}{\mathrm{d}t} + \frac{\partial E_{\omega_0}}{\partial v}\frac{\mathrm{d}v}{\mathrm{d}t} + N\frac{\mathrm{d}X}{\mathrm{d}t}\frac{\mathrm{d}\omega_0}{\mathrm{d}x} = 0 \end{cases} \tag{5.24}$$

With the expression of $E_{\omega_0}(\Omega, v, X) = 4\kappa + N\omega_0(X) = 4\sqrt{1+\Omega-v^2/4} + N\omega_0(X)$ and the definition of the effective mass (5.22), we indeed obtain the equation of motion (5.23).

For the stationary easy-axis soliton of momentum $P = 0$, we obtain a positive effective mass. The soliton propagates in the same direction as the force at the beginning of the motion. This is the opposite case compared to the easy-plane magnetic soliton which has a negative effective mass as shown in [41]. Therefore, we expect the immiscible mixture to be stable against transverse instabilities (due to a non perfect 1D confinement), also known as *snake instabilities* [164, 222], in contrast to the miscible mixture [41][10].

The calculation of the effective mass also gives a complementary interpretation of the dynamics of the magnetic soliton under a constant force. At the beginning of the motion, $P > 0$ for a force directed along $+x$ and the effective mass is positive *i.e.* the velocity of the soliton increases and is positive. However, when P reaches π and continues to grow linearly with time, the effective mass becomes negative (see (5.22)), the velocity decreases and reaches 0 at $P = 2\pi$. The velocity then becomes negative, causing the soliton to turn back towards its initial position in the opposite direction of the force. At $P = 3\pi$, m_{eff} becomes positive again and the velocity of the soliton increases back to 0 at $P = 4\pi$ where the soliton has come back to its initial position.

Similar interpretations have been made for magnetic solitons in immiscible mixtures in [46, 224]. Zhao et al. studied the case $g_{12} = \frac{g_{11}+g_{22}}{2}$ with a constant force applied on the minority component. Even though $g_{11} \neq g_{22} \neq g_{12}$ in this case, the initial bath was completely depleted in the center. Their soliton could thus be classified as a dark-bright soliton. It should be recalled that we do not impose a fully initial depleted bath in our system. They observed oscillations of the soliton position which they interpreted as a consequence of a negative-positive effective mass transition. The soliton started its motion by moving in the opposite direction of the force, as it is predicted for a dark-bright soliton [38] (see also Appendix E). Yu et al. studied the case of a spin-1 BEC and demonstrated that transitions between two types of solitons with opposite effective mass can occur. Additionally, the presence of a constant force induces oscillations of the soliton center of mass.

5.3 Conclusion

5.3.1 Summary

Following Kosevich's work in 1998 [49], we looked at the effect of a non uniform magnetic field on the dynamics of a magnetic soliton in a spin chain. We showed that in the complementary picture of immiscible mixtures close to the Manakov limit, this corresponds to add a differential force between the minority and the majority components. We demonstrated that in the presence of a constant force, the periodic dispersion relation, coupled with a linear variation of P with time, could lead to

[10] The snake instability is expected to appear as soon as the transverse size of the cloud is larger than the width of the soliton. The latter is given by the healing length for dark soliton (typically $\sim 0.1\,\mu\text{m}$) or the spin healing length for easy-plane magnetic soliton (typically $\sim 1\,\mu\text{m}$). Thus, the latter is more robust to snake instabilities than the former. The snake instability together with the decay of the dark soliton into a vortex ring was observed in [223] for a superfluid Fermi gas.

Bloch-like oscillations of the soliton position. For that, an adiabatic approximation was performed and we discussed numerically the regime of working parameters. In Appendix E, we demonstrate that this is a specificity of the magnetic soliton and a consequence of having an inter-component interaction parameter different from the intra-component interaction parameters.

Finally, we interpreted this counter-intuitive phenomenon by taking a step back from the analytical and numerical results. We deepened the link with Bloch oscillations, which are usually seen in periodic structures. Following the recent analysis by Bresolin et al. [48], the oscillations were also interpreted as an AC Josephson effect in the presence of a mobile barrier. The minority component plays the role of the barrier. We also briefly provided a complementary description relying on the effective mass evolution and its change of sign.

5.3.2 Outlook

The results presented in this chapter and the previous one (Chapter 4) were obtained in the thermodynamic limit, where the system size is large enough to ensure that the soliton propagation is not affected by the system's borders. Additionally, we utilized open boundary conditions. In particular, we assumed that the phase profile was flat at infinity (*i.e.* $\frac{\partial \phi}{\partial x}(\pm\infty) = 0$). When this is not the case, the *backflow*, or *counterflow*, plays a more important role. This is a notion introduced by Pitaevskii [225, 89] in the ring geometry. To maintain a single-valued majority component phase at the system's borders, it is necessary to compensate for the phase jump that occurs at the soliton position by smoothly varying its phase outside the soliton. A backflow propagating[11] at the velocity $v_{\text{back}} = \frac{\hbar}{m}\frac{|\Delta\phi_1|}{2\pi R}$ with R the ring radius thus takes place.

In the thermodynamic limit, the velocity associated with the backflow vanishes, as well as its contribution to the energy. However, the momentum associated with the backflow remains finite [225]. This situation is similar to the one discussed in the case of an impurity propagating in a 1D strongly-interacting Bose gas (see section 5.2.1). In the thermodynamic limit where the backflow contribution to the energy is negligible, we recover Haldane's prediction [52] of a periodic dispersion relation (4.49). However, for finite size rings, the backflow contribution to the energy is expected to play an important and interesting role. We expect the backflow contribution to also exist in a linear geometry of finite size. However, its interpretation may be complicated by the boundaries as the flow rebounds off the walls.

[11] The term "counterflow" is a bit misleading as the flow is always in the same direction as the force. It first moves in the same direction as the minority component motion, then in the opposite direction, then the same etc.

Chapter 6

Realization of a magnetic soliton and observation of Bloch-like oscillations under a constant force

This chapter presents our experimental realization of a magnetic soliton within an immiscible mixture. We describe the key experimental ingredients to probe their physics as described in Chapter 4 and 5. Specifically, we demonstrate the emergence of Bloch-like oscillations in the system when the immiscible mixture is subjected to a small differential force. We compare our results with the analytical predictions derived in Chapter 5. Finally, we measure the phase of the bath, a crucial quantity for explaining the oscillation phenomenon. The experimental results presented here were obtained in close collaboration with the other PhD students, Franco Rabec and Guillaume Brochier.

6.1 Experiments on magnetic solitons in miscible mixtures

The chapter begins by providing context for the experimental work. In Chapter 4, we discussed experimental realizations of various solitary waves of the 1D NLSE, including dark, bright, dark-bright, Peregrine solitons, in different physical systems such as optical waveguides, classical fluids, plasmas, and ultracold atomic gases. We emphasized that the latter platform was especially suitable for studying the physics of multi-component (or vector) solitons with mixtures, which exhibit even richer underlying physics. We discussed the experimental realization of the dark-bright soliton, which emerges when a bright soliton is trapped within a dark soliton. It was introduced by Busch and Anglin [38] in 2001. However, if we do not impose an initial fully depleted ("dark") cloud and the π phase jump of the majority component at the position of the soliton, another type of soliton, known as the magnetic soliton, emerges close to the Manakov limit. The excitation that gives rise to the magnetic soliton is formed by a local population imbalance in the mixture (or magnetization in the spin chain language). The total density of the mixture is conserved close to the Manakov limit [41]. We then identified two types of magnetic solitons that arise in miscible or immiscible mixtures close to the Manakov limit. To provide a comprehensive overview of the realization of solitons in weakly-interacting BECs, we will briefly discuss two recent experiments that successfully produced and studied magnetic solitons in miscible mixtures.

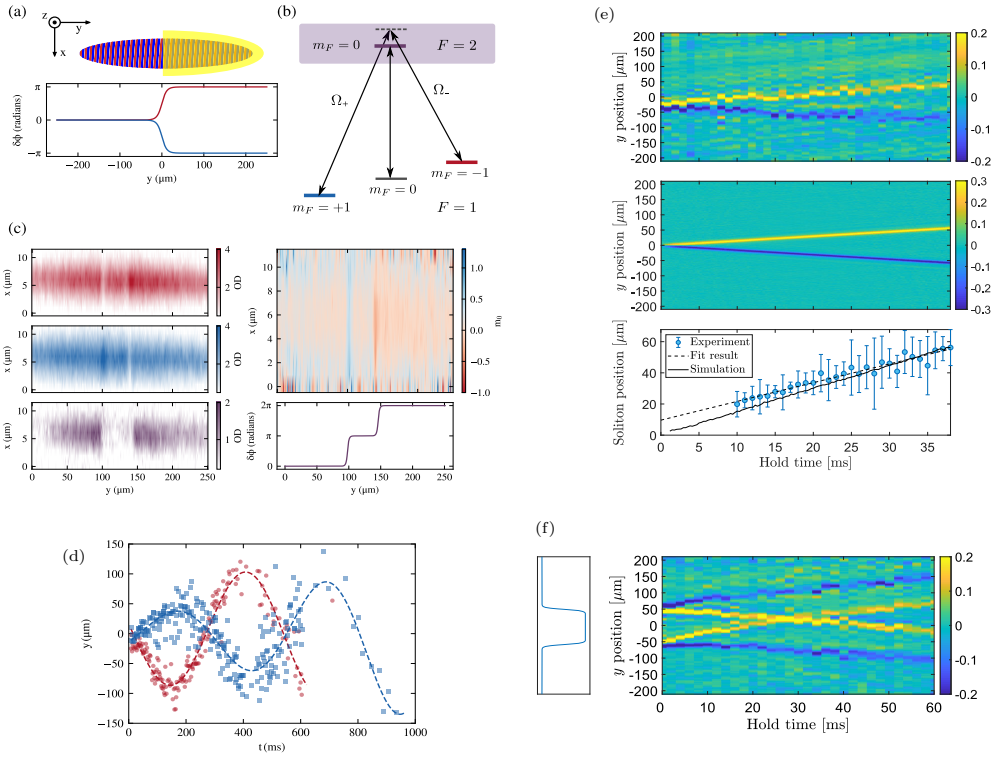

FIGURE 6.1: Experiments on easy-plane magnetic solitons in the ultracold atoms platform. Figures (a), (b), (c) and (d) adapted from [44] and (e) and (f) adapted from [45]. (a): An optical potential, applied to half of the cloud, produces a relative 2π phase shift between the two components $|1,-1\rangle$ and $|1,+1\rangle$ of a miscible mixture placed in an elongated BEC of Na atoms. (b): Scheme of the levels and the MW fields used to create the mixture and image it[1]. (c): OD spatial map for $m_F = -1$ atoms in red, $m_F = +1$ atoms in blue and the relative phase in violet, 15 ms after the application of the pulse of far-off resonant light. Density holes and bumps coincide with phase jump of $\pm\pi$ across them. The two magnetic solitons created have opposite magnetization $n_{|1,+1\rangle} - n_{|1,-1\rangle}$ (top right panel). (d): Out-of-phase oscillations of the two magnetic solitons (blue one for the positive velocity and red for the negative) in a harmonic trap. (e): Evolution of the magnetization over time and space. The top panel is the experimental data, the middle panel is the simulation data and the bottom panel compares the two. Two solitons of opposite magnetization with an absolute value $\simeq 0.2$ propagate at a typical velocity of $\simeq$ 1 mm/s. (f): Adapting the intensity mask used (left panel), two pairs of magnetic solitons at $\simeq \pm 50\,\mu$m were created and their collisions were studied. The two solitons of equal and positive magnetization meet and exit practically undisturbed.

In 2020, Farolfi et al. [44] and Chai et al. [45] realized, almost simultaneously, easy-plane magnetic solitons by using the miscible mixture $|1,-1\rangle/|1,+1\rangle$ of ^{23}Na atoms with a parameter $\delta g/g \simeq -0.07 < 0$[2]. They used cigar-shaped BECs with a transverse Thomas-Fermi radius sufficiently small compared to a few spin healing lengths (typically $\lesssim 5\xi_s$) so that the magnetic soliton does not suffer from snake instability. A roughly balanced spin mixture of $|1,-1\rangle$ and $|1,+1\rangle$ atoms is generated. Magnetic solitons are then produced by illuminating half of the cloud with a pulse

[1] A MW field, blue-detuned from the transition $|1,0\rangle/|2,0\rangle$ is also applied for stabilizing the mixture against spin relaxation.

[2] We recall that our definition of δg is $\delta g = g_{12} - g$.

of a far-off resonance light beam. The wavelength chosen is the tune-out wavelength for which the scalar light shift for the $3S_{1/2}$ level is zero. The dominant term is thus the vectorial light shift. With a circularly polarized beam, a symmetric differential phase shift is obtained on the mixture $|1,-1\rangle/|1,+1\rangle$, because they have opposite spin projections m_F. The duration of the pulse, typically 100 µs, can be adjusted to imprint a 2π relative phase shift between the components in the illuminated zone. Since the duration of the excitation pulse is small compared to the characteristic time scale of the spin dynamics $\tau_s = \frac{\hbar}{n_0|\delta g|} \simeq 5\,\text{ms}$, there is no additional density excitation in the system. Thus, since the total magnetization is conserved by this method, the generated magnetic solitons are formed by pairs of opposite magnetization. Changing the intensity gradient of the light alters the relative phase at the center of the cloud, thereby modifying the velocity of the magnetic solitons formed. In both experiments, they access the populations in each hyperfine state. They showed that a density dip (respectively density hole), together with a counterpropagating density hole (resp. density dip) propagate through the BEC in the $|1,-1\rangle$ (resp. $|1,+1\rangle$) component. Using a Ramsey interferometric scheme, the two teams measured the relative phase and observed a constant relative π phase across each magnetic soliton propagating in opposite directions. Additionally, they imprinted two pairs of magnetic solitons and studied their collisions.

The detection of the solitons in these experiments was possible either directly *in situ*[3] or with a short time of flight thanks to the typical micrometer length scale of the magnetic soliton, given by the spin healing length. We will also use this key point to precisely measure the profiles of magnetic solitons in the following.

Trento's group also studied the longitudinal motion of magnetic solitons in a harmonic trap. The typical longitudinal confinement frequency in their cigar-shaped BEC is $f_y \simeq 10\,\text{Hz}$. They imposed a velocity on their magnetic solitons and observed that they undergo oscillations inside the harmonic trap, as shown in Figure 6.1(d). This was predicted for magnetic solitons in [41] and the observed oscillations agree with Qu et al.'s prediction. No changes in the width of the oscillating magnetic soliton were observed within their imaging resolution.

Dark and dark-bright solitons also exhibit an oscillatory motion in a harmonic trap, as studied experimentally by Becker et al. [39]. The oscillation period of a dark soliton does not depend on the interaction parameter and is equal to $T = \sqrt{2}T_y$ where $T_y = 1/f_y$ is the oscillation period associated with the harmonic trap [171, 39]. This period is smaller than the one observed for a magnetic soliton or a dark-bright soliton [38, 39] (see also Appendix E). It should be noted that the observed oscillatory motions were in a harmonic trap, where the force acting on the wavepacket is position-dependent and changes sign at the center of the trap. The presence of oscillations in this type of system is therefore expected treating the soliton as a macro object following classical dynamics.

Magnetic solitons in miscible mixtures have thus been substantially studied experimentally. In the following section, we outline the experimental requirements for creating magnetic solitons in immiscible mixtures in a flat potential. Submitting a differential force between the minority and the majority components, as in the proposal [48], is also considered.

[3] The profiles were broadened by the finite imaging resolution of $\simeq 2\,\mu\text{m}$.

6.2 Experimental ingredients

6.2.1 The 1D regime for spin dynamics

A first ingredient to realize a magnetic soliton experimentally is a 1D confinement, as it was the case in the experiments described in the previous section. In our current experimental setup, as described in Chapter 1, the physics being studied is kinematically 2D. Without installing new experimental tools on the optical table, we cannot enter the stricly thermodynamic 1D regime for a single component gas. Indeed, it would require transverse confinement frequencies $\omega_\perp \gtrsim \frac{k_B T}{\hbar}$, $\frac{\mu}{\hbar} \simeq 2\pi \times 1\,\mathrm{kHz}$ where μ is the chemical potential $\mu = gn$.

However, when dealing with binary mixtures, the above condition is less restrictive. Indeed, the spin dynamics introduce a new energy scale, which is $\delta g \times n$. For a weakly miscible (as in the Sodium experiments described in the previous section) or immiscible mixture, the interaction parameters usually verify $|\delta g/g| \lesssim 0.05$. This led us to say that the magnetic solitons are easier to access experimentally than single-component solitons, comparing the spin healing length to the healing length. Thus, the spin dynamics are effectively 1D if $\omega_\perp \gtrsim \frac{\delta g\, n}{\hbar} \gtrsim 2\pi \times 50\,\mathrm{Hz}$.

Experimentally, we confine the 2D gas inside a 1D tube thanks to a DMD, called DMD1 in Chapter 1. If we were to load the tube geometry directly, the final atom number would be extremely poor ($< 5 \times 10^3$ instead of 1×10^5 usually). To improve the loading, the condensate is first placed in a 2D rectangular shape $40 \times 60\,\mu\mathrm{m}$. Within 500 ms, we compress the gas into a tube of $3 \times 60\,\mu\mathrm{m}$ by displaying a "movie" on DMD1 *i.e.* 50 images going continuously from the initial rectangle to the final one (Figure 6.4). Once this is done, we evaporate the gas in the tube during 500 ms by lowering the power of the box confinement and letting it thermalize. It seems crucial for the most efficient loading to evaporate in the tube and not in the initial rectangular box. Still, we lose $\sim 30\%$ of the atoms during the movie (from 1×10^5 to 6×10^4). We did not see any further improvement by increasing the number of frames displayed or the time between each image.

The decision to use a 3 µm tube size is a result of a trade-off. Larger tubes have a transverse size that exceeds the spin healing length, making it unclear how to apply the 1D physics of magnetic solitons discussed in the previous chapters. Smaller tubes have lower loading efficiency in terms of density and our finite resolution imaging begins to limit us.

In Figure 6.4, we plot a transverse cut of the gas profile in the 3 µm tube. We assume that the transverse planar confinement due to the DMD can be approximated by a harmonic confinement. In this case, a Gaussian fit yields a transverse harmonic confinement length $l_x \simeq 1.5\,\mu\mathrm{m}$ (see section 4.1.1 for its definition)[4]. Thus, the confinement angular frequency along the transverse planar direction of the tube is approximately $\omega_x \simeq 2\pi \times 50\,\mathrm{Hz}$. Therefore, given the temperature energy scale $\frac{k_B T}{\hbar} \gtrsim 2\pi \times 400\,\mathrm{Hz}$, several excited states of the harmonic oscillator along x are populated and the system is not thermodynamically 1D. We recall that the strong 2D confinement gives an angular vertical frequency $\omega_z \simeq 2\pi \times 4\,\mathrm{kHz}$.

The transverse confinement is quantified by the geometric mean of the two previous quantities: $\omega_\perp = \sqrt{\omega_z \omega_x}$ (see section 4.1.1) and we get an estimate of $\omega_\perp \simeq 2\pi \times 400\,\mathrm{Hz}$. This is an approximate guess, and we will compare it with another estimate, which has been obtained by determining the stationary profile of the magnetic soliton.

[4] This is a lower bound and our finite PSF would broaden the profile.

Therefore, even though the system is not thermodynamically 1D, the effective spin dynamics are in good approximation unidimensional since $\hbar\omega_{x,z} \gtrsim \delta g\, n$. This suggests that using a transverse tube size of the same order of magnitude as the spin healing length is suitable for studying the physics of 1D weakly-immiscible mixtures, where the spin and density dynamics can be decoupled.

6.2.2 An immiscible and long-lived mixture

The various hyperfine states of Rubidium offer several options for selecting a weakly immiscible mixture. However, certain requirements must be considered when making this choice. Firstly, it is highly preferable to choose a long-lived mixture, keeping in mind the adiabatic application of a constant force on the magnetic soliton (small velocities for the soliton (5.13)). The dynamics depend crucially (and non-linearly) on the atom number of the minority component and the density of the bath. We must prevent the loss of atoms due to spin relaxation for times typically shorter than a few hundred of ms. This argument excludes the clock state mixture $|1,0\rangle/|2,0\rangle$, within which a Townes soliton was realized in the team [190]. More generally, it excludes mixtures containing atoms in states $F = 2$[5], subjected to spin relaxation.

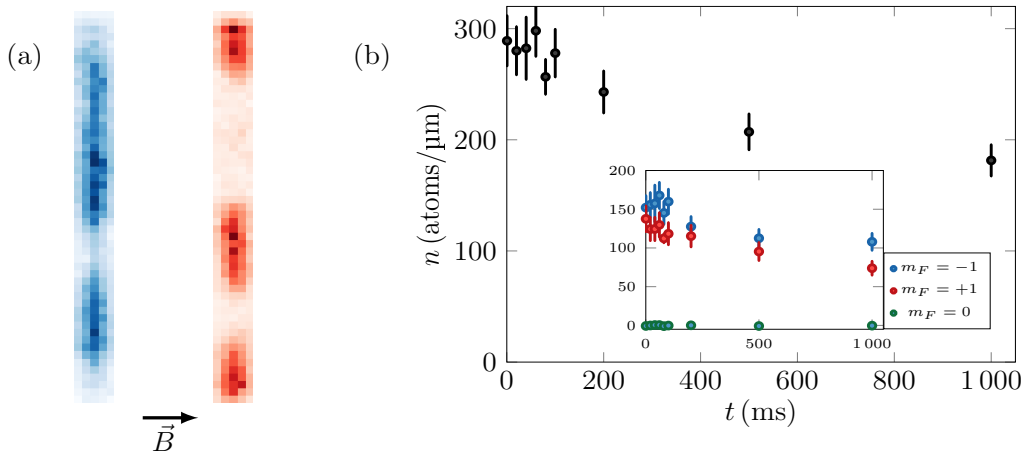

FIGURE 6.2: The mixture $|1,-1\rangle/|1,+1\rangle$. (a): It is an immiscible mixture and is thus subjected to demixing (see [72] for the description of demixing in the ultracold atoms platform). We show absorption images of respectively the states $|1,-1\rangle$ in blue and $|1,+1\rangle$ in red after 200 ms of evolution for an initial 50/50 mixture with a total density $n = 300$ atoms/µm. The chosen geometry is the tube geometry of size 3×60 µm. The two images are not taken in a single sequence. (b): Lifetime of the mixture. A loss graph of the mixture still in the tube geometry was performed with an initial total density of 300 atoms/µm, split approximately in half between $|1,-1\rangle$ and $|1,+1\rangle$ atoms. The black points represent the total density of the gas. The inset shows its distribution over time between the different spin states, which can be accessed with a Stern-Gerlach experiment. Although 3-body losses are observed, 2/3 of the initial cloud remains after 1 s of hold time: the mixture is long-lived.

Therefore, there remain two possible choices for the mixture only involving $F = 1$ states: $|1,-1\rangle/|1,0\rangle$ and $|1,-1\rangle/|1,+1\rangle$. Another task is to select two states with different sensitivities to an external magnetic field. Indeed, when applying a constant force through a magnetic gradient to investigate the physics discussed in the previous

[5]The stretched mixtures $|1,-1\rangle/|2,-2\rangle$ or $|1,-1\rangle/|2,+2\rangle$ are long-lived but we did not see any demixing patterns experimentally.

chapter, it is important that the minority and majority components do not respond in the same manner. This requirement is satisfied bor both mixtures.

The miscibility parameter is used to quantify the difference between them. It is written $\Delta = \frac{a_{12}^2}{a_{11}a_{22}}$ where 1 and 2 denote the 2 components of the mixture. The scattering length values can be calculated by combining the bare scattering lengths a_0 and a_2 weighted by Clebsch-Gordan coefficients [226, 227]. Without taking into account magnetic dipole-dipole interactions for the moment, we obtain the following values in units of the Bohr radius a_B:

- $|1,-1\rangle/|1,0\rangle$ mixture: $a_{-1,-1} = a_2 = 100.36\,a_B$; $a_{0,0} = \frac{1}{3}a_0 + \frac{2}{3}a_2 = 100.86\,a_B$; $a_{-1,0} = a_2 = 100.36\,a_B$. The mixture is predicted to be weakly miscible: $\Delta = 0.995$ [228]. However, experimentally, patterns of demixion are seen in [229] (and also in our setup).

- $|1,-1\rangle/|1,+1\rangle$ mixture: $a_{-1,-1} = a_2 = 100.36\,a_B$; $a_{+1,+1} = a_{-1,-1} = 100.36\,a_B$; $a_{-1,+1} = \frac{2}{3}a_0 + \frac{1}{3}a_2 = 101.36\,a_B$. The mixture is predicted to be weakly immiscible: $\Delta = 1.02$. In [230], the authors confirmed this statement by observing the formation of spin domains after the system was quenched into an equal superposition of the two immiscible states.

Therefore, we have decided not to use the mixture $|1,-1\rangle/|1,0\rangle$ due to its proximity to the miscibility/immiscibility transition. Indeed, even though it is an immiscible mixture, the small value of δg increases the characteristic time scale of the spin dynamics $\tau_s \propto 1/\delta g$.

The above predictions are slightly modified when considering an additional small effect: the magnetic dipole-dipole interactions (MDDI). Indeed, the team demonstrated in a recent study in 2D [231] that even in alkali Bose gases with small magnetic moments, magnetic dipolar interactions affect the description of collisions between two atoms in the clock hyperfine states $|1,0\rangle$ and $|2,0\rangle$. Their effect was absorbed in the modification of the inter-component scattering length a_{12}. The team demonstrated the anisotropic nature of these interactions, which is in contrast to the s-wave contact interactions. They were able to change the miscibility parameter of the mixture between $\Delta = 1.05$ (for a magnetic field parallel to the vertical axis z) and $\Delta = 1.007$ (for a magnetic field in the horizontal plane).

For the $|1,-1\rangle/|1,+1\rangle$ mixture, the effect of the magnetic dipolar interactions is smaller and affects the inter-component and intra-component scattering lengths. We can calculate this effect following [231] and we get a variation of the miscibility parameter between $\Delta = 1.006$ (magnetic field parallel to z) and $\Delta = 1.027$ (magnetic field in the horizontal plane). The values of the scattering lengths in the latter magnetic field configuration are predicted to be: $a_{-1,-1} = a_{+1,+1} = (100.36 - 0.175)\,a_B = 100.19\,a_B$ and $a_{-1,+1} = (101.36 + 0.175)\,a_B = 101.54\,a_B$. It yields a value of $\delta g/g \simeq 0.013$.

As a result, when the magnetic field is in the atomic plane, this mixture is sufficiently on the immiscible side of the transition that the associated spin dynamics are not too slow (see Figure 6.2). We recall that the associated characteristic time scale for the spin dynamics is $\tau_s = \frac{\hbar}{n_0 \delta g}$. Furthermore, it still largely satisfies the requirement $\delta g/g \ll 1$, so that the mapping between the coupled GPEs and the LLE is valid to a good approximation.

The expected period and amplitude of the oscillations can now be calculated once the chosen mixture is known[6]. The adimensionalized quantities N and F introduced

[6] Actually, we did not need to know δg to calculate the oscillation period, since it does not depend on the mixture under consideration.

in the previous chapters are also used here. The density n_0, the number of atoms in the minority component N_2, and the applied force f are varied. For each set of values, denoted by a point (N, F), the period and amplitude of the expected oscillations are calculated. We recall that the simulations performed in the previous chapter agree well with the calculations when the adiabatic condition $F \ll 1$ and the condition on the velocity of the soliton $v < c_s$, corresponding to $N \gtrsim 2.6$, are fulfilled. In these regions, there is a zone around $F \simeq 0.1$ and $N \simeq 5$ for which the period is of the order of a few hundred of ms and the amplitude of the order of a few µm, which would enable the experimental study of the oscillation phenomenon (Figure 6.3).

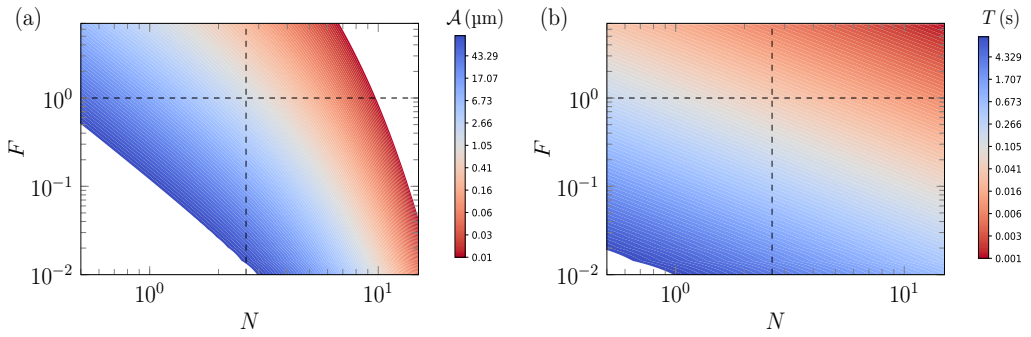

FIGURE 6.3: Numerical map of the amplitude and the period of the oscillations of the magnetic soliton as a function of the adimensionalized parameters N and F defined in Chapter 4. The only fixed parameters are the ratio $\delta g/g \simeq 0.013$ corresponding to the chosen mixture and the total density $n_0 = 3.3 \times 10^8$ atoms/m. We vary the atom number of the minority component N_2 and the force f. The dashed vertical line corresponds to the equation $v = c_s$ and the horizontal line is the equation $F = 1$. The regime without fragmentation, where an adiabatic approximation can be performed, is located in the lower right panel.

6.2.3 Imprinting a spin-selective spatial profile

To realize a magnetic soliton, it is necessary to control the spatial distribution of the density of the two spin components. To achieve this, we utilize a DMD in combination with Raman beams, as explained in Chapter 1. However, we cannot control the phase distribution with the DMD and, therefore, cannot impart a velocity to the soliton ($v = 0$).

It is recalled that the choice of the wavelength of the Raman beams is determined by the cancellation of the scalar shifts acting on the states $F = 1$ and $F = 2$: $\lambda_R = 790.0\,\text{nm}$.

The Raman beams are detuned by $\simeq 6.8\,\text{GHz}$ to perform a two-photon transfer from a state in $F = 1$ to a state in $F = 2$. Thus, the obtention of a spatially-selective spin mixture $|1, -1\rangle/|1, +1\rangle$ naturally passes through the state $|F = 2, m_F = 0\rangle$ whose total spin projection is in between the other two states[7].

The mixture is created in a two-step transfer process. Firstly, a two-photon Raman transfer is used to transfer atoms from $|1, -1\rangle$ to $|2, 0\rangle$ in a spatially selective manner, allowing for the shaping of the density profile of atoms in $|F = 2, m_F = 0\rangle$. Immediately after, a MW pulse is applied to fully transfer the $F = 2$ atoms to

[7] In the following discussion of polarization of the two beams, it will become clear why we did not remove the EOM to directly perform a two-photon transfer between the $|1, -1\rangle$ and $|1, +1\rangle$ states.

$|F = 1, m_F = +1\rangle$. The atoms in $|F = 1, m_F = -1\rangle$ remain unaffected as there is no one-photon resonant transfer possible with this MW field (see Figure 6.4(d)).

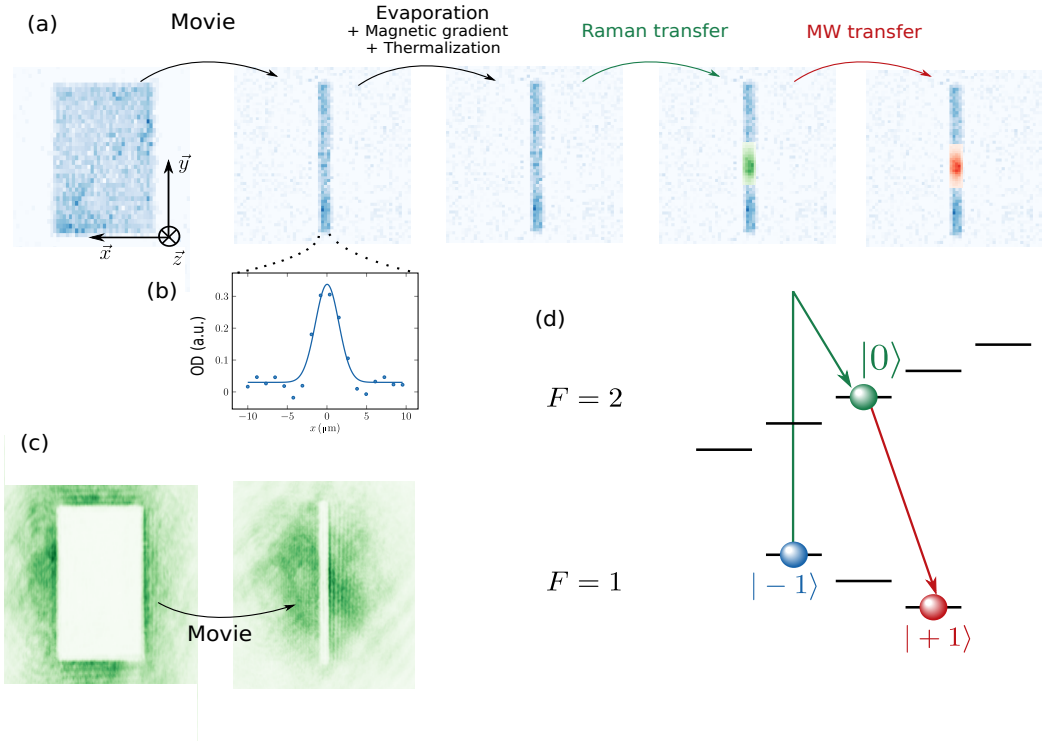

FIGURE 6.4: Protocol for the realization of an easy-axis magnetic soliton. (a): Sequence steps and illustration with absorption images. After loading the atoms into a 2D rectangular box of size $60 \times 40\,\mu$m, a movie of 50 images separated by 10 ms is displayed on the DMD. The final image is a tube of size $60 \times 3\,\mu$m. After an evaporation step in the tube of 500 ms, the bias fields are ramped during 200 ms to a chosen value in order to impose a magnetic gradient or not and to choose the orientation of the magnetic field. A thermalization step of 500 ms follows. A pulse of Raman light is then applied to the $|1, -1\rangle$ atoms to imprint a spatially spin selective profile. The transferred atoms are in the $|2, 0\rangle$ state and they are all immediately flipped to the $|1, +1\rangle$ state with a MW illumination. (b): Average profile along the transverse direction of the tube. The blue solid line is a Gaussian fit of standard deviation $l_x = 1.5\,\mu$m. (c): Light images of the DMD taken with a control camera before and after the movie. (d): Scheme of the hyperfine ground states of Rb. The double green arrow represents the two-photon Raman transfer (here chosen with the polarizations π/σ^-, but it also works with σ^+/π). The red arrow represents the MW transfer to $|1, +1\rangle$.

The question of the polarization of the Raman beams should be asked when atoms are transferred from $|1, -1\rangle$ to $|2, 0\rangle$. This is done by absorbing a σ^+ photon and re-emitting a π photon (or by absorbing a π photon and re-emitting a σ^- photon). Thus, the orientation axis of the magnetic field should be chosen carefully so that a Raman beam can perform a π transfer. Since the propagation axis of the Raman beams before the cell is the vertical axis z, it is not possible to transfer atoms from $|1, -1\rangle$ to $|2, 0\rangle$ with a vertical magnetic field. Instead, the magnetic field direction is chosen to be in the horizontal plane, along the x direction, perpendicular to the tube axis (see Figure 6.4(a)). Its magnitude is $B_x \simeq 1.3\,$G. The linear and orthogonal polarizations of the Raman beams lie in the horizontal plane (x,y) when propagating vertically to the atoms. Thus, one of the two beams realizes the desired π-transfer. The other

beam polarization, linear along the y axis, can be decomposed into a sum of left and right circular polarizations. One of these polarizations provides the necessary σ^+ or σ^- photon for the Raman transfer.

This selection of a magnetic field in the horizontal plane is good news, as we saw earlier that it was also the optimal choice for maximizing the immiscibility parameter. This choice does not allow for a direct transfer from $|1,-1\rangle$ to $|1,+1\rangle$[8]. Therefore, it is necessary to pass through the state $|2,0\rangle$.

6.2.4 Imposing a constant differential force

The above ingredients are sufficient to realize a stationary magnetic soliton. To conclude this section, we will recall how to impose a small differential constant force on the mixture, under which the soliton is expected to undergo a periodic oscillation.

To achieve this, a magnetic gradient is applied (mainly) along the tube axis y. This is accomplished by using a quadrupolar magnetic field created with the MOT coils and adding a small bias field along y, following the same procedure as the one described in Chapter 3. To cancel out the gradient along the x axis, which is perpendicular to the tube, a coil is added near the cell with its main axis being the x axis (see Chapter 1).

The dynamics of the mixture under a constant force are slightly more complicated than what was derived in the previous chapter due to the non-zero sensitivity to a magnetic field gradient of the atoms in the state $|1,-1\rangle$ (referred to as the majority component and not affected by the coherent transfers). This was discussed in [48] where it was shown that the tilted bath affects the motion of the soliton and results in a high frequency component in the oscillations. However, this effect is only visible in the oscillations when $\delta g/g$ is sufficiently large. The simulations performed with the Rb mixture $|1,-1\rangle/|1,+1\rangle$ show that the dynamics observed for a majority component submitted to $-f$ and a minority component submitted to $+f$ are identical to those of a minority component submitted to $+2f$. In other terms, the observed oscillations are only sensitive to the relative difference of forces felt by the two components, for sufficiently weakly immiscible mixtures.

6.3 Stationary magnetic soliton

In this section, we explain how to create a stationary magnetic soliton using the tools described in the previous section. The scheme of the experiment is depicted in Figure 6.5. The mixture is characterized by measuring the parameter δg.

6.3.1 Low depleted stationary soliton

One way to realize a magnetic soliton deterministically is to choose the appropriate amplitude modulation on the DMD $\mathcal{D}(x,y)$ so that the transferred density in the minority component is of the form given by the solution $n_2(y) = n_0\frac{1+C(y)}{2}$ of (4.34). In contrast to the experiments discussed in section 6.1, our method for imprinting a magnetic soliton does not allow for the application of a velocity to the soliton. We imprint solitons with zero velocity ($v = 0$). More precisely, using the equation (1.4) given in Chapter 1, the modulation function on the DMD is chosen to be:

[8] We could think that this transfer could be done by removing the EOM and by directly absorbing a σ^+ photon and emiting a σ^- photon. Indeed, when the two beams are polarized in the horizontal plane but none of them along the magnetic field, each polarization has a σ^+ and a σ^- component (but not *pure* σ^+ and σ^- components). However, a destructive interference effect between the exchange of photons prevents from doing such a transfer, as it can be seen with a development of the spin populations as a function of the Clebsch-Gordan coefficients, similar to what is done in [71].

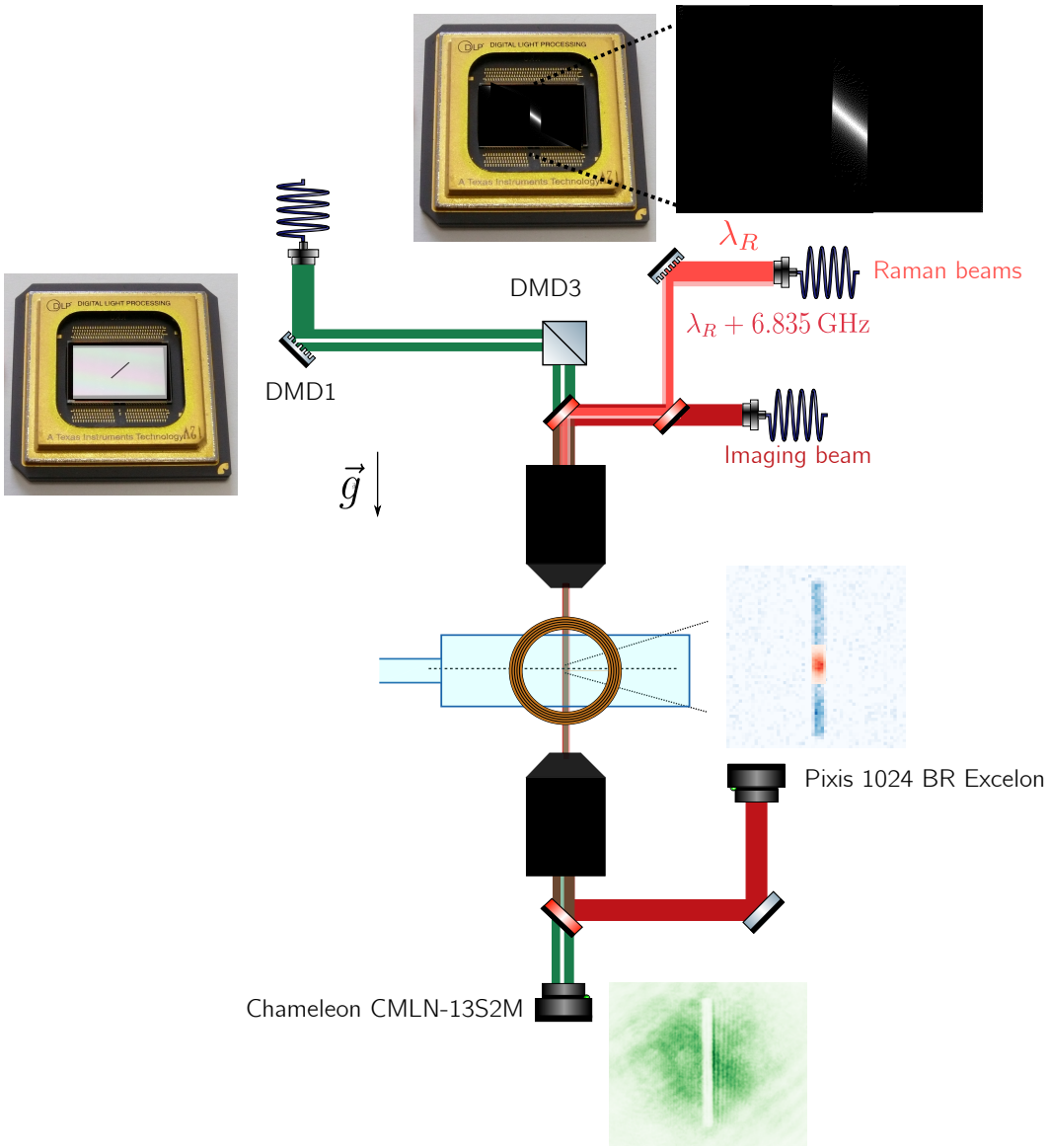

FIGURE 6.5: Optical table used for the magnetic soliton project. A tube pattern is projected onto the atoms using DMD1 and is combined with the copropagating Raman beams and the vertical imaging beam. DMD3 is used to shape the Raman beams and thus the spatial profile transferred to $|2,0\rangle$. All of the beams are directed, via a microscope objective, onto the atomic plane, which is marked with a horizontal dashed line. An absorption image of the planar cloud is acquired through another microscope objective on a Pixis camera. We have separate access (not on the same run) to both hyperfine states of the mixture: $|1,-1\rangle$ in blue and $|1,+1\rangle$ in red. A control camera images the plane of the DMD to monitor the green light sent to the atoms. We present one of the MOT coils, which, together with the bias coils (not shown), creates a magnetic gradient along the y axis of the tube.

$$\mathcal{D}(x,y) \propto \sqrt{\frac{\arcsin\left(\sqrt{\frac{n_2(x,y)}{n_0}}\right)}{\arcsin\left(\sqrt{d}\right)}}, \text{ with } \frac{n_2(x,y)}{n_0} = \frac{2(1+\Omega)}{2+\Omega-\Omega\cosh(2\kappa y)} \tag{6.1}$$

and $d \equiv \frac{n_2^{(\max)}}{n_0} = \kappa^2 = 1 + \Omega$ is the targeted depletion. We used that for a magnetic soliton at rest ($P = 0$), we have $\Omega < 0$ (see (4.45)). The preservation of the shape of the wavepacket over time would then be a criterion to confirm that we are effectively creating a stationary soliton. This has been done, for example, for the deterministic realization of a Townes soliton [190].

Let us first consider the case of low depleted clouds, *i.e.* for which the maximum density of the minority component is small compared to n_0 ($d \ll 1$). In this case, the quantity $N = \frac{2N_2}{n_0 \xi_s}$ is much smaller than 1 and the expression of the density simplifies. Indeed, in this case, $N/2 \simeq \sinh(N/2) = -\frac{2\sqrt{1+\Omega}}{\Omega}$. Therefore, the limit $N \to 0$ implies to take $\Omega \to -1$ for a soliton characterized by $v = 0$. Thus, we obtain: $N \simeq 4\kappa$. The magnetization is equal to the energy of the soliton in this limit. Using $\cosh(2\kappa y) = 2\cosh^2(\kappa y) - 1$ and the limit $\Omega \to -1$, we obtain:

$$\frac{n_2(y)}{n_0} = \frac{\kappa^2}{\cosh^2(\kappa y)} \tag{6.2}$$

with $\kappa = \sqrt{1+\Omega} \to 0$ as $N \to 0$.

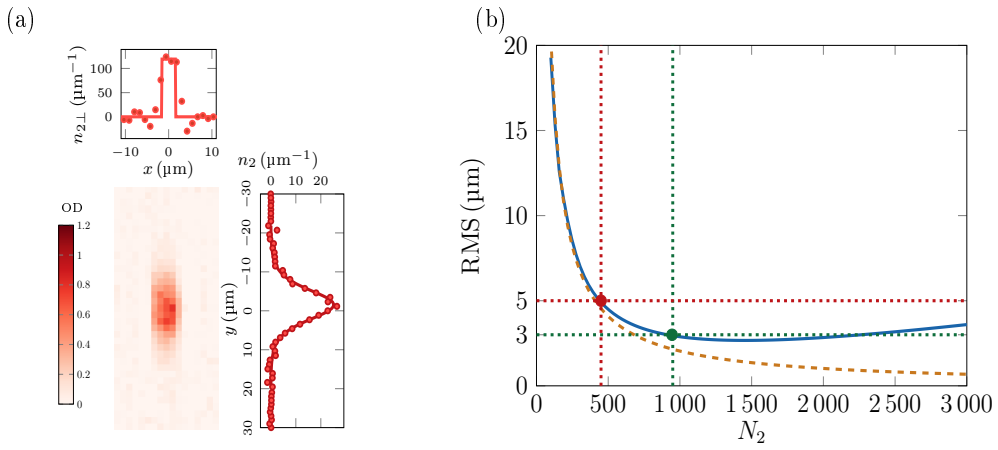

FIGURE 6.6: Experimental and numerical stationary magnetic soliton. (a): Absorption image of a magnetic soliton in a 1D tube geometry with $N_2 \simeq 350$. We imprint a $\cosh^{-1/2}(y/\sigma)$ function on DMD3, with $\sigma = 5\,\mu$m and the feedback loop was run in order to optimize the profile. A longitudinal average profile is shown on the right along with a $1/\cosh^2$ fit with a solid line. A transverse average profile is plotted above. We also draw a square of size 3 µm with a solid line[9]. (b): Numerical RMS size (*i.e.* $\int y^2 |\psi_2(y)|^2 \, \mathrm{d}y$) of the stationary minority wavepacket as a function of the atom number in the minority component N_2 in blue. It is obtained by analyzing the stationary profiles given by the GP simulations with $\delta g/g \simeq 0.013$. The orange dashed line represents the hyperbolic single-component link between the two quantities (6.5). At low depletions, the two curves coincide, and the effective single-component description of the mixture is a good approximation of the stationary profile. In red dotted lines, we pinpoint the solution corresponding to an RMS size of 5 µm (case of (a)) and in green, the lowest N_2 solution for 3 µm. The variation of the RMS size near the red circle is stronger than that around the green circle.

[9]We choose to plot a square rather than a Gaussian as we did in Figure 6.4(b) because the atomic profile is optimized with a feedback loop in order to obtain a flat density transverse profile.

This expression should remind us of the bright soliton solution of the one-component GP equation (4.5). Could we have guessed this connection at low depletion?

The answer is positive. It can be shown that in the low depletion regime, the dynamics of the majority component, denoted 1, occurs on a short time scale ($\propto 1/n_\infty$) compared to the minority dynamics ($\propto 1/n_2$). Thus, one can assume that the bath is always at equilibrium on the time scale of the minority dynamics [190]. This simplifies the coupled 2D dynamics of the mixture. In the low depletion regime, the minority component, denoted 2, follows an effective single-component GPE with an interaction parameter $g_{\text{eff}} = g_{22} - \frac{g_{12}^2}{g_{11}}$:

$$-\frac{\hbar^2}{2m}\frac{\partial^2\psi_2}{\partial y^2} + g_{\text{eff}}\left|\psi_2\right|^2\psi_2 = \mathrm{i}\hbar\frac{\partial\psi_2}{\partial t} \tag{6.3}$$

For an immiscible symmetric mixture, such as $|1,-1\rangle/|1,+1\rangle$ for Rb atoms, $g_{\text{eff}} < 0$ and a stationary solution, normalized to N_2, is given by a bright soliton form:

$$|\psi_2(y)|^2 \equiv n_2(y) = \frac{N_2\kappa'}{2}\frac{1}{\cosh^2(\kappa' y)} \tag{6.4}$$

where we introduce κ' the typical inverse size of this effective bright soliton. The number of atoms N_2 and the size of the soliton are not independent parameters. In the low depletion limit, the minimization of the energy functional $E[\psi_2] = \int \mathrm{d}y \left[\frac{\hbar^2}{2m}\left|\frac{\partial\psi_2}{\partial y}\right|^2 + \frac{g_{\text{eff}}}{2}|\psi_2|^4\right]$ with the ansatz (6.4) connects the two parameters as:

$$N_2 = -\frac{2\hbar^2\kappa'}{m g_{\text{eff}}} \tag{6.5}$$

Furthermore, in the limit $\delta g = g_{12} - g \ll g$, we have $g_{\text{eff}} \simeq -2\delta g$, so (6.5) is rewritten as $N_2 = \frac{\hbar^2\kappa'}{m\,\delta g}$. To compare with the low depleted magnetic soliton solution (6.2), we adimensionalize the position by the spin healing length ξ_s (and κ' by $1/\xi_s$). Introducing $N = \frac{2N_2}{n_0\xi_s}$, the condition (6.5) writes: $N = 4\kappa'$. For the effective attractive single component picture (6.4), we thus get the following adimensionalized expression:

$$\frac{n_2(y)}{n_0} = \frac{\kappa' N}{4}\frac{1}{\cosh^2(\kappa' y)} = \kappa'^2\frac{1}{\cosh^2(\kappa' y)} \tag{6.6}$$

When considering the low depletion regime, the easy-axis magnetic soliton of the immiscible mixture is thus recovered using the effective attractive single component picture ($\kappa' = \kappa$).

We check numerically the proportionality relation $N_2 \propto \kappa \propto 1/\sigma_{\text{RMS}}$ (6.5) at low depletions (Figure 6.6(b)). For higher depletions, the variation of the RMS size with N_2 is smoother.

At low depletions $d \ll 1$, the profile put on DMD3 does not depend on the depletion since the arcsine functions of (6.1) can be linearized[10]. We thus imprint $\mathcal{D}(x,y) = \left(\frac{1}{\cosh^2(\kappa y)}\right)^{1/4}$ on DMD3 for a fixed value of κ and we vary the duration of the Raman pulse until we reach a number of atoms in the minority component that verifies (6.5). If d is not negligible compared to 1, the amplitude modulation function on the DMD depends on the targeted depletion and a priori the DMD modulation function should be changed each time a different depletion is targeted.

[10] For low depletions, we approximate $\arcsin\left(\sqrt{n_2/n_0}\right)$ by $\sqrt{n_2/n_0} = \sqrt{d}\frac{1}{\cosh(\kappa y)}$.

6.3.2 δg calibration

For low depletions and a fixed soliton size $1/\kappa$, there is only one atom number for which the wavepacket remains stationary (see Figure 6.6(b)). For a number of atoms smaller than the one checking (6.5), the wavepacket expands due to the larger kinetic energy compared to the interaction energy. Conversely, when the value of N_2 is greater, the wavepacket contracts as a result of the effective attractive interaction energy (see Figure 6.7).

Experimentally, we choose to realize a stationary magnetic soliton with $\sigma = 1/\kappa \simeq 5\,\mu\text{m}$ (Figure 6.6(a)). This results from a trade-off. For larger sizes, the stationary atom number (6.5) is < 200 and the atomic signals have to be averaged a lot for a good signal-to-noise ratio. For smaller sizes, the evolution $N(\sigma)$ is smoother (Figure 6.6(b)) and we could not distinguish an expansion or a contraction of the wavepacket when varying the atom number of the soliton. This is confirmed by numerical simulations (Figure 6.7(d)).

To achieve the most accurate $1/\cosh^2(\kappa y)$ density profile on the atoms, we implemented a feedback loop and adjusted the dithered profile on DMD3 until the difference between the targeted profile and the atomic one could no longer be improved (see Chapter 1).

For $\sigma = 5\,\mu\text{m}$, the evolution of the size for different N_2 is clear and we can isolate the atom number that leads to a stationary wavepacket up to a precision of ± 50 atoms. More precisely, we approximate the evolution of the RMS size of the wavepacket over time with a parabolic law. In 2D homogeneous Bose gases, this is an exact result from the Virial theorem [104]. In 1D, we also choose this form to fit the evolutions, but only with a phenomenological motivation. The expansion coefficient Γ, defined as $\sigma = \sigma_0 + \Gamma t^2$, is then plotted as a function of the atom number N_2. The stationary soliton, characterized by an expansion coefficient $\Gamma = 0$, is then isolated. We get $N_{2,\text{stat}} = 370 \pm 50$ with $\sigma = 5.3 \pm 0.3\,\mu\text{m}$.

At low depletions, the stationary atom number is directly proportional to the interaction parameter δg as shown in (6.5). Therefore, we can calculate it based on the previous measurement:

$$\frac{\delta g}{2\hbar} = (1.9 \pm 0.3) \times 10^{-7}\text{m/s} \tag{6.7}$$

We can compare this value with the one obtained in the previous section: we estimated $\omega_\perp \simeq 2\pi \times 400\,\text{Hz}$ and calculated $\delta a = 1.35\,a_B$ (with MDDI). This results in $\frac{\delta g}{2\hbar} = \omega_\perp \delta a = 1.7 \times 10^{-7}\text{m/s}$. The value obtained from the stationary low-depleted magnetic soliton is thus compatible with this estimation.

6.3.3 Conclusion

In conclusion, we were able to deterministically create a stationary magnetic soliton at low depletions. The evaluation of the stationary atom number resulted in a value of the parameter δg that is in good agreement with the prediction.

For higher atom numbers, as mentioned above, we were not able to clearly prove the stationarity of the wavepacket. For this, we tried to imprint the true solitonic waveform at a given depletion, deviating from a $1/\cosh^2(\kappa y)$ (see Figure 4.6), but we did not see a significant expansion or contraction when varying the atom number. This is numerically justified in Figure 6.7. More precisely, let us imagine that $N_2 = 1000$ corresponds to a soliton of RMS size $\sim 3\,\mu\text{m}$. Then, even if the depletion of the magnetic soliton is different when changing N_2 from 1000 to 1500, the RMS size does not change significantly (Figure 6.6), unlike the case for lower atom numbers

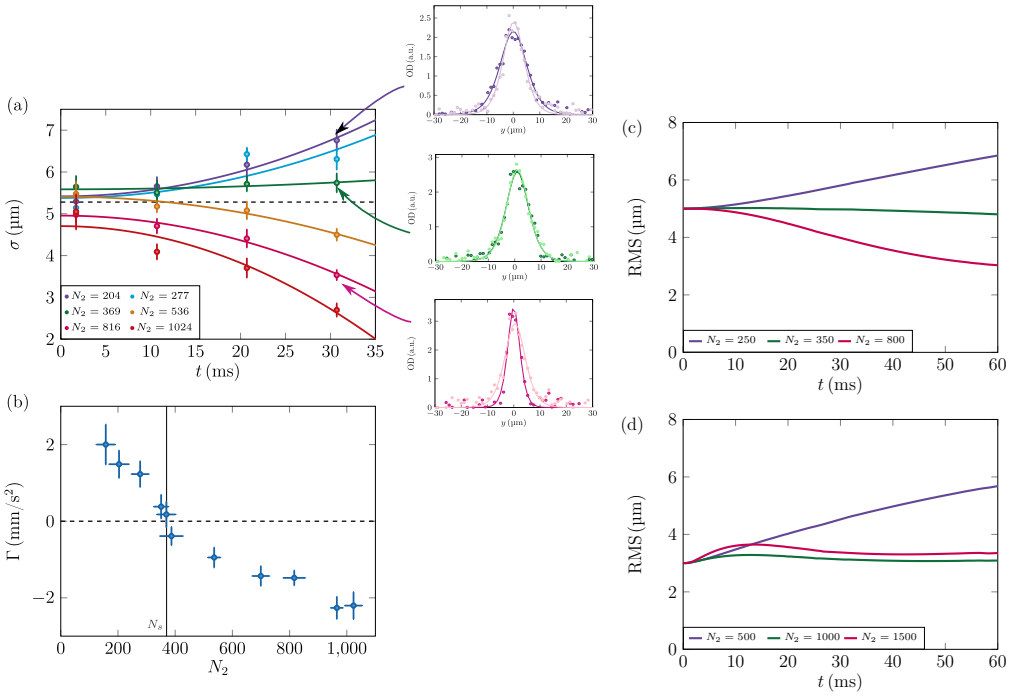

FIGURE 6.7: Experimental and numerical determinations of the stationary profile without a force. Calibration of δg. (a): The amplitude modulation on DMD3 is chosen to be of the form $1/\sqrt{\cosh(y/\sigma)}$ with $\sigma = 5\,\mu\text{m}$. The feedback loop is utilized to optimize on the atomic profiles the dithered pattern put on DMD3. The atom number in the minority component is varied (by varying the duration of the Raman pulse) and the evolution of the wavepacket size σ over time is observed in the regime of low depletions. In the case of small atom numbers, the wavepacket expands (violet example), while in the case of large atom numbers, the wavepacket shrinks (pink example). For intermediate atom numbers, the wavepacket undergoes minimal evolution (as shown by the green example, which represents the average longitudinal profile of Figure 6.6(a)). For the profiles, we show with a darker color the wavepacket for $t = 30\,\text{ms}$ and with a lighter color the initial wavepacket at $t = 1\,\text{ms}$. The dashed line corresponds to the average value of the initial sizes: $\sigma_0 = 5.3\,\mu\text{m}$. (b): From the previous evolutions, we extract an expansion coefficient Γ fitting the RMS sizes as $\sigma = \sigma_0 + \Gamma t^2$. We plot the evolution of this coefficient as a function of N_2. The stationary atom number N_s corresponds to $\Gamma = 0$ and its value is given by the vertical solid line. (c) and (d): We look numerically at the evolution over time of an initial wavepacket of the form $n_2 \propto 1/\cosh^2(y/\sigma)$ with $\sigma = 5\,\mu\text{m}$ (c) and $\sigma = 3\,\mu\text{m}$ (d). The experimental evolutions seen in (a) are confirmed by (c). In the case of (d), no clear contraction of the wavepacket is observed even for large atom numbers. This observation is interpreted as a consequence of the plateau seen in the evolution of $N(\sigma)$ in Figure 6.6(b) near $\sigma = 3\,\mu\text{m}$. Therefore, for large depletions, it is difficult to experimentally isolate the stationary profile within our spatial resolution.

when changing N_2 from 300 to 600. Thus, the wavepacket at $N_2 = 1500$ is a good approximation of the stationary wavepacket with RMS size $3\,\mu\text{m}$ and it does not evolve significantly over time. In other words, the scalar product between the two wavefunctions of $N_2 = 1000$ and $N_2 = 1500$ atoms is not significantly different from 1, unlike the scalar product between the two wavefunctions of $N_2 = 300$ and $N_2 = 600$ for example. The simulations indicate that a finer spatial resolution of the soliton size

evolution is necessary to determine a stationary wavepacket for large depletions. This smooth evolution of the stationary RMS size as a function of N_2 for large N_2 will prove to be "advantageous" in the next section. Indeed, since the RMS size of the true wavepacket is not far from 3 µm in the range N_2 between 800 and 1500, we will imprint the $1/\cosh^2(y/\sigma)$ profile with $\sigma = 3\,\mu\text{m}$ for all atom numbers. We will discover that the non-strict stationarity of this wavepacket does not perturb the soliton within our spatial resolution. It will greatly simplify the recipe for observing the oscillations and show that the phenomenon of Bloch-like oscillations is robust to the particular shape of the initial wavepacket used [48].

6.4 Oscillation of magnetic oscillations under a constant force

In Chapter 5, we demonstrated the peculiar response of an easy-axis magnetic soliton under a constant force. We now describe experimentally what happens to the soliton when it is submitted to such a linear potential. In practice, after preparing the gas in the tube and evaporating it, we add a small current in the MOT coils ($\sim 100\,\text{mA}$) and a bias field of $\sim 100\,\text{mG}$ along the y direction (longitudinal direction of the tube) to apply a magnetic gradient to the cloud, which is composed of atoms in the $|1,-1\rangle$ state. We let it thermalize for $\sim 500\,\text{ms}$ in the presence of this gradient. We then create the mixture with a Raman pulse followed by a MW pulse (see Figure 6.4). This corresponds to a quench of the application of the differential force by changing the internal state of part of the cloud. We then record the following dynamics.

6.4.1 Short times dynamics

First, it is natural to consider the beginning of the motion that could not be affected by the boundary conditions, eventual inhomogeneities in the box potential or atom number losses. We thus focus first on the short time dynamics of the wavepacket motion. Under an external adimensionalized force F, the solitonic wavepacket of magnetization N undergoes a force NF since we showed that its total momentum evolves as $\frac{\mathrm{d}P}{\mathrm{d}t} = NF$ (5.3). The dimensional expression for the center of mass motion (5.8) $y(t) = \mathcal{A}\left[1 - \cos\left(2\pi\frac{t}{T}\right)\right] + y_0$ can be linearized for $t \ll T$:

$$y(t) = y_0 + \frac{1}{2}\mathcal{A}\left(\frac{2\pi t}{T}\right)^2 \tag{6.8}$$

with $\mathcal{A} = \frac{2n_0^2\,\delta g\,\xi_s}{N_2 f \sinh\left(\frac{N_2}{n_0\xi_s}\right)}$ the amplitude of the oscillation (half of the peak-to-peak amplitude) and $T = \frac{2\pi\hbar n_0}{N_2 f}$ its period. Inserting the expressions of T and $\mathcal{A}$ in (6.8), we can also write it as:

$$y(t) = y_0 + \frac{f_{\text{eff}}}{2m}t^2, \text{with } f_{\text{eff}} = 4\pi^2 m\frac{\mathcal{A}}{T^2} = \frac{N_2 f}{n_0\xi_s \sinh\left(\frac{N_2}{n_0\xi_s}\right)} \tag{6.9}$$

At low times, the solitonic wavepacket thus exhibits particle-like behavior, with its dynamics governed by a Newtonian law of motion. However, the force in the expression represents an effective force experienced by the wavepacket. In adimensionalized units, the effective force writes: $F_{\text{eff}} = F\frac{N/2}{\sinh(N/2)}$. For low atom numbers in the minority component: $N_2 \ll n_0\xi_s$, the effective force coincides with the single-particle force acting on the system: $F_{\text{eff}} \simeq F$. It is reminiscent of the study of bright solitons under

a constant force (see Appendix E). This finding is not surprising since we showed in the section 6.3.1 that the dynamics of the magnetic soliton can be mapped onto effective single-component bright soliton dynamics in the low depletion regime.

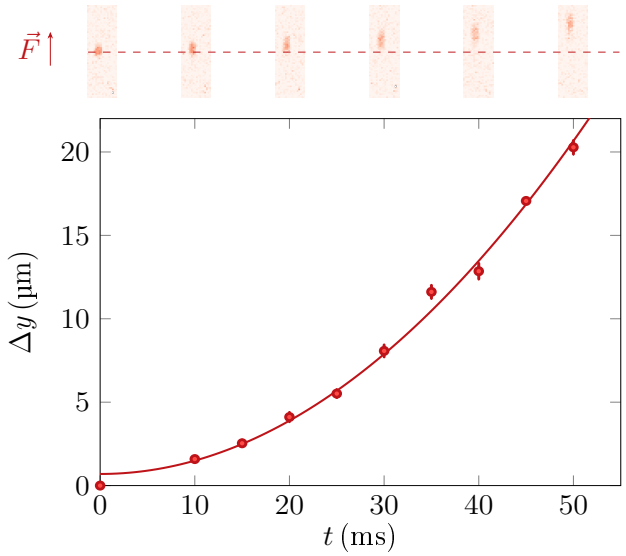

FIGURE 6.8: Short time dynamics of the wavepacket under a constant force. We apply a magnetic gradient $b' = 2.5\,\mathrm{G/m}$ to a wavepacket of $N_2 \simeq 150$ atoms in $|1,+1\rangle$ immersed in a bath of atoms in $|1,-1\rangle$ of density $n_0 = 3\times10^8$ atoms/m. The amplitude modulation on the DMD is $\left(\frac{1}{\cosh^2(\kappa y)}\right)^{1/4}$ with $\kappa = 1/(5\,\mu\mathrm{m})$. The dashed red line represents the initial position of the soliton wavepacket. The images shown are absorption images of the $|1,+1\rangle$ state only every 10 ms. The solitonic shape is lost during the evolution. The center of mass positions of the localized wavepacket are represented by the red dots. These positions are recorded as a function of the time spent by the mixture in the presence of the magnetic gradient. The solid line is a parabolic fit (see main text for the values).

Moreover, the expression (6.9) can be obtained from the expression of the effective mass of the magnetic soliton (5.22) at low velocities v, which is $m_{\mathrm{eff}} = \sinh(N/2)$.

We examine the solution (6.9) experimentally. As in the previous section, we locally shape the density profile of the transferred atoms in $|1,+1\rangle$ with a $1/\cosh^2(y/\sigma)$ function, $\sigma = 5\,\mu\mathrm{m}$. We operate at low depletions with atom numbers in the minority component checking $100 \lesssim N_2 \lesssim 200$ and a background bath density $n_0 \simeq 3\times10^8$ atoms/m. With such numbers, the $1/\cosh^2$ form of the wavepacket is in good approximation a stationary wavepacket. Moreover, with $\xi_s \simeq 2\,\mu\mathrm{m}$ for this density, we have $\frac{N_2}{n_0\xi_s} \lesssim 0.3$ and the approximation of the effective force by the external force leads to an error of only a few percent.

We apply a magnetic gradient directed mainly along the y direction given by $b' \simeq (2.5\pm0.1)\,\mathrm{G/m}$ measured with Ramsey spectroscopy (see Chapter 3 for a description of the calibration of the magnetic field gradient). We record the motion of the minority component wavepacket for times $t < 50\,\mathrm{ms}$ (the predicted period is $T \gtrsim 1\,\mathrm{s}$ for this small atom number). The result is shown in Figure 6.8. A parabolic fit accurately models the motion when a force is applied. From the fit, we extract a force $f = (2.1\pm0.2)\times10^{-27}\,\mathrm{N}$. We recall that this force is felt by the two components of the mixture which have opposite spin projections m_F and a Landé factor

$g_F = 1/2$. Thus, the magnetic gradient extracted from this low time dynamics expansion is $b' = \frac{f}{2g_F\mu_B} = (2.3 \pm 0.2)\,\mathrm{G/m}$. This value is compatible within 10% with the Ramsey spectroscopy calibration.

This study confirms the validity of the dynamical model for short time durations and low atom numbers. The measurement can also be considered as a precise force calibration when changing the point of view.

6.4.2 Bloch-like oscillations

The main experimental result of this chapter concerns the behavior of the magnetic soliton under a small magnetic gradient and for large atom numbers in the minority component.

More specifically, we vary the magnetic gradient between $\simeq 0.5\,\mathrm{G/m}$ and $2\,\mathrm{G/m}$. The 1D background density in the tube is kept constant at $\simeq 3.5 \times 10^8\,\mathrm{atoms/m}$. The number of atoms in the minority component can be changed between $\simeq 1000$ and $\simeq 1800$[11]. For the mixture $|1,-1\rangle/|1,+1\rangle$ of Rb, this leads to typical values of $N \simeq 5$ and $F \simeq 0.1$. From Figure 6.3, we deduce that these numbers are in the working regime identified in Chapter 5 from the adiabatic condition $F \ll 1$ and the low velocity condition $v_{\max} \lesssim c_s$. Moreover, the orders of magnitude give a period of $\sim 100\,\mathrm{ms}$ and an amplitude of a few µm, a regime accessible experimentally.

For these chosen atom numbers, we apply an amplitude modulation on DMD3 of the form $\left(1/\cosh^2(y/\sigma)\right)^{1/4}$ with $\sigma = 3\,\mu\mathrm{m}$. Ideally, if we want to imprint a stationary highly depleted soliton, we would have to change the waveform of the modulation on the DMD each time we vary N_2. This is due to the fact that the general modulation form depends on the depletion (6.1). However, experimentally, it is more convenient to work with a fixed pattern on the DMD and vary the atom number without changing the pattern's family of functions. As previously stated, the wavepacket created should not be significantly disturbed during evolution, even if it is not perfectly stationary and a "true" soliton. Indeed, the $1/\cosh^2$ profile with $\sigma = 3\,\mu\mathrm{m}$ only slightly deviates from the true solitonic profile within the explored range of atom numbers (see Figures 4.6 and 6.6). However, it was not initially evident that the interpretation of Bloch-like oscillations would persist prior to conducting the experiment with these initial profiles.

Figure 6.9 displays examples of absorption images of the $|1,+1\rangle$ atomic density distribution in the tube at different hold times in presence of the force. The $|1,+1\rangle$ atoms are immersed in a bath of $|1,-1\rangle$ atoms, which are not seen on these images[12]. Under the influence of a constant force, the localized wavepacket initially moves in the direction of the force $+\mathbf{y}$. The wavepacket contracts (b) and then turns back after $\simeq 100\,\mathrm{ms}$ of evolution. It reaches the initial point after $\simeq 200\,\mathrm{ms}$. For some atom numbers, we observe up to four periods of oscillation. We cannot record further due to the inevitable loss of atoms in the mixture (see Figure 6.2). The tube length is 60 µm and the wavepacket's observed U-turn cannot be attributed to the borders of the tube.

Furthermore, when varying the parameters, particularly N_2 by changing the duration of the Raman pulse and the magnetic gradient, Figure 6.10 confirms a dependence of the oscillation frequency ν on most of the points in the form of $\nu = N_2 f/(h n_0)$.

[11] The atom number N_2 and the bath density n_0 are extracted by a pixel count in time-of-flight measurements. *In situ* measurements lead to a slight ($\sim 10\%$) underestimation of these quantities.

[12] We also imaged the $|1,-1\rangle$ atoms separately, but it was experimentally difficult to resolve the hole in their density profiles, even for large depletions. However, we confirmed that the total density remains constant during the evolution.

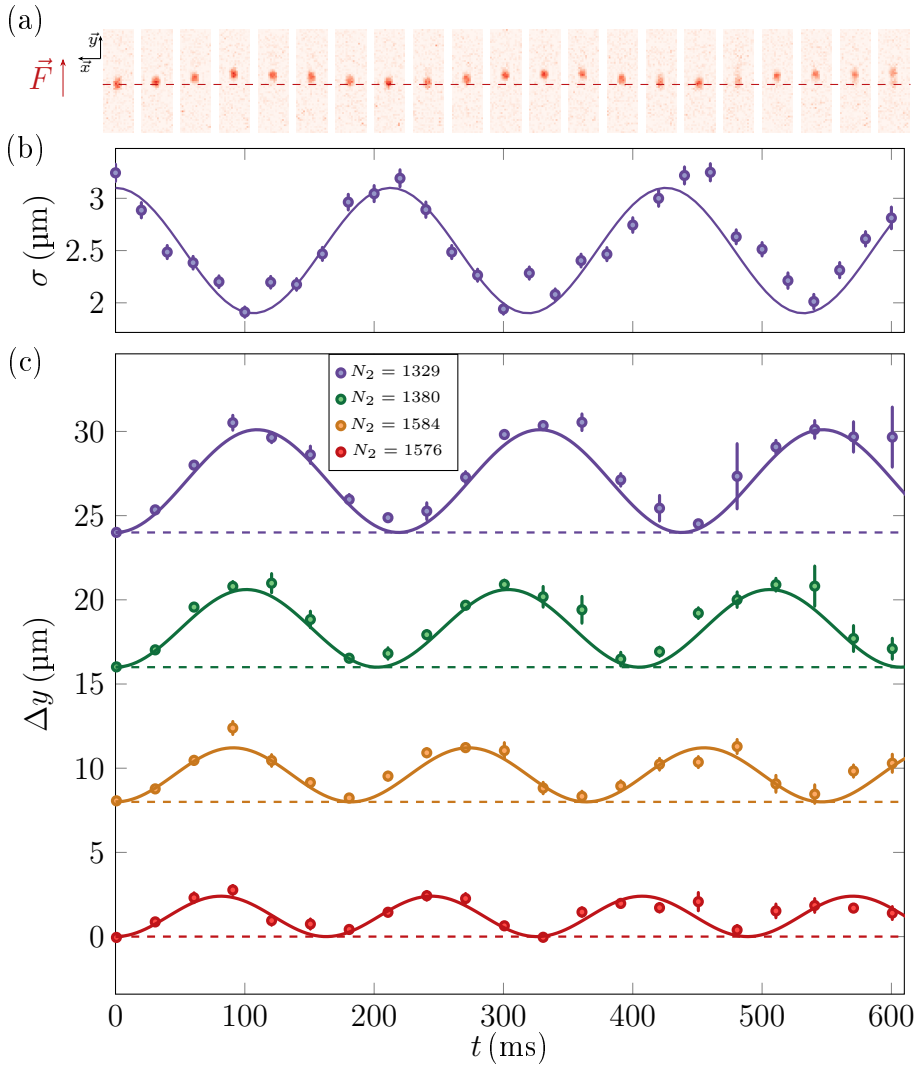

FIGURE 6.9: Bloch-like oscillations in a tube. We prepare an immiscible mixture with a localized wavepacket in the center with a $1/\cosh^2(y/\sigma)$ profile, with $\sigma = 3\,\mu\text{m}$, and subject it to a constant force $f = 9.2 \times 10^{-28}\text{N}$ (*i.e.* a magnetic gradient $b' = 1\,\text{G/m}$). We let it evolve for a certain time t in the presence of the force. (a): Absorption images of the density profile of the $|1, +1\rangle$ atoms for an atom number $N_2 = 1329 \pm 50$. The time between each frame is 30 ms. (b): Evolution of the typical size σ of the wavepackets of (a). We obtain it with a fit of the density profiles with a function $1/\cosh^2(y/\sigma)$. The solid line is a sine fit for the time evolution of the size. (c): The evolution of the wavepacket's center of mass was observed for different atom numbers N_2 under the same force. The amplitude of the oscillations decreased as the atom number increased, and the period of oscillation decreased as well. The top curve corresponds to the soliton's movement observed in the absorption images in (a), as well as its size evolution in (b). Sinusoidal fits were performed and are represented by the solid lines.

This phenomenon is interpreted as Bloch-like oscillations in this system that exhibits a periodic dispersion relation, as seen in Chapter 4.

For the gradients between 0.5 and 1.5 G/m, we observe a good agreement between the expected period and the measurement over a range of frequencies between 3 and 7 Hz. For larger magnetic gradients, our measurements deviate systematically from

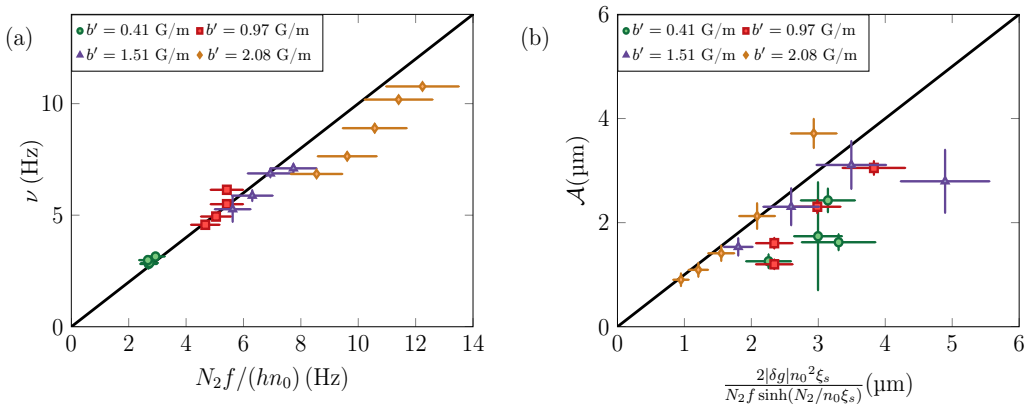

FIGURE 6.10: Experimental measurement of the period and amplitude of the Bloch oscillations for different magnetic gradients. We extract them with sinusoidal fits to the center of mass evolutions (examples were given in Figure 6.9). The horizontal axes are rescaled so that the analytical predictions (5.12) are linear lines with slope 1 (black solid line). The points of Figure 6.9 are the red squares.

the predictions. It is not clear why this is the case. The GP simulations performed still give a good agreement with the analytical predictions. Regarding the amplitude of the oscillations, the agreement with the analytical prediction is only qualitative. However, its expression as a function of the physical parameters is non-linear and less fundamental than the period formula.

In conclusion, we were able to observe and characterize Bloch oscillations in an immiscible mixture in the adiabatic regime. The agreement with analytical predictions is satisfactory. The observed phenomenon appears to be robust with respect to the initial wavepacket shape.

6.4.3 Beyond the adiabatic regime

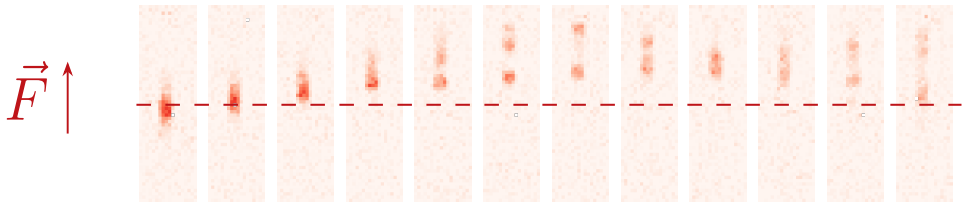

FIGURE 6.11: Fragmentation of the soliton. Absorption images of the $|1,+1\rangle$ component are shown for an initial cloud of $N_2 = 1300$ atoms (same as in Figure 6.9) and a force $f = 3.7 \times 10^{-27}$ N, corresponding to a gradient $b' = 4\,\mathrm{G/m}$ applied to the mixture (four times larger than the one of Figure 6.9). They are taken every 10 ms. The analytical prediction would give a period $T \simeq 35$ ms and an amplitude $\mathcal{A} \simeq 3$ µm. However, we observe at $t \simeq 20$ ms $\simeq T/2$ that the soliton fragments into two wavepackets. One of them continues to move in the direction of the force until it reaches the boundaries of the tube at $t \sim 60$ ms while the other remains approximately at the same position. The wavepackets "meet" again at time $t \sim 80$ ms.

When the force, or more generally the adimensionalized parameter $F = f\xi_s/(n_0\delta g)$, is increased, the analysis of the wavepacket dynamics is more complex.

As demonstrated in the simulations, the wavepacket experiences dislocation during propagation, resulting in the loss of the soliton's particle-like nature. An example of such a time evolution is presented in Figure 6.11.

6.4.4 Bath phase evolution

In Chapter 5 we saw the importance of the phase of the majority component in interpreting this phenomenon. Following the work of Bresolin et al. [48], the observed oscillations were explained as a consequence of an AC Josephson effect with a non-standard barrier: the mobile minority component itself. It arises from a peculiarity of the magnetic soliton: the majority component phase difference between each side of the localized wavepacket is directly proportional to the total momentum of the soliton.

To continue the experimental study of these oscillations, we thus measure the phase of the majority component while applying a constant force.

To do this, we slightly modify the experimental procedure. We prepare the condensate in $|1,-1\rangle$ in a two-tube geometry of $60 \times 3\,\mu\text{m}$ each, instead of one tube, with DMD1 (still with 50 images separated by 10 ms, see Figure 6.12). We then apply a magnetic gradient to the cloud and let it thermalize for $\sim 500\,\text{ms}$. A localized wavepacket is then formed only at the center of the right tube by adapting the DMD pattern. The atoms in the left tube are not affected by the Raman pulse and serve as a reference with a uniform matter-wave phase.

We then wait for a certain amount of time in presence of the constant force. The soliton in the right tube experiences Bloch-like oscillations, while the (tilted) bath remains stationary in the left tube.

The initial tubes are separated by $d_t = 4\,\mu\text{m}$. After a time of flight t_{TOF} of a few ms, we expect phase-coherent clouds to interfere. For linear tubes expanded in the plane, we predict to see spatial fringes, parallel to the axis of the tubes, with a period i given by $i = \frac{2\pi\hbar t_{\text{TOF}}}{m d_t}$ (see for example the historical experiment [12]). For a distance $d_t = 4\,\mu\text{m}$ between the tubes and a TOF duration of $t_{\text{TOF}} = 4\,\text{ms}$, we get an interfringe of $\simeq 5\,\mu\text{m}$, which is accessible with our imaging system. The g_1 correlation function, briefly introduced at the end of Chapter 2, reflects the spatial phase ordering of a matter wave. When the gas is confined in 1D/2D, there is no true long range order even at $T = 0$. At large distances, the phase coherence is lost, causing g_1 to decrease to zero. However, in these finite-sized systems, g_1 remains sufficiently close to 1 throughout the tube, so that the phase coherence is maintained and the interference of the two tubes can be observed with a good contrast.

If this is the case and if the left tube keeps the same uniform phase as before the separation into two tubes, the measurement of the relative position of the fringes across the soliton at positions y_+ (above the soliton) and y_- (below the soliton) provides access to its momentum P (see (4.44)):

$$\phi_{1,y_-} - \phi_{1,y_+} = \frac{1}{2}P \tag{6.10}$$

In other words, this interference method translates the measurement of the spatial phase of the interference pattern to the measurement of the phase of the wavefunction.

Experimentally, the procedure is more complex than it initially appears. Releasing the strong confinement along the vertical direction causes the cloud to rapidly expand

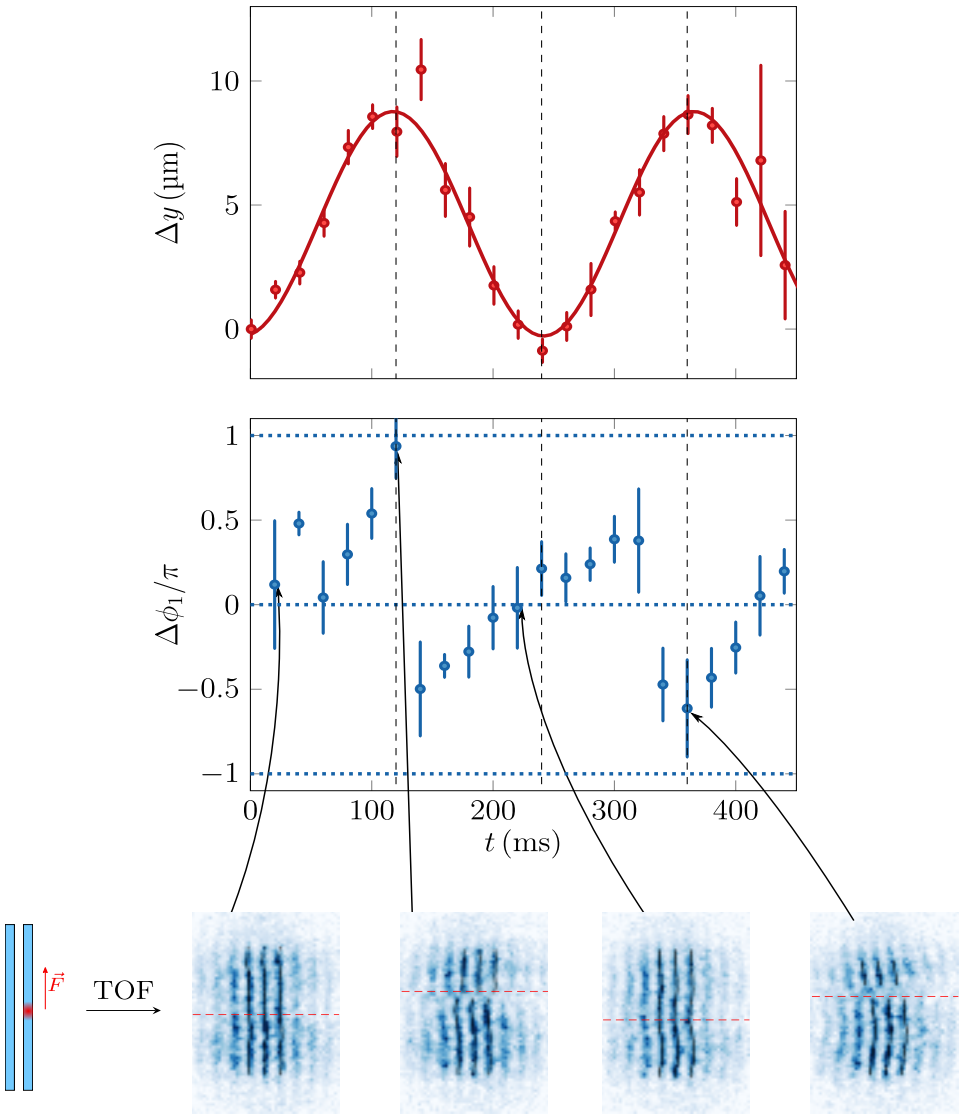

FIGURE 6.12: Bath phase difference across the soliton under the action of a constant force. We prepare two tubes filled with atoms in $|1,-1\rangle$ as described in the main text with a density $n_0 = 3 \times 10^8$ atoms/m. A constant force is applied to the cloud with a magnetic gradient of $b' = 1\,\mathrm{G/m}$. We spatially shape the density profile of the atoms transferred in $|2,0\rangle$ with a $1/\cosh(y/\sigma)^{1/4}$ function on DMD3 ($\sigma = 3\,\mu\mathrm{m}$) and Raman beams. The atom number in component 2 is $N_2 = 1200$. A mask is applied on the left tube so that only the right tube is populated with atoms in $|2,0\rangle$. A MW pulse is then applied to create the immiscible mixture $|1,-1\rangle/|1,+1\rangle$. Then, for each waiting time t in the presence of the force, we perform two different sequences. Either we image the $|1,+1\rangle$ atoms and record the position of the minority component wavepacket (which we call the soliton position) as we did in Figure 6.9 (top panel), or we perform a phase measurement by turning off the trap confinements and letting the two tubes interfere. We image the $|1,-1\rangle$ atoms and get interference patterns like those represented in the bottom panel. An analysis of the phase of the fringes above and below the soliton yields the phase difference of the majority component matter-wave across the soliton and is plotted in the middle panel. The vertical dashed lines represent integer multiples of $T/2$. The blue dotted line marks $\Delta\phi_1 = \pm\pi$ and the red horizontal dashed line shows the position of the soliton as determined in the top panel.

within the box, resulting in a noisy fringe signal. To mitigate this issue, the following experimental steps are performed:

- After the mixture is held for a varied amount of time in the presence of the magnetic gradient, we abruptly lower the power of the accordion beams by a factor ~ 7 and thus lower the accordion frequency by a factor $\sqrt{7} \sim 2.6$ ending up at $\omega_z \simeq 2\pi \times 1.5\,\mathrm{kHz}$.
- It triggers a horizontal plane breathing mode at the specific frequency $2\omega_z$ [104]. To be insensitive to this breathing mode, we thus wait half a period of this oscillation: $t_{\mathrm{wait}} = \pi/\omega_z \simeq 150\,\mu\mathrm{s}$ before turning off the box potential.
- We then perform a 2D TOF (with the accordion still lowered) of 3 ms.
- Finally, we switch off the accordion completely and perform a 3D TOF of 4 ms.

With these experimental parameters, interference patterns similar to the ones shown in Figure 6.12 were obtained. Solid black lines were added to the absorption images to guide the reader, and were obtained by finding the extrema for each picture line. Additionally, an oscillation run for the center of mass was interlaced with the interference run. For a given waiting time in the presence of the force, we can thus extract the center of mass position of the soliton (top panel) and the corresponding map of the phase of the bath through the fringe images. A dashed red line indicates the position of the soliton. The fringes are not perfectly parallel to the tube's axis, which is unexpected. This is likely due to slight spatial decoherence over time between the two tubes. For a waiting time $t \sim 120\,\mathrm{ms}$, corresponding to the first wavepacket's U-turn, there is a noticeable dislocation of the fringes around the position of the soliton. Maxima of the interference pattern above the soliton are prolonged with minima of the interference pattern below the soliton, *i.e.* the difference of the majority component matter-wave phases above the soliton and below $\Delta\phi_1$ is close to π. This is what we expect in the Josephson picture.

More quantitatively, we measure the phase difference of the bath across the soliton for each waiting time. To do this, we take a region of 8 pixels ($\sim 9\,\mu\mathrm{m}$) above and below the soliton[13]. For each of the two zones, we calculate the average phase of the interference pattern over 4 fringes. $\Delta\phi_1$ is then obtained by taking the difference of the phase of the interference patterns above and below the soliton. However, this analysis procedure resulted in blurred signals due to the tilt of some fringes. To address this issue, we applied a high-pass filter to the phase difference signal. The resulting data is shown in the middle panel of Figure 6.12.

We recall that since P is proportional to $\Delta\phi_1$, and since P evolves linearly in time due to the constant force, the evolution of $\Delta\phi_1$ is predicted to be piecewise affine, with phase jumps of 2π every $t = (2k+1)T$, where k is an integer and T is the period of the oscillation. The π phase difference at $t = T$ and $t = 3T$ are well predicted. However, there are some deviations from the piecewise affine evolution. To ensure a better phase coherence of the tubes and reduce noise in the data, additional care may be required in preparing the tubes. It is worth noting that this interference experiment was repeated for other parameters, and π phase differences at the turning point position of the soliton were also observed.

[13] Its position is determined in a juxtaposed run as we said above.

6.5 Conclusion

In this chapter, we experimentally demonstrated the realization of an easy-axis magnetic soliton within an immiscible mixture and analyzed its response to a constant differential force, as proposed by Bresolin et al. [48].

First, we described two related experiments that also realized magnetic solitons, but with miscible mixtures, known as easy-plane magnetic solitons. We then discussed the necessary experimental ingredients to achieve our objective: a (quasi-)1D geometry for the spin dynamics, an immiscible and long-lived mixture, a spatial control of the spin density profile and the application of a small differential force. The first realization (to the best of our knowledge) of a stationary easy-axis magnetic soliton was described in the third section. It was demonstrated that the stability of the magnetic soliton is maintained in this non-strictly one-dimensional geometry as long as the spin healing length, which is the key length scale of the problem, is small or of the same order of magnitude as the transverse size of the tube. We showed how to calibrate the δg coefficient of the mixture in the low depletion regime.

In the last section, we experimentally demonstrated that a magnetic soliton reacts to a constant force by exhibiting periodic oscillation, a quantum effect. Our results are in agreement with the theoretical predictions for times up to 1 s. The period of oscillations can be used to measure a small constant force with high precision, such as in the case of Bloch oscillations in optical lattices and the measurement of the gravity acceleration g [207]. It was found that as long as the adiabatic approximation can be carried out, the observed oscillations remain robust even if the initial shape of the wavepacket is not exact. Additionally, the description was extended to include measurements not only of the position of the soliton X, but also its total momentum P. Data for the bath phase during the evolution under the constant force were presented using an interference method. We identified a π phase difference for the bath matter-wave across the soliton for times $t = (2k+1)T$ where k is an integer, as predicted. The measurements of the two variables, namely the center of mass position of the soliton and its momentum, are in good agreement with each other and with the theoretical predictions in the adiabatic regime. Thus, we obtain a comprehensive understanding of the dynamics of a magnetic soliton under a constant force.

To go further, we can consider the presence of a non-constant external magnetic gradient, acting as a non-constant external force, which may modify the oscillatory behavior. Furthermore, the tube's geometry complicates the discussion of the *backflow* concept introduced at the end of Chapter 5, as the bath experiences multiple reflections against the walls. To address these two topics, one approach is to keep a constant applied force and examine a finite annular geometry with periodic boundary conditions. This approach is suitable because the soliton movement can be described using polar coordinates and the force remains unidirectional. As a result, the potential seen by the soliton is sinusoidal instead of linear. Additionally, the periodic boundary conditions provide a better framework for highlighting the backflow. This project is ongoing within the team.

Can Bloch-like oscillations be observed in nonlinear systems other than the ultracold atoms platform? Let us consider the photonics platform. Recently, temporal vector solitons were demonstrated in single-mode birefringent fibers, where cross-polarization phase modulation couples the two orthogonally polarized modes propagating in the fiber. An example of this is the realization of a dark-bright soliton in [177] and their analytical description can be found in [232]. However, it is unclear how to apply a differential potential on the two polarization modes in this system. Other

platforms, such as polaritons or quantum fluids, could be considered to observe this phenomenon.

Part IV

Production of an all-optical Rb BEC for a new generation of experiments

Chapter 7

An all-optical Rubidium Bose-Einstein Condensate for Rydberg dressing

This chapter describes the construction of a new setup designed to address Rydberg excitations in cold samples of Rubidium atoms in the near future. We obtain a Bose-Einstein Condensate without a magnetic trap and with a sequence lasting under 10 s. The laser and vacuum systems are similar to the ones of the setup already in place in the team at Collège de France, which has been producing uniform atomic 2D samples of Rubidium since 2016 (as detailed in Chapter 1), and with whom we discussed scientific projects in Chapters 3 and 6. The main novelty is the implementation of the *painting* technique to load more atoms from the molasses, without the need for a magnetic trap. This technique may be useful in the future of the team and we will report its principle and use. In the coming years, the two setups may be merged to combine the specificities of the already running 2D experiment (accordion lattice, DMDs, Raman beams, precise MW field generation) with this new one (painting, Rydberg dressing) to study strongly interacting gases in reduced dimensions.

7.1 Design and goal of the setup

The design of this setup is now clarified, following a set of guiding principles.

7.1.1 Goal

Transferring atoms into a quadrupole trap, as described in Chapter 1, is a reliable method to increase the density of the cloud before loading the atoms into an optical dipole trap. However, it has some drawbacks. Firstly, the transfer to the quadrupole magnetic trap and the subsequent evaporation step, which lasts about 12 s, are the most-time consuming steps of the sequence, accounting for nearly half of the total sequence duration. Secondly, the magnetic trap requires large coils around the cell to create a gradient of approximately 200 G/cm. To handle such high currents during ~ 10 s, water-cooling of the coils is necessary. This introduces an additional complication that we aim to avoid. Additionally, thermalizing the quadrupole coils typically takes one hour per day.

If no additional steps are included in the sequence, getting rid of the magnetic trap step before going into a conservative optical trap obviously worsens the loading of very dilute optical molasses (a volume of 1 mm^3 typically) into the dipole trap (a typical volume of $100 \times 30 \times 30\,\mu m^3$). Several optical techniques have been developed in the community to obtain a large BEC (typically 10^6 atoms) without a quadrupole trap. We can consider using an optical lattice to perform polarization gradient cooling [233],

or cooling the sample via Raman beams [234]. Instead, in our case, we directly load an optical dipole trap from the molasses using intermediary optical powers available on the table. A high loading efficiency is achieved by using dynamically shaped dipole beams via the painting technique. Further details on the process can be found in section 7.3.4.

7.1.2 Design and vacuum system

With these ideas in mind, we began building a new setup in January 2021. In March 2021, the system was put under high vacuum, and in May 2021, we obtained the first signal of atoms trapped in a Magneto-Optical Trap. Together with Franco Rabec, another PhD student, we optimized this signal and implemented the painting technique to reach an optical dipole trap by the end of 2021. Guillaume Brochier joined in April 2022, and we attained the first BEC in July 2022.

Our vacuum system operates on the following principle. We separate the atomic source cell, where the atoms are realeased from a dispenser, and the science cell, where we manipulate, cool and trap the cloud. To avoid collisions between the Rubidium atoms and residual ones, which would decrease the cloud lifetime, extremely low pressures are required in the science cell. To achieve this, we use two stages of differential pumping to decrease the pressure between the atomic source cell and the science cell. The vacuum system was designed to minimize the distance between the two cells, resulting in negligible atom fall during propagation. This allows for the use of small aperture connections to capture atoms from the atomic source cell and further reduce pressure in the science cell.

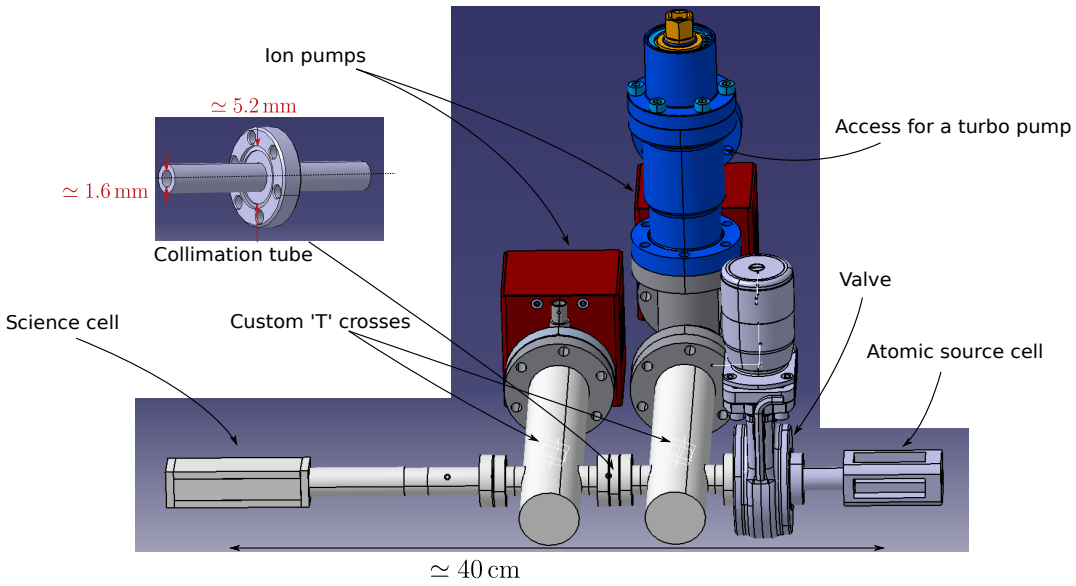

FIGURE 7.1: Drawing of the vacuum system. On the right is the atom source cell where the 2D MOT is performed. It is separated from the main vacuum system by a valve. Two ion pumps together with a differential pumping tube allow to reach $< 1 \times 10^{-10}$ mbar in the science cell shown on the left of the drawing. We display a zoom on the collimation tube carrying out one of the differential pumping stages. There is also an access to a turbo pump near one of the ion pumps. The total longitudinal distance of the vacuum system is $\simeq 40$ cm.

We use a commercial cold atom source of Rubidium provided by ColdQuanta. It consists of a compact $25 \times 15 \times 15$ mm glass cell with metal dispensers, integrated into

our vacuum system. A vapor source of Rubidium is released in the cell through Joule heating of one of the dispensers. A typical electrical current of 3 A under a voltage of 1.5 V is used. For a higher current, the number of atoms loaded is not increased and for a lower current, the number of released atoms is poor.

A valve (VAT Mini UHV gate valve, Series 010, DN16) is positioned next to the atom source cell to have the possibility to isolate it from the Ultra High Vacuum system. Two stages of differential pumping are used in order to decrease the pressure between the two cells. The two ingredients needed for differential pumping are a difference of diameter in the vacuum connection and a pump on the side where the vacuum is higher. The first stage is provided by a pinhole at the output of the 2D MOT cell and a first ion pump. We use a differential pumping tube reducing the diameter of the connection to the science cell from $\simeq 5.2\,\mathrm{mm}$ to $\simeq 1.6\,\mathrm{mm}$ and another ion pump for the second stage. The two ion pumps (SAES NEXT Torr Z200) pump at a rate of $\simeq 1\,\mathrm{L/s}$. They use the non-evaporable getter technology, which increases the pumping rate up to $\sim 200\,\mathrm{L/s}$. It is composed of a film of an alloy of various elements, such as Zirconium and Titanium, which captures and removes residual gases in the system either through adsorption or chemical means.

When the system was placed under high-vacuum, we activated the ion pumps once the pressure dropped below 10^{-5} mbar (obtained thanks to a turbo pump). The getter was activated later once the pressure reached below 10^{-7} mbar. It was only necessary to activate it once.

An exact measurement of the pressure in the vacuum system is not available. Only typical pressures below $1 \times 10^{-10}\,\mathrm{mbar}$ are given by the read-out of the ion pumps. We had to bake out the atomic source cell for a few days at $200\,^{\circ}\mathrm{C}$ in order to increase desorption rates on the cell walls. The pressure next to this cell decreased from 10^{-8} to $1 \times 10^{-10}\,\mathrm{mbar}$. Figure 7.1 provides an overview of the vacuum system.

The ion pumps are connected to the main axis of the vacuum system using custom "T" crosses in order to minimize the distance between the atomic source cell and the science cell. The remaining limiting factor if we were to do a more compact system is probably the size of the science cell from Hellma, which is 15 cm long to optimize the metal/glass contact.

7.2 Cooling and imaging: 780 nm lasers

We now detail the laser setup at 780 nm. This allows us to cool the cloud up to the molasses step and image it.

7.2.1 Preparation of the beams

The light used for the cooling stages is provided by a 3 W Toptica TA PRO laser at 780 nm. The beams are prepared on a separate table using AOMs to precisely control their frequencies and powers (Figure 7.2). The arrangement of the table is similar to what is done on the already running experiment, described in Chapter 1, and detailed in [68, 69]. The laser output frequency should be well-controlled to avoid drifts over time caused by temperature, current variation of the diode or alignment change of the grating. Implementing a feedback action on these parameters and using an independent frequency reference are necessary. To accomplish this, a saturated absorption setup with a Rb cell is used. The cell contains only the ^{87}Rb isotope. The

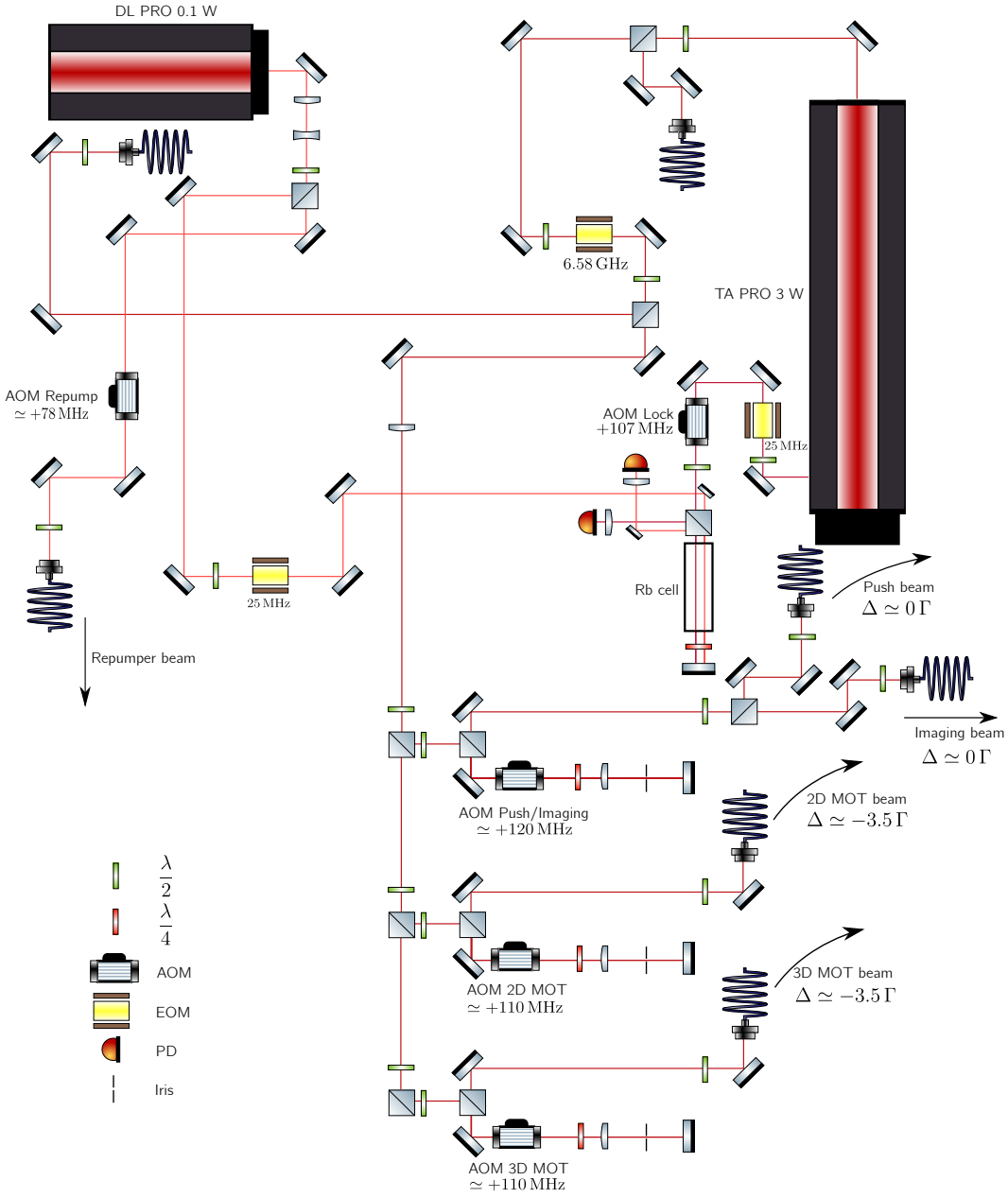

FIGURE 7.2: Drawing of the 780 nm lasers preparation table. On the right, we use light coming from a TA PRO 3 W to provide the light needed for the 3D MOT, 2D MOT, push and imaging beams. We give the values of the detunings compared to the $F = 2 \rightarrow F' = 3$ line during the MOT loading in units of $\Gamma \simeq 6$ MHz, the natural line width of the first electronic excited level. A lock on a Rb cell is also represented. On the left, we prepare the light needed for the repumper beam. It is also locked on the same Rb cell.

targeted line is the crossover (CO) $F' = 2$ / $F' = 3$ line (Figure 1.1). A Qubig wedged[1] EOM (PM7 - NIR), which generates sidebands at ± 25 MHz, modulates the laser light which, after passing through the Rb cell twice, reaches a photodiode. Demodulation

[1] In principle, the wedged design allows the elimination of the interference between the carrier and the two orthogonal sidebands and thus enables the reduction of noise in the modulated light [235].

within a Pound-Drever-Hall electronic scheme results in an antisymmetric error signal, needed for the feedback action[2] and locking of the laser on the atomic line.

The main output of the laser at 2.5 W goes through an EOM (New Focus 4851) which modulates the light at 6.58 GHz[3]. The level of the created sidebands is $\simeq 10\%$. One of them is essential in the cooling process to pick up atoms that have accidentally fallen into $F = 1$ and thus to have a cycling transition $F = 2 \rightarrow F' = 3$.

After passing through the EOM, the beams carry the two sidebands. Their amplitude can be controlled using a mixer[4] and their relative position with respect to the carrier can be adjusted with a VCO (Voltage Controlled Oscillator ZX95-6740C-S+ from Mini-Circuits).

The outgoing beam is then splitted into three different parts: Imaging/Push, which should output a resonant light, 2D MOT and 3D MOT light which are typically detuned by -20 MHz with respect to the cooling transition. To precisely control the power and frequency of these paths, we use AOMs (AA MT110-A1.5-IR) mounted in a double-pass configuration [236] so that the alignment of the fiber is unchanged when the frequency of the AOM is modified. They are aligned with a cat's eye [237] lens to further increase the frequency range of high diffraction efficiencies. We typically reach 50% of efficiency for the combination of double-pass AOMs and fiber couplings.

The repumping light produced by the sidebands of the EOM is essential for the cooling up to the molasses step. However, it is convenient to have another generation of repumping light, independent of the 2D MOT and 3D MOT beams, for example to bring atoms from the long-lived $F = 1$ state to the imaging light-sensitive $F = 2$ state. For this we use light from a diode laser DL PRO from Toptica[5]. It is locked on the same Rb cell as the TA laser, but on a different line, the CO $F' = 1$ / $F' = 2$[6]. An AOM (AA MT80-A1.5-IR) allows to specifically target the repumping line (see Figure 1.1).

7.2.2 2D MOT

We now return to the main table experiment and describe the various steps of cooling.

The production of a cold atomic sample begins in the atomic source cell where a dispenser of Rb is heated to $\sim 60\,^{\circ}$C, releasing atoms into the cell. They are captured in a 2D Magneto-Optical-Trap, the combination of two circularly polarized retroreflected beams along two orthogonal directions and a magnetic gradient. ColdQuanta provides the permanent magnets that generate a quadrupolar magnetic field of $\simeq 37$ G/cm needed to trap the atoms in the 2D MOT cell. The 2D MOT beams are shaped with cylindrical lenses of aspect ratio 2:3 to fit the shape of the cell so as to cool the largest possible number of atoms. The optical power per beam is $P \simeq 60$ mW and their waist is $\simeq 8 \times 12$ mm. They are detuned by $\simeq -20$ MHz from the resonance.

Another light beam, linearly polarized and called the push beam, is switched on simultaneously to transfer the trapped atoms into the main cell. It propagates in the

[2] The feedback acts on the diode current.

[3] The frequency is chosen so that atoms can be repumped from $F = 1$ to $F' = 2$ with this light passing through the double-pass AOMs.

[4] We need for example to suppress them for the imaging step. Its reference is ZAD-1H+ from Mini-Circuits.

[5] It would be difficult to use this laser for repumping atoms during the cooling steps because we would have to overlap the beam with the 2D and 3D MOT beams.

[6] This is different from the choice of the Rb experiment already running at Collège de France, used throughout this thesis, where the line chosen was the line $F = 1 \rightarrow F' = 2$.

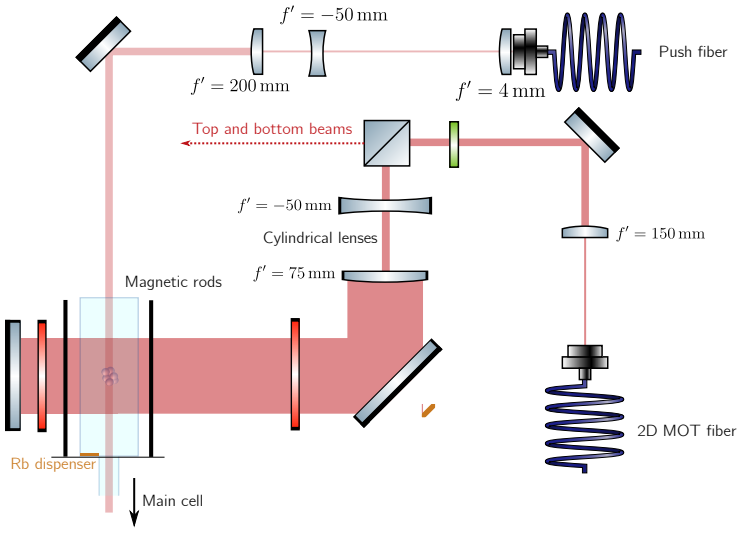

FIGURE 7.3: Drawing of the 2D MOT table. Two retroflected beams illuminate the atomic source cell where a piece of Rb is heated. The required circularly polarized beams are obtained with $\frac{\lambda}{4}$ waveplates. Permanent magnets (black rods) around the cell furnish the proper magnetic field map (we draw two of them but there are two others not shown here). Cylindrical lenses allow anisotropic shaping of the beams. We have not shown the retroflected beams that cool the atoms in the vertical direction. A push beam brings the cloud to the main cell where the other cooling steps take place.

non-trapped direction, the longitudinal axis of the vacuum system. Its waist is $\sim 2\,\mathrm{mm}$ and its power is $\sim 2\,\mathrm{mW}$. It is resonant with the cycling transition $F = 2 \rightarrow F' = 3$.

7.2.3 3D MOT

On the other side of the vacuum system, *i.e.* in what we call the science cell, a 3D MOT is performed. We shine, during 3 s, six MOT beams at the center of a quadrupole trap provided by two vertical circular coils. This is where the cold atomic sample, pushed out of the 2D MOT cell, is further cooled along the three directions and captured. There are four orthogonal beams in the plane, two of which form an angle of 45° with respect to the push beam direction. The other two propagate vertically and pass through the MOT coils. Each beam has a power of $\simeq 40\,\mathrm{mW}$, a detuning of $-20\,\mathrm{MHz}$, and a waist of $\simeq 6\,\mathrm{mm}$[7].

The MOT coils are mounted on a 1 inch base circular plate. They are placed vertically as close to the cell as possible and consist of 15 turns. A current of 5 A is sufficient to provide the required gradient of $\simeq 30\,\mathrm{G/cm}$. Additional bias coils, mounted in Helmholtz configuration, allow the magnetic field around the cell to be controlled and thus the center of the quadrupole trap to be shifted.

Two imaging beams are used. One of them is located in the horizontal plane and makes an angle of 60° with respect to the push beam. Its magnification can be changed between the values 1.3 and 0.4. The other one is almost vertical (there is a small angle with respect to one of the vertical MOT beams, so we can separate the two beams under the table) and its magnification is 2.5. The camera used are Lumenera Camera LM-135M.

[7] We are limited by the size of the optics used to bring the 3D MOT beams to the cell.

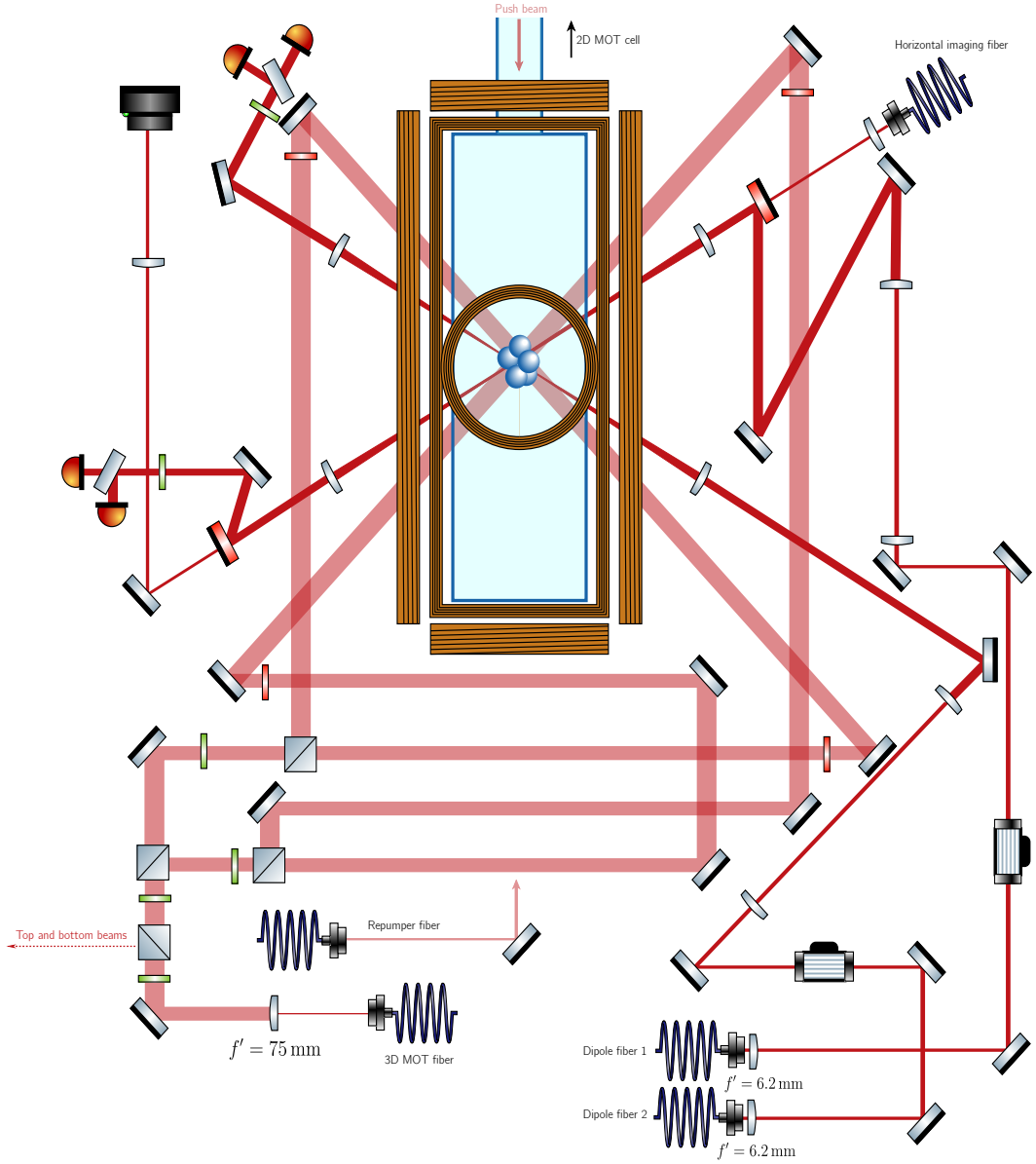

FIGURE 7.4: Drawing of the 3D MOT table. Six MOT beams (only four of them are shown propagating in the horizontal plane) are used to cool the atoms, coming from the 2D MOT cell via the push beam, in a 3D MOT. $\frac{\lambda}{4}$ waveplates are required to circularly polarize the beams. A pair of vertical circular coils mounted in an anti-Helmholtz configuration provides the quadrupole trap needed to trap the cloud (only one of them is shown). Three pairs of rectangular coils (the bottom vertical coil is not represented), mounted in Helmholtz configuration, provide control of the bias fields around the cell. Absorption imaging on this cloud can be performed thanks to imaging beams (only the horizontal one is represented). The two independent dipole beams are also shown. Each of them passes through an AOM, which realizes time-averaged potentials. A telescope is also used to increase the size of each beam before it is focused on the atomic plane. Their power is locked via two photodiodes for each beam.

Thanks to absorption imaging, we extract information on the cloud[8]. After the MOT step, the atom number is $\sim 10^9$ at a temperature of $\sim 5 \times 10^2\,\mu\mathrm{K}$. It is difficult

[8] We use a $50\,\mu\mathrm{s}$ pulse of repumping light to transfer atoms to $F = 2$ before imaging them.

to estimate a temperature with a time of flight (TOF) expansion due to the size of the cloud. The loading rates in the science cell are typically 3×10^8 atoms/s.

The next experimental steps will be used to further reduce the temperature of the cloud below the Doppler limit and then to increase its density.

7.2.4 Compressed MOT and Molasses

After the MOT loading, during 20 ms, we detune the MOT beams from -20 MHz to -40 MHz and reduce the current in the MOT coils from 5 to 3 A in the so-called compressed MOT (cMOT) step. This cools the cloud by reducing light scattering. Then a first molasses step of 10 ms cools it further. The magnetic gradient is turned off, the MOT beams are further red-detuned to end up at -50 MHz from resonance, and their power is reduced to 10 mW per beam. The cloud then falls into the crossed dipole trap that was turned on during the cMOT step. We use a second molasses step during which the sidebands of the EOM are progressively turned off, so that at the end of this timestep, the cloud is polarized in $F = 1$, with $\simeq 6 \times 10^8$ atoms at a temperature of 25 µK.

7.3 Production of a BEC in a cODT thanks to the painting technique

At the end of these steps, in the setup described in Chapter 1 and used throughout this thesis, we loaded the cloud into a quadrupole trap that trapped only the $|F = 1, m_F = -1\rangle$ atoms. Radio-frequency evaporation was then performed for 12 s to increase the density of the cloud. Afterwards, the cloud was loaded into the crossed optical dipole trap (cODT). As previously mentioned, we aim to remove this quadrupole magnetic trap step in this new setup. We now present various alternative solutions to replace it while still reaching a BEC in the cODT. The final decision is guided by the amount of optical power available on the table.

7.3.1 Direct loading in a crossed optical dipole trap

The direct loading of molasses inside a dipole trap has been used in the community. However, without sufficient optical power, attempting to load large molasses into a tightly confined trap of small volume would result in poor loading efficiency. The addition of a dimple beam could increase the collision rate and potentially help reach the BEC regime, although the resulting BEC would likely be small. For instance, a BEC of 2×10^4 Rubidium atoms has recently been reported in [238].

For non alkali atoms, alternative methods have been developed to reach a BEC by directly loading the molasses into a dipole trap. Stellmer et al. [239] combined two cooling transitions of Strontium atoms to achieve a high phase space density (PSD) in the molasses. They then used several high-power red-detuned beams of different waists to reach a BEC without evaporative cooling in a total time of 2 s.

7.3.2 All-optical cooling solutions

The direct loading of an ODT, even with the addition of a dimple, is thus not sufficient for our goals in terms of condensed atom numbers ($\sim 1 \times 10^5$) given the optical power we choose to put on the optical table (~ 10 W). Still, other solutions are possible, which involve intermediary optical powers. These solutions will be detailed in the following lines. It is worth noting that we refer to them as "all-optical"

solutions, although this term may be usually reserved for solutions that do not involve evaporative cooling. Here, this term includes all solutions that do not utilize a magnetic trap.

One of them uses the principle of Raman cooling [240], which consists in removing excess in kinetic energy via two-photon Raman transitions inside a crossed ODT. It is combined with optical pumping. For instance, using this technique, Urvoy et al. reach a Rb BEC of 2.5×10^4 atoms in less than 2 s without the need for evaporative cooling [241]. Although this technique is initially quite efficient[9] ($\gamma \simeq 7$), it was realized for rather small clouds in ODTs of waists $\simeq 10\,\mu$m and the performances of cooling to the BEC is said to be density-limited.

Other approaches use an intermediate far-off-resonance optical lattice (FORL) as an intermediate step to load the molasses into the ODT. It allows to limit the losses by pinning the atoms to the lattice sites. A first idea is then to continue polarization gradient cooling inside this lattice [233]. The phase space density at the end of this step can be relatively high (~ 0.002 in [233]) so that the loading and evaporation steps inside the dipole trap are more efficient than without the FORL. In addition, a moving lens was used in order to dynamically reduce the volume of the ODT. A final BEC of 3.5×10^5 atoms in 3 s was produced[10].

A second idea is to use an optical lattice in combination with Raman beams (which can also be the lattice beams) and repumper beams. This technique is called degenerate Raman sideband cooling. At each lattice site, the atoms are cooled to the lowest vibrational level of the site. The technique was pioneered in the group of Chu [234] in the case of Cesium atoms and was recently applied to another alkali atom, Potassium, in [243]. The temperatures obtained at the end of this step can reach the sub µK regime. Loading and evaporation in the optical dipole trap can then be performed efficiently.

Although these methods may be efficient, they require the addition of several beams, which we would like to avoid in our compact setup.

Instead, the technique of dynamical loading into the ODT was chosen. The waist of the dipole beams, which determines the trapping volume in the ODT, should ideally be large during loading and small at the end of the evaporation step to achieve the BEC. A dynamical change in the waist would allow for a connection between these two regimes.

Instead of using a moving lens (as done in [233] or in Greiner's team [244], where they managed to produce a BEC of Erbium atoms in less than 1 s by carefully optimizing the sequence), we use time-averaged potentials, obtained from rapidly moving beams. More precisely, the angle of each dipolar beam is changed so rapidly that an averaged trap is created with a volume determined by the extreme positions of the laser beam [245]. This technique is often referred to as "painting" because it is reminiscent of the way a painter would move a brush (the laser) on a canvas (the trapping region). We will describe it in more details in the following, but first we discuss the parameters that influence the loading and evaporation in the ODT. This

[9] The efficiency of the cooling is usually determined by the factor γ, which is defined as the gain in PSD at the cost of losing atoms:

$$\gamma = -\frac{\mathrm{d}\ln(\mathrm{PSD})}{\mathrm{d}\ln(N)} \tag{7.1}$$

[10] The same procedure with a more complicated arrangement of the dipole traps was performed in [242] for which they obtained a BEC of $\sim 10^6$ atoms, still in 3 s.

will further motivate the use of the painting technique by independently controlling both the power and the waist of each beam.

7.3.3 A two-parameter control during the evaporation process

The parameters that determine both loading and evaporation efficiencies in an optical dipole trap are the waists of the beams (mean waist $\bar{w}$) and their powers P. They affect the two following characteristics of the trap: its depth U and its frequency $\bar{\omega}$.

The depth of the trap is given by $U \propto \frac{P}{\bar{w}^2}$ (see [147] and Chapter 3). Concerning the longitudinal trapping frequencies $\bar{\omega}$, the scaling for a Gaussian beam with fixed waist is: $\bar{\omega} \propto \frac{\sqrt{U}}{\bar{w}} \propto \frac{\sqrt{P}}{\bar{w}^2}$. The scaling $U/k_BT \simeq 10$ is typical for optical dipole traps and thus a necessary condition for loading a cloud at temperature T is to have a sufficiently profound trap with depth $U \gtrsim 10\, k_BT$. This is well verified with two beams at $\lambda = 1064\,\text{nm}$ of power $P \simeq 10\,\text{W}$[11] and waist on the atoms $\bar{w} \simeq 50\,\mu\text{m}$.

For the loading step, the higher the optical power, the more atoms are loaded into the trap. As mentioned above, the choice of the waist during the loading results from a trade-off between the larger possible loaded volume (large $\bar{w}$) and the larger possible potential depth (small $\bar{w}$). If it is possible to vary the waist dynamically during the evaporation, the former solution will prevail and we will compensate for the decrease in potential depth with a large optical power.

The evaporation step requires a lot of care to reach the BEC regime, because simply doing it by lowering the trap depth leads to a lower collision rate and thus a lower efficiency. Concerning the evaporation step, there is thus also a trade-off in the choice of waist. In order to lower the temperature, a larger waist would contribute to a decrease in trap depth. However, it would reduce the atomic density and the optimization of the phase space density is not guaranteed. Moreover, the elastic collision rate Γ_{el} is also a key quantity for an efficient evaporation and its maximization would require small trapping volumes and thus small waists. Indeed, there are unavoidable atomic losses in the optical trap that do not contribute to any gain in the phase space density. Thus, the time scale of the "good collisions" that allow thermalization of the cloud at a smaller temperature ($\propto 1/\Gamma_{\text{el}}$) must be smaller than the time scale of the "bad collisions" that cause atomic losses without the thermalization effect ($\propto 1/\Gamma_{\text{loss}}$). The competition between the two timescales is contained in the parameter:

$$R = \frac{\Gamma_{\text{el}}}{\Gamma_{\text{loss}}} \tag{7.2}$$

A good evaporation ramp requires keeping this ratio R high while optimizing the phase space density $n\lambda_{\text{th}}^3 \propto \frac{N\bar{w}^0}{P^{3/2}}$. Depending on the dominant loss process, the scaling of R with the different parameters varies: it is $\propto \frac{N\bar{\omega}^3}{T} \propto N\frac{P^{1/2}}{\bar{w}^4}$ when 1-body losses dominate, while it is $\propto \frac{T^2}{N\bar{\omega}^3} \propto \frac{1}{N}\bar{w}^2P^{1/2}$ for 3-body losses[12]. At the beginning of the evaporation ramp, one-body losses dominate and the evaporation efficiency $\gamma = -\frac{\mathrm{d}\ln(\text{PSD})}{\mathrm{d}\ln(N)}$ and the collision rate can be optimized simultaneously with a small waist. However, when 3-body losses become dominant, keeping a large value of R is incompatible with a large atom number and a small waist.

Moreover, as Γ_{el} increases, the ideal regime of *runaway evaporation* can be obtained: the cooler the cloud, the more efficient the evaporation. It was said to be

[11] The amount of heating, due to spontaneous scattering, remains negligible for this level of power and detuning, a few nK/s.

[12] There are no 2-body losses in the $F = 1$ state.

unattainable in the case of a single dipole beam [246] for the reason given above concerning the dominance of 3-body losses. However, in the case of a tilted potential via a magnetic gradient [247] or an off-centered crossed beam configuration [248], it has been demonstrated that runaway evaporation is doable in an optical trap. In these two realizations, the key point is the independent control of the trap confinement given by $\bar{\omega}$ (via the waist of the smallest dipole beam in [248]) and the trap depth U (via the power of the wide uncentered beam in [248]). The relation $U \propto \bar{\omega}^2$ is no longer verified in either case (since $\bar{w}$ is not kept constant), and the reasoning done above about R is not so simple. In this case, the trade-off on $\bar{w}$ can be (partially) avoided: the lowering of the trap depth is not as simply related to the lowering of the trap frequencies as before.

The painting technique, via time-averaged potentials, also decouples the degrees of freedom of trap depth and trap confinement via a dynamic variation of the beam waist, a key advantage for an efficient evaporative cooling, as we have seen here.

7.3.4 Time-averaged potentials

Principle

The following section describes the painting technique used in our setup to achieve a BEC without the use of a magnetic trap.

Each high power dipole beam is sent through an AOM, and we will describe what happens for only one of the two identical systems. The AOM is frequency modulated at ω_{mod} from $-F$ to $+F$, which moves the angle the beam makes with respect to the direction of propagation from $-\theta_{\text{max}}$ to $+\theta_{\text{max}}$. The manner in which the frequency is varied over time during each modulation period is controlled by an Arbitrary Waveform Generator (AWG). After passing through a converging lens, the angular variation of the beam is transformed into a transverse variation of the position of the beam in the focal plane of the lens. The modulation with the AWG results in a specific variation of this position called $\xi(t)$, whose extrema are denoted as $-h_0$ and $+h_0$. If the modulation frequency is sufficiently high compared to the frequencies of the trapped cloud, the atoms feel an effective potential, which is the average over time of the potential created by the modulated dipole beam. Therefore, the average intensity profile at position ξ' results from the time that the laser beam spends at that position.

More quantitatively, following [245], we note $I\left[\xi(t)\right] = P_0\delta\left[\xi(t)\right]$ the unmodulated (*i.e.* at a fixed time) beam intensity at the position on the atoms $\xi(t)$, where δ is the Dirac distribution. To simplify the calculations, we do not take I to be a Gaussian function. This leads to small differences in the averaged time potential, especially for large modulation frequencies F [245]. We now want to find the specific variation of $\xi(t)$ to obtain the following time-averaged intensity profile:

$$\tilde{I}(\xi') = \tilde{I}_0\, f(\xi') \tag{7.3}$$

where $\tilde{I}_0 = \tilde{I}(0)$ is the averaged central intensity and f is the desired variation of the time-averaged intensity.

Since we assume a delta function for the unmodulated intensity, the time the beam spends at the position ξ' satisfies:

$$\frac{\mathrm{d}t\left(\xi = \xi'\right)}{\mathrm{d}t\left(\xi = 0\right)} = \frac{\tilde{I}(\xi')}{\tilde{I}(0)} = f(\xi') \tag{7.4}$$

Writing $\mathrm{d}t$ as $\frac{\mathrm{d}\xi}{\dot{\xi}}$ and $v_0 = \dot{\xi}(\xi = 0)$, we get:

$$\dot{\xi}(\xi = \xi') = \frac{v_0}{f(\xi')} \tag{7.5}$$

We thus see that at a maximum of the averaged intensity, the time variation of the center position modulation should be minimal. This confirms our previous statement that the laser beam "spends more time in the regions where the desired average intensity profile is high".

In the case of a harmonic time-averaged potential of the form: $f(\xi') = 1 - \left(\frac{\xi'}{h_0}\right)^2$, which is a first simple choice for an average trapping intensity profile, the integration of the differential equation involving $\xi(t)$ (7.5) leads to the implicit equation: $\xi(t)^3/3h_0^2 - \xi(t) + v_0 t = 0$. One of the roots $\xi_0(t)$, centered at $\xi' = 0$, will be the desired center position modulation evolution to obtain an averaged intensity variation of the form (7.3). It is represented in Figure 7.6 together with other types of modulation shapes. The principle of the painting technique is summarized in Figure 7.5.

Experimental implementation

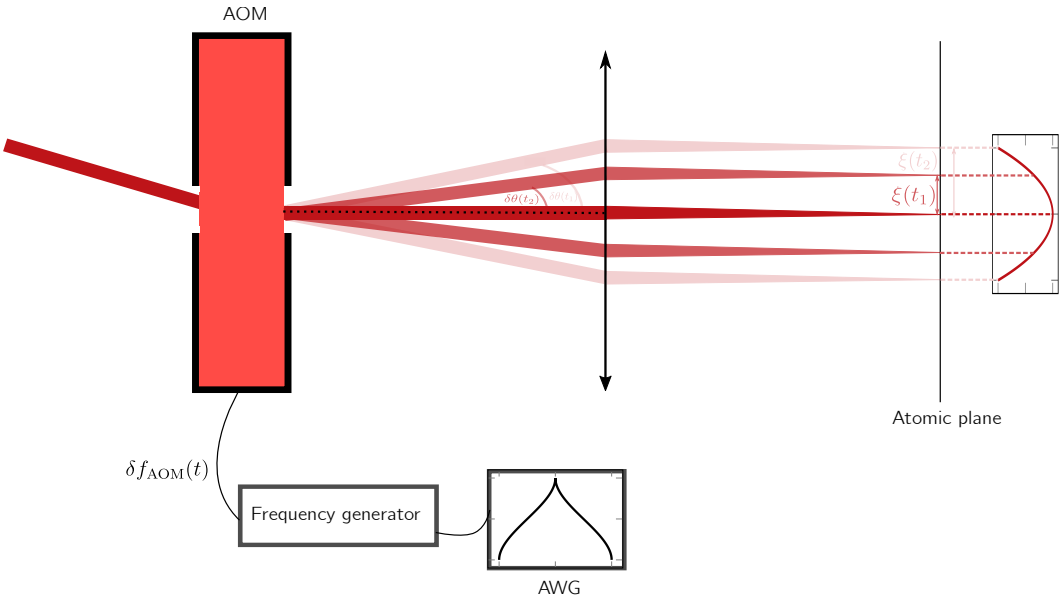

FIGURE 7.5: Description of the time-averaged potential technique. An arbitrary waveform generator is used to modulate a Rigol frequency generator, which then sends the RF signal to an AOM. This causes a time modulation of the angle $\delta\theta(t)$ made by the first-order diffracted beam. After being focused by a converging lens, the beam's position in the atomic plane $\xi(t)$ is modulated in time. The modulation is fast enough to ensure that the potential felt by the atoms is averaged over time. We present the case of an averaged harmonic potential felt by the atoms.

We now discuss the experimental implementation of the painting technique on our setup. For each beam, a converging lens of focal length $f_3' = 100\,\mathrm{mm}$ is used in order to focus sharply the beam onto the atoms to create the dipole trap. The angle $\delta\theta(t)$ made by the beam with respect to the unmodulated beam is related to the center position modulation as $\delta\theta(t) \simeq \frac{\xi(t)}{f_3'}$ in the limit of small modulation angles. Since $\delta\theta(t)$ is itself proportional to the AOM frequency shift $\delta f_{\mathrm{AOM}}(t) = \frac{c\,\delta\theta(t)}{\lambda}$ (c is the sound frequency in the AOM crystal and $\lambda = 1064\,\mathrm{nm}$ is the wavelength of the dipole

beams), we thus obtain the desired evolution of the AOM frequency when we know $\xi(t)$:

$$\delta f_{\mathrm{AOM}}(t) = \frac{c\,\xi(t)}{\lambda f_3'} \tag{7.6}$$

The expected average potential will be generated provided that the modulation frequency of the AOM is high enough in front of the trapping frequencies of the cloud. We typically use a frequency modulation $\omega_{\mathrm{mod}} = 2\pi \times 200\,\mathrm{kHz}$ which is at least an order of magnitude larger than the trapping frequencies (see section 7.3.6 for their measurements). Another requirement is to place the AOM in the object-side focal plane of the lens. This ensures that the outgoing modulated beams will exit the lens parallel to each other, validating the above calculation.

Actually, we use two other lenses of focal lengths (f_1', f_2'), forming a telescope 2:1 between the AOM and the last focusing lens. Indeed, to obtain an unmodulated beam of waist $w_0 \simeq 30\,\mu\mathrm{m}$, the waist of the beam before the last lens should typically be 1 mm. For our AOM (MT80-A1.5-1064 from AA OptoElectronics)[13], we have to limit the waist of the beam before the AOM to 0.5 mm, hence the need of a telescope after the AOM. The AOM should be positioned in the focal plane of the optical system, which is now composed of three lenses, to ensure proper operation of the time-averaged potential technique. The formula (7.6) is modified to take this telescope into account and reads:

$$\xi(t) = \frac{f_1' f_3'}{f_2'} \frac{\lambda\,\delta f_{\mathrm{AOM}}(t)}{c} \tag{7.7}$$

Using the value of $c = 4200\,\mathrm{m/s}$ for the speed of sound in the TeO_2 crystal of the AOM, for a maximum deviation frequency of $\delta f_{\mathrm{AOM}} = F = 20\,\mathrm{MHz}$ we get a center position variation $h_0^{(\mathrm{max})}$ of $\pm 250\,\mu\mathrm{m} \simeq 10 \times w_0$. This is the typical expected order of magnitude for an efficient loading in the dipole trap for the intermediate power ($\sim 10\,\mathrm{W}$) used in our setup.

After discussing how the painting technique allows for precise control of the effective waist felt by the atoms, let us now briefly consider the other key parameter in the dipole trap: optical power. We can control this parameter independently with the same AOM via Voltage Variable Attenuators. The total optical power diffracted by the AOM and directed to the atoms is $\sim 10\,\mathrm{W}$ (per arm) during the loading step. We use high-power fibers to transport the light from a side table to the main table. We first tried using 2 m Shäfter-Kirchhoff end cap fibers to get the highest coupling efficiencies. However, they broke very quickly, so we switched to Thorlabs fibers (P3-1064PM-FC-2-PM), which seem to be more robust, although the coupling efficiency is slightly lower. In addition, rotating waveplates are utilized on the side table and controlled by a computer through RS232 communication to prevent continuous excessive heating of the fibers and degradation.

[13] We initially used Gooch and Housego (model I-M080-2C10G-4-AM3) AOMs, but they were more sensitive to thermal effects. As the RF power was varied, we observed a shift in focus position up to 300 µm. We still saw a bit this shift with the AA OptoElectronics AOMs but we corrected it by tilting the second lens of the telescope by $\sim 5^\circ$ (inspired by [249]).

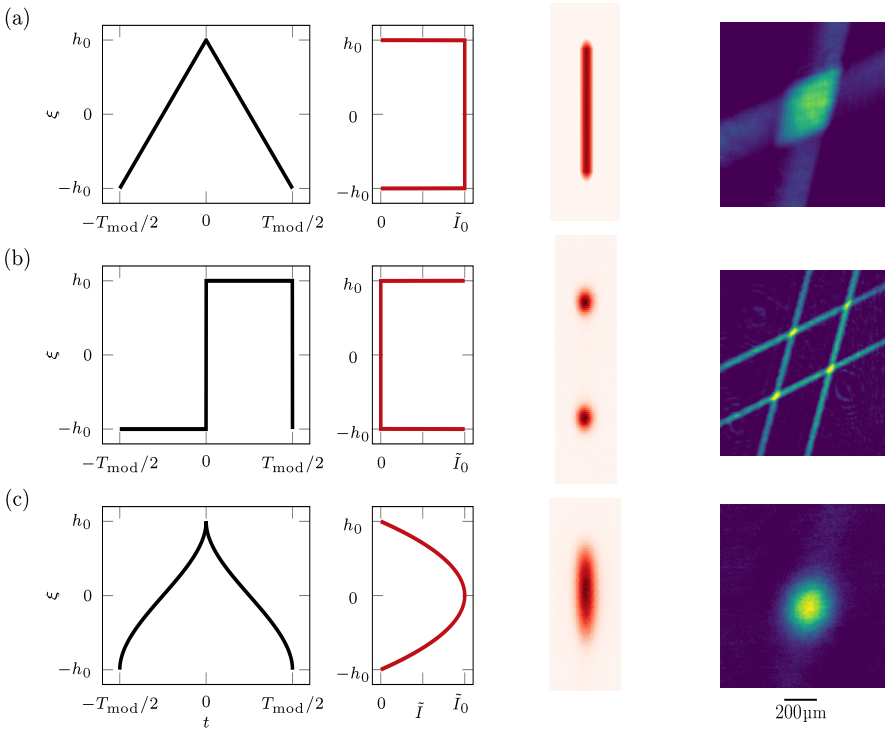

FIGURE 7.6: Waveform variation effect. We vary the waveform modulating the frequency generator at $1/T_{\mathrm{mod}} = 200\,\mathrm{kHz}$. The first column represents the center position modulation, which is directly proportional to the frequency modulation waveform via (7.7). The second column contains the resulting average intensity profile $\tilde{I}(\xi)$. The third column shows 2D intensity profiles obtained by modulating only one dipole arm. The fourth column presents atomic absorption images taken with vertical imaging. The corresponding modulation is switched on along the two arms forming an angle of 60 °. (a): Triangular modulation. The derivative of $\xi(t)$ is discontinuous at h_0 and $-h_0$ and constant otherwise, resulting in flat intensity and atomic profiles. (b): Square modulation. The beam will "spend time" at h_0 and $-h_0$ due to the square shape and no time everywhere else, leading to the bimodal intensity distribution. Crossing the two modulated dipole beams, we obtain a 2×2 lattice. (c): Solution of $\xi(t)^3/3h_0^2 - \xi(t) + v_0 t = 0$ equation. The derivative is discontinuous in $-h_0$ and h_0 and varies smoothly otherwise. The beam spends more time around $\xi = 0$. It leads to an averaged parabolic intensity profile on the camera and to a Gaussian atomic density profile. We use $h_0 \simeq 250\,\mu\mathrm{m}$ for both the light and absorption images.

To verify the proper functioning of the painting, we measure the number of atoms loaded in the crossed dipole trap as a function of the modulation amplitude, while keeping the optical power coming into the AOMs constant. Without painting, the atom number is $< 10^6$ atoms, while it reaches more than 1×10^7 atoms with the maximum amplitude of painting ($h_0^{(\mathrm{max})} = 250\,\mu\mathrm{m}$). After a holding time of 0.5 s, the number of atoms decreases to $\sim 6 \times 10^6$. The temperature after the loading is similar to what we get at the end of the molasses step $\simeq 30\,\mu\mathrm{K}$, confirming that the trap depth is adapted to the loading of the molasses.

Since the atom number loaded does not increase for $h_0 \gtrsim 200\,\mu\mathrm{m}$, we conclude that we load the maximum atom number with the available optical power and our molasses. The atom number loaded in the dipole trap is the chosen figure of merit at this stage, but this choice could be debated.

We thus have two degrees of freedom: painting amplitude and optical power, which

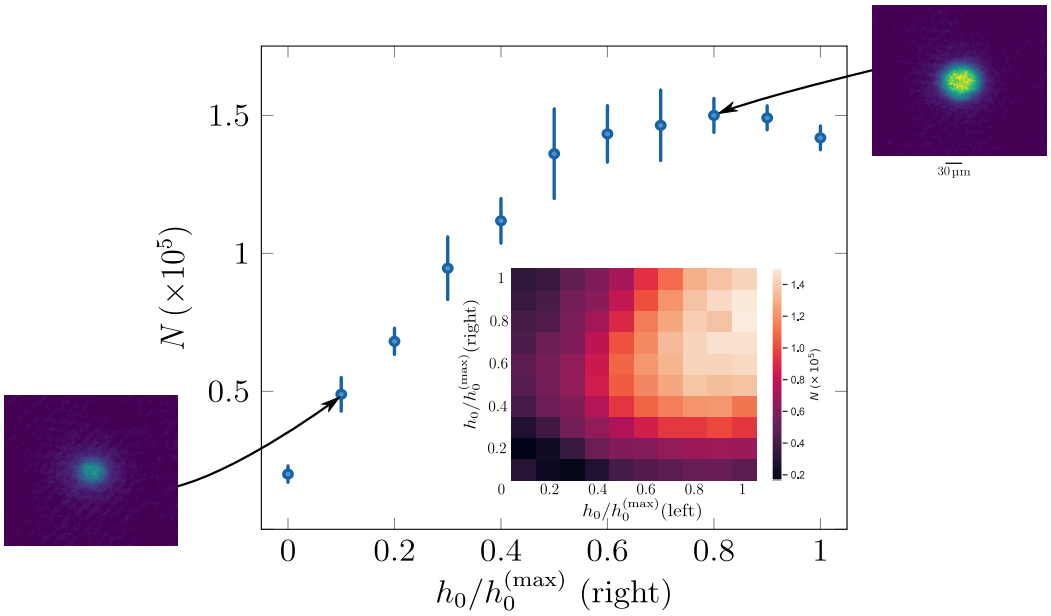

FIGURE 7.7: Variation of the painting amplitude. We change the painting amplitude along the right arm during the loading of the dipole trap and we look at the number of atoms obtained in the BEC after a TOF of 15 ms with a maximum painting amplitude along the left arm during the loading ($h_0/h_0^{(\max)}(\text{left}) = 1$). We also vary the painting amplitudes of both arms in the inset. The two arms are nearly symmetrical to each other. The end points of the painting amplitudes after the evaporation ramp are kept fixed at $h_0 = 0$ (no more painting). The colormap for the BEC absorption images is kept fixed. To get a more complete description of the painting effect, we could have looked at the temperature of the cloud as a function of the painting amplitude.

can be used to differentially affect trap depth and trap frequencies, making them useful tools for an evaporation ramp.

7.3.5 Evaporation

PID control of the dipole beam power is essential to properly control the evaporation ramps. For this we use photodiodes (PD) in combination with an analog PID controller from Stanford Research (SRS) and a VVA for each AOM. Actually, the large power range (from 10 W to $\simeq$ 10 mW) requires a pair of photodiodes with different gains for each dipole arm. At the beginning of the first evaporation ramp, which is chosen to be linear, we intentionnaly saturate one PD and when the power becomes so low that we are limited by noise on the other PD, the one that was saturated takes over and locks the power that we ramp exponentially to its final value. A beam sampler separates the optical path to the two PDs for each arm, as shown in Figure 7.4.

The evaporation time step is divided into two distinct steps. During the first one, which lasts 0.9 s, we linearly decrease the deviation frequency of each AOM in 0.5 s from $F = \pm 20$ MHz to $F = 0$, thus decreasing the trapping region. Each beam at the end of this step is no longer modulated and has a waist $w_0 \simeq 30$ µm on the atoms. The power of the dipole beams is also ramped linearly from 10 W to 1 W. Then, during the second evaporation ramp, the optical power is ramped down exponentially in 3 s from 1 W to 25 mW.

In addition, during the second evaporation ramp, we perform spin distillation [250, 251]. Indeed, since there is no quadrupole trap in this setup, the atoms are not polarized in a particular spin state when they are in the dipole trap. To have a single spin state BEC, we add a vertical magnetic field gradient with the MOT coils of $\simeq 10\,\mathrm{G/cm}$ and shift the zero of magnetic field above the initial position by $\sim 50\,\mu\mathrm{m}$ by adding a bias field along the vertical direction. This allows us to vertically trap the low-field seeker state *i.e.* the $m_F = -1$ state which is also trapped in the plane directions (see Figure 7.8). We turn on this magnetic gradient only during the second step of evaporation, when the trap is no longer deep enough to hold the cloud against gravity. We verify that this magnetic gradient is adequate to distill the cloud (Figure 7.8).

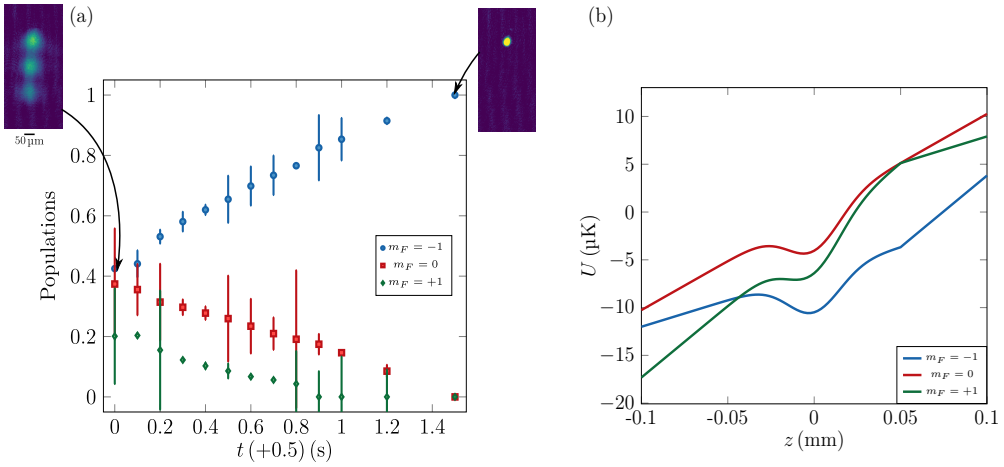

FIGURE 7.8: Spin distillation. We apply a magnetic gradient and a bias field to the cloud to distill it into one m_F state. The displacement of the magnetic field center above the cloud allows to trap the $m_F = -1$ state, as confirmed by the simulation of the trap depth performed in our team by Guillaume Brochier (b). The simulation parameters are those of the end of evaporation. To properly resolve the evolution of the spin populations in (a), we start the spin distillation 0.5 s after the beginning of the second evaporation ramp[14]. The absorption images are obtained after a TOF of 30 ms, for which we compensate the gravity (Stern-Gerlach sequence).

We measure the different spin populations at different points of the evaporation ramp by switching off the trap for a time of flight of $\sim 30\,\mathrm{ms}$ while applying a magnetic gradient that separates the different spin populations. The magnetic gradient used for this measurement is larger than the one used for the spin distillation in order to compensate for gravity for the $m_F = -1$ state ($30\,\mathrm{G/cm}$).

[14] In the sequence that maximizes the number of atoms in the BEC, the spin distillation is started at the same time as the second evaporation ramp. Here, we delay the beginning of the spin distillation step by 0.5 s for better visualization.

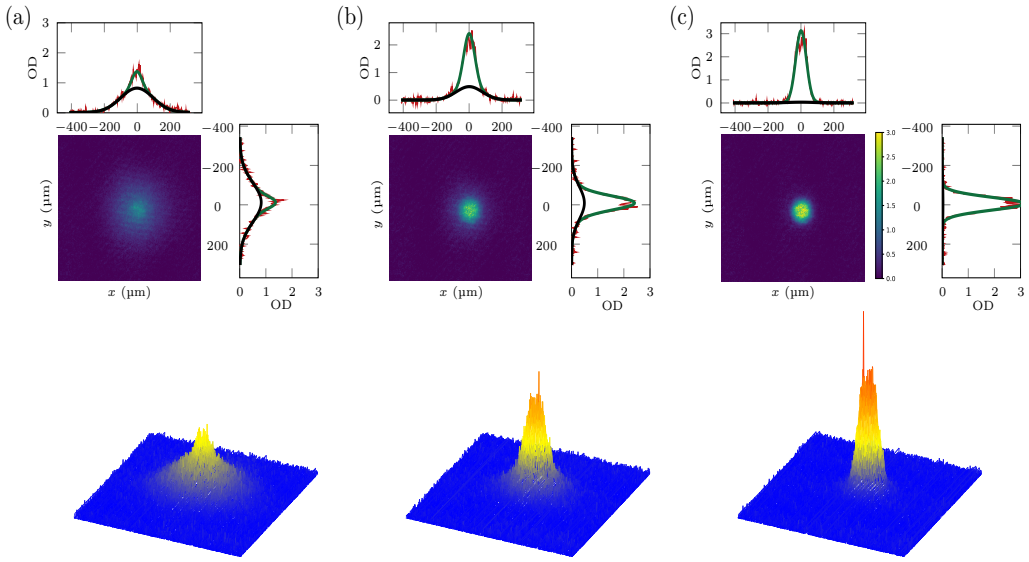

FIGURE 7.9: Transition to the BEC. We vary the end power of the evaporation ramp. (a): $P_f = 45\,\mathrm{mW}$, (b): $P_f = 30\,\mathrm{mW}$, and (c): $P_f = 20\,\mathrm{mW}$. For each of them, we plot the corresponding absorption images after a time of flight of 15 ms, taken with horizontal imaging, together with cuts along the two directions. A Gaussian fit is plotted with a black solid line while a sum of two Gaussian fits[15], representing the condensed and thermal fractions, respectively, is depicted with a green solid line. The associated three-dimensional images are shown. The colorbar is fixed for all the plots.

By using all the tools described above, we manage to reach the BEC regime $\sim 5\,\mathrm{s}$ after loading the dipole trap. We look at the evolution of the atom number and temperature (measured with a ballistic expansion) during the evaporation ramps. Then, thanks to the knowledge of the size of the cloud, we calculate the phase space density and the efficiency of the evaporation, shown in Figure 7.10. It should be noted that as soon as a condensate fraction appears, the measurement of the cloud temperature by ballistic expansion is no longer valid. However, it gives a rough estimate. We reach the BEC phase with $N \sim 1.5 \times 10^5$ atoms and a temperature of $\sim 30\,\mathrm{nK}$ with a total sequence time of just under 10 s (Figure 7.9). The average efficiency during the evaporation $\gamma \sim 3.5$ is typical (see for example [252]), though far from the highest reached in the community. Nevertheless, the numbers obtained, together with the sequence time, are satisfactory. It seems that we are not limited by the painting amplitude during the loading of the dipole trap (see Figure 7.7), but rather by the amount of optical power on the table. The painting technique allows to gain at least a factor ~ 3 on the atom number obtained in the BEC.

7.3.6 Frequencies of the ODT

To fully characterize the BEC, we can extract the trap frequencies in the optical dipole trap. Several techniques exist, but in this case, the painting technique is used to observe the cloud's response to a perturbation. More precisely, after obtaining the BEC, we re-activate the center position modulation on one of the dipole arms using a different waveform (square shape (b) in Figure 7.6) for 0.3 ms. This abrupt trigger

[15] Ideally, the condensed fraction should be modeled using a Thomas-Fermi fit. However, due to our low imaging resolution, we use the sum of two Gaussian fits.

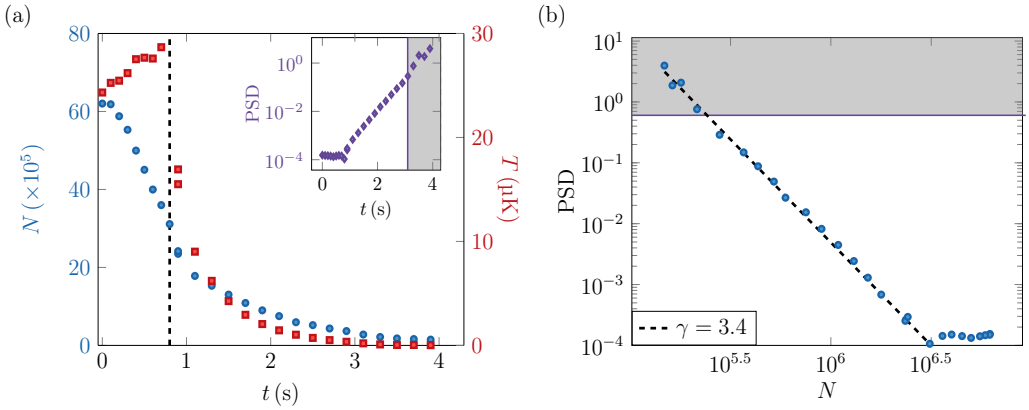

FIGURE 7.10: Efficiency of the evaporation in the dipole trap. (a): We plot the evolution of the atom number (blue circles) and the temperature (red squares) as a function of the evaporation time. The dashed vertical line separates the two evaporation steps: the first one is mainly a compression of the cloud (reduction of the painting) and the second one corresponds to a typical exponential evaporation ramp of the optical power. The evolution of the phase space density is shown in the inset with violet diamonds. The grey area indicates the moment when a condensed fraction becomes visible on the absorption images. The last point is displayed in Figure 7.9(c). (b): The evolution of the PSD is plotted as a function of N using a log-log scale. This allows for the extraction of an efficiency $\gamma \sim 3.4$ for the second evaporation ramp by linearly fitting the points (black dashed line).

causes a left-right movement of the cloud[16]. We record the following evolution of the center of mass position of the cloud and extract one of the trapping frequencies (see Figure 7.11).

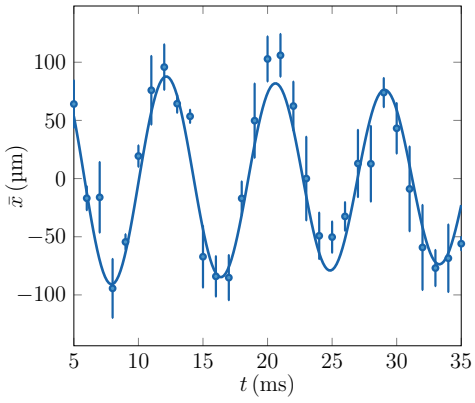

FIGURE 7.11: Trap frequency measurement by the painting technique. We trigger a transverse atomic motion in the plane by changing the modulation waveform on one of the two AOMs. The result is an oscillation of the center of mass position of the cloud around its equilibrium position. A sinusoidal fit allows us to access the frequency of the trap along the Push direction: $f_x = (123 \pm 5)$ Hz.

[16]This is for the highest in-plane frequency (along the Push direction). For the other one (in plane perpendicular to the Push direction), which we expect to be twice smaller due to the orientation of the arms, we quench both arms in opposite directions. Regarding the vertical frequency, we quench the power of the dipole arms.

In summary, the measured trapping frequencies along the (x,y,z) directions are $(123 \pm 5,\ 63 \pm 8,\ 130 \pm 18)$ Hz, consistent with the team's numerical simulations: (143, 72, 170) Hz.

In this section, we demonstrated how a cloud can be cooled to the BEC regime solely through optical techniques. The importance of the painting technique to reach the BEC regime with more than 10^5 atoms was emphasized. Optimizing the evolution of the two degrees of freedom, namely painting amplitude and power, enabled us to reach the degenerate regime in less than 10 s. The obtained numbers are adequate for further exploration on this setup.

For larger BECs, higher power dipole beams are probably necessary. One possible upgrade, without changing the lasers, would be to eliminate the fibers, resulting in an optical power increase of $\sim 40\%$.

7.4 Outlook

To conclude this chapter, we present the future scientific directions that are available after obtaining a degenerate cloud in this compact setup. We will not delve too deeply into the details.

7.4.1 The versatily of the painting technique

The spatial modulation tool offers various possibilities. As previously mentioned, the choice of the modulation waveform allows for the manipulation of the dipole trap's geometry. In the previous section, a waveform resulting in a harmonic averaged intensity profile was utilized. However, other types of modulation waveforms, such as a step function, could be considered. This would result in several clouds, each separated by $\sim 100\,\mu$m and containing $\sim 10^5$ atoms (see Figure 7.12(a)).

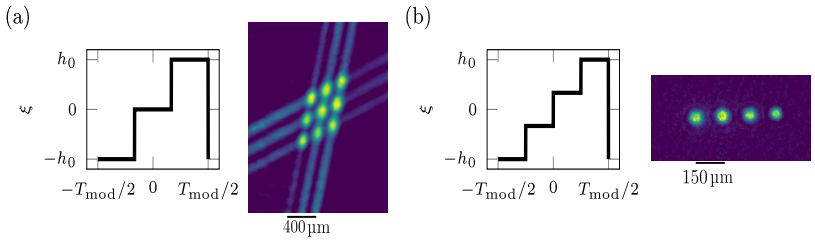

FIGURE 7.12: Illustration of the versatility of the painting technique. (a): the optical dipole trap is loaded with a step function instead of a modulation resulting in an averaged harmonic intensity profile. This modulation on the two arms leads to a lattice of 3×3 sites on the atoms. An absorption image taken with vertical imaging is shown. (b): the BEC is split by switching on the modulation again after obtaining the BEC. A 4-step function is utilized to divide the BEC into 4 distinct BECs, separated by a few tens of microns, each containing $\sim 2 \times 10^4$ atoms. Before horizontally imaging the cloud, a time of flight of 15 ms is used to reduce its optical depth.

More importantly, this type of step-modulated waveform can be used to split a BEC into several BECs (Figure 7.12(b)) after it has been obtained. To achieve an equivalent splitting of the BEC, the bias fields must be adjusted to eliminate any magnetic gradient that would favor one trap over the others during the splitting process. Additionally, the step function should be made asymmetrical. Taking a symmetric step function results in deeper central traps compared to the side ones due

to the Gaussian intensity profile of the beams. To address this, we slightly increase the length of the side "plateaus" of the modulation waveform compared to the central ones. Additionally, we multiply the power of each arm by 4 to maintain the same potential depth per site as the single BEC.

We mention that Direct Digital Synthesis (DDS) could be used to manually shape the modulation instead of changing the waveform on the AWGs.

7.4.2 Future of the setup

As stated in the introduction, this setup was constructed to investigate Rydberg excitations on small ensembles of cold atoms. This can include resonant or off-resonant Rydberg excitations, resulting in *dressed interactions* for the ground state atoms in the latter case.

The former approach has successfully simulated Ising Hamiltonians [253], observed Rydberg blockade [254], and realized a one-dimensional topological lattice system [255]. This topic is being studied by several cold atom groups worldwide. The latter approach of Rydberg dressing partially circumvents the problem of the short lifetime (a few tens of µs) of Rydberg atoms by weakly admixing the Rydberg excitation on ground state atoms. A wealth of proposals have been put forward to realize many-body phases of matter (see for example [256, 257]) through the use of Rydberg dressing.

The team purchased a UV laser from LEOS that lases $\simeq 200\,\mathrm{mW}$ at $\lambda \simeq 297\,\mathrm{nm}$ after a two-stage frequency doubling scheme. This laser enables switching from resonant to off-resonant interactions. This single-photon excitation approach, previously developed in Munich [258], avoids the constraint of phase-locking the two lasers required for a double-photon excitation scheme and eliminates the scattering on the intermediate level.

A first scientific project could be to create a global Rydberg excitation that would be shared by small ensembles of atoms. This raises the question of how to create such small ensembles. One might think that the tool described in section 7.4.1 would be sufficient to create the ensembles. However, using light at $\lambda = 1064\,\mathrm{nm}$, red-detuned compared to the D2 line of Rubidium, photoionizes the Rydberg atoms and further limits their lifetimes. Instead, the use of blue-detuned beams allows to trap both ground state and Rydberg excited state atoms [259], an important advantage for their study. It is thus more suitable for a longer-lived ensemble to trap atoms at intensity minima and image them by fluorescence imaging. To do this, the team is currently working on creating arrays of green microtraps, obtained by imaging a dark spot on the cloud, where both the ground state and Rydberg excited state atoms would be trapped.

Combined with the painting technique using an AOM, this should allow the creation of an array of mesoscopic ensembles (a few units, each containing ~ 100 atoms), from 3 to $\simeq 15\,\mu\mathrm{m}$ apart, that can be addressed with the UV laser.

Once this is mastered, a plan would be to combine the specificities of the 2D setup (accordion lattice, DMDs, Raman beams...) and the new tools developed on this side setup (painting, Rydberg dressing). For this new setup, a science chamber with aspherical lenses and electrodes under vacuum will be considered in order to properly control the electric field near the atoms and tune it, for example, near Förster resonances [260]. The future scientific projects could then be the Rydberg dressing of reduced dimensional gases, especially 1D, which are expected to be longer lived [261] compared to 2D and 3D Rydberg excited gases, and the study of quantum transport in them.

7.5 Conclusion

This chapter described the construction of a new Rubidium ultracold platform and the achievement of a high repetition rate BEC by replacing the quadrupole trap with a more sophisticated dipole trap compared to the experiment described in Chapter 1. Time-averaged potentials were utilized to dynamically reduce the waist of the dipole beams between the loading and the evaporation steps. This control, combined with the optical power control, allowed for the attainment of the BEC state with over 1×10^5 atoms in under 10 s. Finally, we briefly discussed future directions offered by this setup, including the study of Rydberg excitations on small ensembles.

Conclusion

This thesis reported on various studies related to dynamics of weakly-interacting Bose gases at zero temperature. The main scientific projects focused on investigating superfluidity in a 2D density-modulated system and observing Bloch-like oscillations of magnetic solitons within an immiscible mixture cold atom platform.

Chapter 1 presented a cold atom experimental platform that produces reduced dimension samples of Rubidium 87 atoms with controllable geometry. The chapter highlighted the key experimental tools used to produce and study these 2D samples, including an accordion lattice, three DMDs, Raman beams, and MW antennas. Chapter 2 provided key theoretical ingredients for describing the mean-field physics of these weakly-interacting samples. The derivation of the Gross-Pitaevskii equation, which governs the dynamics of our gases at zero temperature, was detailed. A recent mean-field study [87] related to weakly-bound dimers and their interactions with a bath of atoms was briefly discussed. The focus then shifted to the superfluidity property. The emergence of this property in weakly-interacting uniform Bose gases was justified at the end of Chapter 2.

In Chapter 3, we examined the survival of superfluidity in a spatially modulated Bose gas. We first investigated the case of a 2D Bose gas modulated along one direction, using analytical, numerical and experimental methods, as described in our recent work [67]. In this particular case, we were able to measure the superfluid fraction of the modulated gas using two different methods. The first method relied on the anisotropic nature of the sound spectra along two perpendicular directions of the gas. Sound propagated more slowly along the modulated direction compared to the orthogonal direction to the lattice. The superfluid fraction of the gas was calculated by taking the squared ratio of these sound velocities. The second method relied on Leggett's formula, which connects the superfluid fraction to the knowledge of the density profile. The direct relationship between the superfluid fraction, a dynamical quantity, and the static density profile is remarkable and valid as long as the system is well-approximated by a mean-field approach and is separable along the two orthogonal directions. Our precise measurement of the gas density profiles allowed us to extract the superfluid fraction. As a future outlook, we numerically studied mean-field systems with non-separable geometries for which Leggett provided bounds on the superfluid fraction [66]. Since Leggett's inequalities are no longer saturated and sound velocities are not always anisotropic, it was necessary to find an alternative method to measure the superfluid fraction. We relied on the numerical compressibility determination. Our research suggested that it may be possible to experimentally investigate deviations from Leggett's bounds in 2D modulated systems. Our findings provided a foundation for studying superfluidity in other density modulated systems, including supersolids.

Chapters 4 and 5 dealt with the main study of this thesis: the magnetic soliton and its response to a linear potential. The magnetic soliton was introduced as a stationary solution of the non-linear Landau-Lifschitz equation (LLE), which governs the dynamics of the magnetization vector of a ferromagnetic spin chain placed in a magnetic field. We demonstrated that by considering a mixture of two 1D Bose-Einstein Condensates with similar but not equal interaction parameters, the two coupled GP

equations could be mapped onto the LLE. Following Kosevich's work [43], we then established the existence of a periodic dispersion relation for the magnetic soliton. By adding a linear potential to the problem, we demonstrated that the momentum of the soliton evolved linearly with time. This, under the adiabatic approximation, caused the soliton's position to vary periodically with time. Therefore, we proved the existence of Bloch oscillations without a lattice in this system. We developed this analogy and also interpreted it as an AC Josephson effect. The observed oscillations could then be explained by the phase difference of the majority component across the soliton being equal to its total momentum.

Chapter 6 was dedicated to the experimental observation of the Bloch-like oscillations of magnetic solitons. The realization of a stationary magnetic soliton was discussed, followed by its response to a linear potential, interpreted as a constant force, in a linear geometry. The two conjugated variables, the center of mass position of the soliton and its momentum, were examined. The measured periods of the motion were shown to be in good agreement with the predicted values. Additionally, we extracted the phase of the bath using an interference measurement. In the future, it may be fruitful to explore non-rectilinear geometries in which the same system would be subjected to non-constant forces. Furthermore, a ring geometry could be used to investigate the impact of the backflow on the soliton motion.

Finally, in Chapter 7, we discussed the building of a new setup aimed at inducing Rydberg excitations on small ensembles of Rubidium atoms. We described the production of a Bose-Einstein condensate without the use of magnetic traps. We introduced the painting technique, which is efficient for loading the molasses inside the dipole trap and offers various trapping possibilities. In the near future, we plan to address Rydberg excitations and study strongly-correlated phases of reduced-dimensional systems, going beyond the mean-field description used throughout this thesis.

Appendices

Appendix A

List of publications

During my thesis, I participated in several projects that were discussed in the manuscript and resulted in the following publications:

- Optical control of the density and spin spatial profiles of a planar Bose gas, Y.-Q. Zou, É. Le Cerf, B. Bakkali-Hassani, C. Maury, G. Chauveau, P. C. M. Castilho, R. Saint-Jalm, S. Nascimbene, J. Dalibard and J. Beugnon, *Journal of Physics B: Atomic, Molecular, and Optical Physics* 54, 08LT01 (2021).
- Precision measurement of atom-dimer interaction in a uniform planar Bose gas, C. Maury, B. Bakkali-Hassani, G. Chauveau, F. Rabec, S. Nascimbene, J. Dalibard and J. Beugnon, *Physical Review Research* 5, L012020 (2023).
- Superfluid fraction in an interacting spatially modulated Bose-Einstein condensate, G. Chauveau, C. Maury, F. Rabec, C. Heintze, G. Brochier, S. Nascimbene, J. Dalibard and J. Beugnon, *Physical Review Letters* 130, 226003 (2023).

An article is being prepared on the experimental demonstration of Bloch oscillations of magnetic solitons, which was the subject of the project described in Chapters 4, 5 and 6.

Appendix B

Numerical simulations of the Gross-Pitaevskii equation

This appendix briefly describes the numerical methods used in the two science projects of this thesis to solve the Gross-Pitaevskii equation. The split-step algorithm is employed for both the 2D case in the presence of a sinusoidal potential (Chapter 3) and the 1D case with an immiscible mixture and a linear potential (Chapters 4 and 5). The chosen adimensionalized variables and numerical parameters are also discussed.

B.1 Split-step method

The general Hamiltonian of the system is decomposed into its different contributions $\hat{H} = \hat{H}_{\text{kin}} + \hat{H}_{\text{int}} + \hat{H}_{\text{pot}}$ and we write the order parameter of the system, which we want to access, as φ. Let us imagine that we have written an adimensionalized form of the Gross-Pitaevskii equation as $\mathrm{i}\frac{\partial\varphi}{\partial t} = \hat{H}\,\varphi$. Extracting φ or the energy structure of the system (eigenvalues of $\hat{H}$) can be a complex task without simplifications. This is due to the presence of the nonlinear term describing the interactions in the GP equation.

To go further, we introduce the evolution operator $\hat{U}(t) = \exp\Big(-\mathrm{i}\hat{H}t\Big)$ so that we can write the GP equation in the form:

$$\varphi(t) = \hat{U}(t)\,\varphi(0) \tag{B.1}$$

We now discretize the problem in time and introduce a small timestep $\mathrm{d}t$ and write the time t as $t = p\,\mathrm{d}t$ where p is an integer. Since the evolution operator satisfies $\hat{U}(t) = \Big(\hat{U}(\mathrm{d}t)\Big)^p$, we can evaluate $\varphi(t+\mathrm{d}t)$ knowing $\varphi(t)$ using $\hat{U}(\mathrm{d}t)$:

$$\varphi(t+\mathrm{d}t) = \hat{U}(\mathrm{d}t)\varphi(t) \tag{B.2}$$

This evaluation of φ, timestep by timestep, gives part of the name to this numerical method [262, 263]. The other part "split" comes from the next assumption that we make to calculate $\varphi(t+\mathrm{d}t)$ in practice. Indeed, the direct evaluation of the effect of the total Hamiltonian on the wavefunction can be difficult to compute because of the different characteristics of the terms entering $\hat{H}$ (*e.g.* momentum operator for the kinetic term while position operator for the potential term). In order to proceed, we ignore the non-commutativity of the different terms of the Hamiltonian and split (B.2) as:

$$\varphi(t+\mathrm{d}t) \simeq \exp\Big(-\mathrm{i}\hat{H}_{\text{kin}}\,\mathrm{d}t\Big) \times \exp\Big(-\mathrm{i}\hat{H}_{\text{int}}\,\mathrm{d}t\Big) \times \exp\Big(-\mathrm{i}\hat{H}_{\text{pot}}\,\mathrm{d}t\Big)\varphi(t) \tag{B.3}$$

The errors made by doing this appoximation involve the commutators between the different terms of the Hamiltonian and are thus terms scaling in $(\mathrm{d}t)^2$. Therefore, we understand that (B.3) gives a good approximation of the order parameter if $\mathrm{d}t$ is sufficiently small. More precisely, for this development to be valid, what should be small is instead each of the arguments inside the exponentials. We will give numbers in the next sections when we will have an expression for the adimensionalized Hamiltonians.

Let us imagine that we know how to evaluate the action of each hamiltonian on a wavefunction φ, then we are able to calculate φ at time $t + \mathrm{d}t$ knowing $\varphi(t)$. If we repeat that a certain number of time p, we are able to calculate it at any desired time $t = p\,\mathrm{d}t$. This is called *real-time propagation*.

A significant advantage of the split-step method is the ability not only to extract real-time dynamics, but also to calculate the ground state of the system. This numerical method is known as *imaginary-time propagation* in contrast to the former method. Indeed, if we take $\tilde{t} = -it$ in the expression (B.1), we obtain:

$$\varphi(\tilde{t}) = \exp\left(-\hat{H}\tilde{t}\right)\varphi(0) \tag{B.4}$$

This equation has no physical meaning because it deals with imaginary time. However, it allows us to obtain the stationary state of the system for sufficiently long computational imaginary times. Indeed, if we write φ_j and E_j as the eigenstates and eigenvalues of the Hamiltonian $\hat{H}$, each eigenstate will evolve in imaginary time as $\varphi_j(\tilde{t}) = \exp\left(-E_j\tilde{t}\right)\varphi_j(0)$. The imaginary time evolution starts with a wavefunction $\varphi(0)$, which can be decomposed on the eigenbasis $\{\varphi_j\}_j$. After a long enough imaginary time, only the state of minimal energy will remain, while the other eigenstates will decrease exponentially faster (see (B.4)). Therefore, this method gives us the ground state of the system. In practice, we also need a similar splitting of the total Hamiltonian, as in (B.3), to calculate the wavefunction at the next imaginary time. The number of timesteps required to reach the stationary state depends on the desired level of precision[1]. Additionally, the convergence speed is affected by the initial state chosen, specifically its proximity to the ground state of the system. Furthermore, the convergence speed differs depending on the distance between the first excited state and the ground state.

B.2 2D GPE numerical resolution

In this section, we will demonstrate how to handle the various terms in the Hamiltonian. We will start with the 2D equation, which was used in Chapter 3, and include a linear potential term in addition to a sinusoidal potential. The dimensional equation, with φ normalized to the number of atoms N, writes:

$$\mathrm{i}\hbar\frac{\partial\varphi}{\partial t} = -\frac{\hbar^2}{2m}\Delta\varphi + \frac{\hbar^2}{m}\tilde{g}|\varphi|^2\varphi + V\varphi \tag{B.5}$$

with $V(x) = V_0\cos(qx) + g_F m_F \mu_B b' x$ the total potential, which depends only on the position coordinates x and y.

To adimensionalize this equation, we introduce an arbitrary length scale l, a corresponding pulsation scale $\omega = \hbar/(ml^2)$ and define new adimensionalized variables: $\bar{x}, \bar{y} = x, y/l$, $\bar{t} = \omega t$ and $\bar{\varphi} = \varphi \times l$. The equation (B.5) then transforms into:

[1] We usually stop the loop when the relative difference of wavefunction at time t and at time $t + \mathrm{d}t$ is less than 10^{-5}.

$$\mathrm{i}\frac{\partial\bar{\varphi}}{\partial\bar{t}} = \underbrace{-\frac{1}{2}\bar{\Delta}\bar{\varphi}}_{\hat{H}_{\mathrm{kin}}\bar{\varphi}} + \underbrace{\tilde{g}|\bar{\varphi}|^2\bar{\varphi}}_{\hat{H}_{\mathrm{int}}\bar{\varphi}} + \underbrace{\frac{V(x)}{\hbar\omega}\bar{\varphi}}_{\hat{H}_{\mathrm{pot}}\bar{\varphi}} \tag{B.6}$$

We will omit the bars on the variables in the following, but the problem is now adimensionalized. How can we evaluate the effects of the different Hamiltonians on the wavefunction φ? For this, we have to discretize the problem not only in time variables, as we already did, but also in space variables. We introduce a spacestep $\mathrm{d}x$, a number of spacesteps n_x and the grid size is then $L_x = n_x \times \mathrm{d}x$. The list of the position coordinates is chosen to be symmetric around 0 and goes from $-L_x/2$ to $L_x/2$ in steps of $\mathrm{d}x$. The 2D wavefunction $\bar{\varphi}$ is then a matrix $n_x \times n_x$. The action of $\hat{H}_{\mathrm{int}}$ and $\hat{H}_{\mathrm{pot}}$ are natural to evaluate in the position basis, since these two operators are diagonal in it. Their results at the discretized position x is simply to multiply the wavefunction at the previous timestep φ by $\tilde{g}|\varphi(x)|^2$ and by $V(x)/\hbar\omega$, respectively. However, assessing the action of $\hat{H}_{\mathrm{kin}}$ in the position basis is not straightforward since this operator is diagonal in the Fourier basis but not in the position basis. This is why we needed to split the Hamiltonian into its different parts. Nevertheless, one can still Fourier transform $\varphi(x)$ into $\tilde{\varphi}(q_x)$, and the action of the kinetic Hamiltonian will simply be the transformation: $\tilde{\varphi}(q_x) \to q_x^2/2 \times \tilde{\varphi}(q_x)$, where q_x are the spatial frequencies associated with the discretized x list. Then, after this evaluation, we compute an inverse Fourier transform of the modified wavefunction to come back in the position space and start the next timestep.

Having described the numerical protocol, how do we choose the values of n_x, $\mathrm{d}x$, $\mathrm{d}t$? We want to simulate our experiment which takes place in a box of typical size $L \simeq 40\,\mu\mathrm{m}$. In the numerics, we choose for example a dimensional grid size $L_x = 50\,\mu\mathrm{m}$. Then we need the space discretization $\mathrm{d}x$ to be small compared to all the characteristic length scales of the problem and especially the healing length, which for us is typically in 2D: $\xi \simeq 0.25\,\mu\mathrm{m}$. In practice, we take $\mathrm{d}x = 0.097\,\mu\mathrm{m}$ so that $\mathrm{d}x \leq \xi/2$ and such that the number of points is $n_x = 512$ a power of 2, which allows a faster computation of the Fourier transforms. Then, the time discretization is chosen such that the conditions of the split-step method are satisfied: all arguments of the exponential terms should be small compared to 1[2] . We take $\mathrm{d}t = 10^{-3}$ along with the length for adimensionalization $l = 1\,\mu\mathrm{m}$ to satisfy these equations. With these numbers, we verify that the total energy of the system is conserved up to the 10^{-5} level during real-time propagation. This level of precision is sufficient for our purposes.

B.3 1D coupled GPEs numerical resolution

Chapters 4, 5 and 6 discuss the physics of magnetic solitons. These solitons were initially introduced as stationary solutions of the Landau-Lifschitz Equation in a 1D ferromagnetic spin chain. A mapping was demonstrated between this system and weakly-interacting mixtures following coupled GPEs in certain conditions [42]. The mixture under consideration must be weakly miscible or immiscible to maintain a constant total density. The numerical resolution of the coupled GPEs, leading near the Manakov regime to the emergence of magnetic solitons, is described below.

[2]The various conditions can be roughly summarized as follows:

$$\mathrm{d}t \times \left(\frac{\pi}{\mathrm{d}x}\right)^2 \ll 1, \quad V_0 \times \mathrm{d}t \ll 1, \quad \mathrm{d}t \times \frac{N\tilde{g}}{n_x^2} \ll 1 \tag{B.7}$$

The 1D dimensional equations for the order parameters ψ_1, ψ_2 of the states 1 and 2 with the 1D interaction parameters $g_{ij} = 2\hbar\omega_\perp a_{ij}$ ($\omega_\perp$ is the angular frequency characterizing the transverse confinement) are:

$$\begin{cases} \mathrm{i}\hbar\frac{\partial\psi_1}{\partial t} = -\frac{\hbar^2}{2m}\frac{\partial^2\psi_1}{\partial x^2} + g_{11}|\psi_1|^2\psi_1 + g_{12}|\psi_2|^2\psi_1 + V_1\psi_1 \\ \mathrm{i}\hbar\frac{\partial\psi_2}{\partial t} = -\frac{\hbar^2}{2m}\frac{\partial^2\psi_2}{\partial x^2} + g_{22}|\psi_2|^2\psi_2 + g_{12}|\psi_1|^2\psi_2 + V_2\psi_1 \end{cases} \tag{B.8}$$

where ψ_1 (respectively ψ_2) is normalized to N_1 (resp. N_2) and where V_1 and V_2 are the potentials felt by the states 1 and 2. In the following, we consider the case of linear potentials due to an external magnetic gradient b' and states of opposite hyperfine spin projection $m_F = \pm 1$: $V_1(x) = -V_2(x) = g_F\mu_B b' x$.

As in the 2D case, we introduce an arbitrary length scale l and a corresponding frequency scale $\omega = \hbar/(ml^2)$. The equations can be adimensionalized for the order parameters $\bar{\psi}_{1,2} = \psi_{1,2} \times \sqrt{l}$:

$$\begin{cases} \mathrm{i}\frac{\partial\bar{\psi}_1}{\partial t} = -\frac{1}{2}\frac{\partial^2\bar{\psi}_1}{\partial\bar{x}^2} + 2\frac{\omega_\perp}{\omega}\frac{a_{11}}{l}|\bar{\psi}_1|^2\bar{\psi}_1 + 2\frac{\omega_\perp}{\omega}\frac{a_{12}}{l}|\bar{\psi}_2|^2\bar{\psi}_1 + \frac{V_1(x)}{\hbar\omega}\bar{\psi}_1 \\ \mathrm{i}\frac{\partial\bar{\psi}_2}{\partial t} = -\frac{1}{2}\frac{\partial^2\bar{\psi}_2}{\partial\bar{x}^2} + 2\frac{\omega_\perp}{\omega}\frac{a_{22}}{l}|\bar{\psi}_2|^2\bar{\psi}_2 + 2\frac{\omega_\perp}{\omega}\frac{a_{12}}{l}|\bar{\psi}_1|^2\bar{\psi}_2 + \frac{V_2(x)}{\hbar\omega}\bar{\psi}_2 \end{cases} \tag{B.9}$$

The bars will be omitted in the following. The numerical recipe for solving the coupled GPEs in mixtures is similar to that of a single-component state. A split-step method is used, and at each time step (imaginary or real), the two wavefunctions are calculated by evaluating the actions of the kinetic Hamiltonian in the Fourier basis. Then, the potential and interaction Hamiltonians are assessed in the direct basis. We write the interaction Hamiltonians that have been modified by the presence of the mixture as: $\hat{H}_{\mathrm{int},1}\,\psi_1 = 2\frac{\omega_\perp}{\omega}\left(\frac{a_{11}}{l}|\psi_1|^2 + \frac{a_{12}}{l}|\psi_2|^2\right)\psi_1$ and similarly $\hat{H}_{\mathrm{int},2}\,\psi_2 = 2\frac{\omega_\perp}{\omega}\left(\frac{a_{22}}{l}|\psi_2|^2 + \frac{a_{12}}{l}|\psi_1|^2\right)\psi_2$ where ψ_1 and ψ_2 are evaluated at the previous timesteps in the right expressions.

The split-step method relies on the approximation of the non-commutativity of the incremental terms of the Hamiltonian and it gives a good estimate of the stationary state or the real-time evolution if all the arguments within the exponentials of (B.3) are small compared to 1. To fulfill these conditions with a longer 1D tube, we use a larger grid compared to the 2D case. Otherwise we use similar parameters[3]:

- $n_x = 1024$, $\mathrm{d}x = 0.097\,\mu\mathrm{m} \leq \xi/2$, $L_x = n_x\,\mathrm{d}x = 100\,\mu\mathrm{m}$, $l = 1\,\mu\mathrm{m}$
- $\mathrm{d}t = 10^{-3}$
- $\omega_\perp = 2\pi \times 400\,\mathrm{Hz}$, $g_F = 1/2$, $a_{11} = a_{22} = 100.19\,a_B$ and $a_{12} = 101.54\,a_B$ where a_B is the Bohr radius. These numbers are the one measured in our experiment for the $|1,-1\rangle/|1,+1\rangle$ mixture.

Starting from a Gaussian wavepacket for the minority component and the complementary shape for the majority one, these numbers lead to the formation of a magnetic soliton through imaginary time evolution. When a differential linear gradient is applied, the position of the magnetic soliton oscillates over time, as seen in Chapter 5.

[3] This is because the new length scale introduced by the mixture, ξ_s, the spin healing length, is much larger than the healing length ($\xi_s \sim 10\xi$ in our case). The latter thus remains the smaller relevant length scale in the problem compared to which the space discretization should be small.

Appendix C

Analytical expressions of the density modulation under a sinusoidal potential at low modulation depths

This appendix aims to describe the procedure by which we obtain analytical expressions for the amplitudes of the harmonics and the compressibility at low modulation depths in Chapter 3.

We write the 2D stationary GP equation for the order parameter φ in the potential $V(x) = V_0 \cos(qx)$ with an interaction parameter g and a chemical potential μ as:

$$\mu\varphi = g\varphi^3 + V(x)\varphi - \frac{\hbar^2}{2m}\frac{\partial^2\varphi}{\partial x^2} \tag{C.1}$$

We now expand the order parameter and the chemical potential in powers of V_0 (the index i means an expansion of the quantity at order i in V_0):

$$\varphi(x) = \varphi_0 + \varphi_1(x) + \varphi_2(x) + ..., \quad \mu = \mu_0 + \mu_1 + \mu_2 + ... \tag{C.2}$$

which results in the following expansion for the density:

$$n(x) = \varphi^2 = \underbrace{\varphi_0^2}_{n_0} + \underbrace{2\varphi_0\varphi_1(x)}_{n_1(x)} + \underbrace{2\varphi_2\varphi_0 + \varphi_1^2}_{n_2(x)} \tag{C.3}$$

C.1 Order 0 in V_0

At order 0, the chemical potential is fixed by the mean density in the system:

$$\mu_0 = g\varphi_0^2 \tag{C.4}$$

C.2 Order 1 in V_0

The first order terms in the equation (C.1) satisfy:

$$\mu_0\varphi_1 + \mu_1\varphi_0 = 3g\varphi_0^2\varphi_1 + V_0\cos(qx)\varphi_0 - \frac{\hbar^2}{2m}\frac{\partial^2\varphi_1}{\partial x^2} \tag{C.5}$$

Guided by the expression of the potential, we write $\varphi_1(x) = A_1\cos(qx)$. Since n_1 is direcly proportional to φ_1, and the spatial average of n_1 should be zero, we have $\langle\varphi_1\rangle = 0$, where $\langle\cdot\rangle$ means a spatial average. In (C.5), it translates into:

$$\mu_1 = 0 \tag{C.6}$$

We now plug the expression of φ_1 into (C.5) to get the equation satisfied by A_1:

$$A_1 = -\frac{V_0}{\epsilon_q + 2\mu_0}\varphi_0 \tag{C.7}$$

where $\epsilon_q = \frac{\hbar^2 q^2}{2m}$ is the recoil energy associated with the wavevector of the lattice q. From the development of the density in powers of V_0, we thus find $n_1(x) = n_1 \cos(qx)$ with:

$$\frac{n_1}{n_0} = -\frac{2V_0}{\epsilon_q + 2\mu_0} \tag{C.8}$$

C.3 Order 2 in V_0

The GP equation for the second order terms writes:

$$\mu_0\varphi_2 + \mu_2\varphi_0 = 3g\varphi_0^2\varphi_2 + 3g\varphi_0\varphi_1^2 + V_0\varphi_1\cos(qx) - \frac{\hbar^2}{2m}\frac{\partial^2\varphi_2}{\partial x^2} \tag{C.9}$$

From the expression of $n_2(x)$ in (C.3) and since we impose its spatial average to be zero, we obtain: $\langle\varphi_2\rangle \equiv B_2 = -\frac{A_1^2}{4\varphi_0}$. We then write $\varphi_2 = B_2 + A_2\cos(2qx)$. Taking the spatial mean in (C.9) and using the previously derived expression of A_1, we obtain an expression for the chemical potential at second order in V_0:

$$\mu_2 = gA_1^2 + V_0\frac{A_1}{2} = -\frac{\epsilon_q}{2(\epsilon_q + 2\mu_0)^2}V_0^2 \tag{C.10}$$

We can then extract the first non-zero term in the expansion of the compressibility in powers of V_0 $\kappa = \left(n_0\frac{\partial\mu}{\partial n_0}\right)^{-1}$ with $\mu = \mu_0 + \mu_2$:

$$\kappa = \mu_0^{-1}\left(1 - \frac{2\epsilon_q V_0^2}{(\epsilon_q + 2\mu_0)^3}\right) \tag{C.11}$$

When we identify the terms in $\cos(2qx)$ in (C.9), we extract the expression of A_2:

$$A_2 = \frac{\epsilon_q - \mu_0}{2(\epsilon_q + 2\mu_0)^2(2\mu_0 + 4\epsilon_q)}V_0^2\varphi_0 \tag{C.12}$$

Finally, with the definition of the second harmonic $n_2(x) = n_2\cos(2qx)$, we express it as:

$$n_2 = \frac{A_1^2}{2} + 2A_2\phi_0 = \frac{3\epsilon_q}{(\epsilon_q + 2\mu_0)^2(2\mu_0 + 4\epsilon_q)} \tag{C.13}$$

The expansion can be continued to the next order (order 3 in V_0). However, for the range of explored values of $V_0/\epsilon_q \lesssim 10$, expanding up to order 2 is sufficient to capture most of the physics.

Appendix D

Evaluation of the correcting factors in the *in situ* density measurements

This appendix provides a detailed description of how we access the density profiles of our density-modulated cloud and overcome the filtering of the atomic contrast caused by the finite resolution of our imaging system.

D.1 Notations

For a lattice with wavevector q, several effects can reduce the contrast of the atomic density modulation on the Princeton camera used for absorption imaging:

- a non perfect transfer function from the DMD to the atoms, labeled $T_{D\to A}(q)$. The potential depth V_0 felt by the atoms is then $V_0 = T_{D\to A}(q) \times \gamma \times I$ with γ the ideal link between the potential and the light intensity I.
- a non perfect transfer function from the atoms to the Princeton camera, labelled $T_{A\to C}(q)$.
- a pixelization effect on the Princeton camera due to the finite effective pixelsize of the atoms on the Princeton camera (1.15 µm). We write the loss of contrast caused by this pixelization effect $p(q)$.

They are summarized in Figure D.1.

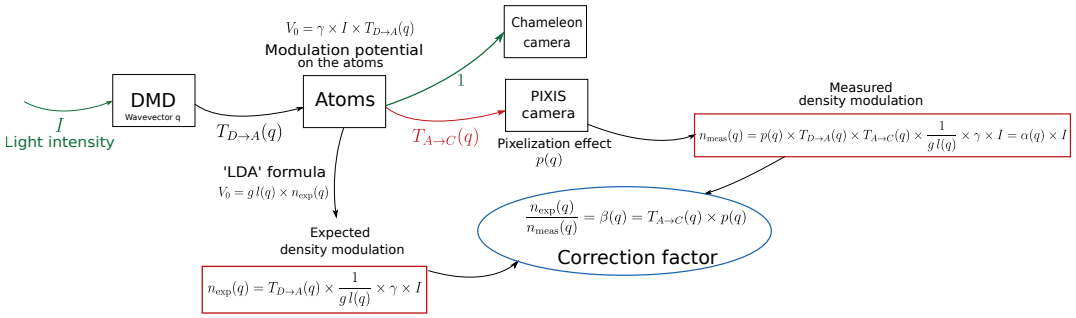

FIGURE D.1: Explanation of the different notations and factors which provok a reduction of the density contrast.

At low modulation depths, the connection between the potential depth and the density modulation has been written in Chapter 3 and Appendix C, and reads:

$$V_0 = g\left(1 + \frac{\epsilon_q}{2\mu_0}\right) n_1 \tag{D.1}$$

We rewrite it as: $V_0 = gl(q)n_1$, with $l(q) = 1 + \frac{\epsilon_q}{2\mu_0}$.

Thus, taking all these effects into account, we write the measured density as:

$$n_{\text{meas}}(q) = p(q) \times T_{D\to A}(q) \times T_{A\to C}(q) \times \frac{1}{gl(q)} \times \gamma \times I = \alpha(q) \times I \tag{D.2}$$

where $\alpha(q)$ are the linear slopes of the density modulations at low intensities, determined on Figure 3.6. What we would expect if detection were perfect is:

$$n_{\text{exp}}(q) = T_{D\to A}(q) \times \frac{1}{gl(q)} \times \gamma \times I \tag{D.3}$$

Thus, with the definition of the β factor used in the text: $\beta(q) = n_{\text{meas}}(q)/n_{\text{exp}}(q)$, we write it as:

$$\beta(q) = p(q) \times T_{A\to C}(q) \tag{D.4}$$

D.2 Pixelization effect

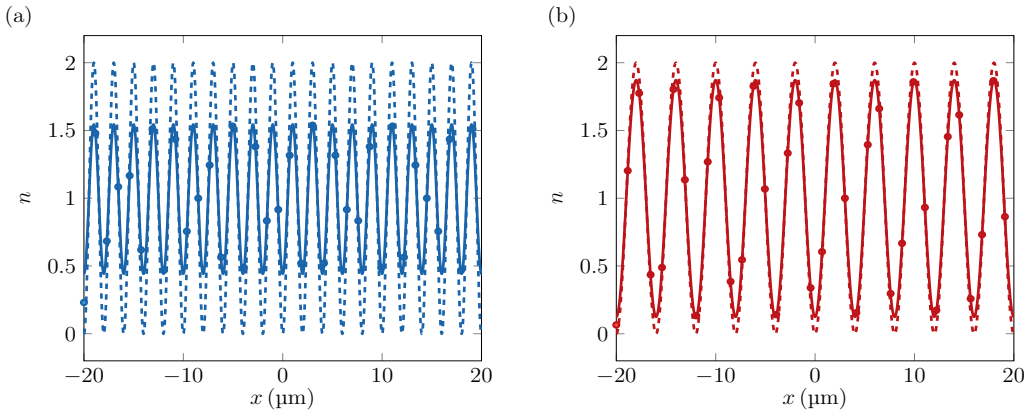

FIGURE D.2: Reduction of the atomic contrast due to the finite effective pixelsize of the absorption imaging camera. (a): the 2 µm lattice case. (b): the 4 µm lattice case. The circles represent points spaced at 1.15 µm intervals, with their ordinate calculated as the integral of the ideal sinusoid (shown as a dashed line) between the preceding pixel and the current one. The solid lines are sinusoidal fits of these discretized signals and the dashed lines are the desired density evolutions. The ratio of the fitted amplitude to the desired amplitude is used to determine the effect of pixelization. We extract respectively $p = 0.55$ and $p = 0.87$ for the 2 µm and the 4 µm lattices.

To compute the impact of the pixelization effect on the reduction of contrast observed on the Princeton camera[1], we construct a numerical ideal sinusoidal function. At intervals of 1.15 µm (the effective pixelsize of the Princeton camera), we integrate this function from the previous pixel to the current one, simulating the operation of

[1]The pixelization effect on the control camera has been disregarded due to the effective pixel size being 0.1 µm.

a camera. A sinusoidal function was fitted to the pixelized signal, resulting in the graphs shown in Figure D.2, for the lattices at 4 µm and 2 µm. A reduction in the atomic contrast is oberved and accounted for in the $p(q)$ factor (Figure D.2).

D.3 Determination of the $\beta(q)$ coefficients

For the β coefficients, we now only need to compute the transfer function from the atoms to the camera $T_{A\to C}(q)$. Since the transfer function between the DMD and the atoms also enters the expression of the measured density (D.2), we can only determine the value of $T_{A\to C}(q)$ by taking the ratio of equation (D.2) evaluated at different lattice wavevectors q and q':

$$\frac{T_{A\to C}(q)}{T_{A\to C}(q')} = \frac{\alpha(q)l(q)}{p(q)T_{D\to A}(q)} \times \frac{p(q')T_{D\to A}(q')}{\alpha(q')l(q')} \tag{D.5}$$

The transfer function from the DMD to the atoms is directly proportional to the light contrast $\mathcal{C}(q)$, plotted in Figure 3.6, and observed on the control camera[2]:

$$\frac{T_{D\to A}(q)}{T_{D\to A}(q')} = \frac{\mathcal{C}(q)}{\mathcal{C}(q')} \tag{D.6}$$

All quantities can now be evaluated, assuming that $T_{D\to A}(q) = T_{A\to C}(q) = 1$ for the lattices of spacings $d \geq 8$ µm (see Figure 3.6). The results are summarized in the following table:

Lattice period d (µm)	$\mathcal{C}(q)$	$T_{D\to A}(q)$	$T_{A\to C}(q)$	$l(q)$	$p(q)$	$\alpha(q)$ (a.u.)	$\beta(q)$
≥ 8	0.75	1	1	1	1	54.4	1
4	0.75	1	0.85	1.07	0.87	37.3	0.73
2	0.51	0.6	0.4	1.28	0.55	6.1	0.21

[2]We assume that the transfer function from the atoms to the control camera imaging system is equal to 1 regardless of the wavevector q.

Appendix E

Dynamics of solitons of the 1D NLSE under a linear potential

This appendix examines the effect of a constant force on various types of solitons of the 1D NLSE introduced in Chapter 4. It will emphasize the peculiar periodic oscillation seen in the case of easy-axis magnetic solitons and discussed in Chapter 5.

E.1 Bright soliton of the 1D NLSE

We recall the mathematical expression of a bright soliton moving at velocity v given in (4.6):

$$\psi_v(x,t) = \frac{\sqrt{\kappa N/2}}{\cosh\left[\kappa(x-vt)\right]}\,\mathrm{e}^{-\mathrm{i}\Omega t}\,\mathrm{e}^{\mathrm{i}m(xv-v^2t/2)/\hbar} \tag{E.1}$$

with N the atom number in the wavepacket, $\kappa = \frac{mN|g|}{2\hbar^2}$ and $\hbar\Omega = -\frac{mg^2N^2}{8\hbar^2}$. The energy can be computed as $E = \int \mathrm{d}x \left[\frac{\hbar^2}{2m}\left(\frac{\partial\psi_v}{\partial x}\right)^2 - \frac{g}{2}|\psi_v|^4\right]$. We obtain:

$$E(N,v) = -\frac{1}{24}mg^2N^3 + \frac{1}{2}Nmv^2 \tag{E.2}$$

The momentum of the bright soliton is defined as follows:

$$p = -\mathrm{i}\hbar\int \psi_v^*\frac{\partial\psi_v}{\partial x}\,\mathrm{d}x = Nmv \tag{E.3}$$

Under the action of a constant force f, the momentum follows $\frac{\mathrm{d}p}{\mathrm{d}t} = Nf$ and the momentum expression (E.3) leads to a linear variation of the velocity in time, thus a classical equation of motion for the position of the soliton:

$$x = \frac{f}{2m}t^2 \tag{E.4}$$

The equation of motion is a single-particle equation, and remarkably the dynamics are not affected by the number of atoms in the wavepacket. This is verified in Figure E.1.

E.2 Dark soliton of the 1D NLSE

We now discuss the case of a moving dark soliton for which we recall the expression of the wavefunction:

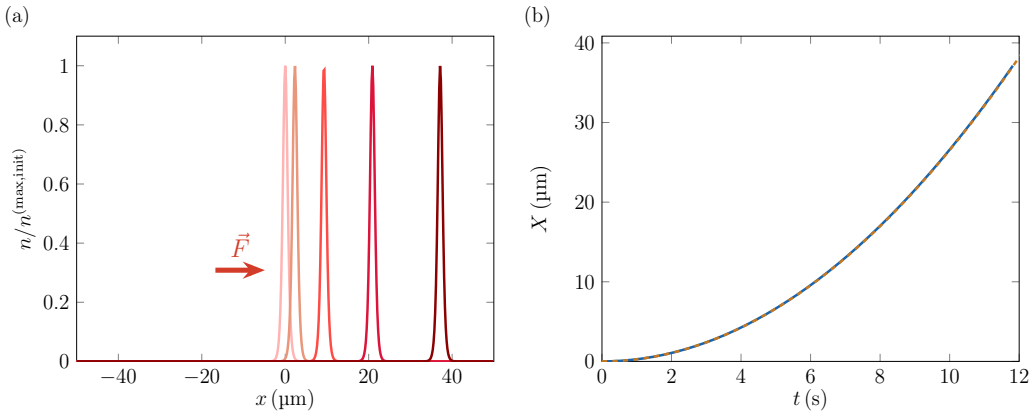

FIGURE E.1: Numerical simulation of a bright soliton under a constant force directed along $+x$. The GP simulation is run for a negative scattering length $a = -100a_B$, $N = 2000$ atoms, a magnetic force $g_F\mu_B b' \simeq 5 \times 10^{-8} mg$ (g is the gravity acceleration here). (a): Profiles every $\Delta t = 3\,\mathrm{s}$. The darker the color the longer the time. The profiles are not distorted. (b): Center of mass evolution with the blue solid line. The orange dashed line is the prediction (E.4).

$$\psi_v(x,t) = \sqrt{\frac{\mu}{g}}\left\{\mathrm{i}\frac{v}{c_B} + \sqrt{1-\frac{v^2}{c_B^2}}\tanh\left[\kappa\sqrt{1-\frac{v^2}{c_B^2}}(x-vt)\right]\right\}\mathrm{e}^{-\mathrm{i}\mu t/\hbar} \tag{E.5}$$

with $\kappa = \frac{1}{\hbar}\sqrt{m\mu}$. A π phase jump at the soliton position is associated. It is important to note that this is a crucial requirement for obtaining a stabilized wavepacket.

The grand canonical energy of the dark soliton is the quantity adapted to the problem [264]:

$$E_{\mathrm{GC}}(\mu, v) = \frac{\hbar^2}{2m}\int\left|\frac{\partial\psi_v}{\partial x}\right|^2 \mathrm{d}x + \frac{g}{2}\int|\psi_v|^4\,\mathrm{d}x - \mu\int|\psi_v|^2\,\mathrm{d}x \tag{E.6}$$

Konotop et al. (see also [89]) then write it as a contribution of two terms: the grand canonical energy present without the soliton and an additional term due only to the dark soliton:

$$E_{\mathrm{GC}}(\mu, v) = E_0'(\mu) + E_g'(\mu, v)\,, \text{with}\, E_g'(\mu, v) = \frac{4}{3}\hbar\frac{\mu^{3/2}}{g\sqrt{m}}\left(1-\frac{v^2}{c_B^2}\right)^{3/2} \tag{E.7}$$

To describe the motion under the force derived from the potential $V_{\mathrm{ext}}(x)$, *i.e.* $f = -\frac{\mathrm{d}V_{\mathrm{ext}}}{\mathrm{d}x}$, one uses the local density approximation for a weakly non uniform trap [265, 202], which states that $E_g'(\mu, v) = E_g'(\mu - V_{\mathrm{ext}}(x), v)$ and its conservation in time to write:

$$\frac{\mathrm{d}E_g'}{\mathrm{d}t} = 0 \Rightarrow -\left(\frac{\partial E_g'}{\partial\mu}\right)_v\frac{\mathrm{d}V_{\mathrm{ext}}}{\mathrm{d}x}\frac{\mathrm{d}x}{\mathrm{d}t} + \left(\frac{\partial E_g'}{\partial v}\right)_\mu\frac{\mathrm{d}v}{\mathrm{d}t} = 0 \tag{E.8}$$

From the expression of the energy (E.7) and the energy conservation (E.8) we obtain the equation of motion:

$$2m\frac{\mathrm{d}v}{\mathrm{d}t} = f \tag{E.9}$$

As for the bright soliton, we obtain a single-particle behaviour. The dark soliton propagates in the direction of the applied force with an acceleration which is twice smaller compared to the "naive" expectation [171, 264, 265]:

$$x(t) = \frac{f}{4m}t^2 \tag{E.10}$$

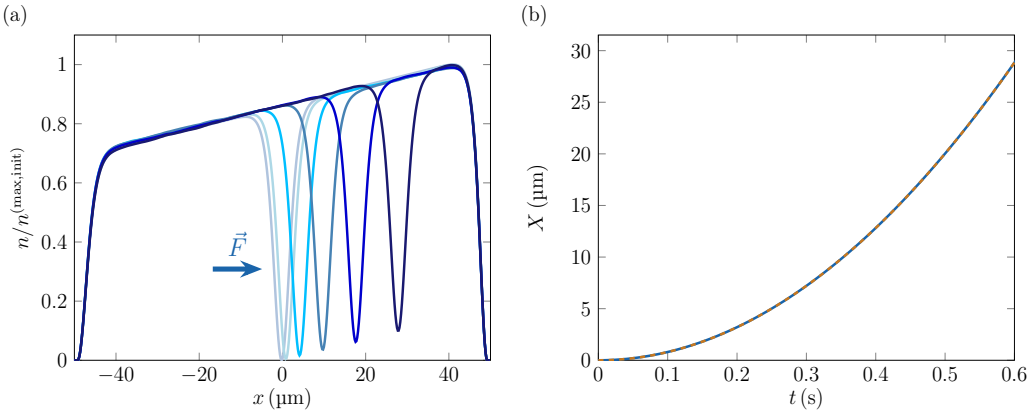

FIGURE E.2: Numerical simulation of a dark soliton under a constant force directed along $+\vec{x}$. The GP simulation is run for a positive scattering length $a = 2.63a_B$, $N = 10000$ atoms, a magnetic force $g_F\mu_B b \simeq 3\times10^{-5}mg$ (g is the gravity acceleration here). The force is applied on a condensate already at equilibrium with the force. (a): Profiles every $\Delta t = 0.3\,\mathrm{s}$. The darker the color the longer the time. The background density is tilted due to the force. (b): The position of the density hole of the wavepacket as a function of time is represented with a blue solid line. The orange dashed line is the prediction (E.10).

The density hole as well as its size are constant during the propagation as we can verify numerically in Figure E.2.

Finally, we mention that even if the dark soliton equation of motion is "natural", expect for the factor 2, it is misleading because the negative effective mass of the dark soliton does not appear in this formula. The latter can be defined as [202]:

$$m_{\mathrm{eff}} = \frac{1}{v}\left(\frac{\partial E_g'}{\partial v}\right)_\mu = -4\,(n_0\xi)\sqrt{1-\left(\frac{v}{c_B}\right)^2}\,m \tag{E.11}$$

where $n_0 = \sqrt{\mu/g}$ is the background density and $\xi = \hbar/\sqrt{mgn_0}$ is the healing length.

We recall that the velocity of a dark soliton cannot exceed the Bogoliubov speed of sound c_B, and that the mean-field approximation used here requires the product of the background density n_0 multiplied by the healing length ξ to be much larger than 1 in order to have many atoms in the hole wavepacket. This negative effective mass is consistent with the picture of the dark soliton as a quasi-particle acting as a hole in the system, which is not stable against snake instabilities as briefly discussed in Chapter 4 [164, 222]. We can reconcile the equation of motion (E.9) with the negative effective mass of the soliton by introducing an effective number of atoms [202], the conjugate variable associated with the chemical potential:

$N_s = \left(\frac{\partial E'_g}{\partial \mu}\right)_v = -2(n_0\xi)\sqrt{1-\left(\frac{v}{c_B}\right)^2}$, which is also negative. One can indeed show that the equation of motion (E.9) can be written:

$$m_{\text{eff}}\frac{\mathrm{d}v}{\mathrm{d}t} = N_s f \tag{E.12}$$

Therefore, the negative effective mass of the dark soliton is not inconsistent with the motion of the wavepacket towards the direction of the force.

E.3 Dark-bright soliton of the 1D NLSE

The following section examines the behavior of a vector soliton, which is made up of a bright soliton trapped in a dark soliton, under a constant force. The analytical case, in which all interaction parameters are equal, is the first to be considered. We recall the expression of a dark-bright soliton moving at velocity v [38] and for which the bright component is submitted to a uniform potential V_2:

$$\begin{cases} \psi_{1,v}(x) = \sqrt{n_0}\left\{\mathrm{i}\sin(\alpha) + \cos(\alpha)\tanh\left[\kappa(x-vt)\right]\right\} \\ \psi_{2,v}(x) = \frac{\sqrt{\kappa N_2/2}}{\cosh[\kappa(x-vt)]}\,\mathrm{e}^{\mathrm{i}mvx/\hbar}\,\mathrm{e}^{-\mathrm{i}\omega t}\,\mathrm{e}^{-\mathrm{i}V_2 t/\hbar} \end{cases} \tag{E.13}$$

The parameters are connected to the velocity v as: $\frac{v}{c_B} = \kappa\xi = -\frac{\bar{N}_2}{4} + \sqrt{\cos^2\alpha + \frac{\bar{N}_2^2}{16}}$ with $\bar{N}_2 = \frac{N_2}{n_0\xi}$ and $\xi = \frac{\hbar}{\sqrt{mgn_0}}$. Besides, we have $\hbar\omega = \frac{1}{2}mv^2 - \frac{\hbar^2\kappa^2}{2m}$.

As for the dark soliton study, we calculate the excess in the grand canonical energy caused by the presence of the dark-bright soliton[1]. We obtain:

$$E'_g(\mu, v, N_2, V_2) = \frac{4}{3}\frac{\hbar^4\kappa^3}{m^2 g} + \left(\frac{\hbar^2\kappa^2}{2m} + \frac{1}{2}mv^2\right)N_2 + V_2 N_2 \tag{E.14}$$

We now use the same argument as for the dark soliton. We assume the conservation of the energy (E.14) throughout the evolution (adiabatic invariant):

$$\frac{\mathrm{d}E'_g}{\mathrm{d}t} = 0 \Rightarrow \left(\frac{\partial E'_g}{\partial v}\right)_\mu \frac{\mathrm{d}v}{\mathrm{d}t} + \frac{\mathrm{d}V_{\text{ext}}}{\mathrm{d}x}\frac{\mathrm{d}x}{\mathrm{d}t} = 0 \tag{E.15}$$

Defining the effective mass as $m_{\text{eff}} = \frac{1}{v}\left(\frac{\partial E'_g}{\partial v}\right)_{\mu,N_2,V_2}$ [202], we get the equation of motion:

$$m_{\text{eff}}\frac{\mathrm{d}v}{\mathrm{d}t} = N_2 f_2 \tag{E.16}$$

where $f_2 = -\frac{\mathrm{d}V_2}{\mathrm{d}x}$ is the constant force applied on the component 2. With the definition of the momentum: $p(v) - p(0) = \int_0^v \frac{1}{v'}\left(\frac{\partial E'_g}{\partial v'}\right)_{\mu,N_2,V_2}\mathrm{d}v'$, it can also be written: $\frac{\mathrm{d}p}{\mathrm{d}t} = N_2 f_2$. In the presence of a constant force, p thus evolves linearly with time.

[1] Unlike the dark soliton, the energy written here includes already the effect of the force.

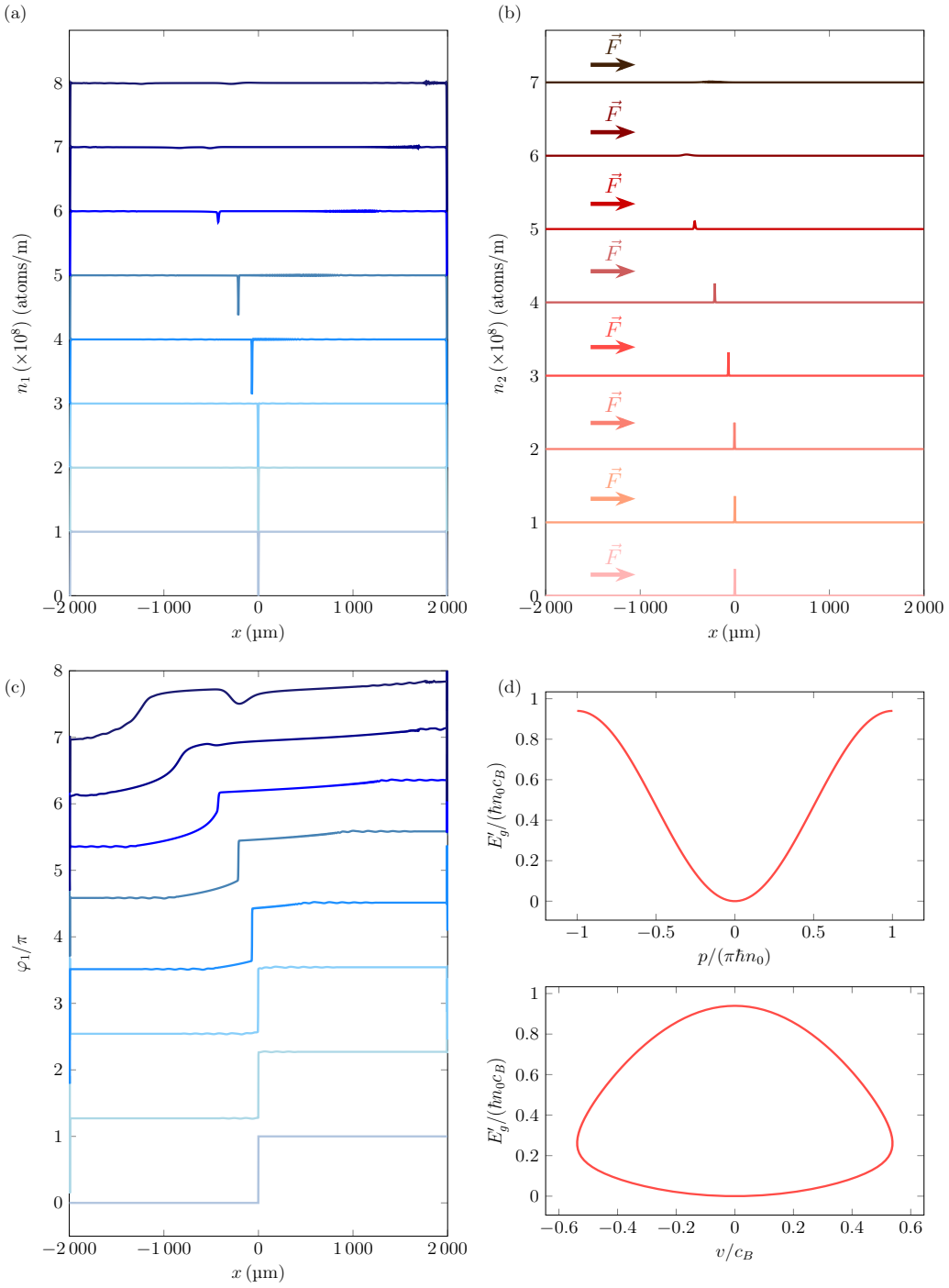

FIGURE E.3: Numerical simulation of a dark-bright soliton under a constant force directed along $+x$. The number of atoms in the minority component $N_2 = 10000$, the background density is $n_0 = 6 \times 10^8$atoms/m and the scattering lengths were chosen all equal to $1\,a_B$. A force is applied on the bright component only and its value is $f_2 = g_F \mu_B b \simeq 3 \times 10^{-5} mg$. (a): Dark component density evolution. (b): Bright component density evolution. (c): Dark component phase evolution. We shift the profiles for better clarity. We display them every $\Delta t = 0.8\,\mathrm{s}$. They should be viewed from bottom to top: the darker the color, the longer the time. The wavepacket continuously expands, making it impossible to adiabatically follow the periodic dispersion curve shown in (d). The graphs in (d) are obtained from (E.14) and a numerical integration to calculate p with the parameters $V_2 = 0$ and $\bar{N}_2 = 1$.

The behavior of the soliton in the presence of the force is determined by its effective mass. The general calculation of the effective mass is complicated because the dependance of the energy (E.14) on v is not trivial. However, we can consider a low velocity expansion of the energy (E.14) to obtain the sign of the effective mass at the beginning of the motion [38]. The relevant adimensional small parameter of this expansion is α. It can be shown that up to order 2 in α, the expression of the excess of grand canonical energy due to the soliton is:

$$E'_g(\mu, v, N_2, V_2) = E'_g(\mu, 0, N_2, V_2) - 2(n_0\xi)mv^2\sqrt{1+\frac{\bar{N}_2^2}{16}} + \mathcal{O}(\alpha^3) \tag{E.17}$$

Therefore, the effective mass for low velocities is [38]:

$$m_{\text{eff}} = -4(n_0\xi)\sqrt{1+\frac{\bar{N}_2^2}{16}}m + \mathcal{O}(\alpha^2) \tag{E.18}$$

A sanity check is the examination of the limiting case where the atom number in the bright component N_2 is small. Indeed, when $\bar{N}_2 \ll 1$, we recover the effective mass of the dark soliton (E.11) in the low velocity limit: $m_{\text{eff}} \simeq -4(n_0\xi)m$. In the opposite limiting case of $\bar{N}_2 \gg 1$, we get: $m_{\text{eff}} = -N_2 m$. The effective mass remains negative and is the opposite of the result for the bright component alone, which may have been naively expected in this limiting case.

As the effective mass is negative at low velocities, regardless of the parameter values, we expect the dark-bright matter wave to propagate in the opposite direction of the applied force at the beginning of the movement. This is confirmed numerically in Figure E.3.

For longer times, we rely on a numerical integration to calculate the evolution of p, v and the energy E'_g as a function of the parameter α. We can obtain the dispersion relation by eliminating α: $E'_g(p)$ (or $E'_g(v)$) are plotted in Figure E.3(d) for a fixed value of $V_2 = 0$ and $\bar{N}_2$. We observe a periodic relationship for $E'_g(p)$. This result, combined with the linear time variation of the momentum p, could lead to Bloch-like oscillations, as we discussed in Chapter 5 and 6. However, an adiabatic approximation should also be made to observe the oscillations as we emphasized in those chapters. Here, the trajectories at the turning point cross the point $\alpha = \pi/2$, where $v = 0$. $\alpha = \pi/2$ means an extension of the wavepacket which diverges: $1/\kappa \to \infty$. Thus, the work of the force over the size of the soliton becomes obligatory large in front of the chemical potential: $f_2/\kappa \gg \mu$ even for extremely small external force.

We numerically confirm that Bloch-like oscillations are not seen for dark-bright solitons in the case of equal interaction parameters. The wavepacket extends over the whole box when the momentum reaches $p \simeq 0$ starting from $p = \pi\hbar n_0 c_B$.

The magnetic soliton did not exhibit the infinite extension of the wavepacket at the turning point. Instead, the wavepacket was observed to shrink as it moved.

We now explore the relaxation of the constraint on equal interaction parameters. If a dark-bright soliton is prepared, *i.e.* a fully depleted bath accompanied with a π phase jump is imposed for the starting position, Bloch-like oscillations are observed in the adiabatic regime. Unlike the easy-axis magnetic soliton, the wavepacket begins its motion by propagating in the opposite direction of the constant force. Although, its depletion diminishes, it does not reach zero as it did for equal interaction parameters. This allows the soliton to return to its initial position without collapsing. In this case, why do we observe Bloch oscillations? At the turning point where the bath is fully depleted, the state of the easy-axis magnetic soliton, described in Chapter 5, is

equivalent to a dark-bright soliton (phase jump of π for the majority component). Therefore, it is not surprising to observe Bloch-like oscillations in the case of a dark-bright soliton with non equal interaction parameters, which start in the opposite direction to the force. This is because its dynamics are the same as those of an easy-axis magnetic soliton during the second half of one period of motion.

In this appendix, we observed the movement of various solitons of the 1D NLSE under a constant force. The magnetic soliton, described in this thesis, exhibits Bloch-like oscillations, which are a specific feature. However, it is important to note its connection with a dark-bright soliton that has unequal interaction parameters.

Bibliography

[1] M. Planck. "Über das Gesetz der Energieverteilung im Normalspectrum". In: *Annalen der Physik* 309.3 (1901), pp. 553–563 (Cited on page 1).

[2] N. Bohr. "Discussion with Einstein on Epistemological Problems in Atomic Physics". Cambridge University Press (1949) (Cited on page 1).

[3] M. Schlosshauer, J. Kofler, and A. Zeilinger. "A snapshot of foundational attitudes toward quantum mechanics". In: *Studies in History and Philosophy of Science Part B: Studies in History and Philosophy of Modern Physics* 44.3 (2013), pp. 222–230 (Cited on page 1).

[4] S. Frabboni, G. C. Gazzadi, and G. Pozzi. "Young's double-slit interference experiment with electrons". In: *American Journal of Physics* 75.11 (2007), pp. 1053–1055 (Cited on page 1).

[5] P. Kapitza. "Viscosity of Liquid Helium below the λ-Point". In: *Nature* 141.3558 (1938), p. 74 (Cited on pages 1, 35).

[6] J. F. Allen and A. D. Misener. "Flow of Liquid Helium II". In: *Nature* 141.3558 (1938), p. 75 (Cited on pages 1, 35).

[7] G. B. Hess and W. M. Fairbank. "Measurements of Angular Momentum in Superfluid Helium". In: *Physical Review Letters* 19.5 (1967), pp. 216–218 (Cited on pages 2, 35).

[8] M. M. Salomaa and G. E. Volovik. "Quantized vortices in superfluid ^{3}He". In: *Review Modern Physics* 59.3 (1987), pp. 533–613 (Cited on page 2).

[9] A. Einstein. "Quantentheorie des einatomigen idealen Gases". Sitzungsberichte der Preussischen Akademie der Wissenschaften (1924), pp. 261–267 (Cited on page 2).

[10] M. H. Anderson, J. R. Ensher, M. R. Matthews, C. E. Wieman, and E. A. Cornell. "Observation of Bose-Einstein Condensation in a Dilute Atomic Vapor". In: *Science* 269.5221 (1995), pp. 198–201 (Cited on pages 2, 9).

[11] K. B. Davis, M.-O. Mewes, M. R. Andrews, N. J. van Druten, D. S. Durfee, D. M. Kurn, and W. Ketterle. "Bose-Einstein Condensation in a Gas of Sodium Atoms". In: *Physical Review Letters* 75.22 (1995), pp. 3969–3973 (Cited on page 2).

[12] I. Bloch, T. W. Hänsch, and T. Esslinger. "Measurement of the spatial coherence of a trapped Bose gas at the phase transition". In: *Nature* 403.6766 (2000), pp. 166–170 (Cited on pages 2, 137).

[13] A. Görlitz, J. M. Vogels, A. E. Leanhardt, C. Raman, T. L. Gustavson, J. R. Abo-Shaeer, A. P. Chikkatur, S. Gupta, S. Inouye, T. Rosenband, and W. Ketterle. "Realization of Bose-Einstein Condensates in Lower Dimensions". In: *Physical Review Letters* 87.13 (2001), p. 130402 (Cited on page 2).

[14] K. Henderson, C. Ryu, C. MacCormick, and M. G. Boshier. "Experimental demonstration of painting arbitrary and dynamic potentials for Bose–Einstein condensates". In: *New Journal of Physics* 11.4 (2009), p. 043030 (Cited on page 2).

[15] I. Bloch. "Ultracold quantum gases in optical lattices". In: *Nature Physics* 1.1 (2005), pp. 23–30 (Cited on page 2).

[16] N. Schlosser, G. Reymond, I. Protsenko, and P. Grangier. "Sub-poissonian loading of single atoms in a microscopic dipole trap". In: *Nature* 411.6841 (2001), pp. 1024–1027 (Cited on page 2).

[17] Ph. Courteille, R. S. Freeland, D. J. Heinzen, F. A. van Abeelen, and B. J. Verhaar. "Observation of a Feshbach Resonance in Cold Atom Scattering". In: *Physical Review Letters* 81.1 (1998), pp. 69–72 (Cited on page 2).

[18] V. L. Berezinskii. "Destruction of long-range order in one-dimensional and two-dimensional systems possessing a continuous symmetry group. II. Quantum systems". In: *Soviet Physics Journal of Experimental and Theoretical Physics* 34.3 (1972), pp. 610–616 (Cited on pages 2, 42, 43).

[19] J. M. Kosterlitz and D. J. Thouless. "Ordering, metastability and phase transitions in two-dimensional systems". In: *Journal of Physics C: Solid State Physics* 6.7 (1973), pp. 1181–1203 (Cited on pages 2, 42, 43).

[20] Z. Hadzibabic, P. Krüger, M. Cheneau, B. Battelier, and J. Dalibard. "Berezinskii-Kosterlitz-Thouless crossover in a trapped atomic gas". In: *Nature* 441.7097 (2006), pp. 1118–1121 (Cited on pages 2, 42).

[21] K. W. Madison, F. Chevy, W. Wohlleben, and J. Dalibard. "Vortex Formation in a Stirred Bose-Einstein Condensate". In: *Physical Review Letters* 84.5 (2000), pp. 806–809 (Cited on page 2).

[22] J. R. Abo-Shaeer, C. Raman, J. M. Vogels, and W. Ketterle. "Observation of Vortex Lattices in Bose-Einstein Condensates". In: *Science* 292.5516 (2001), pp. 476–479 (Cited on page 2).

[23] R. Desbuquois, L. Chomaz, T. Yefsah, J. Léonard, J. Beugnon, C. Weitenberg, and J. Dalibard. "Superfluid behaviour of a two-dimensional Bose gas". In: *Nature Physics* 8.9 (2012), pp. 645–648 (Cited on pages 2, 36).

[24] J. L. Ville, R. Saint-Jalm, É. Le Cerf, M. Aidelsburger, S. Nascimbène, J. Dalibard, and J. Beugnon. "Sound Propagation in a Uniform Superfluid Two-Dimensional Bose Gas". In: *Physical Review Letters* 121.14 (2018), p. 145301 (Cited on pages 2, 40, 51, 56, 75).

[25] P. Christodoulou, M. Gałka, N. Dogra, R. Lopes, J. Schmitt, and Z. Hadzibabic. "Observation of first and second sound in a BKT superfluid". In: *Nature* 594.7862 (2021), pp. 191–194 (Cited on pages 2, 37, 43, 51, 54, 75).

[26] T. Yefsah, R. Desbuquois, L. Chomaz, K. J. Günter, and J. Dalibard. "Exploring the Thermodynamics of a Two-Dimensional Bose Gas". In: *Physical Review Letters* 107.13 (2011), p. 130401 (Cited on pages 2, 30).

[27] R. Saint-Jalm, P. C. M. Castilho, É. Le Cerf, B. Bakkali-Hassani, J.-L. Ville, S. Nascimbene, J. Beugnon, and J. Dalibard. "Dynamical Symmetry and Breathers in a Two-Dimensional Bose Gas". In: *Physical Review X* 9.2 (2019), p. 021035 (Cited on pages 2, 20, 30, 31).

[28] E. P. Gross. "Structure of a quantized vortex in boson systems". In: *Il Nuovo Cimento (1955-1965)* 20.3 (1961), pp. 454–477 (Cited on pages 2, 28).

[29] L. P. Pitaevskii. "Vortex Lines in an imperfect Bose gas". In: *Soviet Physics Journal of Experimental and Theoretical Physics* 13.2 (1961), pp. 451–454 (Cited on pages 2, 28).

[30] T. Dauxois and M. Peyrard. "Physics of Solitons". Cambridge University Press (2006) (Cited on pages 3, 78, 80).

[31] J. S. Russell. "Report on Waves". British Association for the Advancement of Science (1845) (Cited on pages 3, 79).

[32] D. J. Korteweg and G. de Vries. "XLI. On the change of form of long waves advancing in a rectangular canal, and on a new type of long stationary waves". In: *The London, Edinburgh, and Dublin Philosophical Magazine and Journal of Science* 39.240 (1895), pp. 422–443 (Cited on pages 3, 79).

[33] N. J. Zabusky and M. D. Kruskal. "Interaction of "Solitons" in a Collisionless Plasma and the Recurrence of Initial States". In: *Physical Review Letters* 15.6 (1965), pp. 240–243 (Cited on pages 3, 80).

[34] L. F. Mollenauer, R. H. Stolen, and J. P. Gordon. "Experimental Observation of Picosecond Pulse Narrowing and Solitons in Optical Fibers". In: *Physical Review Letters* 45.13 (1980), pp. 1095–1098 (Cited on pages 3, 80–82).

[35] A. Barthelemy, S. Maneuf, and C. Froehly. "Propagation soliton et auto-confinement de faisceaux laser par non linearité optique de kerr". In: *Optics Communications* 55.3 (1985), pp. 201–206 (Cited on pages 3, 82).

[36] L. Khaykovich, F. Schreck, G. Ferrari, T. Bourdel, J. Cubizolles, L. D. Carr, Y. Castin, and C. Salomon. "Formation of a Matter-Wave Bright Soliton". In: *Science* 296.5571 (2002), pp. 1290–1293 (Cited on pages 3, 82, 83).

[37] J. Denschlag, J. E. Simsarian, D. L. Feder, Charles W. Clark, L. A. Collins, J. Cubizolles, L. Deng, E. W. Hagley, K. Helmerson, W. P. Reinhardt, S. L. Rolston, B. I. Schneider, and W. D. Phillips. "Generating Solitons by Phase Engineering of a Bose-Einstein Condensate". In: *Science* 287.5450 (2000), pp. 97–101 (Cited on pages 3, 83).

[38] Th. Busch and J. R. Anglin. "Dark-Bright Solitons in Inhomogeneous Bose-Einstein Condensates". In: *Physical Review Letters* 87.1 (2001), p. 010401 (Cited on pages 3, 84, 115, 118, 120, 187, 189).

[39] C. Becker, S. Stellmer, P. Soltan-Panahi, S. Dörscher, M. Baumert, E.-M. Richter, J. Kronjäger, K. Bongs, and K. Sengstock. "Oscillations and interactions of dark and dark–bright solitons in Bose–Einstein condensates". In: *Nature Physics* 4.6 (2008), pp. 496–501 (Cited on pages 3, 85, 120).

[40] C. Hamner, J. J. Chang, P. Engels, and M. A. Hoefer. "Generation of Dark-Bright Soliton Trains in Superfluid-Superfluid Counterflow". In: *Physical Review Letters* 106.6 (2011), p. 065302 (Cited on pages 3, 83, 85).

[41] C. Qu, L. P. Pitaevskii, and S. Stringari. "Magnetic Solitons in a Binary Bose-Einstein Condensate". In: *Physical Review Letters* 116.16 (2016), p. 160402 (Cited on pages 3, 89, 91, 93, 94, 115, 118, 120).

[42] T. Congy, A. M. Kamchatnov, and N. Pavloff. "Dispersive hydrodynamics of nonlinear polarization waves in two-component Bose-Einstein condensates". In: *SciPost Physics* 1.1 (2016), p. 006 (Cited on pages 3, 90, 93, 94, 174).

[43] A. M. Kosevich, B. A. Ivanov, and A. S. Kovalev. "Magnetic Solitons". In: *Physics Reports* 194.3 (1990), pp. 117–238 (Cited on pages 4, 86–88, 90–92, 94, 96–98, 167).

[44] A. Farolfi, D. Trypogeorgos, C. Mordini, G. Lamporesi, and G. Ferrari. "Observation of Magnetic Solitons in Two-Component Bose-Einstein Condensates". In: *Physical Review Letters* 125.3 (2020), p. 030401 (Cited on pages 4, 119).

[45] X. Chai, D. Lao, K. Fujimoto, R. Hamazaki, M. Ueda, and C. Raman. "Magnetic Solitons in a Spin-1 Bose-Einstein Condensate". In: *Physical Review Letters* 125.3 (2020), p. 030402 (Cited on pages 4, 119).

[46] L.-C. Zhao, W. Wang, Q. Tang, Z.-Y. Yang, W.-L. Yang, and J. Liu. "Spin soliton with a negative-positive mass transition". In: *Physical Review A* 101.4 (2020), p. 043621 (Cited on pages 4, 94, 103, 115).

[47] X. Chai, L. You, and C. Raman. "Magnetic solitons in an immiscible two-component Bose-Einstein condensate". In: *Physical Review A* 105.1 (2022), p. 013313 (Cited on pages 4, 94).

[48] S. Bresolin, A. Roy, G. Ferrari, A. Recati, and N. Pavloff. "Oscillating Solitons and ac Josephson Effect in Ferromagnetic Bose-Bose Mixtures". In: *Physical Review Letters* 130.22 (2023), p. 220403 (Cited on pages 4, 94, 97, 103, 106, 108, 112–114, 116, 120, 126, 132, 137, 140).

[49] A. M. Kosevich, V. V. Gann, A. I. Zhukov, and V. P. Voronov. "Magnetic soliton motion in a nonuniform magnetic field". In: *Journal of Experimental and Theoretical Physics* 87.2 (1998), pp. 401–407 (Cited on pages 4, 97, 98, 102, 104, 106, 115).

[50] C. Zener. "A Theory of the Electrical Breakdown of Solid Dielectrics". In: *Proceedings of the Royal Society of London. Series A, Containing Papers of a Mathematical and Physical Character* 145.855 (1934), pp. 523–529 (Cited on pages 4, 108).

[51] M. Schecter, D. M. Gangardt, and A. Kamenev. "Dynamics and Bloch oscillations of mobile impurities in one-dimensional quantum liquids". In: *Annals of Physics* 327.3 (2012), pp. 639–670 (Cited on pages 4, 111).

[52] F. D. M. Haldane. ""Luttinger liquid theory" of one-dimensional quantum fluids. I. Properties of the Luttinger model and their extension to the general 1D interacting spinless Fermi gas". In: *Journal of Physics C: Solid State Physics* 14.19 (1981), p. 2585 (Cited on pages 4, 111, 116).

[53] D. M. Gangardt and A. Kamenev. "Bloch Oscillations in a One-Dimensional Spinor Gas". In: *Physical Review Letters* 102.7 (2009), p. 070402 (Cited on pages 4, 111).

[54] F. Meinert, M. Knap, E. Kirilov, K. Jag-Lauber, M. B. Zvonarev, E. Demler, and H.-C. Nägerl. "Bloch oscillations in the absence of a lattice". In: *Science* 356.6341 (2017), pp. 945–948 (Cited on pages 4, 110, 111).

[55] D. S. Petrov. "Quantum Mechanical Stabilization of a Collapsing Bose-Bose Mixture". In: *Physical Review Letters* 115.15 (2015), p. 155302 (Cited on pages 4, 85, 86).

[56] C. R. Cabrera, L. Tanzi, J. Sanz, B. Naylor, P. Thomas, P. Cheiney, and L. Tarruell. "Quantum liquid droplets in a mixture of Bose-Einstein condensates". In: *Science* 359.6373 (2018), pp. 301–304 (Cited on pages 4, 86).

[57] G. Semeghini, G. Ferioli, L. Masi, C. Mazzinghi, L. Wolswijk, F. Minardi, M. Modugno, G. Modugno, M. Inguscio, and M. Fattori. "Self-Bound Quantum Droplets of Atomic Mixtures in Free Space". In: *Physical Review Letters* 120.23 (2018), p. 235301 (Cited on pages 4, 86).

[58] I. Ferrier-Barbut, H. Kadau, M. Schmitt, M. Wenzel, and T. Pfau. "Observation of Quantum Droplets in a Strongly Dipolar Bose Gas". In: *Physical Review Letters* 116.21 (2016), p. 215301 (Cited on pages 4, 86).

[59] P. Cheiney, C. R. Cabrera, J. Sanz, B. Naylor, L. Tanzi, and L. Tarruell. "Bright Soliton to Quantum Droplet Transition in a Mixture of Bose-Einstein Condensates". In: *Physical Review Letters* 120.13 (2018), p. 135301 (Cited on pages 4, 86).

[60] F. Böttcher, J.-N. Schmidt, M. Wenzel, J. Hertkorn, M. Guo, T. Langen, and T. Pfau. "Transient Supersolid Properties in an Array of Dipolar Quantum Droplets". In: *Physical Review X* 9.1 (2019), p. 011051 (Cited on page 4).

[61] L. Tanzi, E. Lucioni, F. Famà, J. Catani, A. Fioretti, C. Gabbanini, R. N. Bisset, L. Santos, and G. Modugno. "Observation of a Dipolar Quantum Gas with Metastable Supersolid Properties". In: *Physical Review Letters* 122.13 (2019), p. 130405 (Cited on pages 4, 47).

[62] L. Chomaz, D. Petter, P. Ilzhöfer, G. Natale, A. Trautmann, C. Politi, G. Durastante, R. M. W. van Bijnen, A. Patscheider, M. Sohmen, M. J. Mark, and F. Ferlaino. "Long-Lived and Transient Supersolid Behaviors in Dipolar Quantum Gases". In: *Physical Review X* 9.2 (2019), p. 021012 (Cited on pages 4, 47).

[63] A. J. Leggett. "Can a Solid Be "Superfluid"?" In: *Physical Review Letters* 25.22 (1970), pp. 1543–1546 (Cited on pages 4, 5, 41, 47, 48).

[64] J. Léonard, A. Morales, P. Zupancic, T. Esslinger, and T. Donner. "Supersolid formation in a quantum gas breaking a continuous translational symmetry". In: *Nature* 543.7643 (2017), pp. 87–90 (Cited on pages 4, 47).

[65] J.-R. Li, J. Lee, W. Huang, S. Burchesky, B. Shteynas, F. Ç. Top, A. O. Jamison, and W. Ketterle. "A stripe phase with supersolid properties in spin–orbit-coupled Bose–Einstein condensates". In: *Nature* 543.7643 (2017), pp. 91–94 (Cited on pages 4, 47).

[66] A. J. Leggett. "On the superfluid fraction of an arbitrary many-body system at T = 0". In: *Journal of Statistical Physics* 93.3-4 (1998), pp. 927–941 (Cited on pages 4, 50, 70, 166).

[67] G. Chauveau, C. Maury, F. Rabec, C. Heintze, G. Brochier, S. Nascimbene, J. Dalibard, J. Beugnon, S. M. Roccuzzo, and S. Stringari. "Superfluid Fraction in an Interacting Spatially Modulated Bose-Einstein Condensate". In: *Physical Review Letters* 130.22 (2023), p. 226003 (Cited on pages 5, 53, 69, 72, 166).

[68] K. Kleinlein. "Setting up a new experiment for investigating artificial magnetism of two-dimensional Bose gases". MA thesis. Ludwig Maximilians Universität München (2014) (Cited on pages 8, 146).

[69] L. Corman. "The two-dimensional Bose Gas in box potentials". PhD thesis. Université Paris Sciences et Lettres (2016) (Cited on pages 8, 11, 146).

[70] J.-L. Ville. "Quantum gases in box potentials : sound and light in bosonic Flatland". PhD thesis. Université Paris Sciences et Lettres (2018) (Cited on pages 8, 13).

[71] R. Saint-Jalm. "Exploring two-dimensional physics with Bose gases in box potentials : phase ordering and dynamical symmetry". PhD thesis. Université Paris Sciences et Lettres (2019) (Cited on pages 8, 13, 14, 20–22, 126).

[72] É. Le Cerf. "Demixing phenomena in 2D bose gases". PhD thesis. Sorbonne Université (2020) (Cited on pages 8, 18, 21, 122).

[73] D. A. Steck. "Rubidium 87 D Line Data" (2003) (Cited on page 10).

[74] A. Keshet and W. Ketterle. "A distributed, graphical user interface based, computer control system for atomic physics experiments". In: *Review of Scientific Instruments* 84.1 (2013) (Cited on page 10).

[75] J. Li, K. Lim, S. Das, T. Zanon-Willette, C.-H. Feng, P. Robert, A. Bertoldi, P. Bouyer, C. C. Kwong, S.-Y. Lan, and D. Wilkowski. "Bi-color atomic beam slower and magnetic field compensation for ultracold gases". In: *AVS Quantum Science* 4.4 (2022) (Cited on page 13).

[76] T. C. Li, H. Kelkar, D. Medellin, and M. G. Raizen. "Real-time control of the periodicity of a standing wave: an optical accordion". In: *Optics Express* 16.8 (2008), pp. 5465–5470 (Cited on page 13).

[77] B. Bakkali-Hassani. "Testing scale invariance in a two-dimensional Bose gas : preparation and characterization of solitary waves". PhD thesis. Sorbonne Université (2021) (Cited on pages 14, 85).

[78] C. Dorrer and J. D. Zuegel. "Design and analysis of binary beam shapers using error diffusion". In: *Journal of the Optical Society of America B* 24.6 (2007), pp. 1268–1275 (Cited on pages 14, 16).

[79] K. Hueck, N. Luick, L. Sobirey, J. Siegl, T. Lompe, and H. Moritz. "Two-Dimensional Homogeneous Fermi Gases". In: *Physical Review Letters* 120.6 (2018), p. 060402 (Cited on page 16).

[80] R. W. Floyd and L. Steinberg. "An adaptive algorithm for spatial gray scale". In: *Proceedings of the Society for Information Display* 17 (1975) (Cited on page 16).

[81] Y.-Q. Zou, É. Le Cerf, B. Bakkali-Hassani, C. Maury, G. Chauveau, P. C. M. Castilho, R. Saint-Jalm, S. Nascimbene, J. Dalibard, and J. Beugnon. "Optical control of the density and spin spatial profiles of a planar Bose gas". In: *Journal of Physics B: Atomic, Molecular and Optical Physics* 54.8 (2021), p. 08LT01 (Cited on page 18).

[82] I. I. Rabi, J. R. Zacharias, S. Millman, and P. Kusch. "A New Method of Measuring Nuclear Magnetic Moment". In: *Physical Review* 53.4 (1938), pp. 318–318 (Cited on page 18).

[83] C. Maury. "Probing few and many-body physics in a planar Bose gas : Atom-dimer interactions and zero-temperature superfluid fraction". PhD thesis. Sorbonne Université (2023) (Cited on pages 19, 31, 33, 35, 46, 51, 72).

[84] L. Corman, J. L. Ville, R. Saint-Jalm, M. Aidelsburger, T. Bienaimé, S. Nascimbène, J. Dalibard, and J. Beugnon. "Transmission of near-resonant light through a dense slab of cold atoms". In: *Physical Review A* 96.5 (2017), p. 053629 (Cited on page 19).

[85] R. Saint-Jalm, M. Aidelsburger, J. L. Ville, L. Corman, Z. Hadzibabic, D. Delande, S. Nascimbene, N. Cherroret, J. Dalibard, and J. Beugnon. "Resonant-light diffusion in a disordered atomic layer". In: *Physical Review A* 97.6 (2018), p. 061801 (Cited on page 19).

[86] Y.-Q. Zou, B. Bakkali-Hassani, C. Maury, É. Le Cerf, S. Nascimbene, J. Dalibard, and J. Beugnon. "Tan's two-body contact across the superfluid transition of a planar Bose gas". In: *Nature Communications* 12.1 (2021), p. 760 (Cited on pages 20, 35).

[87] C. Maury, B. Bakkali-Hassani, G. Chauveau, F. Rabec, S. Nascimbene, J. Dalibard, and J. Beugnon. "Precision measurement of atom-dimer interaction in a uniform planar Bose gas". In: *Physical Review Research* 5.1 (2023), p. L012020 (Cited on pages 20, 32–35, 166).

[88] I. Dotsenko, W. Alt, S. Kuhr, D. Schrader, M. Müller, Y. Miroshnychenko, V. Gomer, A. Rauschenbeutel, and D. Meschede. "Application of electro-optically generated light fields for Raman spectroscopy of trapped cesium atoms". In: *Applied Physics B* 78.6 (2004), pp. 711–717 (Cited on page 21).

[89] L. P. Pitaevskii and S. Stringari. "Bose-Einstein Condensation and Superfluidity". Oxford University Press (2016) (Cited on pages 24, 29, 37–39, 50, 51, 116, 185).

[90] B. A. Lippmann and J. Schwinger. "Variational Principles for Scattering Processes. I". In: *Physical Review* 79.3 (1950), pp. 469–480 (Cited on page 25).

[91] J. Weiner, V. S. Bagnato, S. Zilio, and P. S. Julienne. "Experiments and theory in cold and ultracold collisions". In: *Review Modern Physics* 71.1 (1999), pp. 1–85 (Cited on pages 25, 32).

[92] A. Messiah. "Mécanique quantique". Dunod (2003) (Cited on page 26).

[93] S. K. Adhikari. "Quantum scattering in two dimensions". In: *American Journal of Physics* 54.4 (1986), pp. 362–367 (Cited on page 26).

[94] Z. Hadzibabic and J. Dalibard. "Two-dimensional Bose fluids: An atomic physics perspective". In: *La Rivista del Nuovo Cimento* 34.6 (2011), pp. 389–434 (Cited on pages 26, 29).

[95] D. S. Petrov, M. Holzmann, and G. V. Shlyapnikov. "Bose-Einstein Condensation in Quasi-2D Trapped Gases". In: *Physical Review Letters* 84.12 (2000), pp. 2551–2555 (Cited on pages 26, 29).

[96] D. S. Petrov and G. V. Shlyapnikov. "Interatomic collisions in a tightly confined Bose gas". In: *Physical Review A* 64.1 (2001), p. 012706 (Cited on page 26).

[97] C. Chin, R. Grimm, P. S. Julienne, and E. Tiesinga. "Feshbach resonances in ultracold gases". In: *Review Modern Physics* 82.2 (2010), pp. 1225–1286 (Cited on page 27).

[98] A. Marte, T. Volz, J. Schuster, S. Dürr, G. Rempe, E. G. M. van Kempen, and B. J. Verhaar. "Feshbach Resonances in Rubidium 87: Precision Measurement and Analysis". In: *Physical Review Letters* 89.28 (2002), p. 283202 (Cited on page 27).

[99] D. S. Petrov, D. M. Gangardt, and G. V. Shlyapnikov. "Low-dimensional trapped gases". In: *Journal Physics IV France* 116 (2004), pp. 5–44 (Cited on pages 27, 79).

[100] J.-L. Lagrange. "Mécanique Analytique". Cambridge University Press (2009) (Cited on page 28).

[101] J. Dalibard. "Fluides quantiques de basse dimension et transition de Kosterlitz-Thouless". Collège de France lectures (2017) (Cited on page 30).

[102] W. Zwerger. "The BCS-BEC crossover and the unitary Fermi gas". Springer Science & Business Media (2011) (Cited on page 30).

[103] C.-L. Hung, X. Zhang, N. Gemelke, and C. Chin. "Observation of scale invariance and universality in two-dimensional Bose gases". In: *Nature* 470.7333 (2011), pp. 236–239 (Cited on page 30).

[104] L. P. Pitaevskii and A. Rosch. "Breathing modes and hidden symmetry of trapped atoms in two dimensions". In: *Physical Review A* 55.2 (1997), R853–R856 (Cited on pages 30, 130, 139).

[105] F. Chevy, V. Bretin, P. Rosenbusch, K. W. Madison, and J. Dalibard. "Transverse Breathing Mode of an Elongated Bose-Einstein Condensate". In: *Physical Review Letters* 88.25 (2002), p. 250402 (Cited on page 30).

[106] Z.-Y. Shi, C. Gao, and H. Zhai. "Ideal-Gas Approach to Hydrodynamics". In: *Physical Review X* 11.4 (2021), p. 041031 (Cited on page 30).

[107] M. Olshanii, H. Perrin, and V. Lorent. "Example of a Quantum Anomaly in the Physics of Ultracold Gases". In: *Physical Review Letters* 105.9 (2010), p. 095302 (Cited on page 30).

[108] L.-C. Ha, C.-L. Hung, X. Zhang, U. Eismann, S.-K. Tung, and C. Chin. "Strongly interacting two-dimensional Bose gases". In: *Physical Review Letters* 110.14 (2013), p. 145302 (Cited on page 30).

[109] R. Freeland. "Photoassociation spectroscopy of ultracold and Bose-condensed atomic gases". PhD thesis. University of Texas, Austin (2001) (Cited on page 33).

[110] I. Mordovin. "Radio-frequency induced association of molecules in ^{87}Rb". PhD thesis. Swinburne University of Technology (2015) (Cited on page 33).

[111] J. Dalibard. "Cohérence et superfluidité dans les gaz atomiques". Collège de France lectures (2016) (Cited on pages 35–38, 41, 82).

[112] T. Mori. "Electronic Properties of Organic Conductors". Springer Japan (2016), pp. 227–252 (Cited on page 35).

[113] S. Eckel, J. G. Lee, F. Jendrzejewski, N. Murray, C. W. Clark, C. J. Lobb, W. D. Phillips, M. Edwards, and G. K. Campbell. "Hysteresis in a quantized superfluid "atomtronic" circuit". In: *Nature* 506.7487 (2014), pp. 200–203 (Cited on page 36).

[114] A. Griffin. "Excitations in a Bose–Condensed Liquid". Cambridge University Press (1993) (Cited on page 37).

[115] L. Tisza. "Transport Phenomena in Helium II". In: *Nature* 141.3577 (1938), pp. 913–913 (Cited on page 37).

[116] L. Landau. "Theory of the Superfluidity of Helium II". In: *Physical Review* 60.4 (1941), pp. 356–358 (Cited on page 37).

[117] V. Peshkov. "Determination of the velocity of propagation of the second sound in helium II". In: *Soviet Journal of Experimental and Theoretical Physics* 10.1 (1946), pp. 389–398 (Cited on page 37).

[118] L. A. Sidorenkov, M. K. Tey, R. Grimm, Y.-H. Hou, L. P. Pitaevskii, and S. Stringari. "Second sound and the superfluid fraction in a Fermi gas with resonant interactions". In: *Nature* 498.7452 (2013), pp. 78–81 (Cited on pages 37, 43, 75).

[119] Q. Zhu, C. Zhang, and B. Wu. "Exotic superfluidity in spin-orbit coupled Bose-Einstein condensates". In: *Europhysics Letters* 100.5 (2012), p. 50003 (Cited on page 38).

[120] J. S. Stießberger and W. Zwerger. "Critcal velocity of superfluid flow past large obstacles in Bose-Einstein condensates". In: *Physical Review A* 62.6 (2000), p. 061601 (Cited on page 38).

[121] N. N. Bogoliubov. "On the theory of superfluidity". In: *Soviet Journal of Experimental and Theoretical Physics* 11.1 (1947), p. 23 (Cited on page 39).

[122] N. Prokof'ev, O. Ruebenacker, and B. Svistunov. "Critical Point of a Weakly Interacting Two-Dimensional Bose Gas". In: *Physical Review Letters* 87.27 (2001), p. 270402 (Cited on page 42).

[123] D. J. Bishop and J. D. Reppy. "Study of the superfluid transition in two-dimensional ^{4}He films". In: *Physical Review B* 22.11 (1980), pp. 5171–5185 (Cited on page 42).

[124] N. D. Mermin and H. Wagner. "Absence of Ferromagnetism or Antiferromagnetism in One- or Two-Dimensional Isotropic Heisenberg Models". In: *Physical Review Letters* 17.22 (1966), pp. 1133–1136 (Cited on pages 42, 112).

[125] P. C. Hohenberg. "Existence of Long-Range Order in One and Two Dimensions". In: *Physical Review* 158.2 (1967), pp. 383–386 (Cited on page 42).

[126] O. Penrose and L. Onsager. "Bose-Einstein Condensation and Liquid Helium". In: *Physical Review* 104.3 (1956), pp. 576–584 (Cited on pages 43, 47).

[127] S. Sunami, V. P. Singh, D. Garrick, A. Beregi, A. J. Barker, K. Luksch, E. Bentine, L. Mathey, and C. J. Foot. "Observation of the Berezinskii-Kosterlitz-Thouless Transition in a Two-Dimensional Bose Gas via Matter-Wave Interferometry". In: *Physical Review Letters* 128.25 (2022), p. 250402 (Cited on page 43).

[128] R. P. Feynman. "Simulating physics with computers". In: *International Journal of Theoretical Physics* 21.6 (1982), pp. 467–488 (Cited on page 46).

[129] A. Mazurenko, C. S. Chiu, G. Ji, M. F. Parsons, M. Kanász-Nagy, R. Schmidt, F. Grusdt, E. Demler, D. Greif, and M. Greiner. "A cold-atom Fermi–Hubbard antiferromagnet". In: *Nature* 545.7655 (2017), pp. 462–466 (Cited on page 46).

[130] M. Greiner, O. Mandel, T. Esslinger, T. W. Hänsch, and I. Bloch. "Quantum phase transition from a superfluid to a Mott insulator in a gas of ultracold atoms". In: *Nature* 415.6867 (2002), pp. 39–44 (Cited on page 46).

[131] M. Ben Dahan, E. Peik, J. Reichel, Y. Castin, and C. Salomon. "Bloch Oscillations of Atoms in an Optical Potential". In: *Physical Review Letters* 76.24 (1996), pp. 4508–4511 (Cited on pages 46, 110).

[132] C. Gross and I. Bloch. "Quantum simulations with ultracold atoms in optical lattices". In: *Science* 357.6355 (2017), pp. 995–1001 (Cited on page 46).

[133] G. V. Chester. "Speculations on Bose-Einstein Condensation and Quantum Crystals". In: *Physical Review A* 2.1 (1970), pp. 256–258 (Cited on page 47).

[134] E. Kim and M. H. W. Chan. "Observation of Superflow in Solid Helium". In: *Science* 305.5692 (2004), pp. 1941–1944 (Cited on page 47).

[135] J. Day and J. Beamish. "Low-temperature shear modulus changes in solid ^{4}He and connection to supersolidity". In: *Nature* 450.7171 (2007), pp. 853–856 (Cited on page 47).

[136] D. Y. Kim and M. H. W. Chan. "Absence of Supersolidity in Solid Helium in Porous Vycor Glass". In: *Physical Review Letters* 109.15 (2012), p. 155301 (Cited on page 47).

[137] M. Guo, F. Böttcher, J. Hertkorn, J.-N. Schmidt, M. Wenzel, H. P. Büchler, T. Langen, and T. Pfau. "The low-energy Goldstone mode in a trapped dipolar supersolid". In: *Nature* 574.7778 (2019), pp. 386–389 (Cited on page 47).

[138] A. Recati and S. Stringari. "Supersolidity in ultracold dipolar gases". In: *Nature Reviews Physics* 5.12 (2023), pp. 1–9 (Cited on page 47).

[139] N. Sepúlveda, C. Josserand, and S. Rica. "Nonclassical rotational inertia fraction in a one-dimensional model of a supersolid". In: *Physical Review B* 77.5 (2008), p. 054513 (Cited on page 50).

[140] G. Orso and S. Stringari. "Superfluid Fraction and Leggett Bound in a Density Modulated Strongly Interacting Fermi Gas at Zero Temperature". In: *arXiv:2311.16709* (2023) (Cited on pages 50, 51).

[141] A. Griffin and E. Zaremba. "First and second sound in a uniform Bose gas". In: *Physical Review A* 56.6 (1997), pp. 4839–4844 (Cited on page 50).

[142] T. Ozawa and S. Stringari. "Discontinuities in the First and Second Sound Velocities at the Berezinskii-Kosterlitz-Thouless Transition". In: *Physical Review Letters* 112.2 (2014), p. 025302 (Cited on pages 50, 51).

[143] M. Krämer, L. P. Pitaevskii, and S. Stringari. "Macroscopic Dynamics of a Trapped Bose-Einstein Condensate in the Presence of 1D and 2D Optical Lattices". In: *Physical Review Letters* 88.18 (2002), p. 180404 (Cited on page 51).

[144] J. Tao, M. Zhao, and I. B. Spielman. "Observation of Anisotropic Superfluid Density in an Artificial Crystal". In: *Physical Review Letters* 131.16 (2023), p. 163401 (Cited on pages 53, 65, 69).

[145] S. T. Beliaev. "Energy spectrum of a non-ideal Bose gas". In: *Soviet Journal of Experimental and Theoretical Physics* 34.299 (1958) (Cited on page 58).

[146] J. Zhang, C. Eigen, W. Zheng, J. A. P. Glidden, T. A. Hilker, S. J. Garratt, R. Lopes, N. R. Cooper, Z. Hadzibabic, and N. Navon. "Many-Body Decay of the Gapped Lowest Excitation of a Bose-Einstein Condensate". In: *Physical Review Letters* 126.6 (2021), p. 060402 (Cited on page 58).

[147] R. Grimm, M. Weidemüller, and Y. Ovchinnikov. "Optical Dipole Traps for Neutral Atoms". In: *Advances in Atomic, Molecular, and Optical Physics* 42 (2000), p. 95 (Cited on pages 58, 153).

[148] N. Chamel. "Neutron conduction in the inner crust of a neutron star in the framework of the band theory of solids". In: *Physical Review C* 85.3 (2012), p. 035801 (Cited on page 69).

[149] G. Watanabe and C. J. Pethick. "Superfluid Density of Neutrons in the Inner Crust of Neutron Stars: New Life for Pulsar Glitch Models". In: *Physical Review Letters* 119.6 (2017), p. 062701 (Cited on page 69).

[150] P. B. Blakie. "Superfluid fraction tensor of a two-dimensional supersolid". In: *arXiv:2308.14001* (2023) (Cited on pages 71, 73).

[151] P. B. Blakie, L. Chomaz, D. Baillie, and F. Ferlaino. "Compressibility and speeds of sound across the superfluid-to-supersolid phase transition of an elongated dipolar gas". In: *Physical Review Research* 5.3 (2023), p. 033161 (Cited on page 71).

[152] M. Šindik, T. Zawiślak, A. Recati, and S. Stringari. "Sound, superfluidity and layer compressibility in a ring dipolar supersolid". In: *arXiv:2308.05981* (2023) (Cited on page 71).

[153] E. Busley, L. E. Miranda, A. Redmann, C. Kurtscheid, K. K. Umesh, F. Vewinger, M. Weitz, and J. Schmitt. "Compressibility and the equation of state of an optical quantum gas in a box". In: *Science* 375.6587 (2022), pp. 1403–1406 (Cited on page 71).

[154] D. Pérez Cruz. "Superfluid fraction in disordered bosonic gases". MA thesis. Universitat Politècnica de Catalunya, Barcelona (2023) (Cited on page 73).

[155] G. Biagioni, N. Antolini, B. Donelli, L. Pezzè, A. Smerzi, M. Fattori, A. Fioretti, C. Gabbanini, M. Inguscio, L. Tanzi, and G. Modugno. "Sub-unity superfluid fraction of a supersolid from self-induced Josephson effect". In: *arXiv:2311.04757* (2023) (Cited on page 75).

[156] J. M. Dudley, C. Finot, G. Genty, and R. Taylor. "Fifty Years of Fiber Solitons". In: *Optics and Photonics News* 34.5 (2023), pp. 26–33 (Cited on pages 78, 80).

[157] C. S. Gardner, J. M. Greene, M. D. Kruskal, and R. M. Miura. "Method for Solving the Korteweg-deVries Equation". In: *Physical Review Letters* 19.19 (1967), pp. 1095–1097 (Cited on pages 78, 80).

[158] E. H. Lieb and W. Liniger. "Exact Analysis of an Interacting Bose Gas. I. The General Solution and the Ground State". In: *Physical Review* 130.4 (1963), pp. 1605–1616 (Cited on pages 78, 111).

[159] J. N. Fuchs, D. M. Gangardt, T. Keilmann, and G. V. Shlyapnikov. "Spin Waves in a One-Dimensional Spinor Bose Gas". In: *Physical Review Letters* 95.15 (2005), p. 150402 (Cited on page 79).

[160] A. Hasegawa and F. Tappert. "Transmission of stationary nonlinear optical pulses in dispersive dielectric fibers. I. Anomalous dispersion". In: *Applied Physics Letters* 23.3 (1973), pp. 142–144 (Cited on page 80).

[161] V. E. Zakharov and S. Wabnitz. "Optical Solitons: Theoretical Challenges and Industrial Perspectives". Springer-Verlag Berlin Heidelberg (1998) (Cited on page 80).

[162] E. A. Kuznetsov, A. M. Rubenchik, and V. E. Zakharov. "Soliton stability in plasmas and hydrodynamics". In: *Physics Reports* 142.3 (1986), pp. 103–165 (Cited on page 80).

[163] M.-F. Shih, P. Leach, M. Segev, M. H. Garrett, G. Salamo, and G. C. Valley. "Two-dimensional steady-state photorefractive screening solitons". In: *Optics Letters* 21.5 (1996), pp. 324–326 (Cited on page 81).

[164] V. E. Zakharov and A. B. Shabat. "Exact Theory of Two-dimensional Self-focusing and One-dimensional Self-modulation of Waves in Nonlinear Media". In: *Soviet Journal of Experimental and Theoretical Physics* 34.1 (1970), pp. 62–69 (Cited on pages 80, 115, 186).

[165] J. Satsuma and N. Yajima. "B. Initial Value Problems of One-Dimensional Self-Modulation of Nonlinear Waves in Dispersive Media". In: *Progress of Theoretical Physics Supplement* 55 (1974), pp. 284–306 (Cited on page 82).

[166] L. F. Mollenauer, R. H. Stolen, J. P. Gordon, and W. J. Tomlinson. "Extreme picosecond pulse narrowing by means of soliton effect in single-mode optical fibers". In: *Optics Letters* 8.5 (1983), pp. 289–291 (Cited on page 82).

[167] J. E. Bjorkholm and A. A. Ashkin. "cw Self-Focusing and Self-Trapping of Light in Sodium Vapor". In: *Physical Review Letters* 32.4 (1974), pp. 129–132 (Cited on pages 82, 85).

[168] K. E. Strecker, G. B. Partridge, A. G. Truscott, and R. G. Hulet. "Formation and propagation of matter-wave soliton trains". In: *Nature* 417.6885 (2002), pp. 150–153 (Cited on page 82).

[169] L. Salasnich, A. Parola, and L. Reatto. "Modulational Instability and Complex Dynamics of Confined Matter-Wave Solitons". In: *Physical Review Letters* 91.8 (2003), p. 080405 (Cited on page 82).

[170] S. Burger, K. Bongs, S. Dettmer, W. Ertmer, K. Sengstock, A. Sanpera, G. V. Shlyapnikov, and M. Lewenstein. "Dark Solitons in Bose-Einstein Condensates". In: *Physical Review Letters* 83.25 (1999), pp. 5198–5201 (Cited on page 83).

[171] Th. Busch and J. R. Anglin. "Motion of Dark Solitons in Trapped Bose-Einstein Condensates". In: *Physical Review Letters* 84.11 (2000), pp. 2298–2301 (Cited on pages 82, 120, 186).

[172] T. Marest. "Solitons sombres et ondes dispersives dans les fibres optiques". PhD thesis. Université de Lille (2018) (Cited on page 83).

[173] A. M. Weiner, J. P. Heritage, R. J. Hawkins, R. N. Thurston, E. M. Kirschner, D. E. Leaird, and W. J. Tomlinson. "Experimental Observation of the Fundamental Dark Soliton in Optical Fibers". In: *Physical Review Letters* 61.21 (1988), pp. 2445–2448 (Cited on page 83).

[174] S. Trillo, S. Wabnitz, E. M. Wright, and G. I. Stegeman. "Optical solitary waves induced by cross-phase modulation". In: *Optics Letters* 13.10 (1988), pp. 871–873 (Cited on page 84).

[175] S. T. Cundiff, B. C. Collings, N. N. Akhmediev, J. M. Soto-Crespo, K. Bergman, and W. H. Knox. "Observation of Polarization-Locked Vector Solitons in an Optical Fiber". In: *Physical Review Letters* 82.20 (1999), pp. 3988–3991 (Cited on page 84).

[176] G. D. Shao, J. Guo, X. Hu, Y. F. Song, L. M. Zhao, and D. Y. Tang. "Vector dark solitons in a single mode fibre laser". In: *Laser Physics Letters* 16.8 (2019), p. 085110 (Cited on page 84).

[177] J. Ma, G. D. Shao, Y. F. Song, L. M. Zhao, Y. J. Xiang, D. Y. Shen, M. Richardson, and D. Y. Tang. "Observation of dark-bright vector solitons in fiber lasers". In: *Optics Letters* 44.9 (2019), pp. 2185–2188 (Cited on pages 84, 140).

[178] S. V. Manakov. "On the theory of two-dimensional stationary self-focusing of electromagnetic waves". In: *Soviet Physics Journal of Experimental and Theoretical Physics* 38.2 (1974), pp. 248–253 (Cited on pages 84, 93).

[179] G. C. Katsimiga, J. Stockhofe, P. G. Kevrekidis, and P. Schmelcher. "Dark-bright soliton interactions beyond the integrable limit". In: *Physical Review A* 95.1 (2017), p. 013621 (Cited on page 84).

[180] M. O. D. Alotaibi and L. D. Carr. "Dynamics of dark-bright vector solitons in Bose-Einstein condensates". In: *Physical Review A* 96.1 (2017), p. 013601 (Cited on page 84).

[181] B. P. Anderson, P. C. Haljan, C. A. Regal, D. L. Feder, L. A. Collins, C. W. Clark, and E. A. Cornell. "Watching Dark Solitons Decay into Vortex Rings in a Bose-Einstein Condensate". In: *Physical Review Letters* 86.14 (2001), pp. 2926–2929 (Cited on page 85).

[182] M. A. Hoefer, J. J. Chang, C. Hamner, and P. Engels. "Dark-dark solitons and modulational instability in miscible two-component Bose-Einstein condensates". In: *Physical Review A* 84.4 (2011), p. 041605 (Cited on page 85).

[183] E. A. Kuznetsov. "Solitons in a parametrically unstable plasma". Akademiia Nauk SSSR Doklady (1977), pp. 575–577 (Cited on page 85).

[184] B. Kibler, J. Fatome, C. Finot, G. Millot, G. Genty, B. Wetzel, N. Akhmediev, F. Dias, and J. M. Dudley. "Observation of Kuznetsov-Ma soliton dynamics in optical fibre". In: *Scientific Reports* 2.1 (2012), p. 463 (Cited on page 85).

[185] B. Kibler, J. Fatome, C. Finot, G. Millot, F. Dias, G. Genty, N. Akhmediev, and J. M. Dudley. "The Peregrine soliton in nonlinear fibre optics". In: *Nature Physics* 6.10 (2010), pp. 790–795 (Cited on page 85).

[186] D. H. Peregrine. "Water waves, nonlinear Schrödinger equations and their solutions". In: *The ANZIAM Journal* 25.1 (1983), pp. 16–43 (Cited on page 85).

[187] A. Romero-Ros, G. C. Katsimiga, S. I. Mistakidis, S. Mossman, G. Biondini, P. Schmelcher, P. Engels, and P. G. Kevrekidis. "Experimental realization of the Peregrine soliton in repulsive two-component Bose-Einstein condensates". In: *arXiv:2304.05951* (2023) (Cited on page 85).

[188] A. Romero-Ros, G. C. Katsimiga, S. I. Mistakidis, B. Prinari, G. Biondini, P. Schmelcher, and P. G. Kevrekidis. "Theoretical and numerical evidence for the potential realization of the Peregrine soliton in repulsive two-component Bose-Einstein condensates". In: *Physical Review A* 105.5 (2022), p. 053306 (Cited on page 85).

[189] Z. Dutton and C. W. Clark. "Effective one-component description of two-component Bose-Einstein condensate dynamics". In: *Physical Review A* 71.6 (2005), p. 063618 (Cited on page 85).

[190] B. Bakkali-Hassani, C. Maury, Y.-Q. Zou, É. Le Cerf, R. Saint-Jalm, P. C. M. Castilho, S. Nascimbene, J. Dalibard, and J. Beugnon. "Realization of a Townes Soliton in a Two-Component Planar Bose Gas". In: *Physical Review Letters* 127.2 (2021), p. 023603 (Cited on pages 85, 122, 128, 129).

[191] S. L. Cornish, S. T. Thompson, and C. E. Wieman. "Formation of Bright Matter-Wave Solitons during the Collapse of Attractive Bose-Einstein Condensates". In: *Physical Review Letters* 96.17 (2006), p. 170401 (Cited on page 85).

[192] N. Meyer, H. Proud, M. Perea-Ortiz, C. O'Neale, M. Baumert, M. Holynski, J. Kronjäger, G. Barontini, and K. Bongs. "Observation of Two-Dimensional Localized Jones-Roberts Solitons in Bose-Einstein Condensates". In: *Physical Review Letters* 119.15 (2017), p. 150403 (Cited on page 85).

[193] J. W. Fleischer, M. Segev, N. K. Efremidis, and D. N. Christodoulides. "Observation of two-dimensional discrete solitons in optically induced nonlinear photonic lattices". In: *Nature* 422.6928 (2003), pp. 147–150 (Cited on page 85).

[194] J. Yang and Z. H. Musslimani. "Fundamental and vortex solitons in a two-dimensional optical lattice". In: *Optics Letters* 28.21 (2003), pp. 2094–2096 (Cited on page 85).

[195] Y. V. Kartashov, B. A. Malomed, and L. Torner. "Solitons in nonlinear lattices". In: *Review Modern Physics* 83.1 (2011), pp. 247–305 (Cited on page 85).

[196] B. Bakkali-Hassani, C. Maury, S. Stringari, S. Nascimbene, J. Dalibard, and J. Beugnon. "The cross-over from Townes solitons to droplets in a 2D Bose mixture". In: *New Journal of Physics* 25.1 (2023), p. 013007 (Cited on page 86).

[197] L. D. Landau and E. Lifshitz. "On the theory of the dispersion of magnetic permeability in ferromagnetic bodies". In: *Physikalische Zeitschrift der Sowjetunion* 8 (1935), p. 153 (Cited on page 86).

[198] K. A. Long and A. R. Bishop. "Nonlinear excitations in classical ferromagnetic chains". In: *Journal of Physics A: Mathematical and General* 12.8 (1979), p. 1325 (Cited on page 92).

[199] E. Timmermans. "Phase Separation of Bose-Einstein Condensates". In: *Physical Review Letters* 81.26 (1998), pp. 5718–5721 (Cited on page 94).

[200] A. Gallemí, L. P. Pitaevskii, S. Stringari, and A. Recati. "Magnetic defects in an unbalanced mixture of two Bose-Einstein condensates". In: *Physical Review A* 97.6 (2018) (Cited on page 94).

[201] I. S. Gradshteyn and I. M. Ryzhik. "Table of integrals, series, and products". Academic press (2014) (Cited on page 96).

[202] L. P. Pitaevskii. "Dynamics of solitary waves in ultracold gases in terms of observable quantities". In: *Physics-Uspekhi* 59.10 (2016), p. 1028 (Cited on pages 98, 185–187).

[203] N. W. Ashcroft and N. D. Mermin. "Solid state physics". Saunders College Publishing (1976) (Cited on page 108).

[204] F. Bloch. "Über die Quantenmechanik der Elektronen in Kristallgittern". In: *Zeitschrift für Physik* 52.7 (1929), pp. 555–600 (Cited on page 108).

[205] J. Zak. "Berry's phase for energy bands in solids". In: *Physical Review Letters* 62.23 (1989), pp. 2747–2750 (Cited on page 109).

[206] S. R. Wilkinson, C. F. Bharucha, K. W. Madison, Q. Niu, and M. G. Raizen. "Observation of Atomic Wannier-Stark Ladders in an Accelerating Optical Potential". In: *Physical Review Letters* 76.24 (1996), pp. 4512–4515 (Cited on page 110).

[207] B. Pelle, A. Hilico, G. Tackmann, Q. Beaufils, and F. Pereira dos Santos. "State-labeling Wannier-Stark atomic interferometers". In: *Physical Review A* 87.2 (2013), p. 023601 (Cited on pages 110, 140).

[208] I. Carusotto, L. P. Pitaevskii, S. Stringari, G. Modugno, and M. Inguscio. "Sensitive Measurement of Forces at the Micron Scale Using Bloch Oscillations of Ultracold Atoms". In: *Physical Review Letters* 95.9 (2005), p. 093202 (Cited on page 110).

[209] M. D. Girardeau. "Relationship between Systems of Impenetrable Bosons and Fermions in One Dimension". In: *Journal of Mathematical Physics* 1.6 (1960), pp. 516–523 (Cited on page 111).

[210] T. Kinoshita, T. Wenger, and D. S. Weiss. "Observation of a One-Dimensional Tonks-Girardeau Gas". In: *Science* 305.5687 (2004), pp. 1125–1128 (Cited on page 111).

[211] D. K. K. Lee and J. M. F. Gunn. "Polarons and Bose decondensation: A self-trapping approach". In: *Physical Review B* 46.1 (1992), pp. 301–307 (Cited on page 111).

[212] M. Will and M. Fleischhauer. "Dynamics of polaron formation in 1D Bose gases in the strong-coupling regime". In: *New Journal of Physics* 25.8 (2023), p. 083043 (Cited on page 112).

[213] B. D. Josephson. "Possible new effects in superconductive tunnelling". In: *Physics Letters* 1.7 (1962), pp. 251–253 (Cited on page 112).

[214] F. Arute, K. Arya, R. Babbush, D. Bacon, J. C. Bardin, R. Barends, R. Biswas, S. Boixo, F. G. S. L. Brandao, D. A. Buell, B. Burkett, Y. Chen, Z. Chen, B. Chiaro, R. Collins, W. Courtney, A. Dunsworth, E. Farhi, B. Foxen, A. Fowler, C. Gidney, M. Giustina, R. Graff, K. Guerin, S. Habegger, M. P. Harrigan, M. J. Hartmann, A. Ho, M. Hoffmann, T. Huang, T. S. Humble, S. V. Isakov, E. Jeffrey, Z. Jiang, D. Kafri, K. Kechedzhi, J. Kelly, P. V. Klimov, S. Knysh, A. Korotkov, F. Kostritsa, D. Landhuis, M. Lindmark, E. Lucero, D. Lyakh, S. Mandrà, J. R. McClean, M. McEwen, A. Megrant, X. Mi, K. Michielsen, M. Mohseni, J. Mutus, O. Naaman, M. Neeley, C. Neill, M. Y. Niu, E. Ostby, A. Petukhov, J. C. Platt, C. Quintana, E. G. Rieffel, P. Roushan, N. C. Rubin, D. Sank, K. J. Satzinger, V. Smelyanskiy, K. J. Sung, M. D. Trevithick, A. Vainsencher, B. Villalonga, T. White, Z. J. Yao, P. Yeh, A. Zalcman, H. Neven, and J. M. Martinis. "Quantum supremacy using a programmable superconducting processor". In: *Nature* 574.7779 (2019), pp. 505–510 (Cited on page 112).

[215] K. Sukhatme, Y. Mukharsky, T. Chui, and D. Pearson. "Observation of the ideal Josephson effect in superfluid ^{4}He". In: *Nature* 411.6835 (2001), pp. 280–283 (Cited on page 112).

[216] F. S. Cataliotti, S. Burger, C. Fort, P. Maddaloni, F. Minardi, A. Trombettoni, A. Smerzi, and M. Inguscio. "Josephson Junction Arrays with Bose-Einstein Condensates". In: *Science* 293.5531 (2001), pp. 843–846 (Cited on page 112).

[217] M. Albiez, R. Gati, J. Fölling, S. Hunsmann, M. Cristiani, and M. K. Oberthaler. "Direct Observation of Tunneling and Nonlinear Self-Trapping in a Single Bosonic Josephson Junction". In: *Physical Review Letters* 95.1 (2005), p. 010402 (Cited on page 112).

[218] S. Levy, E. Lahoud, I. Shomroni, and J. Steinhauer. "The a.c. and d.c. Josephson effects in a Bose–Einstein condensate". In: *Nature* 449.7162 (2007), pp. 579–583 (Cited on page 112).

[219] F. S. Nogueira and K.-H. Bennemann. "Spin Josephson effect in ferromagnet/ferromagnet tunnel junctions". In: *Europhysics Letters* 67.4 (2004), p. 620 (Cited on page 112).

[220] A. S. Borovik-Romanov, Y. M. Bunkov, V. V. Dmitriev, Y. M. Mukharskiy, and D. A. Sergatskov. "Investigation of spin supercurrents in ^3B". In: *Physical Review Letters* 62.14 (1989), pp. 1631–1634 (Cited on page 112).

[221] M. Schecter, D. M. Gangardt, and A. Kamenev. "Quantum impurities: from mobile Josephson junctions to depletons". In: *New Journal of Physics* 18.6 (2016), p. 065002 (Cited on page 114).

[222] Y. S. Kivshar and D. E. Pelinovsky. "Self-focusing and transverse instabilities of solitary waves". In: *Physics Reports* 331.4 (2000), pp. 117–195 (Cited on pages 115, 186).

[223] M. J. H. Ku, B. Mukherjee, T. Yefsah, and M. W. Zwierlein. "Cascade of Solitonic Excitations in a Superfluid Fermi gas: From Planar Solitons to Vortex Rings and Lines". In: *Physical Review Letters* 116.4 (2016), p. 045304 (Cited on page 115).

[224] X. Yu and P. B. Blakie. "Propagating Ferrodark Solitons in a Superfluid: Exact Solutions and Anomalous Dynamics". In: *Physical Review Letters* 128.12 (2022), p. 125301 (Cited on page 115).

[225] L. P. Pitaevskii. "On the momentum of solitons and vortex rings in a superfluid". In: *Journal of Experimental and Theoretical Physics* 119.6 (2014), pp. 1097–1101 (Cited on page 116).

[226] A. Widera, F. Gerbier, S. Fölling, T. Gericke, O. Mandel, and I. Bloch. "Precision measurement of spin-dependent interaction strengths for spin-1 and spin-2 ^{87}Rb atoms". In: *New Journal of Physics* 8.8 (2006), p. 152 (Cited on page 123).

[227] E. G. M. van Kempen, S. J. J. M. F. Kokkelmans, D. J. Heinzen, and B. J. Verhaar. "Interisotope Determination of Ultracold Rubidium Interactions from Three High-Precision Experiments". In: *Physical Review Letters* 88.9 (2002), p. 093201 (Cited on page 123).

[228] Y. Eto, M. Takahashi, M. Kunimi, H. Saito, and T. Hirano. "Corrigendum: Non-equilibrium dynamics induced by miscible–immiscible transition in binary Bose–Einstein condensates (2016 New J. Phys. 18 073029)". In: *New Journal of Physics* 20.1 (2018), p. 019501 (Cited on page 123).

[229] Y. Eto, M. Takahashi, M. Kunimi, H. Saito, and T. Hirano. "Nonequilibrium dynamics induced by miscible–immiscible transition in binary Bose–Einstein condensates". In: *New Journal of Physics* 18.7 (2016), p. 073029 (Cited on page 123).

[230] S. De, D. L. Campbell, R. M. Price, A. Putra, B. M. Anderson, and I. B. Spielman. "Quenched binary Bose-Einstein condensates: Spin-domain formation and coarsening". In: *Physical Review A* 89.3 (2014), p. 033631 (Cited on page 123).

[231] Y.-Q. Zou, B. Bakkali-Hassani, C. Maury, É. Le Cerf, S. Nascimbene, J. Dalibard, and J. Beugnon. "Magnetic Dipolar Interaction between Hyperfine Clock States in a Planar Alkali Bose Gas". In: *Physical Review Letters* 125.23 (2020), p. 233604 (Cited on page 123).

[232] D. N. Christodoulides. "Black and white vector solitons in weakly birefringent optical fibers". In: *Physics Letters A* 132.8 (1988), pp. 451–452 (Cited on page 140).

[233] T. Kinoshita, T. Wenger, and D. S. Weiss. "All-optical Bose-Einstein condensation using a compressible crossed dipole trap". In: *Physical Review A* 71.1 (2005), p. 011602 (Cited on pages 144, 152).

[234] V. Vuletic, C. Chin, A. J. Kerman, and S. Chu. "Degenerate Raman Sideband Cooling of Trapped Cesium Atoms at Very High Atomic Densities". In: *Physical Review Letters* 81.26 (1998), pp. 5768–5771 (Cited on pages 145, 152).

[235] Z. Li, W. Ma, W. Yang, Y. Wang, and Y. Zheng. "Reduction of zero baseline drift of the Pound–Drever–Hall error signal with a wedged electro-optical crystal for squeezed state generation". In: *Optics Letters* 41.14 (2016), pp. 3331–3334 (Cited on page 147).

[236] E. A. Donley, T. P. Heavner, F. Levi, M. O. Tataw, and S. R. Jefferts. "Double-pass acousto-optic modulator system". In: *Review of Scientific Instruments* 76.6 (2005), p. 063112 (Cited on page 148).

[237] J. J. Snyder. "Paraxial ray analysis of a cat's-eye retroreflector". In: *Applied Optics* 14.8 (1975), pp. 1825–1828 (Cited on page 148).

[238] M. Bordoux. "Développement d'une source de condensats de Bose-Einstein pour l'interférométrie atomique". PhD thesis. Université Toulouse III - Paul Sabatier (2019) (Cited on page 151).

[239] S. Stellmer, R. Grimm, and F. Schreck. "Production of quantum-degenerate strontium gases". In: *Physical Review A* 87.1 (2013), p. 013611 (Cited on page 151).

[240] H. J. Lee, C. S. Adams, M. Kasevich, and S. Chu. "Raman Cooling of Atoms in an Optical Dipole Trap". In: *Physical Review Letters* 76.15 (1996), pp. 2658–2661 (Cited on page 152).

[241] A. Urvoy, Z. Vendeiro, J. Ramette, A. Adiyatullin, and V. Vuletic. "Direct Laser Cooling to Bose-Einstein Condensation in a Dipole Trap". In: *Physical Review Letters* 122.20 (2019), p. 203202 (Cited on page 152).

[242] K. Yamashita, K. Hanasaki, A. Ando, M. Takahama, and T. Kinoshita. "All-optical production of a large Bose-Einstein condensate in a double compressible crossed dipole trap". In: *Physical Review A* 95.1 (2017), p. 013609 (Cited on page 152).

[243] M. Gröbner, P. Weinmann, E. Kirilov, and H.-C. Nägerl. "Degenerate Raman sideband cooling of ^{39}K". In: *Physical Review A* 95.3 (2017), p. 033412 (Cited on page 152).

[244] G. A. Phelps, A. Hébert, A. Krahn, S. Dickerson, F. Öztürk, S. Ebadi, L. Su, and M. Greiner. "Sub-second production of a quantum degenerate gas". In: *arXiv:2007.10807* (2020) (Cited on page 152).

[245] R. Roy, A. Green, R. Bowler, and S. Gupta. "Rapid cooling to quantum degeneracy in dynamically shaped atom traps". In: *Physical Review A* 93.4 (2016), p. 043403 (Cited on pages 152, 154).

[246] K. M. O'Hara, M. E. Gehm, S. R. Granade, and J. E. Thomas. "Scaling laws for evaporative cooling in time-dependent optical traps". In: *Physical Review A* 64.5 (2001), p. 051403 (Cited on page 154).

[247] C.-L. Hung, X. Zhang, N. Gemelke, and C. Chin. "Accelerating evaporative cooling of atoms into Bose-Einstein condensation in optical traps". In: *Physical Review A* 78.1 (2008), p. 011604 (Cited on page 154).

[248] J.-F. Clément, J.-P. Brantut, M. Robert-De-Saint-Vincent, R. A. Nyman, A. Aspect, T. Bourdel, and P. Bouyer. "All-optical runaway evaporation to Bose-Einstein condensation". In: *Physical Review A* 79.6 (2009), p. 061406 (Cited on page 154).

[249] H. Albers. "Time-averaged optical potentials for creating and shaping Bose-Einstein condensates". PhD thesis. Gottfried Wilhelm Leibniz Universität (2020) (Cited on page 156).

[250] G. Cennini, G. Ritt, C. Geckeler, and M. Weitz. "All-Optical Realization of an Atom Laser". In: *Physical Review Letters* 91.24 (2003), p. 240408 (Cited on page 159).

[251] A. Couvert. "Production et étude de lasers à atomes guidés, et de leur interaction avec des défauts contrôlés". PhD thesis. Université Pierre et Marie Curie - Paris VI (2009) (Cited on page 159).

[252] A. Évrard. "Non Gaussian Spin States of Ultracold Dysprosium Atoms". PhD thesis. Université Paris Sciences Lettres (2020) (Cited on page 160).

[253] H. Labuhn, D. Barredo, S. Ravets, S. de Léséleuc, T. Macrì, T. Lahaye, and A. Browaeys. "Tunable two-dimensional arrays of single Rydberg atoms for realizing quantum Ising models". In: *Nature* 534.7609 (2016), pp. 667–670 (Cited on page 163).

[254] D. Barredo, S. Ravets, H. Labuhn, L. Béguin, A. Vernier, F. Nogrette, T. Lahaye, and A. Browaeys. "Demonstration of a Strong Rydberg Blockade in Three-Atom Systems with Anisotropic Interactions". In: *Physical Review Letters* 112.18 (2014), p. 183002 (Cited on page 163).

[255] S. de Léséleuc, V. Lienhard, P. Scholl, D. Barredo, S. Weber, N. Lang, H. P. Büchler, T. Lahaye, and A. Browaeys. "Observation of a symmetry-protected topological phase of interacting bosons with Rydberg atoms". In: *Science* 365.6455 (2019), pp. 775–780 (Cited on page 163).

[256] A. W. Glaetzle, M. Dalmonte, R. Nath, C. Gross, I. Bloch, and P. Zoller. "Designing Frustrated Quantum Magnets with Laser-Dressed Rydberg Atoms". In: *Physical Review Letters* 114.17 (2015), p. 173002 (Cited on page 163).

[257] G. Pupillo, A. Micheli, M. Boninsegni, I. Lesanovsky, and P. Zoller. "Strongly Correlated Gases of Rydberg-Dressed Atoms: Quantum and Classical Dynamics". In: *Physical Review Letters* 104.22 (2010), p. 223002 (Cited on page 163).

[258] J. Zeiher, R. van Bijnen, P. Schauß, S. Hild, J. Choi, T. Pohl, I. Bloch, and C. Gross. "Many-body interferometry of a Rydberg-dressed spin lattice". In: *Nature Physics* 12.12 (2016), pp. 1095–1099 (Cited on page 163).

[259] S. Zhang, F. Robicheaux, and M. Saffman. "Magic-wavelength optical traps for Rydberg atoms". In: *Physical Review A* 84.4 (2011), p. 043408 (Cited on page 163).

[260] T. Förster. "Zwischenmolekulare Energiewanderung und Fluoreszenz". In: *Annalen der Physik* 437.1 (1948), pp. 55–75 (Cited on page 163).

[261] M. Plodzień, G. Lochead, J. de Hond, N. J. van Druten, and S. Kokkelmans. "Rydberg dressing of a one-dimensional Bose-Einstein condensate". In: *Physical Review A* 95.4 (2017), p. 043606 (Cited on page 163).

[262] W. Bao, D. Jaksch, and P. A. Markowich. "Numerical solution of the Gross–Pitaevskii equation for Bose–Einstein condensation". In: *Journal of Computational Physics* 187.1 (2003), pp. 318–342 (Cited on page 172).

[263] J. Javanainen and J. Ruostekoski. "Symbolic calculation in development of algorithms: split-step methods for the Gross–Pitaevskii equation". In: *Journal of Physics A: Mathematical and General* 39.12 (2006), p. L179 (Cited on page 172).

[264] V. V. Konotop and L. P. Pitaevskii. "Landau Dynamics of a Grey Soliton in a Trapped Condensate". In: *Physical Review Letters* 93.24 (2004), p. 240403 (Cited on pages 185, 186).

[265] V. A. Brazhnyi, V. V. Konotop, and L. P. Pitaevskii. "Dark solitons as quasiparticles in trapped condensates". In: *Physical Review A* 73.5 (2006), p. 053601 (Cited on pages 185, 186).